C umhuriyet

S cience

J ournal

Cumhuriyet Science Journal (CSJ)

Derginin Eski Adı: Cumhuriyet Üniversitesi Fen-Edebiyat Fakültesi Fen Bilimleri Dergisi

Eski ISSN: 1300-1949

Akademik Dizin / Abstracted/Indexed in

Ulakbim TR-Dizin

Akademik Dizin

Arastirmax Bilimsel Yayın İndeksi

Bielefeld Academic Search Engine (BASE)

Directory of Open Access Journals (DOAJ)

Directory of Research Journal Indexing (DRJI)

Google Scholar

Index Copernicus

Research Gate

Thomson Reuters Zoological

WorldCat

CUMHURİYET SCIENCE JOURNAL

CONTENTS

Growth of Cu₂ZnSnS₄ Thin Films Using Moderate Annealing Temperature and Short Dwell Time

Mehmet Ali OLĞAR[1]* , Ayşe SEYHAN[2]

[1,2]*Department of Physics, Nigde Ömer Halisdemir University, Merkez, 51240 Nigde, Turkey*

[1,2]*Nanotechnology Application and Research Center, Nigde Ömer Halisdemir University, Nigde, Turkey*

Abstract. In this study CZTS thin films were fabricated by a two-stage process that sputter deposition of metallic Cu, Zn, and Sn on Mo coated glass substrates and annealing process at 500 °C using various short dwell times (4, 8, and 12 min) using Rapid Thermal Processing (RTP) approach. The X-ray diffraction (XRD), Raman spectroscopy, Scanning Electron Microscopy (SEM), Energy Dispersive X-ray Spectroscopy (EDX), and photoluminescence were employed to characterize the CZTS samples synthesized employing different sulfurization times. It was observed that all CZTS thin films showed Cu-poor and Zn-rich composition according to EDX results. XRD patterns displayed formation of kesterite CZTS and CuS secondary phases. Raman spectra of the films justified formation of kesterite CZTS phase for all CZTS thin films and formation of CTS phase, which is difficult to distinguish by XRD pattern of the films for CZTS-8 and CZTS-12 samples. SEM images of the films displayed dense, void-free, and inhomogeneous surface structure regardless of the sulfurization time. The optical band gap of the films as determined by photoluminescence was found to be about 1.36-1.37 eV.

Keywords: Cu₂ZnSnS₄, Sputtering, Annealing Time, Annealing Temperature, RTP

Yüksek Olmayan Tavlama Sıcaklığı ve Kısa Bekleme Süresi Kullanılarak Cu₂ZnSnS₄ İnce Filmlerin Üretimi

Özet. Bu çalışmada CZTS ince filmler iki-aşamalı yöntem kullanılarak üretildi; Mo kaplı cam üzerine saçtırma yöntemiyle metalik Cu, Zn ve Sn katmanlarının kaplanması ve sonrasında bu katmanlı yapının 500 °C sıcaklık ve farklı kısa sürelerde (4, 8 ve 12 dakika) hızlı ısıl işlem (RTP) yaklaşımı ile tavlanması. Farklı tavlama süreleri ile üretilen CZTS örnekler X-ışını kırınımı (XRD), Raman spektroskopisi, Taramalı Elektron Mikroskobu (SEM), Enerji Dağılımlı X-ışını Spektroskopisi (EDX) ve fotoluminesans teknikleri kullanılarak karakterize edilmiştir. Üretilen bütün CZTS örneklerin Cu-fakiri ve Zn-zengini kimyasal kompozisyona sahip olduğu ve XRD desenlerinde CZTS fazı oluşumun yanında CuS fazının da oluştuğu görülmüştür. Raman spektroskopisi ile hem CZTS fazının oluştuğu doğrulanmış olup hem de XRD ile ayırt edilemeyen CTS fazının oluştuğu tespit edilmiştir. SEM ile elde edilen film yüzey görüntülerinin sülfürleme süresinden bağımsız olarak yoğun, deliksiz ve homojen olmayan bir yapıya sahip oldukları tespit edilmiştir. Fotolüminesans spektrumları ile optik yasak enerji aralığının 1.36-137 civarında olduğu belirlenmiştir.

Anahtar Kelimeler: Cu₂ZnSnS₄, saçtırma, tavlama süresi; tavlama sıcaklığı, RTP

---

* Corresponding author. *Email address:* mehmetaliolgar@gmail.com

1. INTRODUCTION

Thin film solar cells have attracted increasing interest due to the usage of fewer materials and high conversion efficiency. The current record conversion efficiency of CIGS-based thin film solar cells have already reached 22.9 % [1]. Despite its high conversion efficiency, scarcity of In and Ga has been shown as a major issue for further developments of CIGS-based thin film solar cells. Thin film solar cells can be further developed by exploring new materials which includes both earth-abundant and environmental-friendly raw materials. Based on the research in the literature, kesterite Cu_2ZnSnS_4 (CZTS) thin film compound has been considered as a promising material in place of CIGS in the last decade since it contains more abundant elements (Zn and Sn instead of Ga and In) and shows superior optical properties for thin film solar cell applications such as p-type conductivity, at around of 1.4-1.5 eV optical band gap energy and over 10^4 cm^{-1} absorption coefficient [2]. Although Shockley–Queisser limit demonstrated that the theoretical limit is over %30 [3] for CZTS-based thin film solar cell, so far the record conversion efficiency is still 12.6% obtained by $Cu_2ZnSn(S, Se)_4$ thin film compound fabricated using hydrazine-based solution method [4]. The difference between theoretical limit and reported record conversion efficiency value may be attributed to several reasons. Therefore, further investigations should be performed to decrease the gap between the theoretical limit and reported efficiencies.

CZTS thin films can be synthesized using different methods. For example, thermal evaporation [5], e-beam evaporation [6], sputtering [7], and pulse laser deposition (PLD) [8] are vacuum-based methods, sol-gel deposition [9], electro-deposition [10], spin coating [11] and spray pyrolysis [12] methods non-vacuum methods. The vacuum-based preparation techniques are preferable rather than non-vacuum methods with respect to controlling thickness of metallic precursor layers and composition of the films, homogenous film structure and reproducibility of the fabrication process. Sputtering method is one of the vacuum-based technique and the most common method for fabrication of thin film precursor layers since it can easily be scaled up for large area film deposition. After deposition of the metallic precursor layers (Cu, Zn, and Sn) using sputteing method, they are annealed to obtain complete CZTS structure. The Rapid Thermal Processing (RTP) method is more suitable for industrial applications thanks to usage of less energy and higher throughput. In addition, the RTP is an attractive method since the shorter dwell time at high reaction temperature restricts decomposition of the reaction hence restricts loss of elements.

To obtain high conversion efficiency CZTS-based thin film solar cells, many different approaches have been used. Most of the reported studies have focused on the optimizing fabrication parameters of the CZTS absorber layer since solar cell efficiency is strongly-dependent on the quality of the absorber layer. These studies include optimization of the sulfurization temperature[13] , sulfurization time [14], variation order of the metallic stack [15], composition of film [16, 17], and the pressure of the sulfurization [18, 19] etc. The prior works have suggested that although high reaction temperatures (> 500 °C) may enhance the grain morphology, it also gives rise to loss of Sn and Zn thanks to the high vapor pressure of SnS and Zn [20]. Many different approaches were used to prevent Sn-loss from films. For example, employing different sulfurization temperatures and time [7, 13], variation of the sulfurization pressure [18, 19] and stacking order of the metallic Cu, Zn, and Sn layers [15], alloying of Sn with Cu or heating of the metallic constitutes prior sulfurization process [21, 22], and using single target in replace of metallic layers [23], etc.

In this study, it was targeted to grow Sn loss-free CZTS thin films by employing moderate sulfurization temperatures. Therefore, the Mo/Cu/Sn/Zn/Cu metallic stack which was firstly suggested by our research group was utilized [15] and presents promising results for solar cell performance [24] . Then, the metallic stacks were annealed at 500 °C for short dwell times (4, 8, and 12 min) using RTP approach.

2. MATERIAL AND METHOD

The metallic layers (Cu, Zn, and Sn) were sequentially deposited on molybdenum (Mo) coated glass employing DC magnetron sputtering to obtain Cu/Sn/Zn/Cu metallic stacks. High purity Cu (%99.99), Sn (%99.999), and Zn (%99.99) were utilized for sputtering process. The base pressure of the sputter chamber before the deposition process was 10^{-6} torr and operation pressure through the

deposition process was 10^{-3} torr. The thickness of the metallic films was calibrated to 175, 165, and 230 nm for Cu, Zn, and Sn layers, respectively. 120 nm of Cu layer was deposited on Mo and 55 nm of Cu was deposited on top of Zn. DektakXT profilometer was utilized for thickness calibration of the films. For example, one of the thickness calibration measurement taking from profilometer was given in Figure 1.   In the present figure,

calibration measurement of Zn layer was displayed. As can be seen in the figure, the thickness of the Zn layer was found around 165 nm. It is worth noting that this measurement is one of the several calibration measurement. The real value was obtained by taking average of several measurements from different points.
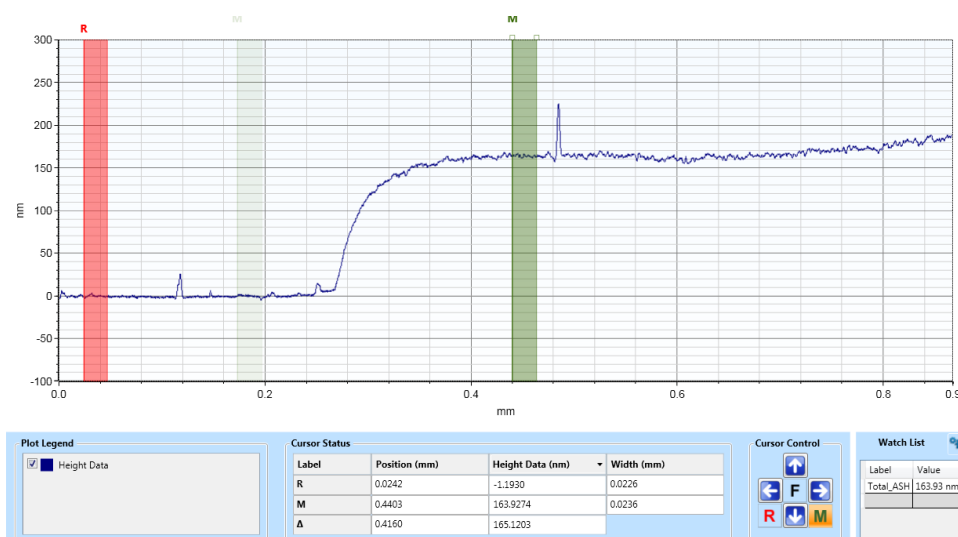
Figure 1. Thickness calibration measurement of Zn layer taken from profilometer.

After loading of the metallic stacks into a graphite box with elemental sulfur, the sulfurization process was carried out at 500 °C using quartz lamps at a rate of 3 °C/s in a 95% Ar + 5%H_2 gas mixture for dwell times of 4, 8, and 12 min at the reaction temperature. Further details about the annealing process have been reported elsewhere [7]. The CZTS samples obtained after sulfurization process were encoded according to their sulfurization time. For example, CZTS-4 stands for the sample sulfurized at 500 °C for dwell time of 4 min, and CZTS-8 represents the sample sulfurized for dwell time of 8 min (see Table 1).

PANalytical Empyrean diffractometer (λ=1.5405 Å) was employed to characterize crystalline quality of the films. Raman analysis was carried out using Renishaw inVia Spectrometer (λ=633 nm). The microstructure and concentration of the films were examined by Scanning electron microscope (SEM)

Zeiss Evo 40 and an EDAX energy dispersive X-ray spectroscopy (EDX) system. Optical properties of the films were characterized by photoluminescence spectra (Renishaw inVia Spectrometer, λ= 532 nm) obtained at ambient temperature.

Table 1. Fabrication parameters of CZTS thin films.

Specimen	Layer Order	Annealing Temperature (°C)	Annealing Time (min)
CZTS-4	Cu/Sn/Zn/Cu	500	4
CZTS-8	Cu/Sn/Zn/Cu	500	8
CZTS-12	Cu/Sn/Zn/Cu	500	12

3.   RESULTS AND DISCUSSION

3.1. EDX

The atomic percentage of the metallic precursor (Cu/Sn/Zn/Cu) and CZTS thin films taken by EDX was displayed in their EDX spectrum of the samples (Figure 2).
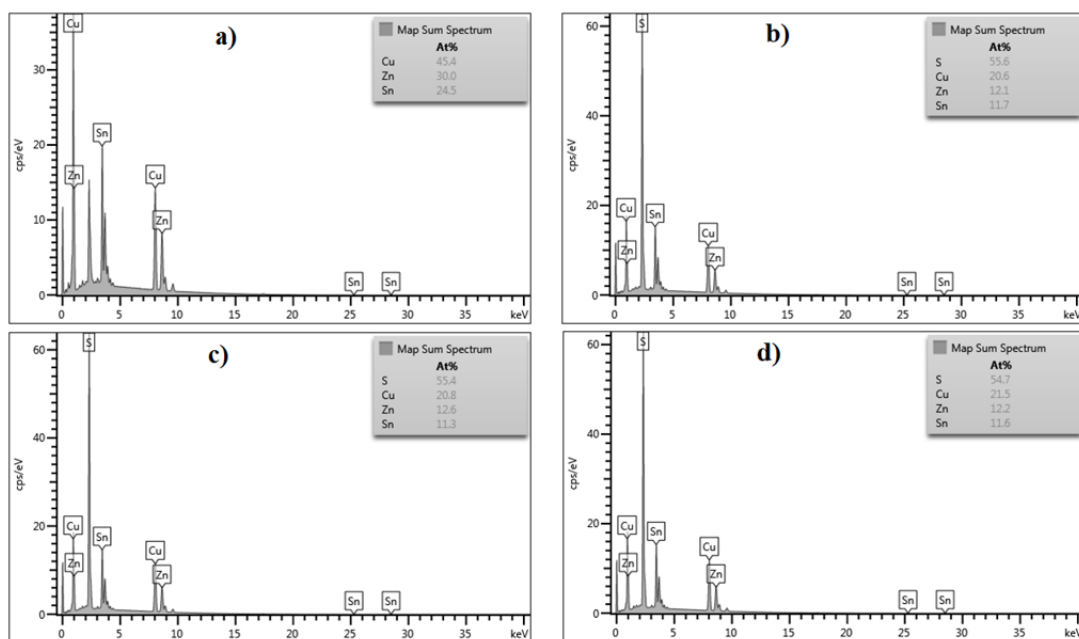
Figure 2. EDX spectrum of metallic precursor (a), CZTS-4 (b), CZTS-8 (c), and CZTS-12 (d) films.

In order to show how composition of the films change with variation of the sulfurization time more clearly, atomic ratio of the metallic precursor and CZTS thin films was also summarized in Table 2. As shown in Table 2, the metallic precursor film showed compositionally Zn-rich (Zn/Sn>1) and Cu-poor (Cu/(Zn+Sn)<1) chemical composition which desired property for solar cell applications [4]. The atomic ratio of the films, on the other hand, revealed variability according to their atomic ratios. The Cu/(Zn+Sn) atomic ratio showed variation from 0.83 to 0.90, Zn/Sn ratio from 1.03 to 1.22, and S/Metal ratio from 1.20 to 1.25.

Table 2. Chemical composition of metallic and CZTS samples.

Specimen	Atomic Ratio		
	Cu/(Zn+Sn)	Zn/Sn	S/Metal
Cu/Sn/Zn/Cu	0.83	1.22	-
CZTS-4	0.86	1.03	1.25
CZTS-8	0.87	1.12	1.24
CZTS-12	0.90	1.05	1.20

Regardless of the dwell time of the samples at reaction temperature, all CZTS thin films showed

Cu-poor composition (Cu/Zn+Sn<1) that all films share similar Cu content. However, alteration of sulfurization time caused variability in Zn composition of the films. Although the CZTS-4 and CZTS-12 thin films shared similar Zn composition, the CZTS-8 film had more Zn-composition, respectively. It can be said that all of the CZTS thin films showed Zn-loss but CZTS-4 and CZTS-12 samples showed more Zn deficiency. The Zn-loss for all samples can be explained with high vapor pressure of elemental Zn. It means that some elemental Zn had exist in CZTS-4 and CZTS-12 thin films due to probable decomposition process or incomplete reaction and evaporated during sulfurization process. All CZTS samples exhibited amount of sulfur more than necessary for complete Cu_2ZnSnS_4 structure. Excess amount of sulfur may stem from the fact that the graphite box was pulled to cool zone of the furnace with cap over it. Some residual sulfur could have precipitated on the surfaces of the films. It can be concluded that although some compositional variations were observed in the films, all reacted samples displayed compositionally Cu poor and Zn rich chemical composition, as targeted.

3.2. XRD

The XRD patterns of metallic Cu/Sn/Cu/Zn precursor and CZTS thin films were presented in Figure 3. The intended diffraction peaks for elemental Cu, Sn and Zn were labeled in the figure. Although diffraction peaks of Sn (JCPDS 03-065-7657) were separated clearly and shown in the figure, the diffraction peaks of Cu (JCPDS 00-003-1015) and Zn (JCPDS 00-004-0831) around at $2\theta = 43.25°$ were not separated since diffraction peak positions of Cu, Zn, CuZn (JCPDS 03-065-9061), and Cu_6Sn_5 (JCPDS 00-045-1488) phases are very close to each other. Additionally, Cu_6Sn_5 at $2\theta = 30.20°$ binary phase was detected even though not any annealing treatment was applied. It means that Cu and Sn elements can form alloy phase even at room temperature. Diffraction peak of Mo (JCPDS 01-089-4896) at $2\theta = 40.55$ due to substrate was also detected in the films.

As can be seen in the Figure 3, regardless of the sulfurization time all CZTS thin films displayed diffraction peaks at $2\theta = 28.44°$, $2\theta = 47.31°$, and $2\theta = 56.17°$ that corresponds (112), (220/204) and (312/116) diffraction planes of kesterite CZTS phase (JCPDS 26-0575). Other characteristic peaks associated with the CZTS are also shown in the figure. Apart from CZTS phase, formation of CuS (JCPDS 01-078-0877) at around $2\theta = 31.80°$ was traced for CZTS-4 and CZTS-12 samples as distinct from CZTS-8 thin film. It is well known that CuS secondary phase can be easily removed from the surface of the films by employing KCN etching process [15]. Additionally, as the sulfurization time increased above 4 min, the CZTS samples showed formation of MoS_2 (JCPDS 00-009-0312) phase as a result of reaction of the sulfur vapor with the substrate. It means that extending the sulfurization time above 4 min may contribute to the penetration of sulfur vapor to the lower part of the film. Overall, it was shown that the CuS-free films was successfully obtained using sulfurization time above 4 min for CZTS-8 thin film. However, extending the sulfurization time above 4 min may cause formation of MoS_2 phase. Therefore, pure CZTS phase can be obtained by calibrating the sulfurization time between 4 and 8 min.
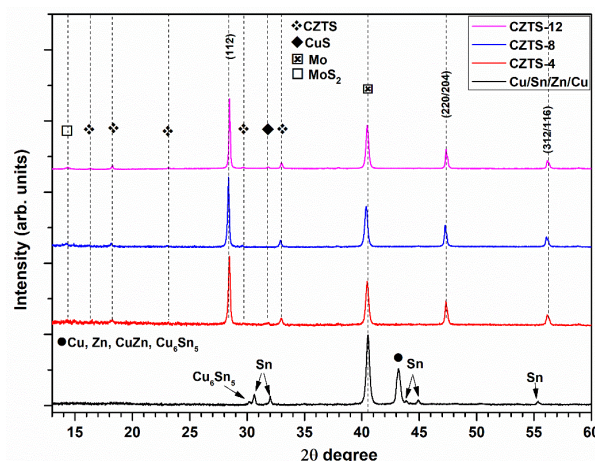
Figure 3. X-ray diffraction patterns of metallic precursor and CZTS thin films.

3.3. Raman Spectroscopy Analysis

Due to the fact that the CZTS, ZnS and Cu_2SnS_3 (CTS) phases share similar XRD patterns, Raman spectroscopy was utilized to prove formation of CZTS phase by distinguishing such phases. Raman spectra of the films which were prepared at different sulfurization times were presented in Figure 4. As can be seen in the figure, Raman spectra of the all films has a dominant peak at around 336-337 cm^{-1} that is ascribed to CZTS phase. The lower intense Raman peaks associated with CZTS phase are displayed in the figure. Except for formation of CZTS phase, the $Cu_{2-x}S$ and Cu_2SnS_3 (CTS) peaks were observed for CZTS-4, CZTS-8, and CZTS-12 respectively [18, 25]. Detection of $Cu_{2-x}S$ phase for CZTS-4 in its Raman spectra supports the XRD pattern of this film. Formation of CTS phase was determined for CZTS-8 and CZTS-12 samples. Such a phase could not be distinguished in their XRD patterns since CZTS and CTS phases have similar XRD patterns. Formation of CTS phase can be explained with the fact that longer sulfurization time may cause decomposition reaction for CZTS-8 and CZTS-12 thin films.
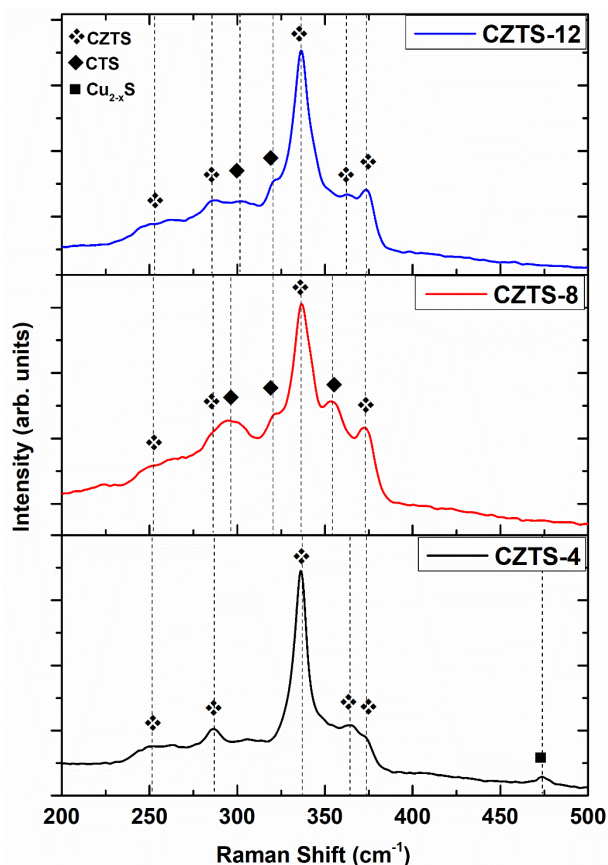
Figure 4. Raman spectra of CZTS-4, CZTS-8, and CZTS-12 thin films.

3.4. SEM

The surface morphology of the films was demonstrated by SEM images in Figure 5 with a broader image (5.00 KX) and their insets (20.00 KX) to show surface of the films more clearly. As shown in the figure, metallic film showed dense and homogenous surface structure (Figure 5 (a)). Regardless of the different sulfurization time, all reacted samples demonstrated dense, void-free, and inhomogeneous surface structure. As the sulfurization time increased, the granular- shaped microstructures decreased and more homogenous surface morphologies were obtained. The EDX results revealed that the micro segregations formed on top of the films (especially for CZTS-8 and CZTS-12) have deficiency of Zn and abundance of Cu-Sn-S elements which may point out probable formation of Cu_2SnS_3 phase. Such result is in good accordance with the Raman spectra of CZTS-8 and CZTS-12 thin films. It means that extending sulfurization time above 4 min may initialize the decomposition process and give rise to formation of CTS phase.
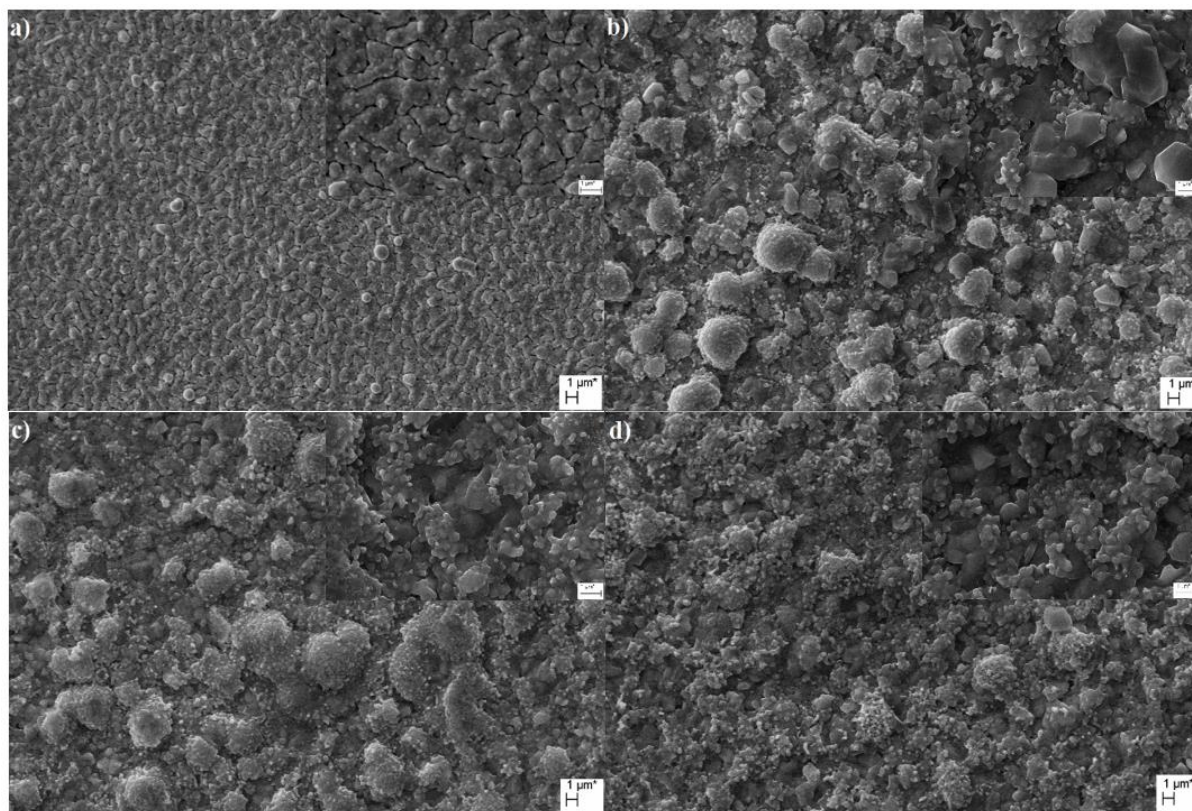
Figure 5. SEM images of metallic (a), CZTS-4 (b), CZTS-8 (c), and CZTS-12 (d) thin films.

3.5. Photoluminescence Analysis

Photoluminescence (PL) spectra obtained at room temperature of the films were displayed in Figure 6. As can be shown in the figure, one broad band at around 1.36-1.37 eV was peaked for all PL spectra of the films. The obtained PL results are compatible with the reported results in the literature [26]. The 1.36-1.37 eV value can be ascribed to conduction band to acceptor transition and involved recombination paths in the CZTS samples [24]. It can also be concluded that the sulfurization time does not affect PL emission results of the CZTS thin films remarkably.
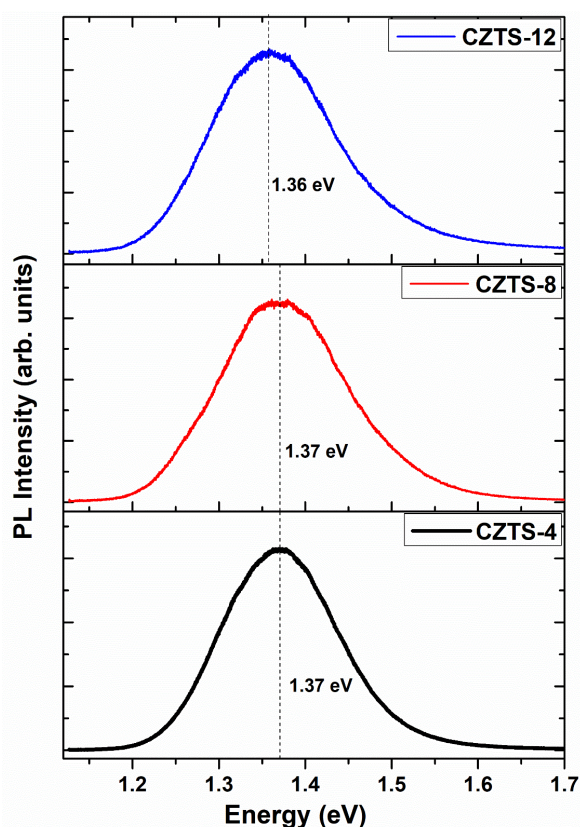
Figure 6. Photoluminescence properties of the CZTS samples.

4. CONSCLUSION

In the present study, CZTS samples were prepared by sequential sputter deposition of Cu, Zn, and Sn on Mo coated glass followed by sulfurization of metallic stacks at 500 °C reaction temperature for various sulfurization times (4, 8, and 12 minutes). The EDX results showed that although some Zn

deficiency was observed for the samples, all CZTS thin films had compositionally Cu-poor and Zn-rich atomic ratio. In addition to CZTS phase, formation of some secondary phases such as CuS and MoS_2 was observed in their XRD patterns. Raman spectra of the films were dominated by a strong peak that attributes to kesterite CZTS phase for all samples and distinguished formation of CTS phase for CZTS-8 and CZTS-12 samples. Surface morphology of the films displayed dense and inhomogeneous morphology regardless of the sulfurization temperature. Band gap of the CZTS samples obtained using different sulfurization time was determined at around 1.36-1.37 eV, which exhibits dwell time of the reaction does not influence the band gap of the films remarkably. Overall, it was shown that the pure CZTS thin film can be obtained at moderate sulfurization temperature either by fine-tuning the short dwell time of sulfurization process or employing proper etching process.

REFERENCES

[1] Kato T., Wu J.L., Hirai Y., Sugimoto H., Bermudez V., Record Efficiency for Thin-Film Polycrystalline Solar Cells Up to 22.9% Achieved by Cs-Treated Cu(In,Ga)(Se,S)(2), Ieee J. Photovolt., 9 (2019) 325-330.

[2] Katagiri H., Sasaguchi N., Hando S., Hoshino S., Ohashi J. and Yokota T., Preparation and evaluation of Cu_2ZnSnS_4 thin films by sulfurization of E-B evaporated precursors, Sol. Energ. Mat. Sol. C., 49 (1997) 407-414.

[3] Shockley W. and Queisser H.J., Detailed Balance Limit of Efficiency of p-n Junction Solar Cells, JPN J. Appl. Phys., 32 (1961) 510-519.

[4] Wang W., Winkler M.T., Gunawan O., Gokmen T., Todorov T.K., Zhu Y. and Mitzi D.B., Device Characteristics of CZTSSe Thin-Film Solar Cells with 12.6% Efficiency, Adv. Energy Mater., 4 (2014) 1301465.

[5] Wang K., Gunawan O., Todorov T., Shin B., Chey S.J., Bojarczuk N.A., Mitzi D. and Guha S., Thermally evaporated Cu_2ZnSnS_4 solar cells, Appl. Phys. Lett., 97 (2010) 143508.

[6] Mkawi E.M., Al-Hadeethi Y., Shalaan E. and Bekyarova E., Substrate temperature effect during the deposition of (Cu/Sn/Cu/Zn) stacked precursor CZTS thin film deposited by electron-beam evaporation, J. Mater. Sci-Mater. El., 29 (2018) 20476-20484.

[7] Olgar M.A., Optimization of sulfurization time and temperature for fabrication of Cu_2ZnSnS_4 (CZTS) thin films, Superlattice Microst., 126 (2019) 32-41.

[8] Vanalakar S.A., Agawane G.L., Shin S.W., Suryawanshi M.P., Gurav K.V., Jeon K.S., Patil P.S., Jeong C.W., Kim J.Y. and Kim J.H., A review on pulsed laser deposited CZTS thin films for solar cell applications, J. Alloy. Compd., 619 (2015) 109-121.

[9] Tanaka K., Fukui Y., Moritake N. and Uchiki H., Chemical composition dependence of morphological and optical properties of Cu_2ZnSnS_4 thin films deposited by sol-gel sulfurization and Cu_2ZnSnS_4 thin film solar cell efficiency, Sol. Energ. Mat. Sol. C., 95 (2011) 838-842.

[10] Hamada T., Fukuyama A., Jiang F., Ikeda S. and Ikari T., Effect of preheating time on uniformity of electrodeposited Cu_2ZnSnS_4 thin films studied by carrier lifetime and photoluminescence measurements, Phys. Status Solidi C., 12 (2015) 725-728.

[11] Hages C.J., Levcenco S., Miskin C.K., Alsmeier J.H., Abou-Ras D., Wilks R.G., Bar M., Unold T. and Agrawal R., Improved performance of Ge-alloyed CZTGeSSe thin-film solar cells through control of elemental losses, Prog. Photovoltaics, 23 (2015) 376-384.

[12] Tanaka K., Kato M., Goto K., Nakano Y. and Uchiki H., Face-to-Face Annealing Process of Cu_2ZnSnS_4 Thin Films Deposited by Spray Pyrolysis Method, Jpn. J. Appl. Phys., 51 (2012) 10S.

[13] Emrani A., Vasekar P. and Westgate C.R., Effects of sulfurization temperature on CZTS thin film solar cell performances, Sol. Energy, 98 (2013) 335-340.

[14] Guan H., Shen H.L., Gao C. and He X.C., Sulfurization time effects on the growth of Cu_2ZnSnS_4 thin films by solution method, J. Mater. Sci-Mater. El., 24 (2013) 2667-2671.

[15] Olgar M.A., Klaer J., Mainz R., Levcenco S., Just J., Bacaksiz E. and Unold T., Effect of precursor stacking order and sulfurization temperature on compositional homogeneity of CZTS thin films, Thin Solid Films, 615 (2016) 402-408.

[16] Olgar M.A., Atasoy Y., Basol B.M., Tomakin M., Aygun G., Ozyuzer L. and Bacaksiz E., Influence of copper composition and reaction temperature on the properties of CZTSe thin films, J. Alloy. Compd., 682 (2016) 610-617.

[17] Espindola-Rodriguez M., Placidi M., Vigil-Galan O., Izquierdo-Roca V., Fontane X., Fairbrother A., Sylla D., Saucedo E. and Perez-Rodriguez A., Compositional optimization of photovoltaic grade Cu_2ZnSnS_4 films grown by pneumatic spray pyrolysis, Thin Solid Films, 535 (2013) 67-72.

[18] Olgar M.A., Bacaksiz E., Tomakin M., Kucukomeroglu T. and Basol B.M., CZTS layers formed under sulfur-limited conditions at above atmospheric pressure, Mat. Sci. Semicon. Proc., 90 (2019) 101-106.

[19] He J., Sun L., Chen Y., Jiang J.C., Yang P.X. and Chu J.H., Influence of sulfurization pressure on Cu_2ZnSnS_4 thin films and solar cells prepared by sulfurization of metallic precursors, J. Power Sources, 273 (2015) 600-607.

[20] Weber A., Mainz R. and Schock H., On the Sn loss from thin films of the material system Cu–Zn–Sn–S in high vacuum, J. Appl. Phys., 107 (2010) 013516.

[21] Olgar M.A., Basol B.M., Tomakin M., Seyhan A., Bacaksiz E., Influence of pre-annealing Cu-Sn on the structural properties of CZTSe thin films grown by a two-stage process, Mat. Sci. Semicon. Proc., 88 (2018) 234-238.

[22] Gurav S.V., Pawar S.M., Shin S.W., Suryawanshi M.P., Agawane G.L., Patil P.S., Moon J.H., Yun J.H. and Kim J.H., Electrosynthesis of CZTS films by

sulfurization of CZT precursor: Effect of soft annealing treatment, Appl. Surf. Sci., 283 (2013) 74-80.

[23] Lin Y.-P., Hsieh T.-E., Chen Y.-C. and Huang K.-P., Characteristics of $Cu_2ZnSn(S_xSe_{1-x})_4$ thin-film solar cells prepared by sputtering deposition using single quaternary Cu_2ZnSnS_4 target followed by selenization/sulfurization treatment, Sol. Energ. Mat. Sol. C., 162 (2017) 55-61.

[24] Olgar M.A., Klaer J., Mainz R., Ozyuzer L. and Unold T., Cu_2ZnSnS_4-based thin films and solar cells by rapid thermal annealing processing, Thin Solid Films, 628 (2017) 1-6.

[25] Fernandes P., Salomé P. and Da Cunha A., Cu_xSnS_{x+1} (x= 2, 3) thin films grown by sulfurization of metallic precursors deposited by dc magnetron sputtering, Physica Status Solidi C, 7 (2010) 901-904.

[26] Chaudhuri T.K. and Tiwari D., Earth-abundant non-toxic Cu_2ZnSnS_4 thin films by direct liquid coating from metal–thiourea precursor solution, Sol. Energ. Mat. Sol. C, 101 (2012) 46-50.

Cumhuriyet Science Journal

CSJ

A Theorem on Absolute Summability of Infinite Series

Bağdagül KARTAL (iD)

Erciyes University, Faculty of Science, Department of Mathematics, 38039, Kayseri, TURKEY

Abstract. In this paper, a theorem on absolute summability of infinite series is obtained by taking almost increasing sequence instead of positive non-decreasing sequence. Also, some results of absolute summability are given.

Keywords: Riesz mean, absolute summability, almost increasing sequence, Hölder inequality, Minkowski inequality.

Sonsuz Serilerin Mutlak Toplanabilmesi Üzerine Bir Teorem

Özet. Bu makalede, pozitif azalmayan dizi yerine hemen hemen artan dizi alınarak, sonsuz serilerin mutlak toplanabilmesi üzerine bir teorem elde edildi. Ayrıca, mutlak toplanabilme ile ilgili bazı sonuçlar verildi.

Anahtar Kelimeler: Riesz ortalaması, mutlak toplanabilme, hemen hemen artan dizi, Hölder eşitsizliği, Minkowski eşitsizliği.

1. INTRODUCTION

A positive sequence (b_n) is said to be almost increasing if there exist a positive increasing sequence (c_n) and two positive constants K and L such that $Kc_n \leq b_n \leq Lc_n$ [1]. Obviously, every increasing sequence is almost increasing. However, the converse need not be true as can be seen by taking the example, say $b_n = ne^{(-1)^n}$. Let $\sum a_n$ be an infinite series with its partial sums (s_n). Let (φ_n) be a sequence of positive real numbers. The series $\sum a_n$ is said to be summable $\varphi - \left| \overline{N}, p_n; \delta \right|_k$, $k \geq 1$ and $\delta \geq 0$, if [2]

$$\sum_{n=1}^{\infty} \varphi_n^{\delta k + k - 1} \left| \theta_n - \theta_{n-1} \right|^k < \infty, \tag{1}$$

where (p_n) is a sequence of positive numbers such that

$$P_n = \sum_{v=0}^{n} p_v \to \infty \quad \text{as} \quad n \to \infty \quad (P_{-i} = p_{-i} = 0, \ i \geq 1) \tag{2}$$

and

$$\theta_n = \frac{1}{P_n} \sum_{v=0}^{n} p_v s_v \tag{3}$$

defines the sequence (θ_n) of the $(\overline{N}, p_n)$ mean of the sequence (s_n) generated by the sequence of coefficients (p_n) [3].

In the special case, if we take $\varphi_n = P_n/p_n$, then $\varphi - |\overline{N}, p_n; \delta|_k$ summability reduces to $|\overline{N}, p_n; \delta|_k$ summability [4]. Also, if we take $\varphi_n = P_n/p_n$ and $\delta = 0$, $\varphi - |\overline{N}, p_n; \delta|_k$ summability reduces to $|\overline{N}, p_n|_k$ summability [5]. Finally, if we take $\varphi_n = n$, $\delta = 0$ and $p_n = 1$ for all values of n, then we get $|C, 1|_k$ summability [6].

2. KNOWN RESULTS

Absolute summability methods are generally used to summability of an infinite series. There is an important application area of these methods. Especially, they have applications on different sequences such as positive non-decreasing, almost increasing and quasi power increasing sequences.

There are many different studies on absolute summability methods (see [2, 7-21]). Among them, in [7], the following theorem was proved.

Theorem 1 *Let (X_n) be a positive non-decreasing sequence and (β_n), (λ_n) be sequences such that*

$$|\Delta \lambda_n| \leq \beta_n, \tag{4}$$

$$\beta_n \to 0 \quad as \quad n \to \infty, \tag{5}$$

$$\sum_{n=1}^{\infty} n |\Delta \beta_n| X_n < \infty, \tag{6}$$

$$|\lambda_n| X_n = O(1) \quad as \quad n \to \infty \tag{7}$$

hold where $\Delta \lambda_n = \lambda_n - \lambda_{n+1}$. If (p_n) is a sequence of positive numbers such that

$$P_n = O(n p_n) \quad as \quad n \to \infty, \tag{8}$$

$$\sum_{n=1}^{m} \frac{p_n}{P_n} |s_n|^k = O(X_m) \quad as \quad m \to \infty, \tag{9}$$

then the series $\sum a_n \lambda_n$ is summable $|\overline{N}, p_n|_k$, $k \geq 1$.

3. MAIN RESULT

Theorem 1 is generalized as in the following form under weaker conditions by using an almost increasing sequence instead of a positive non-decreasing sequence.

Theorem 2 *Let* $\left(X_n \right)$ *be an almost increasing sequence and* $\varphi_n p_n = O\left(P_n \right)$. *If conditions (4)-(8) of Theorem 1 and*

$$\sum_{n=1}^{m} \varphi_n^{\delta k - 1} \left| s_n \right|^k = O(X_m) \quad as \quad m \to \infty, \tag{10}$$

$$\sum_{n=v+1}^{m+1} \varphi_n^{\delta k - 1} \frac{1}{P_{n-1}} = O\left(\varphi_v^{\delta k} \frac{1}{P_v} \right) \quad as \quad m \to \infty \tag{11}$$

are satisfied, then the series $\sum a_n \lambda_n$ *is summable* $\varphi - \left| \overline{N}, p_n; \delta \right|_k$, $k \geq 1$ *and* $0 \leq \delta < 1/k$.

Lemma 3 [22]. Under the conditions of Theorem 2, we have

$$nX_n \beta_n = O(1) \quad as \quad n \to \infty, \tag{12}$$

$$\sum_{n=1}^{\infty} \beta_n X_n < \infty. \tag{13}$$

4. PROOF OF THEOREM 2

Let $\left(M_n \right)$ be the sequence of $\left(\overline{N}, p_n \right)$ mean of the series $\sum a_n \lambda_n$. Then, we get

$$M_n = \frac{1}{P_n} \sum_{v=0}^{n} p_v \sum_{r=0}^{v} a_r \lambda_r = \frac{1}{P_n} \sum_{v=0}^{n} \left(P_n - P_{v-1} \right) a_v \lambda_v.$$

Now, for $n \geq 1$

$$M_n - M_{n-1} = \frac{p_n}{P_n P_{n-1}} \sum_{v=1}^{n} P_{v-1} \lambda_v a_v.$$

From Abel's transformation, we obtain

$$M_n - M_{n-1} = \frac{p_n}{P_n P_{n-1}} \sum_{v=1}^{n-1} P_v \Delta \lambda_v s_v - \frac{p_n}{P_n P_{n-1}} \sum_{v=1}^{n-1} p_v \lambda_v s_v + \frac{p_n s_n \lambda_n}{P_n}$$

$$= M_{n,1} + M_{n,2} + M_{n,3}$$

To prove that $\sum a_n \lambda_n$ is summable $\varphi - \left| \overline{N}, p_n; \delta \right|_k$, it is sufficient to show that

$$\sum_{n=1}^{\infty} \varphi_n^{\delta k + k - 1} \left| M_{n,r} \right|^k < \infty \text{ for } r = 1, 2, 3.$$

First, using the fact that $\varphi_n p_n = O(P_n)$ and the condition (4), we get

$$\sum_{n=2}^{m+1} \varphi_n^{\delta k+k-1} \left| M_{n,1} \right|^k = O(1) \sum_{n=2}^{m+1} \varphi_n^{\delta k-1} \frac{1}{P_{n-1}^k} \left\{ \sum_{v=1}^{n-1} P_v \beta_v |s_v| \right\}^k.$$

Now, using Hölder's inequality and the condition (8),

$$\sum_{n=2}^{m+1} \varphi_n^{\delta k+k-1} \left| M_{n,1} \right|^k = O(1) \sum_{n=2}^{m+1} \varphi_n^{\delta k-1} \frac{1}{P_{n-1}} \left\{ \sum_{v=1}^{n-1} p_v (v\beta_v)^k |s_v|^k \right\} \left\{ \frac{1}{P_{n-1}} \sum_{v=1}^{n-1} p_v \right\}^{k-1}.$$

Then, we obtain

$$\sum_{n=2}^{m+1} \varphi_n^{\delta k+k-1} \left| M_{n,1} \right|^k = O(1) \sum_{v=1}^{m} p_v (v\beta_v)^k |s_v|^k \sum_{n=v+1}^{m+1} \varphi_n^{\delta k-1} \frac{1}{P_{n-1}}.$$

Here, using the condition (11), we get

$$\sum_{n=2}^{m+1} \varphi_n^{\delta k+k-1} \left| M_{n,1} \right|^k = O(1) \sum_{v=1}^{m} \varphi_v^{\delta k} \frac{p_v}{P_v} (v\beta_v)^k |s_v|^k$$

$$= O(1) \sum_{v=1}^{m} \varphi_v^{\delta k-1} \left(\frac{\varphi_v p_v}{P_v} \right) (v\beta_v)^k |s_v|^k,$$

then using the fact that $\varphi_v p_v = O(P_v)$, we obtain

$$\sum_{n=2}^{m+1} \varphi_n^{\delta k+k-1} \left| M_{n,1} \right|^k = O(1) \sum_{v=1}^{m} \varphi_v^{\delta k-1} (v\beta_v)(v\beta_v)^{k-1} |s_v|^k.$$

Now using the fact that the sequence (X_n) is almost increasing and the condition (12), we obtain $(v\beta_v)^{k-1} = O(1)$. Thus, we have

$$\sum_{n=2}^{m+1} \varphi_n^{\delta k+k-1} \left| M_{n,1} \right|^k = O(1) \sum_{v=1}^{m} \varphi_v^{\delta k-1} v\beta_v |s_v|^k.$$

Then, using Abel's transformation, we get

$$\sum_{n=2}^{m+1} \varphi_n^{\delta k+k-1} \left| M_{n,1} \right|^k = O(1) \sum_{v=1}^{m-1} \Delta(v\beta_v) \sum_{i=1}^{v} \varphi_i^{\delta k-1} |s_i|^k + O(1) m\beta_m \sum_{v=1}^{m} \varphi_v^{\delta k-1} |s_v|^k.$$

Here considering the fact that

$$\Delta(v\beta_v) = v\beta_v - (v+1)\beta_{v+1} = v\Delta\beta_v - \beta_{v+1},$$

and using the condition (10), we have

$$\sum_{n=2}^{m+1} \varphi_n^{\delta k+k-1} \left| M_{n,1} \right|^k = O(1) \sum_{v=1}^{m-1} v \left| \Delta \beta_v \right| X_v + O(1) \sum_{v=1}^{m-1} \beta_{v+1} X_{v+1} + O(1) m \beta_m X_m$$

$$= O(1) \quad \text{as} \quad m \to \infty,$$

by (6), (13) and (12), respectively.

Now, again using the fact that $\varphi_n p_n = O(P_n)$ and Hölder's inequality, we have

$$\sum_{n=2}^{m+1} \varphi_n^{\delta k+k-1} \left| M_{n,2} \right|^k = O(1) \sum_{n=2}^{m+1} \varphi_n^{\delta k-1} \frac{1}{P_{n-1}^k} \left\{ \sum_{v=1}^{n-1} p_v \left| \lambda_v \right| \left| s_v \right| \right\}^k$$

$$= O(1) \sum_{n=2}^{m+1} \varphi_n^{\delta k-1} \frac{1}{P_{n-1}} \left\{ \sum_{v=1}^{n-1} p_v \left| \lambda_v \right|^k \left| s_v \right|^k \right\} \left\{ \frac{1}{P_{n-1}} \sum_{v=1}^{n-1} p_v \right\}^{k-1}.$$

Then

$$\sum_{n=2}^{m+1} \varphi_n^{\delta k+k-1} \left| M_{n,2} \right|^k = O(1) \sum_{v=1}^{m} p_v \left| \lambda_v \right| \left| \lambda_v \right|^{k-1} \left| s_v \right|^k \sum_{n=v+1}^{m+1} \varphi_n^{\delta k-1} \frac{1}{P_{n-1}}.$$

Here, using the fact that the sequence $\left(X_n \right)$ is almost increasing and considering the condition (7), it is clear that $\left| \lambda_v \right|^{k-1} = O(1)$. Additionally, using the condition (11), we have

$$\sum_{n=2}^{m+1} \varphi_n^{\delta k+k-1} \left| M_{n,2} \right|^k = O(1) \sum_{v=1}^{m} \varphi_v^{\delta k-1} \left| \lambda_v \right| \left| s_v \right|^k.$$

Hence, we get

$$\sum_{n=2}^{m+1} \varphi_n^{\delta k+k-1} \left| M_{n,2} \right|^k = O(1) \sum_{v=1}^{m-1} \Delta \left| \lambda_v \right| \sum_{i=1}^{v} \varphi_i^{\delta k-1} \left| s_i \right|^k + O(1) \left| \lambda_m \right| \sum_{v=1}^{m} \varphi_v^{\delta k-1} \left| s_v \right|^k$$

$$= O(1) \sum_{v=1}^{m-1} \beta_v X_v + O(1) \left| \lambda_m \right| X_m$$

$$= O(1) \quad \text{as} \quad m \to \infty,$$

by virtue of Abel's transformation, (4), (10), (13) and (7).

Finally, again using the fact that $\varphi_n p_n = O(P_n)$, we have

$$\sum_{n=1}^{m} \varphi_n^{\delta k+k-1} \left| M_{n,3} \right|^k = O(1) \sum_{n=1}^{m} \varphi_n^{\delta k-1} \left| \lambda_n \right| \left| s_n \right|^k$$

$$= O(1) \quad \text{as} \quad m \to \infty,$$

as in $M_{n,2}$. Thence, the proof of Theorem 2 is completed.

5. CONCLUSION

In this paper, generalized absolute summability of an infinite series is studied. A general theorem dealing with absolute summability is obtained. For the special cases of (X_n), (φ_n), (p_n) and δ, some results can be obtained. If we take (X_n) as a positive non-decreasing sequence in Theorem 2, we get an another theorem dealing with $\varphi - \left| \overline{N}, p_n; \delta \right|_k$ summability of an infinite series. If we take $\varphi_n = P_n / p_n$ in Theorem 2, then we get a known theorem on $\left| \overline{N}, p_n; \delta \right|_k$ summability of an infinite series [23]. Also, if we take (X_n) as a positive non-decreasing sequence, $\varphi_n = P_n / p_n$ and $\delta = 0$ in Theorem 2, then the condition (10) reduces to the condition (9) and also the conditions $\varphi_n p_n = O(P_n)$ and (11) are automatically satisfied. Thus, Theorem 2 reduces to Theorem 1. Finally, if we take (X_n) as a positive non-decreasing sequence, $\varphi_n = n$, $\delta = 0$ and $p_n = 1$ for all values of n, then we get a known result of $\left| C, 1 \right|_k$ summability [24].

REFERENCES

[1] Bari N.K. and Stečkin S.B., Best Approximations and Differential Properties of Two Conjugate Functions, Trudy Moskov. Mat. Obšč., 5 (1956) 483-522.

[2] Seyhan H., On the Local Property of $\varphi - \left| \overline{N}, p_n; \delta \right|_k$ Summability of Factored Fourier Series, Bull. Inst. Math. Acad. Sinica, 25-4 (1997) 311-316.

[3] Hardy G.H., Divergent Series, Oxford, Oxford University Press, 1949.

[4] Bor H., On Local Property of $\left| \overline{N}, p_n; \delta \right|_k$ Summability of Factored Fourier Series, J. Math. Anal. Appl., 179-2 (1993) 646-649.

[5] Bor H., On Two Summability Methods, Math. Proc. Cambridge Philos. Soc., 97-1 (1985) 147-149.

[6] Flett T.M., On an Extension of Absolute Summability and Some Theorems of Littlewood and Paley, Proc. London Math. Soc. (3), 7 (1957) 113-141.

[7] Bor H., A Note on Absolute Summability Factors, Internat. J. Math. Math. Sci., 17-3 (1994) 479-482.

[8] Bor H. and Seyhan H., On Almost Increasing Sequences and Its Applications, Indian J. Pure Appl. Math., 30-10 (1999) 1041-1046.

[9] Bor H. and Özarslan H.S., On Absolute Riesz Summability Factors, J. Math. Anal. Appl., 246-2 (2000) 657-663.

[10] Bor H. and Özarslan H.S., An Application of Quasi Power Increasing Sequences, Int. Math. J., 2-2 (2002) 187–191.

[11] Bor H. and Özarslan H.S., On an Application of Quasi Power Increasing Sequences, Indian J. Pure Appl. Math., 33-5 (2002), 769–774.

[12] Bor H. and Özarslan H.S., A Note on Absolute Summability Factors, Adv. Stud. Contemp. Math. (Kyungshang) 6-1 (2003) 1-11.

[13] Bor H. and Özarslan H.S., A Note on Absolute Weighted Mean Summability Factors, Cent. Eur. J. Math., 4-4 (2006) 594–599.

[14] Karakaş A., A Note on Absolute Summability Method Involving Almost Increasing and δ-quasi-monotone sequences, Int. J. Math. Comput. Sci., 13-1 (2018) 73-81.

[15] Kartal B., On Generalized Absolute Riesz Summability Method, Commun. Math. Appl., 8-3 (2017) 359-364.

[16] Özarslan H.S., A Note on $\left|\overline{N}, p_n; \delta\right|_k$ Summability Factors, Indian J. Pure Appl. Math., 33-3 (2002) 361-366.

[17] Özarslan H.S., A Note on Quasi Power Increasing Sequences, Indian J. Pure Appl. Math., 34-5 (2003) 727–732.

[18] Özarslan H.S., On $\left|\overline{N}, p_n; \delta\right|_k$ Summability Factors, Kyungpook Math. J., 43-1 (2003) 107-112.

[19] Seyhan H. and Sönmez A., On $\varphi - \left|\overline{N}, p_n; \delta\right|_k$ Summability Factors, Portugal. Math., 54-4 (1997) 393-398.

[20] Seyhan H., A Note on Absolute Summability Factors, Far East J. Math. Sci., 6-1 (1998) 157-162.

[21] Seyhan H., On the Absolute Summability Factors of Type (A,B), Tamkang J. Math., 30-1 (1999) 59-62.

[22] Mazhar S.M., A Note on Absolute Summability Factors, Bull. Inst. Math. Acad. Sinica, 25-3 (1997) 233-242.

[23] Özarslan H.S., On Almost Increasing Sequences and Its Applications, Int. J. Math. Math. Sci. 25-5 (2001) 293-298.

[24] Mishra K.N. and Srivastava R.S.L., On Absolute Cesàro Summability Factors of Infinite Series, Portugal. Math., 42-1 (1983-84) 53-61.

Cumhuriyet Science Journal

CSJ

Shell Model Calculations for Proton-rich Zn Isotopes via New Generated Effective Interaction by Artificial Neural Networks

Serkan AKKOYUN[1]* *, Tuncay BAYRAM[2]*

[1] *Department of Physics, Faculty of Science, Sivas Cumhuriyet University, Sivas, TURKEY*

[2] *Department of Physics, Faculty of Science, Karadeniz Technical University, Trabzon, TURKEY*

Abstract. In this study, the artificial neural network method has been employed for the generation of the new two-body matrix elements which is used for fpg shell nuclei. For this purpose, jj44b interaction Hamiltonian has been considered as a source. After the generation of the new Hamiltonian, both, original and new generated, are tested on proton-rich Zn isotopes. According to the results, the calculated values are close to the each other. As well the results from new interaction (jj44b_nn) are closer to the available experimental values in some cases.

*Keywords***:** Nuclear shell model, Pfg shell, Jj44b, Artificial neural network.

Yapay Sinir Ağı ile Yeni Üretilen Etkin Etkileşimle Nötron Zengini Zn İzotopları için Kabuk Modeli Hesaplamaları

Özet. Bu çalışmada, fpg kabuk çekirdekleri için kullanılan iki cisim matris elemanlarının üretilmesi için yapay sinir ağı yöntemi kullanılmıştır. Bu amaçla, jj44b etkileşim Hamiltonian'i, kaynak olarak kabul edilmiştir. Yeni Hamiltonian'ın oluşumundan sonra, hem orijinal hem de yeni üretilen etkileşimin her ikisi de nötronca zengin Zn izotopları üzerinde test edilmiştir. Elde edilen sonuçlara göre hesaplanan değerler birbirine yakındır. Ayrıca, yeni etkileşimden (jj44b_nn) elde edilen sonuçlar, mevcut deneysel değerlere ve literatür değerlerine daha yakın sonuç vermiştir.

*Anahtar Kelimeler***:** Nükleer kabuk modeli, Pfg kabuğu, Jj44b, Yapay sinir ağı.

1. INTRODUCTION

For the investigation of nuclear structure, nuclear shell model is a quite successful. Similar to the more familiar model for electronic shell model of atom, the nucleons are considered as located in the shells of a nucleus. If the number of nucleons equals to 2, 8, 20 28, 50, 82 or 126 which is named as nuclear magic number, the shells are said to be closed. The nuclei whose only one type nucleon number is magic are called magic nuclei. In the case of both types are magic, the nucleus is called as doubly-magic nuclei. In nuclear shell model (SM) calculations, a double-magic nucleus is considered as an inert core. The core nucleons do not interact with each other or the nucleons outside the core. Only valance nucleons above the closed shell are taken in the calculations. The space of the valance nucleons is a model space.

The interactions of the nucleons in the model space with each other or the core are obtained via SM calculations [1-7]. Therefore, the correct estimations of the physical results in SM model, determination of the interaction Hamiltonian plays crucial role. In this paper, we have generated new interaction matrix elements from existed jj44b interaction [8]. This interaction is used for SM calculations of the nuclei outside the 56Ni double-magic core and includes 133 two-body interaction matrix elements. The model space is pfg shell and contains the nuclei from mass number A=56 to 100. For the generation, we have applied artificial neural network (ANN) method which mimics the human brain function. Recently, ANN has been used in many fields of nuclear physics [9,13]. After generation of the new interaction matrix elements, the 2+, 4+ energies, R4/2 ratio, B(E2) values for proton-rich Zn isotopes have been calculated in the scope of SM. Kshell shell model code has been used which enables to perform nuclear shell-model calculations with M-scheme representation with the thick-restart Lanczos method [14].

The paper is organized as follows. In section 1, a brief introduction to the subject is given. In section 2, ANN method and shell model calculations have been summarized. Results of the ANN and the SM calculations for existed jj4b interaction and newly generated jj44b_nn interaction for Zn isotopes have been given in comparison with the available literature values in section 3. Finally, in the section 4, discussions on the obtained results have been given with the conclusions.

2. MATERIAL and METHODS

2.1 Artificial Neural Network (ANN) Method

A mathematical tool ANN mimics the human brain functionality [15]. The structure of ANN is composed of several processing units which are called neurons. The neurons are located in different layers and connected each other via adaptive synaptic weights. The first group of neurons is in input layer and receives data from outside. The data is transmitted to next group of neurons in hidden layer by weights. Finally, the processed data flows to the output layer neurons. In our calculation, we have used feed-forward ANN with four layers in order to generate new two-body interaction matrix elements (tbme). The input layer consists of six neurons corresponding to a, b, c, d, J and T. The a, b, c, d values are the single particle orbits of the model space nucleons, J and T are total paired angular momentum and isospin, respectively. Due to the giving best results among the others, two hidden layers with 6 and 9 neurons in each are used as optimized value. The output layer neuron corresponds to the tbme. Therefore, the architecture of ANN is 6-6-9-1 and the total numbers of adjustable weights between neurons are 99 in this work. The hidden neuron activation function is tangent hyperbolic which is a sigmoid-like function generally used in the ANN calculations. For details of the ANN, the reader is referred to Haykin [15].

2.2 Shell Model Calculation

In the SM, valance nucleons move in a finite number of j-orbits and their Hamiltonian of the valance nucleons is given by

$$H = E_0 + \sum_i \varepsilon_i + \sum_{a,b,c,d} <ab;JT|V|cd;JT>$$

where E0 is the energy of the inert core, εi is single particle energies (spe) of the valance orbits and the last term <ab;JT|V|cd;JT> is two-body residual interaction among the valance particles. In the calculations with jj44bor jj44b_nn effective interactions, spe values are -9.2859, -9.6566, -8.2695 and -5.8944 for p3/2, f5/2, p1/2 and g9/2 shells. The valance nucleons are distributed in this pfg shells (Fig.1). The interaction Hamiltonian is defined by a set of 133 tbme. We have considered double magic 56Ni isotope as a core whose proton and neutron numbers are 28. The nucleons in the core with J=0 do not move from the core.
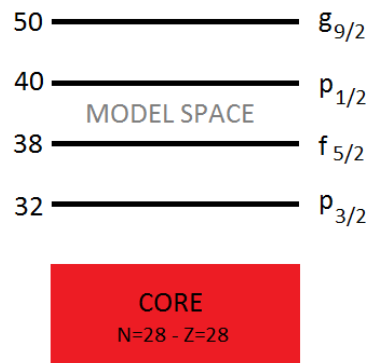
Figure 1 The fpg model space above the 56Ni core for the calculations of Zn isotopes

There are many available codes in the literature which are written for the shell model calculations such as NuShell [16], Redstick [17], Bigstick [18], Antoine [19], Oxbash [20]. For the SM calculations for nuclear properties of proton-rich Zn isotopes, Kshell [14] computer code has been used in this present study. The code is a powerful computer code in order to calculate the energy levels, spins/parities, electric/magnetic quadrupole moments, electric/magnetic transition probabilities and one-particle spectroscopic factors in the nuclei. The code is used on a Linux operating system with a many-core CPU and OpenMP library. It is also used on a parallel computer with hybrid MPI+OpenMP parallel programming. If enough memory is available on the computers, up to tens of billions M-scheme dimension is capable.

3. RESULTS AND DISCUSSIONS

In the first stage of the study, we have employed ANN to generate new interaction matrix elements from an existing data for the shell model calculations of fpg shell nuclei. By using constructed ANN mentioned in Section 2.1, we have obtained the elements whose values are not so far from the original ones. As can be seen in Table 1 that, the maximum difference between original and generated elements is 0.4861 for off-diagonal *<41;50|V|42;50>* tbme. The minimum value is 0 for several tbme. The more the hidden layer neurons the closest the result each other are. For the hidden neuron numbers 8-10, the constructed

ANN starts to memorize the data and the generated tbme from it becomes to be same as the original tbme. Although the values are close each other for used ANN with 6-9 hidden neurons, the results of SM calculations have been improved by using new generated tbme. In order to see this improvement, SM calculations have been performed on proton-rich even-even Zn isotopes.

In Table 2, we have given the 2^+ and 4^+ energies of $^{58-62}$Zn isotopes. For ^{58}Zn, the theoretical calculated 2^+energy values are same from jj44b and jj44b_nn. For ^{60}Zn isotope, jj44b_nn gives results closer to the experimental value whereas for ^{62}Zn isotope, jj44b gives closer results. The calculations of4^+ energy levels, jj44b_nn is better both for ^{58}Zn and ^{60}Zn.

In Table 3, we have shown the B(E2) values for ground state to first 2^+ excited state and from 2^+ excited state to ground state. Only available experimental or adopted literature value is for ground state to 2^+ state in ^{62}Zn isotope. As is clear in the table that the jj44b_nn is slightly closer to the experimental value. For the other Zn isotopes, the results are very close to each other. In Table 4, we have listed the B(E2) values for first 2^+ excited state to first 4^+ excited state and from 4^+ excited state to 2^+ excited state. There is no available experimental or adopted value in the literature for these values.

Table 1. Two-body matrix elements of jj44b and newly generated jj44b_nn interactions. The orbits are labeled by 1=p$_{3/2}$, 2=f$_{5/2}$, 3=p$_{1/2}$ and 4=g$_{9/2}$ single particle orbits. The a, b, c, d values are the single particle orbits, J and T are total paired angular momentum and isospin.

a	b	c	d	J	T	jj44b	jj44b_nn	a	b	c	d	J	T	jj44b	jj44b_nn
1	1	1	1	1	0	-0,8113	-0,8081	4	4	4	4	9	0	-2,1260	-2,1283
1	1	1	1	3	0	-0,4985	-0,5162	1	1	1	1	0	1	-1,3259	-1,2921
1	1	1	1	5	0	-2,1319	-2,1179	1	1	1	1	2	1	-0,3349	-0,3358
1	1	2	1	1	0	0,5205	0,5580	1	1	1	1	4	1	0,3138	0,3728
1	1	2	1	3	0	0,3487	0,3125	1	1	2	1	2	1	-0,2903	-0,2349
1	1	3	1	3	0	-0,6053	-0,6000	1	1	2	1	4	1	-0,4315	-0,4270
1	1	2	2	1	0	0,1736	0,1988	1	1	3	1	2	1	-0,7133	-0,6980
1	1	2	2	3	0	0,0320	0,0320	1	1	2	2	0	1	-0,7430	-0,8444
1	1	3	2	1	0	0,1136	-0,0226	1	1	2	2	2	1	0,0098	0,0499
1	1	3	3	1	0	-0,2385	-0,2908	1	1	3	2	2	1	0,5004	0,4537
1	1	4	4	1	0	-0,8790	-0,8191	1	1	3	3	0	1	-0,4773	-0,4915
1	1	4	4	3	0	-0,3107	-0,2993	1	1	4	4	0	1	1,8722	1,8353
1	1	4	4	5	0	-0,1703	-0,1798	1	1	4	4	2	1	0,2798	0,4341
2	1	2	1	1	0	-1,9735	-1,9779	1	1	4	4	4	1	0,1879	0,0334
2	1	2	1	2	0	-1,2445	-1,2437	2	1	2	1	1	1	0,2446	0,2890
2	1	2	1	3	0	-0,6597	-0,6621	2	1	2	1	2	1	0,4202	0,3899
2	1	2	1	4	0	-1,6087	-1,6137	2	1	2	1	3	1	0,5865	0,6269
2	1	3	1	2	0	-0,7312	-0,6938	2	1	2	1	4	1	-0,1017	-0,1027
2	1	3	1	3	0	0,6758	0,6572	2	1	3	1	2	1	-0,4233	-0,3843
2	1	2	2	1	0	0,0665	0,0659	2	1	3	1	3	1	0,0290	0,0455
2	1	2	2	3	0	0,3863	0,4129	2	1	2	2	2	1	-0,0657	-0,1104
2	1	3	2	1	0	0,6218	0,6408	2	1	3	2	1	1	0,0725	0,0584
2	1	3	2	2	0	-0,3687	-0,4616	2	1	3	2	2	1	-0,0633	-0,1426
2	1	3	3	1	0	0,5089	0,6585	2	1	4	4	2	1	0,5475	0,5788
2	1	4	4	1	0	0,3037	0,2474	2	1	4	4	4	1	0,5235	0,5430
2	1	4	4	3	0	-0,0341	-0,0234	3	1	3	1	2	1	-0,1648	-0,2051
3	1	3	1	2	0	-0,4481	-0,4367	3	1	3	1	3	1	0,6638	0,6220
3	1	3	1	3	0	-1,4983	-1,4898	3	1	2	2	2	1	-0,2554	-0,2632
3	1	2	2	3	0	-0,0006	0,0032	3	1	3	2	2	1	0,4423	0,4458
3	1	3	2	2	0	-0,5797	-0,6143	3	1	4	4	2	1	0,6139	0,5485
3	1	4	4	3	0	-0,1910	-0,1704	4	1	4	1	2	1	-0,6032	-0,6032
4	1	4	1	2	0	-3,5289	-3,5389	4	1	4	1	3	1	-0,0920	-0,0419
4	1	4	1	3	0	-1,8098	-1,8147	4	1	4	1	4	1	0,4452	0,2406
4	1	4	1	4	0	-1,2352	-1,2256	4	1	4	1	5	1	0,2804	0,4718
4	1	4	1	5	0	-1,4659	-1,4834	4	1	4	1	6	1	0,6757	0,6048
4	1	4	1	6	0	-0,8493	-0,8040	4	1	4	1	7	1	-0,7200	-0,7734
4	1	4	1	7	0	-2,3659	-2,4047	4	1	4	2	3	1	-0,5352	-0,4555
4	1	4	2	3	0	-0,8169	-0,7536	4	1	4	2	4	1	-0,1519	-0,2064
4	1	4	2	4	0	0,5634	0,2266	4	1	4	2	5	1	-0,0907	0,0130
4	1	4	2	5	0	-0,1897	0,2964	4	1	4	2	6	1	-0,4143	-0,3692
4	1	4	2	6	0	0,8527	0,6543	4	1	4	3	4	1	0,1336	0,1116
4	1	4	3	4	0	-0,8072	-0,6775	4	1	4	3	5	1	-0,0729	-0,0952
4	1	4	3	5	0	-0,8831	-0,9912	2	2	2	2	0	1	-0,7572	-0,7504
2	2	2	2	1	0	-0,8551	-0,8573	2	2	2	2	2	1	0,0862	0,1305
2	2	2	2	3	0	-2,0525	-2,0635	2	2	3	2	2	1	0,2157	0,2559
2	2	3	2	1	0	-1,3769	-1,3686	2	2	3	3	0	1	-1,1326	-1,1276
2	2	3	3	1	0	0,6256	0,6214	2	2	4	4	0	1	0,9686	0,9654
2	2	4	4	1	0	0,5998	0,5808	2	2	4	4	2	1	0,5567	0,4995
2	2	4	4	3	0	0,4825	0,5337	3	2	3	2	1	1	0,3052	0,3135
3	2	3	2	1	0	-2,3068	-2,3085	3	2	3	2	2	1	-0,3941	-0,4021
3	2	3	2	2	0	-2,0031	-1,9665	3	2	4	4	2	1	-0,1474	-0,0989
3	2	3	3	1	0	-0,3608	-0,3664	4	2	4	2	3	1	-0,8576	-0,8774
3	2	4	4	1	0	0,5368	0,5290	4	2	4	2	4	1	0,1169	0,1576
4	2	4	2	3	0	-0,9996	-1,0071	4	2	4	2	5	1	-0,1975	-0,2201
4	2	4	2	4	0	-0,8777	-0,8467	4	2	4	2	6	1	0,8224	0,7916
4	2	4	2	5	0	-0,3781	-0,4948	4	2	4	3	4	1	0,2570	0,2396
4	2	4	2	6	0	-2,3615	-2,3469	4	2	4	3	5	1	-0,4919	-0,4556
4	2	4	3	4	0	1,0058	0,9069	3	3	3	3	0	1	-0,1139	-0,1060
4	2	4	3	5	0	-0,3069	-0,1848	3	3	4	4	0	1	0,8110	0,8110
3	3	3	3	1	0	-1,0199	-1,0155	4	3	4	3	4	1	0,3293	0,3363
3	3	4	4	1	0	-0,2545	-0,2517	4	3	4	3	5	1	-0,2067	-0,2205
4	3	4	3	4	0	-1,6832	-1,7087	4	4	4	4	0	1	-1,4086	-1,4040
4	3	4	3	5	0	-1,1173	-1,1116	4	4	4	4	2	1	-1,0366	-1,0421
4	4	4	4	1	0	-1,0265	-1,0103	4	4	4	4	4	1	-0,2288	-0,2259
4	4	4	4	3	0	-0,5628	-0,5201	4	4	4	4	6	1	0,2066	0,1920
4	4	4	4	5	0	-0,5590	-0,6344	4	4	4	4	8	1	0,2457	0,2489
4	4	4	4	7	0	-0,8680	-0,8583								

Table 2. First 2+ and 4+ energies of proton rich Zn isotopes

	2$^+$ Energy (keV)			4$^+$ Energy (keV)		
Isotope	*exp*	*jj4b*	*jj4b_nn*	*exp*	*jj4b*	*jj4b_nn*
^{58}**Zn**	1356	1683	1683	2499	2299	2323
^{60}**Zn**	1004	998	1001	2193	2112	2139
^{62}**Zn**	954	958	960	2186	2220	2238

Table 3. B(E2) values between ground state and first 2+ state for proton rich Zn isotopes

Isotope	B(E2;0-2)			B(E2;2-0)		
	exp	jj4b	jj4b_nn	exp	jj4b	jj4b_nn
^{58}Zn	-	466.87	467.41	-	93.37	93.48
^{60}Zn	-	709.39	710.86	-	141.88	142.17
^{62}Zn	1240	807.99	809.55	-	161.60	161.91

Table 4. B(E2) values between first 2+ state and 4+ state for proton rich Zn isotopes

Isotope	B(E2;2-4)			B(E2;4-2)		
	exp	jj4b	jj4b_nn	exp	jj4b	jj4b_nn
^{58}Zn	-	155.68	155.52	-	86.49	86.40
^{60}Zn	-	308.5	309.08	-	171.39	171.71
^{62}Zn	-	373.89	375.27	-	207.72	208.49

We have also calculated $R_{4/2}$ and B(E2; 4->2)/B(E2;2->0) ratios for Zn isotopes. In Fig.2, we have shown the $R_{4/2}$ ratios from experimental results and theoretical results by jj44b and jj44b_nn interactions. It is clear in figure that, the results from newly generated jj44b_nn tbme are slightly closer to the experimental data for $^{58-60}$Zn isotopes.
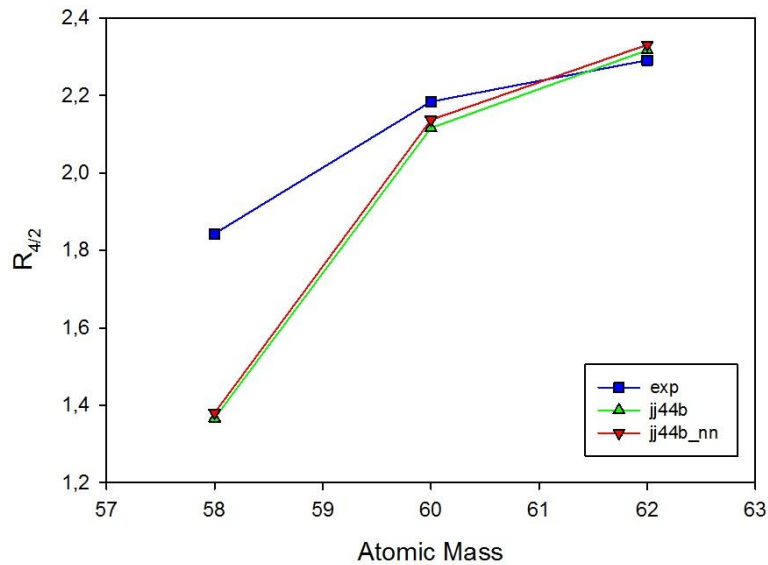
Figure. 2 $R_{4/2}$ values for proton-rich Zn isotopes.

Finally in Fig.3, we have shown the B(E2; 4->2)/B(E2;2->0) ratios from experimental results and theoretical results by jj44b and jj44b_nn interactions. Only available experimental values are for ^{62}Zn isotope with the value of 1.55. Neither jj44b nor jj44b_nn results are close to this value. The results from both calculations is almost same each other.
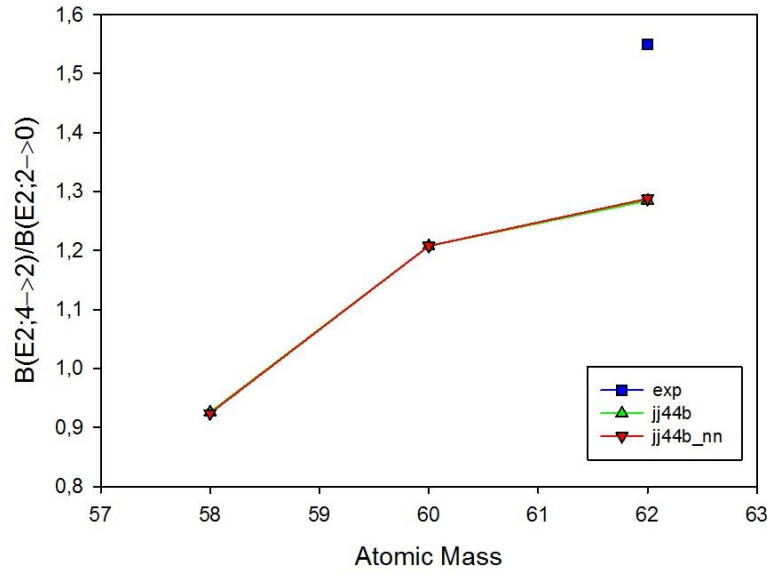
Figure. 3 B(E2; 4->2)/B(E2;2->0) values for proton-rich Zn isotopes.

Acknowledgements

REFERENCES

[1]   Mayer, M.G., On Closed Shells in Nuclei. II, Phys.Rev. 75 (1949) 1969.

[2]   Jensen, J.H.D., et al.,On the "Magic Numbers" in Nuclear Structure, Phys.Rev. 75 (1949) 1766.

[3]   Mayer, M.G., On Closed Shells in Nuclei, Phys.Rev. 74 (1948) 235.

[4]   Mayer, M.G., Nuclear Configurations in the Spin-Orbit Coupling Model. I. Empirical Evidence, Phys.Rev. 78 (1950) 16.

[5]   Talmi, I., 55 Years Of The Shell Model: A Challenge To Nuclear Many-Body Theory, Int.J.Mod.Phys.E 14 (2005) 821.

[6]   Caurier, E., etal., The shell model as a unified view of nuclear structure, Rev.Mod.Phy. 77 (2005) 427.

[7]   Brown, B.A., The nuclear shell model towards the drip lines, Prog.Part.Nucl.Phys. 47 (2001) 517.

[8]   Brown, B.A. and Lisetskiy, A.F., unpublished. The jj44b Hamiltonian was obtained from a fit to about 600 binding energies and excitation energies with a method similar to that used for the JUN45 Hamiltonian.

[9]   Neufcourt, L., et al., Bayesian approach to model-based extrapolation of nuclear observables, Phys.Rev. C 98 (2018) 034318.

[10]   Negoita, G.A., et al., Deep Learning: A Tool for Computational Nuclear Physics, arXiv:1803.03215 [physics.comp-ph] (2018).

[11]   Yildiz, N., et al., Consistent Empirical Physical Formula Construction for Gamma Ray Angular Distribution Coefficients by Layered Feedforward Neural Network, Cumhuriyet Sci.J., 39 (2018) 928.

[12]   Bayram, T., et al., A study on ground-state energies of nuclei by using neural networks, Ann.Nucl.Energy., 63 (2014) 172.

[13]   Akkoyun, S., et al., An artificial neural network application on nuclear charge radii, J. Phys. G: Nucl. Part. Phys., 40 (2013) 055106.

[14] Shimizu, N. Nuclear shell-model code for massive paralel computation, KSHELL, arXiv:1310.5431 [nucl-th] (2013).

[15] Haykin, S., Neural Networks: A Comprehensive Foundation (Englewood Cliffs, NJ: Prentice-Hall) (1999).

[16] Brown, B.A., Rae, W.D.M., The Shell-Model Code NuShellX@MSU Nucl.Data Sheets. 120 (2014) 115.

[17] REDSTICK, http://www.phys.lsu.edu/faculty/cjohnson/redstick.html

[18] Jhonson, C.W., et al., BIGSTICK: A flexible configuration-interaction shell-model code, arXiv:1801.08432v1 [physics.comp-ph] (2018).

[19] ANTOINE, http://www.iphc.cnrs.fr/nutheo/code_antoine/menu.html

[20] B. A. Brown, et al., Oxbash for Windows, MSU_NSCL report number 1289.

Investigation of Cytotoxic Effects of *Inula Viscosa* Extract

Ceylan HEPOKUR [1,*] iD **, Yakup BUDAK** [2] iD **, Hasan Bahri KARAYEL** [2] iD **, Bedrettin SELVİ** [3] iD **,
İlhan YAYLIM** [4] iD

[1] *Cumhuriyet University, Faculty of Pharmacy, Department of Basic Pharmaceutical Sciences, Division of Biochemistry, 58140 Sivas, Turkey*
[2] *Gaziosmanpasa University, Science and Art Faculty, Department of Chemistry, 60240 Tokat, Turkey*
[3] *Gaziosmanpasa University, Science and Art Faculty, Department of Biology, 60240 Tokat, Turkey*
[4] *Istanbul University, The Institute of Experimental Medicine, Department of Molecular Medicine, Istanbul, Turkey,*

Abstract. *Inula viscosa* is a type of Asteraceae family, which widely used for medicinal plant to treatment of different diseases. Inula viscosa contains many biological compounds, such as monoterpenes, sesquiterpenes, diterpenes, flavonoids. Our study aimed to investigate the cytotoxic effects of *Inula viscosa extract* on MCF-7 (breast carcinoma), C6 (glioblostoma cancer), MG63 (bone osteosarcoma), cancer cells and L929 (mouse fibroblostama) cell lines. Cytotoxic effects of the *Inula viscosa* extracts were performed by XTT assay. In this study, *Inula viscosa* extracts showed selective cytotoxic effect on MC-7 compared than L929 cells. The *Inula viscosa* extracts appear to be a promising source of new anticancer agent. Further studies are needed to identify the cytotoxic activity mechanisms on these cancer cell lines.

Keywords: Cancer, Cytotoxic Effect, *Inula Viscosa.*

Inula Viscosa Ekstraktının Sitotoksik Etkilerinin Araştırılması

Özet. Inula viscosa farklı hastalıkların tedavisinde medikal amaçlı kullanılan Asteraceae ailesine ait bir türdür. Inula viscosa monoterpene, seskiterpen, diterpen ve flavonoid gibi pek çok biyolojik bileşen içerir. Çalışmamızda *Inula viscosa* ekstraktlarının MCF-7, C6, MG63 ve L929 hücre hatlarında sitotoksik etkisinin incelenmesini amaçladık.Inula viscosa ekstraklarının sitotoksik etkisi XTT analizi ile yapıldı.Bu çalışmada Inula viscosa ekstrakları MCF-7 hücre hatlarında L929'a göre seçici sitotoksik etki gösterdi. Inula viscosa ekstrakları, ümit verici bir yeni antikanser ajan kaynağı olarak görünmektedir. Bu kanser hücre hatları üzerindeki sitotoksik aktivite mekanizmalarını tanımlamak için daha ileri araştırmalara ihtiyaç vardır.

Anahtar Kelimeler: Kanser, Sitotoksik Etki, Inula Viscosa.

1. INTRODUCTION

Cancer is a pathological condition that occurs in a genetic and developmental process, resulting in loss of cells' excessive proliferation and apoptosis functions. Some cancer types cause death and are one of the most searched health problems for treatment. Lung, stomach, colon, liver and breast cancers are reported to be the most common causes of death [1-4]. Despite the fact that billions of dollars are spent for cancer research every year, the question of how exactly the cancer has developed remains unanswered. Despite advances in methods such as surgery, chemotherapy,

radiation radiotherapy, hormone replacement for cancer treatment, the expected improvement in advanced disease is not at the desired level [5]. Chemotherapy is a frequently used method for cancer. It has disadvantages such as ineffectiveness; serious toxicity and multiple drug resistance reduce the percentage of success [4]. Therefore, new strategies are needed to defeat resistance against anticancer drugs [5].

Inula viscosa is type of Asteraceae family. *Inula helenium L.*, *Inula racemosa* Hook.f and *Inula britannica L.* species are used in medicine. *Inula viscosa* is a perennial herbaceous plant that profusely colonizes sub-nitrophile and sub-saline soils in abandoned and plowed fields in the Mediterranean region [6-7]. Inula species include many bioactive compounds, such as monoterpenoids, sesquiterpenoids, flavonoids, and glycosides [8]. It has many biological activies, such as antiinflammatory, anthelmintic, antipyretic, antiseptic, antiphlogistic, and antitumor [9-11]. It is widely used in traditional medicine for treatment of different diseases especially cancer treatment [12].

In this study, we aim that cytotoxic effects of *Inula viscosa* was determined on bone osteosarcoma (MG63), glioblostoma (C6), breast (MCF-7) cancer cells.

2. MATERIALS AND METHOD

2.1. Materials

Dimethylsulfoxide (DMSO), ethanol purchased from Sigma (St. Louis, USA). Cell Proliferation Kit II (XTT), Dulbecco's Modified Eagle's Medium (high glucose) from Sigma (St. Louis, MO, USA). Penicillin, streptomycin and trypsin from Gibco (Paisley, England), Eagle's Minimum, fetal bovine serum (FBS) from Biochrom (Berlin, Germany), phosphate buffer saline (PBS) tablet from Medicago (Uppsala, Sweden).
Inula Viscosa was collected from Akhisar district of Manisa province, Turkey (Table 1).

2.2. Plant Extraction

2.2.1. Infusion extract *(Yield: 3.08 %)*

Inula viscosa powder (50 g) was added to boiled water (1L) and stirred for 1h. The mixture was filtered through Whatman No.1 filter to remove insoluble particles (should have same text type and size of other parts of manuscript). The water extract was lyophilized (Cryodos 80, 75ºC, 5

m^3/h). Infusion extract is yield 3.08 % [13].

2.2.2. Boiling extract *(Yield: 9.1%)*

Inula viscosa powder (50 g) and 1 liter of water boiled for 1h. The mixture was filtered through Whatman No.1 paper. The water extract was lyophilized (Cryodos 80, 75ºC, 5 m^3/h). Boiling extract is yield 9.1% [14].

2.2.3. Cell Culture

All cell lines were purchased from (ATCC). The medium environment that we used in our study was DMEM, containing 10% fetal bovine serum (FBS), 1% L-glutamine, 100 IU/mL penicillin and 10 mg/mL streptomycin. Cell lines produced using DMEM would be reproduced at 37°C, in an oven with 95% humidity and 5% CO_2.

2.2.4. Cytotoxic Effect

Cytotoxic effects of *Inula Viscosa* extract on MCF-7, C6, MG63, and L929 cells were determined by XTT (2, 3-bis (2-methoxy-4-nitro-5-sulfophenyl)-5-[(phenyl amino) carbonyl]-2H-tetrazolium hydroxide) assay for 24 h after treatment. XTT solution was prepared by mixing XTT agent (Labelling reagent)/ activation agent (electron coupling reagent) at 50/1 ratio. The intensity of the orange color resulting from formazan is proportional to the number of live cells. The cell viability was determined according to the intensity of the orange color observed, which was measured 475 nm [15]. All absorbance was compared to control samples (without any compound) which represented 100% viability. Cell viability was determined as in Eq1.

Cell viability (%)= [(As-Ab)/(Ac-Ab)] *100……1

A_s: Absorbans Sample

A_b: Absorbans Blank

A_c: Absorbans Viable cell (control)

2.2.5. Statistical Analysis

Data were expressed in the form of arithmetic mean ± standard deviation (x ± SD).

Table 1. Collection information of the *Inula Viscosa*

Plant	Collection site	Altitude	Collection period	Voucher number
Inula Viscosa	Turkey:Manisa-Akhisar district,	1100 m	15.08.16	H.B.Karayel (GOPU 7690)

3. RESULTS AND DISCUSSION

Inula viscosa is widely used for treatment different diseases. When the literature is examined, *Inula viscosa* extracts showed potent antifungal, anti-inflammatory, and antioxidant activities (16). Haoui demonstrated that; 23 compounds of *Inula viscosa* essential oil were identified. GC-Ms analysis of several studies showed that *Inula viscosa* contains biological many compounds, including flavonoid, terpenoids, isocostic acid and tomentosin agents [17]. Many studies have highlighted the biological activity of tomentosin [6].

Recently, determine the cytotoxic and antiproliferative effects of plants have become the main strategy for new anticancer agent. Our study, we investigated different concentrations (100-1.56 $\mu g \ mL^{-1}$) of Inula vacosa extracts on MCF-7, C6, MG63, and L929 for 24 h.

IC_{50} values are shown in Table 2. Cytotoxic effect of ınfusion extract is better than boiling extract. We have found a significant cytotoxic effect of *Inula viscosa L.* extracts on against MCF-7 cells. This activity was mainly attributed to the presence of tomentosin, a sesquiterpene lactone [18-19]. As a control group, L929 cells were used.

Table 2. IC_{50} values of *Inula Viscosa*

	$IC_{50}/\mu gml^{-1}$			
*	L929	MCF-7	MG63	C6
Infusion	38.33±1.05	18.76±1.64	20.67±1.11	25.47±0.69
Boiling	57.33±0.95	25.76±1.83	28.98±0.62	35.76±1.31
Cis-platin	20.04±1.78	8.34±0.54	10.54±1.62	12.11±1.42
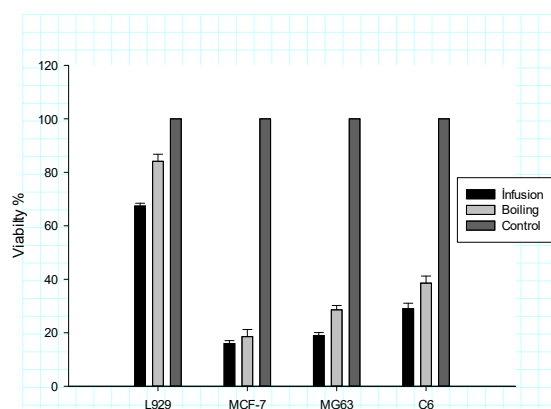
Figure 1. The cytotoxic effect after the treatment with the extract (50 µg mL^{-1}) for 24 h. Bars indicate mean ± standard deviation. All comparisons were made relative to untreated control cells.

Microscopic images of the MCF-7 cells are shown below with boiling and ınfusion extracts in Figure 2.

a.   **b.**   **c.**
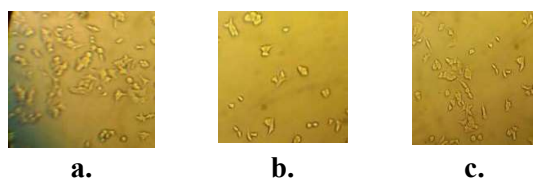
Figure 2. Cytotoxic effects **a.**without extract, **b.** ınfusion extract treatment, **c.** boiling extract treatment on MCF-7 cells.

Obtained results showed that boiling and ınfusion extracts are exhibited cytotoxic activities on MCF-7 for 24 h. Other studies have reported that plants of Inula exhibit *in vitro* cytotoxic effects on various cancer cells [20-21]. The *Inula helenium* extract showed a highly selective cytotoxicity effects different cancer cell lines (HT-29, MCF-7, Capan-2 and G1) [22]. Another study, Rozenblat et al. showed that tomentosin and inuviscolide inhibited the growth of three human melanoma cell lines [18]. Our cytotoxic effects of results were different from the previous reports. This situation may arise from harvested region, chemical composition of the plants, climate [6].

4. CONCLUSION

It was observed that *Inula viscosa* extract has high cytotoxic effects on MCF-7 cells. Thus, *Inula viscosa* might be evaluated candidates to develop natural derived therapeutics. Moreover, it may be also an alternative additive for foods. There is a need for further studies in this area.

REFERENCES

[1] Basanagouda M., Jambagi V.B., Barigidad N.N., Laxmeshwar S.S., Devaru V. and Narayanachar M., Synthesis, Structure-activity relationship of iodinated-4-aryloxymethyl-coumarins as potential anti-cancer and anti-mycobacterial agents, European Journal of Medicinal Chemistry, 74 (2014) 225-233.

[2] Barrett J.M., Mechanisms of Multistep Carcinogenesis and Carcinogen Risk., Environmental Health Perspectives,100 (1993) 9-20.

[3] Tan W., Lu J., Huang M., Li Y., Chen M., Wu G., Gong J., Zhong Z., Xu Z., Dang Y., Guo J., Chen X. and Wang Y., Anti-cancer natural products isolated from Chinese medicinal herbs. Chinese Medicine,6 (2011) 27- 42.

[4] Monteiro L.S., Bastos K.X., Barbosa-Filho J.M., Athayde-Filho P.F., Diniz M.F. and Sobral M.V., Medicinal Plants and Other Living Organisms with Antitumor Potential against Lung Cancer., Evidence-Based Complementary and Alternative Medicine, Article ID 604152 (2014) pp 15.

[5] Brullo S. and Marco G., Taxonomical revision of the genus Dittrichia (Asteraceae), Porttugaliae Actua Biol,19 (2000) 341-54.

[6] Messaoudi M., Chahmi N., El Mzibri M., Gmouh S., Amzazi S., Benbacer L. and El Hassouni M., Cytotoxic Effect and Chemical Composition of Inula viscosa from Three Different Regions of Morocco., European Journal of Medicinal Plants, 16-4 (2016) 1-9.

[7] Ana M.L.S., Grigore A., Diana C.G.A.P. and Artur M.S.S., The genus Inula and their metabolites: From ethnopharmacological tomedicinaluses., Journal of Ethnopharmacology, 154 (2014) 286-310.

[8] Su B.N.,Takaishi Y., Yabuuchi T., Kusumi T., Tori M., Takaoka S., Honda G., Ito M., Takeda Y., Kodzhimatov O. K. and Ashurmetov O. Sesquiterpenes and monoterpenes from the bark of Inula macrophylla., J. Nat. Prod., 64 (2001) 466.

[9] Barbetti P., Chiappini I., Fardella G. and Menghini A., A new eudesmane acid from Dittrichia (Inula) viscosa., Planta Med., 51-5 (1985) 471.

[10] Lauro L. and Rolih C. Observations and research on an extract of Inula viscose Ait. Boll, Soc. Ital. Biol. Sper.,66 (1990) 829-834.

[11] Lev E. and Amar Z. Ethnopharmacological survey of traditional drugs sold in Israel at the end of the 20th century., J. Ethnopharmacol,72 (2000) 191-205.

[12] Zhaoa Y., Zhanga M., Shi Q. and Kiyota H., Chemical Constituents of Plants from the Genus Inula., Chemıstry & Biodiversity, 3 (2006) 371.

[13] Adzu B., Balogun O.S., Sérgio E.D., Donizeti A.I., Mendes S.R., Wagner S.A., Reginaldo V.R.Â., Márcia Selhorst S.B.R., Godinhode O.L., Ireneda S.A., Sabino D.D. and Tabajara de O.M., Evaluation of the safety, gastroprotective activity and mechanism of action of standardised leaves infusion extract of Copaifera malmei Harms., Journal of Ethnopharmacology, 175 (2015) 378-389.

[14] Tanaka R., Shıma K., Taruı S. and Nıshıkawa M., Boiling Method for the Extraction of Gut Glucagon-like Immunoreactive Materials, Endocrinol. Japon, 22-6 (1975) 503-507.

[15] Tutar U., Celik C., Karaman I., Hepokur C. and Atas M. The anti-biofilm and antimicrobial activity of Mentha pulegium L. essential oil against multidrug-resistant Acinetobacter baumannii. Trop J Pharm Res., 15-5 (2016) 1039-1046.

[16] Lastra C., Lopez A. and Motilva V., Gastroprotection and prostaglandin E2 generation in rats by flavonoids of Dittrichia viscosa. Planta Med., 59-6 (1993) 497–501.

[17] Haoui IE., Extraction of Essential Oil from Inula viscosa (L.) Leaves: Composition, Antifungal Activity and Kinetic Data. Journal of essential oil-bearing plants, 19-1 (2016)108-118.

[18] Rozenblat S., Grossman S., Bergman M., Gottlieb H., Cohen Y. and Dovrat S., Induction of G2/M arrest and apoptosis by sesquiterpene lactones in human melanoma cell lines, Biochemical Pharmacology, 75 (2008) 369-82.

[19] El Ouariachi E. and Bouyanzer A., Antioxidant activity of solvent extracts of Inula viscosa from Morocco, Arabian Journal of Chemical and Environmental Research, 1(2014)33-40.

[20] Seca A.M., Grigore A., Pinto D.C. and Silva A.M., The genus Inula and their metabolites:From ethnopharmacological to medicinal uses., J Ethnopharmacol,154-2 (2014) 286-310.

[21] Belayachi L., Aceves-Luquero C., Merghoub N., Bakri Y., Fernández de Mattos S., Amzazi S. and Villalonga P., Screening of North

African Medicinal Plant Extracts for Cytotoxic Activity Against Tumor Cell Lines., European Journal of Medicinal Plants,3-3 (2013) 310-332.

[22] Dorn D.C., Alexenizer M. and Hengstler J.G. Dorn A., Tumor cell specific toxicity of Inula helenium extracts, Phytother Res., 20-11(2006)970-80.

Cumhuriyet Science Journal

CSJ

A Mechanism of Eddy Generation in A Single Lid-Driven T-Shaped Cavity

Ebutalib ÇELİK[1] 🆔 *, Ali DELİCEOĞLU[1,*]* 🆔

[1] *Department of Mathematics, Science Faculty, Erciyes University, Kayseri 38039, TURKEY*

Abstract. The two-dimensional (2D) steady, incompressible, Stokes flow is considered in a T-shaped cavity which has the upper-lid moving in horizontal directions. A Galerkin finite element method is used to investigate a new eddy generation and flow bifurcation. The flow in a cavity is controlled by two parameters h_1 and h_2 which are associated with the heights of the T-shaped domain. By varying h_1 and h_2, the second eddy formation mechanism and the h_1, h_2 control space diagram are obtained.

Keywords: A T-shaped cavity, Stokes flow, eddy generation

Tek Kapağı Sürgülü T-Şeklindeki Kaviti İçerisindeki Girdap Oluşum Mekanizması

Özet. Üst kapağı yatay yönde hareket eden T şeklindeki kaviti içerisindeki iki boyutlu (2D) durağan, sıkıştırılamaz, Stokes akış ele alındı. Yeni girdap oluşumunu ve akış çatallanmasını araştırmak için Galerkin sonlu elemanlar yöntemi kullanıldı. Kaviti içersindeki akış, T-şeklindeki bölgenin h_1 ve h_2 yükseklik parametreleri tarafından kotrol edilir. h_1 ve h_2 yüksekliklerinin değişmesiyle meydana gelen girdap oluşum mekanizması ve h_1, h_2 kontrol uzay diyagramı elde edildi.

Anahtar Kelimeler: T-şekilli kaviti, Stokes akış, girdap oluşumu

1. INTRODUCTION

Stokes flow within the closed domain has always been an interesting area of study in computational fluid dynamics. Thanks to the simplicity of the geometric shapes and the easy installation of the related boundary value problem, a lot of work has been done about the driven cavity [1- 8]. In addition, cavity problems are considered as an application of theoretical studies on the investigation of the qualitative properties of streamlines, which is a subject of fluid dynamics [9-12].

In the literature, there are many studies on the flow of square lid-driven cavity flow both numerically and theoretically [13-18]. Gürcan [19] investigated the flow problem of the rectangular cavity with both a single lid-driven and a double lid-driven and examined the vortex formation mechanism in the cavity. He used the analytical solution of the streamfunction expanded about any critical point in the cavity. The control space diagram (S, A) including the aspect ratio A and the velocity ratio S was obtained and investigated the effect of the changes in the ratio of A on vortex formation.

In addition to the square and rectangular domain commonly used in cavity flow problems, different closed domain are also studied. To investigate the effect of cavity geometry on the flow structure, McQuain [20] studied steady, viscous flow within the square, trapezoidal and triangular cavity. Gaskell [21] considered Stokes flow within the half-filled annulus between rotating coaxial cylinders and showed that changes in flow structure arose directly from stagnation point where a saddle point transformed into a centre and vice versa. The 2-D steady, incompressible flow inside a triangular driven cavity is considered numerically in papers of [6, 22, 23]. Gürcan and Bilgil [24] have obtained the vortex formation mechanism in the sectoral cavity as the A aspect ratio decreases for different lid speed ratio. They formed control space diagram with controller parameters A ∈ (1.6,1.65) and S ∈ [−1,0] which is consisted of the curves representing the flow bifurcation at critical points. Finally, they [25] investigated the effect of Reynolds number on the flow bifurcation and vortex formation on the same domain.

Recently, Deliceoğlu and Aydın [26] have considered the flow problem in a L-shaped cavity which has the lids moving in the opposite direction using the numerical method. They have obtained solutions of the Stokes and the Navier-Stokes equations that govern the flow inside the domain using the Galerkin finite element method. Further, they obtained h_1, h_2 control space diagram for the L-shaped cavity with the height of the lower part h_1 and of the upper part h_2. It was determined how this diagram changed when the Reynolds number was 500. In the continuation of their study [7], they have obtained analytical solutions for the Stokes equation for the steady, viscous and single lid-driven flow on the same region. The flow patterns obtained within the region depending on the heights of h_1 and h_2.

To our knowledge, there is no study on the lid-driven cavity flow inside the T-shaped closed domain in the literature. Unlike other regions, the T-shaped cavity has two symmetrical re-entrant corner points. In this paper, we assume that the flow inside the domain is steady, viscous and incompressible. By changing the heights of the lower and of the upper part of the cavity, flow patterns within the region are obtained and the vortex formation mechanism in the parameter space h_1, h_2 is presented.

2. PROBLEM SPECIFICATION AND FORMULATION

We will consider the fluid flow in a two-dimensional upper lid-driven T-shaped cavity with rigid walls as shown in Figure 1. It is assumed that the fluid is Newtonian and incompressible with density ρ and viscosity μ. The flow is steady and two dimensional in the (x, y) plane with velocity u = (u, v). In non-dimensional form, the width of the cavity is fixed (L = 6), the height of the lower part and upper part, called h_1 and h_2, are varying, then the flow topology is determined.
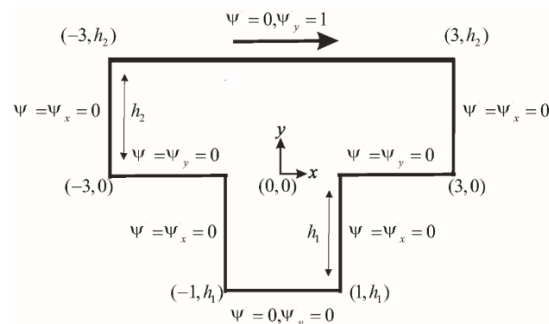

Figure 1: Boundary conditions for the lid-driven T-shaped cavity.

In this paper, it will be concerned that the fluid is steady, incompressible viscous flow. The equation governing the flow field along the cavity is the Stokes equation as the follows:

$$\begin{cases} -\dfrac{1}{\text{Re}}\Delta \mathbf{u} + \nabla p = f & \text{in} \quad \Omega, \\ \nabla \cdot \mathbf{u} = 0 & \text{in} \quad \Omega. \end{cases} \tag{1}$$

If we assume that the external force is negligible so f is zero, then the equation can be written in terms of stream function as follows,

$$\begin{cases} \nabla^4 \psi(x,y) = \left(\dfrac{\partial^4}{\partial x^4} + 2\dfrac{\partial^4}{\partial x^2 \partial y^2} + \dfrac{\partial^4}{\partial y^4} \right) \psi(x,y) = 0, \\ \psi = \text{constant}, \dfrac{\partial \psi}{\partial n} = \text{constant}. \end{cases} \tag{2}$$

The weak formulation of (2) can be written by [27] as follows: find $\Psi \in V = H_0^2(\Omega)$ such that

$$B(\Psi, \Phi) = (\Delta\Psi, \Delta\Phi) = \int_\Omega \Delta\Psi \Delta\Phi d\Omega = 0 \tag{3}$$

for all $\Phi \in H_0^2(\Omega)$ where H_0^2 is the class of all H^2 functions satisfying the boundary condition of (2) and Δ is the Laplacian operator. In this study, the standard Galerkin finite element method is used to solve the bi-harmonic problem (2). In this method, approximation of the problem is determined by the choice of finite dimensional subspace $V_h \subset V$ defined on a family of regular quadrangular discretizations T_h of the domain. A bicubic quadrangular elements are choosed to apply the finite element method as

$$B(\Psi_h, \Phi_h) = (\Delta\Psi_h, \Delta\Phi_h) = 0 \quad \forall(\Psi_h, \Phi_h) \in V_h.$$

Since the test function $\Psi_h \in H^2$, it follows that the basis function Φ_h have continuous first partial derivatives across the boundaries. These provide a two-dimensional version of Hermite interpolation functions as a basis function on a rectangular element. They are constructed by substituting the product of a cubic equation in x by a cubic in y resulting a collection of 16 monomials

$$\begin{bmatrix} 1 \\ x \\ x^2 \\ x^3 \end{bmatrix} \begin{bmatrix} 1 & y & y^2 & y^3 \end{bmatrix} = \begin{bmatrix} 1 & y & y^2 & y^3 \\ x & xy & xy^2 & xy^3 \\ x^2 & x^2 y & x^2 y^2 & x^2 y^3 \\ x^3 & x^3 y & x^3 y^2 & x^3 y^3 \end{bmatrix}$$

For each element, the coefficient of these monomials are calculated using each of the following four quantities:

$$\left\{ \Psi_h, \frac{\partial \Psi_h}{\partial x}, \frac{\partial \Psi_h}{\partial y}, \frac{\partial^2 \Psi_h}{\partial x \partial y} \right\},$$

at each corner of the rectangle. See [27,28] for more information.

3. FLOW STRUCTURES IN THE T-SHAPED CAVITY

In this section, we will show a flow structures topologically occurring and describe the vortex formation within the T-shaped cavity as the varying of the heights of the lower part h_1 and the upper part h_2. By changing of these parameters, bifurcation curves are obtained to reveal changes in the flow structure. Here, the expression of the change in the flow structure refers to the transformation of the type of stationary point from the saddle to the center or vice versa. The (h_1, h_2) parameter space is obtained by finding the critical values of h_1 and h_2 in which structural changes occur.

We consider (h_1, h_2) parameter space in the interval between $-3.5 < h_1 < -0.2$ and $0.2 < h_2 < 10.5$, so we have obtained a 23 different flow topologies shown by Figure 2, Figure 3 and Figure 4. A set of co-dimension-one bifurcation curves in the parameter space are obtained by using the numerical methods. The co-dimension of a bifurcation is the smallest number of parameters needed to find bifurcation. The control-space diagram is formed by fixing h_1 while changing h_2 or vice versa. Then, the related bifurcation curves are illustrated in Figure 5.
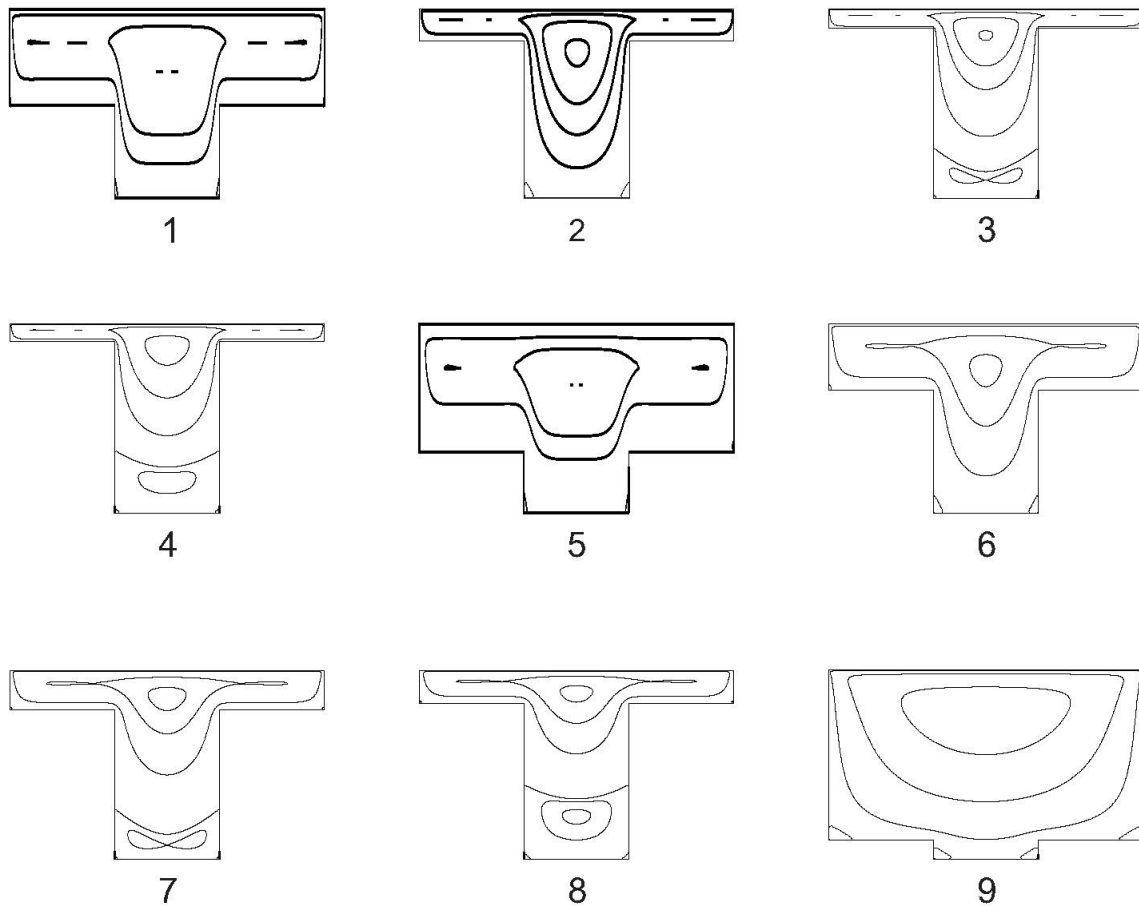
Figure 2. *Representation of the flow patterns within the domain: (1) h_1 = -0.29, h_2 = 0.3, (2) h_1 = -1.75, h_2 = 0.35, (3) h_1 = -3.1, h_2 = 0.35, (4) h_1 = -3.4, h_2 = 0.35, (5) h_1 = -0.205, h_2 = 0.42, (6) h_1 = -1.3, h_2 = 0.7, 7) h_1 =-0.64, h_2 = 0.7, (8) h_1 = -3.3, h_2 = 0.7, (9) h_1 = -0.6, h_2 =5.45.*
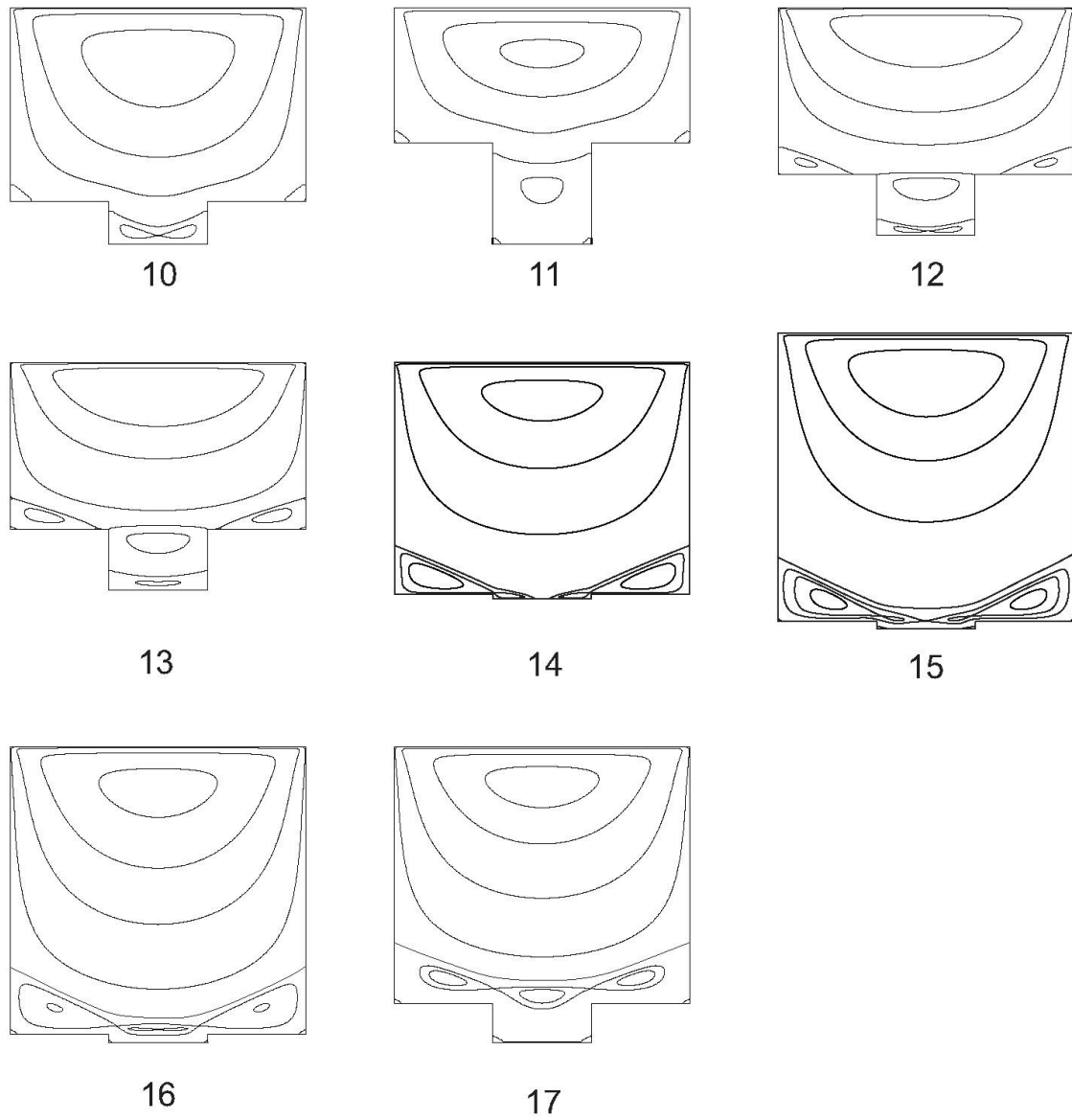
Figure 3. *Representation of the flow patterns within the domain (continued): (10)* $h_1 = -1.1$, $h_2 = 4.95$, *(11)* $h_1 = ---2.6$, $h_2 = 3.45$, *(12)* $h_1 = -3.4$, $h_2 = 9.3$, *(13)* $h_1 = -3.47$, $h_2 = 9.5$, *(14)* $h_1 = -0.2$, $h_2 = 9.605$, *(15)* $h_1 = -0.23$, $h_2 = 9.7$, *(16)* $h_1 = -0.28$, $h_2 = 9.75$, *(17)* $h_1 = -1.5$, $h_2 = 9.9$.
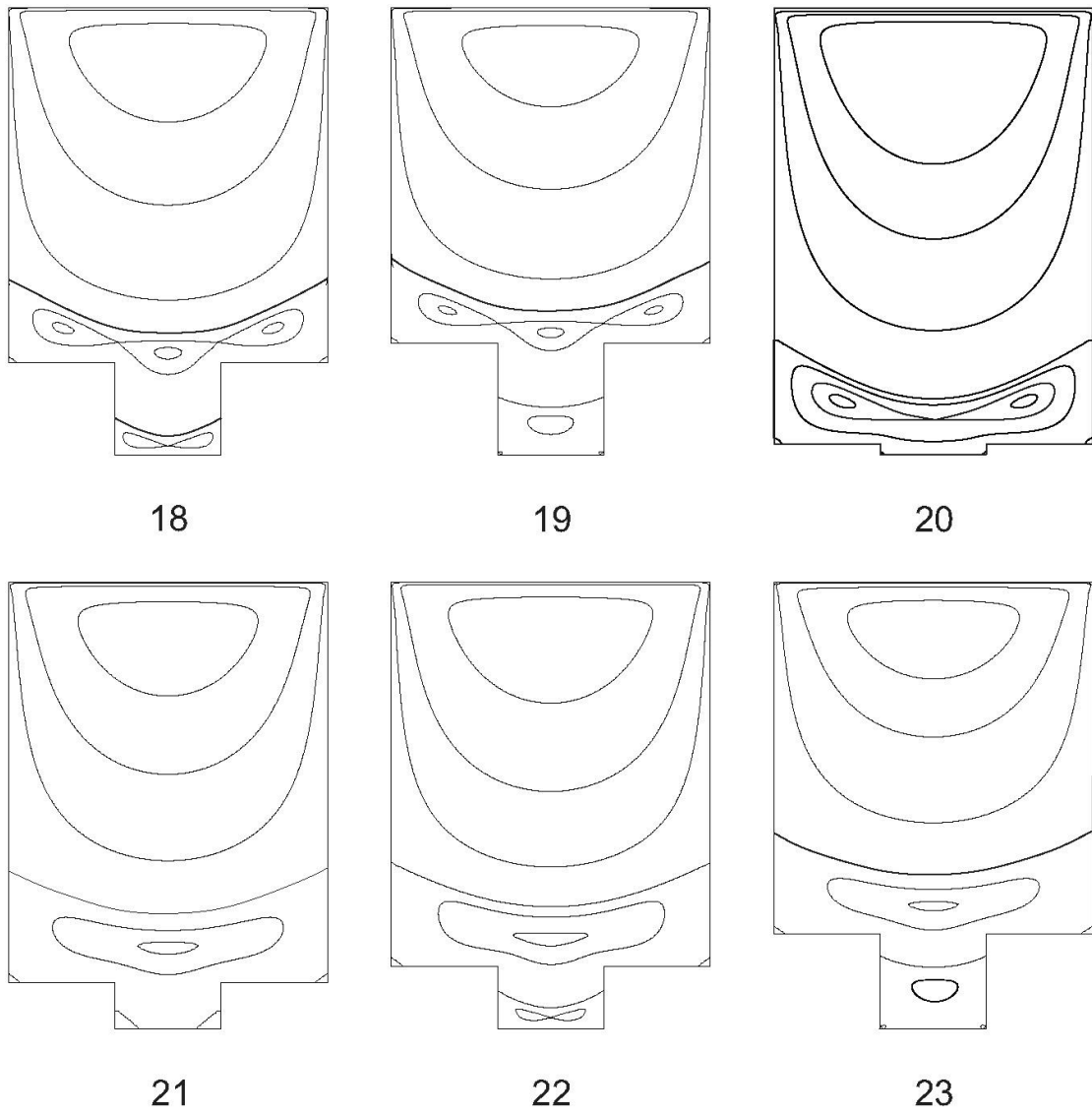
Figure 4. *Representation of the flow patterns within the domain (continued): (18)* $h_1 = -2.57$, $h_2 = 9.87$, *(19)* $h_1 = -3.3$, $h_2 = 9.9$, *(20)* $h_1 = -0.23$, $h_2 = 10.1$, *(21)* $h_1 = -1.2$, $h_2 = 10.4$, *(22)* $h_1 = -1.7$, $h_2 = 10.4$, *(23)* $h_1 = -2.8$, $h_2 = 10.4$.
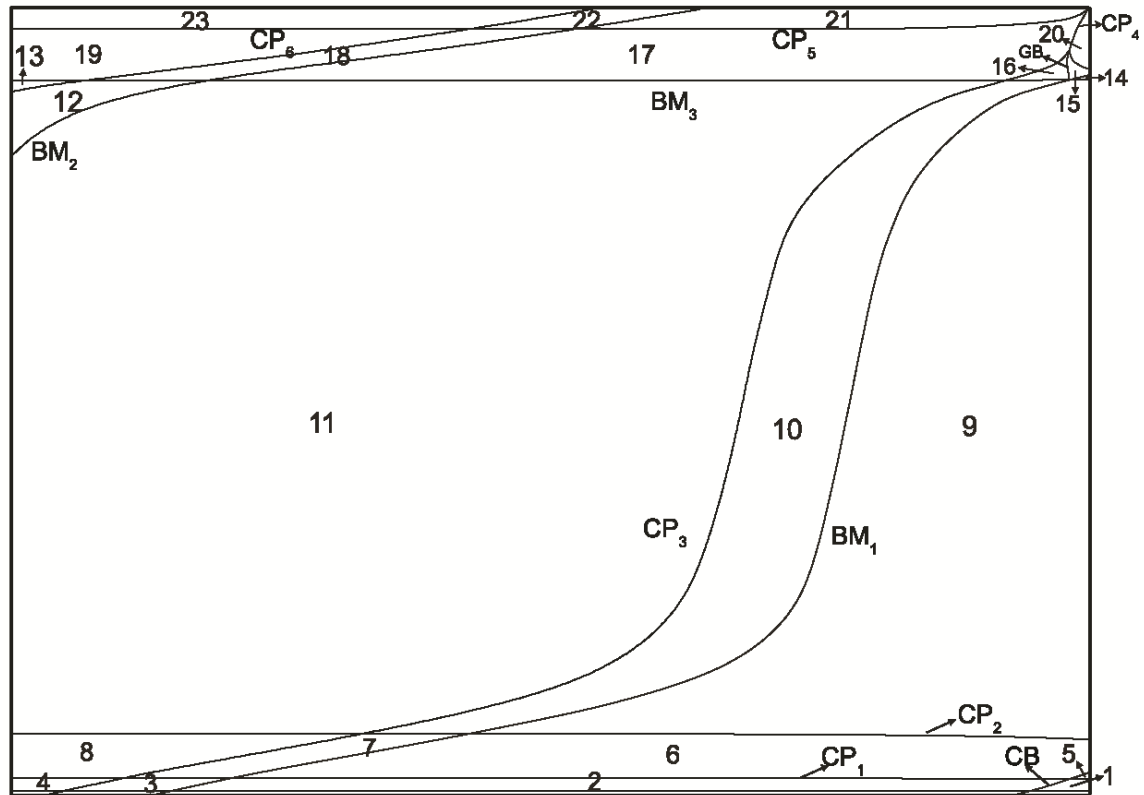
Figure 5. (h_1, h_2) control space diagram for the cavity. The numbers in each region refer to flow strustures in Figure 2, Figure 3 and Figure 4.

4.   THE MECHANISM OF EDDY GENERATION WITHIN THE DOMAIN

Four types of bifurcation are observed in parameter space (h_1, h_2). The first type of bifurcation appears on the wall at which two on-wall saddle points come together to form an off-wall saddle point. The curves representing this bifurcation in the diagram are called BM. In the second type of bifurcation, the degenerate points are transformed from the saddle into the centre point inside the flow such that it is called cusp bifurcation and denoted by CP in the parameter space. These types of degenerate critical points are illustrated in Figure 6. In the global bifurcation which is named by GB, there is a change in the flow structure but no change in the number of critical points. In the last type, the center point transform into saddle and vice versa. This type of bifurcation is named by CB.
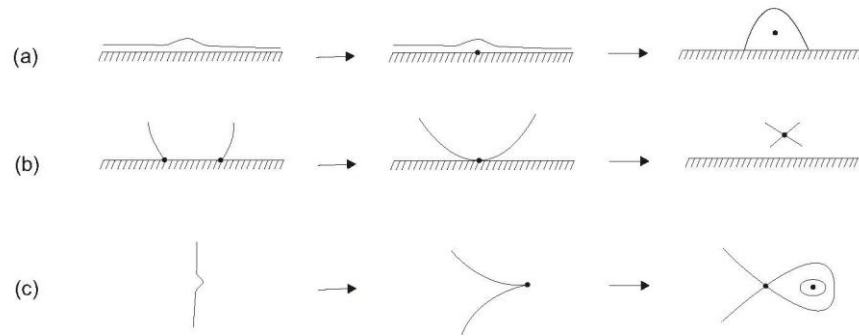
Figure 6. Streamline topology near a stationary wall (a)-(b) and away from boundary (c).

A mechanism of flow transformation according to varying the heights of the lower part and upper part of the cavity is given in Figure 2, Figure 3 and Figure 4. When the upper part of the cavity is small, for example $0.2 < h_2 < 1.0$, the discontinuity of the stream lines causes the flow structure not to be fully understood. In this case, the bi-section method given by Gaskell [21] is used to understand whether the critical point is a saddle or centre. In this study, the vertical velocity decided the type of structures near the critical point, depending on the sign exchange in the vector component. A similar approach is used in this study in regions 1-8 in Figure 2.

Below the curve of the CP_1, there is a flow pattern giving rise to a separatrix enclosing the five sub-eddies at the upper part of the cavity and two corner eddies at the lower part. In the flow structure illustrated in Figure 2(1), the main vortex of separatrix contains 2 separatrices nested within the central section. When we cross to the second region by CB curve, the saddle critical point at the central section of the first structure is transformed into the centre critical point. When h_2 is constant and the h_1 is decreased, the formation of the second vortex in the lower part of the cavity occurs by the known vortex formation mechanism, as shown in Figure 2 ($2 \rightarrow 3 \rightarrow 4$). This mechanism was observed in the square cavity by Gürcan [19] and in the L-shaped cavity by Deliceoğlu [26] for the S = 0. There is also a similar flow transformation series between the CP_1 and CP_2, Figure 2($6 \rightarrow 7 \rightarrow 8$), or CP_2 and BM_3 curve, Figure 2-Figure3 ($9 \rightarrow 10 \rightarrow 11$). While this series occurs, the separation line that separates the lower cavity and the upper cavity moves upward. However, the saddle-node bifurcation, where the corners of the upper cavity and the separation line coalesce, occurs at the same value of h_1.
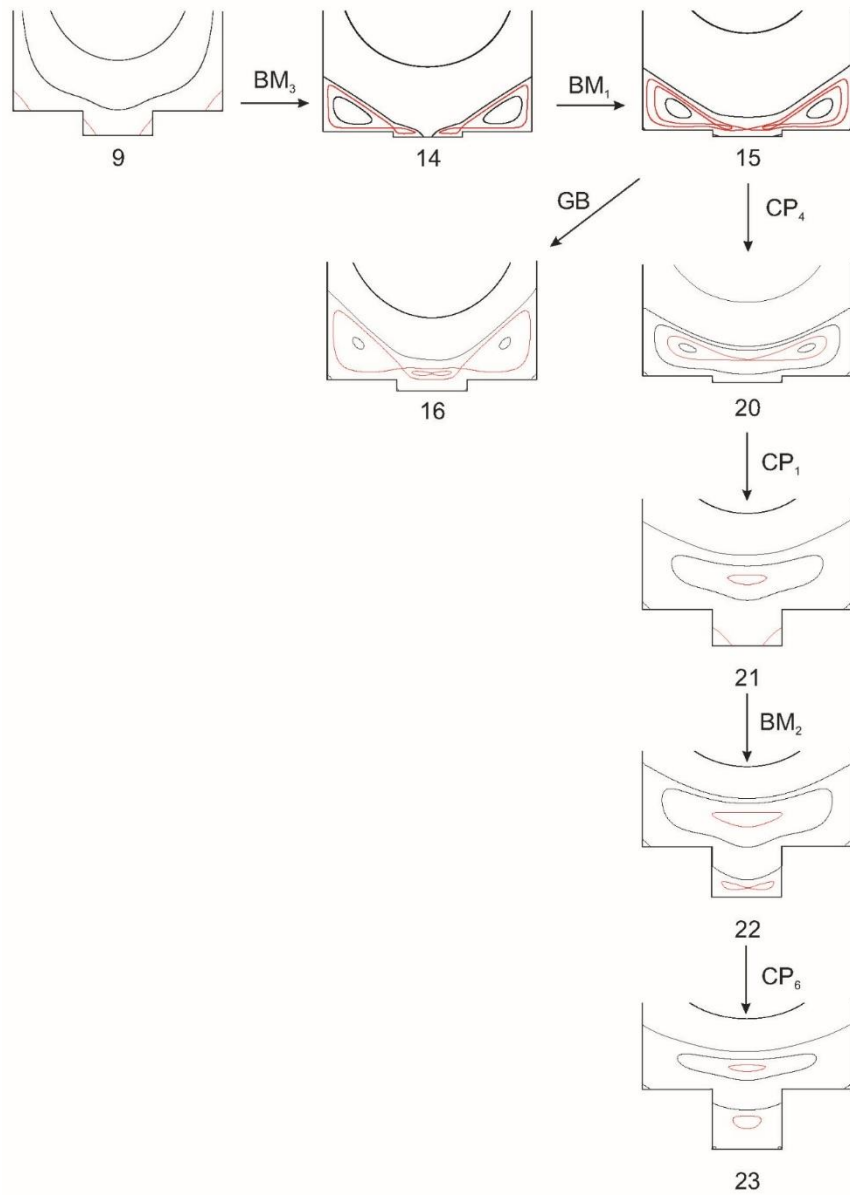
Figure 7. The mechanism of eddy generation via several transformation which is similar with in the rectangular cavity.
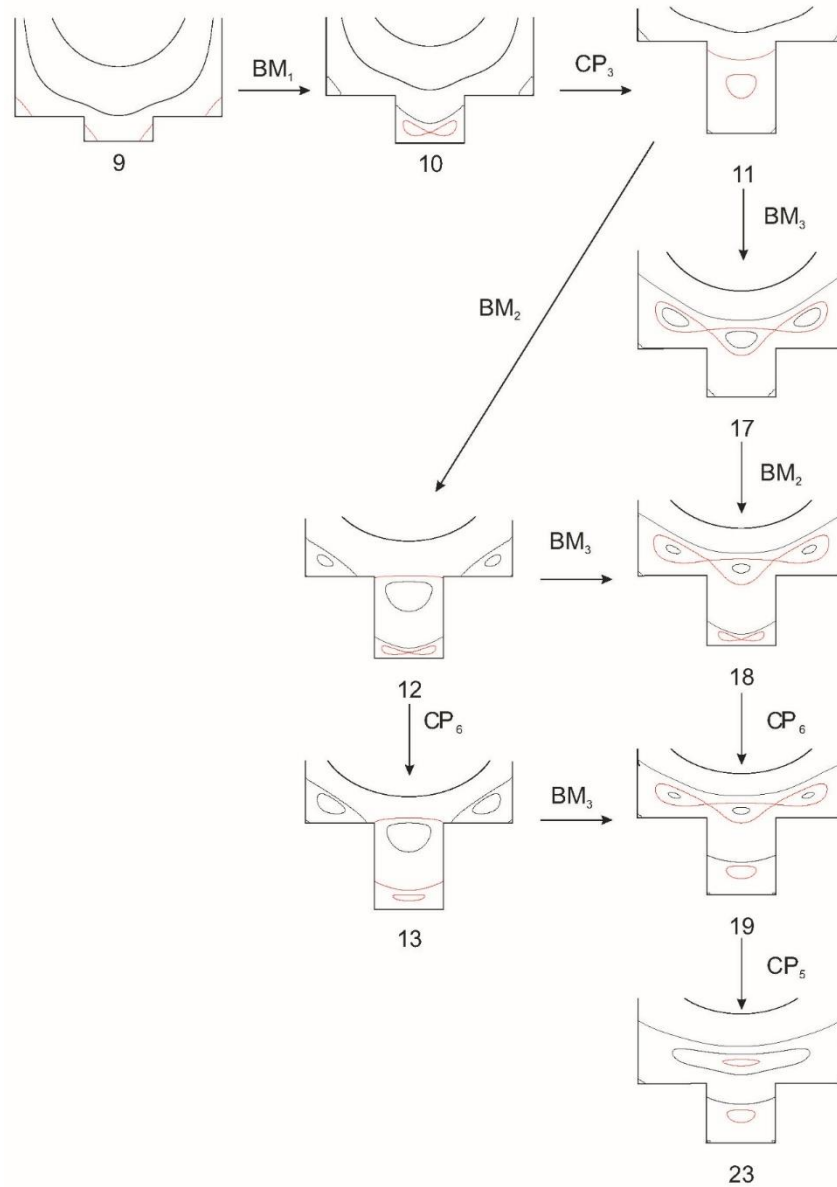
Figure 8. The series of bifurcation which is previously unseen.

Another vortex formation scenario is seen when the lower cavity height is sufficiently small. The corner vortices of the lower cavity coalesce with the corner vortices of the upper cavity before they are joined together. Thus, there are two corner vortices containing separatrix inside the cavity. After BM and CP bifurcation, separatrix is formed inside the fluid as in the square cavity and after the CP bifurcation, the second vortex is formed as in Figure 7 ($9 \rightarrow 14 \rightarrow 15 \rightarrow 20 \rightarrow 21$). There are a few basic scenarios for the new vortex formation, where the separation line crosses the corner point and is coalesced with the corner vortices. These different flow transformation scenarios are shown in Figure 8.

5. CONCLUSION

In this study, we have shown the flow patterns and eddy generation in a T-shaped cavity. The flow is generated by the motion of the upper lid of the cavity. The (h_1, h_2) control space diagram have obtained for the interval between $-3.5 < h_1 < -0.2$ and $0.2 < h_2 < 10.5$. It is observed that the bifurcation transformation series in order to increase the number of eddies in the lower cavity is the same as in the square cavity as h_2 is constant. Furthermore, when h_1 was sufficiently small, it is observed for the first

time that the vortex formation occurred by joining the corner vortices together. In other cases, the number of vortices within the cavity increases as a result of various bifurcations series of the dividing line with corner vortices.

REFERENCES

[1] Shankar, P. N., The eddy structure in Stokes flow in a cavity, Journal of Fluid Mechanics, 250 (1993) 371–383.

[2] Gaskell, P. H., Gürcan, F., Savage, M. D., Thompson, H. M., Stokes flow in a double-lid-driven cavity with free surface side walls, Proceedings of the Institution of Mechanical Engineers, Part C: Journal of Mechanical Engineering Science, 212(5) (1998) 387–403.

[3] Gürcan, F., Gaskell, P. H., Savage, M. D., Wilson, M. C. T., Eddy genesis and transformation of Stokes flow in a double-lid driven cavity, Proceedings of the Institution of Mechanical Engineers, Part C: Journal of Mechanical Engineering Science, 217(3) (2003) 353–364.

[4] Liu, C., Joseph, D., Stokes flow in wedge-shaped trenches, Journal of Fluid Mechanics, 80(3) (1977) 443-463.

[5] R Schreiber, H.B Keller, Driven cavity flows by efficient numerical techniques, Journal of Computational Physics, 49(2) (1983) 310-333.

[6] Erturk, E., Gokcol, O., Fine Grid Numerical Solutions of Triangular Cavity Flow, Applied Physics, 38(1) (2007) 97–105.

[7] Deliceoğlu, A., Aydin, S. H. Topological flow structures in an L-shaped cavity with horizontal motion of the upper lid, Journal of Computational and Applied Mathematics, 259(PART B) (2014) 937–943.

[8] Gürcan, F., Bilgil, H., Bifurcations and eddy genesis of Stokes flow within a sectorial cavity, European Journal of Mechanics, B/Fluids, 39 (2013) 42-51.

[9] Brøns, M., Hartnack, J. N., Streamline topologies near simple degenerate critical points in two-dimensional flow away from boundaries, Physics of Fluids, 11(2) (1999) 314–324.

[10] Gürcan, F., Deliceoğlu, A., Bakker, P. G., Streamline topologies near a non-simple degenerate critical point close to a stationary wall using normal forms, Journal of Fluid Mechanics, 539 (2005) 299–311.

[11] Gürcan, F., Deliceoğlu, A., Streamline topologies near non-simple degenerate points in two-dimensional flows with double symmetry away from boundaries and an application, Physics of Fluids, 17(9) (2005) 1–7.

[12] Hartnack, J. N., Streamlines topologies near a fixed wall using normal forms, Acta Mechanica, 75 (1999) 55–75.

[13] Erturk, E., Corke, T. C. and Gökçöl, C., Numerical solutions of 2-D steady incompressible driven cavity flow at high Reynolds numbers. Int. J. Numer. Meth. Fluids, 48 (2005) 747-774.

[14] Botella, O., Peyret, R., Benchmark Spectral Results on the Lid Driven Cavity Flow, Computers and Fluids, 27(4) (1998) 421–433.

[15]   Driesen, CH, Kuerten, JGM and Streng, M., Low-Reynols-Number flow over partially covered cavities, J. Eng. Math., 34 (1998) 3-20.

[16]   Gaskell, PH, Savage, MD, Summers, JL and Thompson, HM., Stokes flow in closed, rectangular domains, Applied Mathematical Modelling, 22 (1998) 727-743.

[17]   Ghia, U, Ghia, KN and Shin, CT., High-Re solution for incompressible flow using the Navier-Stokes equations and a multigrid method, J. Comp. Physics, 48 (1982) 387-411.

[18]   Gürcan, F., Effect of the Reynolds number on streamline bifurcations in a double-lid-driven cavity with free surfaces, Computers and Fluids, 32 (2003) 1283-1298.

[19]   Gürcan, F., Flow bifurcations in rectangular, lid-driven, cavity flows. PhD. Thesis (1996), University of Leeds.

[20]   William D. McQuain, Calvin J. Ribbens, C.-Y. Wang, Layne T. Watson., Steady viscous flow in a trapezoidal cavity, Computers and Fluids, 23(4) (1994) 613-626.

[21]   Gaskell, P., Savage, M., Wilson, M., Stokes flow in a half-filled annulus between rotating coaxial cylinders, Journal of Fluid Mechanics, 337 (1997) 263-282.

[22]   Ribbens, C. J., Watson, L. T., Wang, C.-Y., Steady Viscous Flow in a Triangular Cavity, Journal of Computational Physics, 112(1) (1994) 173–181.

[23]   Gaskell, P.H., Thompson, H, Savage, M., A finite element analysis of steady viscous flow in triangular cavities, Proceedings of The Institution of Mechanical Engineers Part C-journal of Mechanical Engineering Science, 213 (1999) 263-276.

[24]   Gurcan, F., Bilgil, H., Bifurcations and eddy genesis of Stokes flow within a sectorial cavity PART II: Co-moving lids, European Journal of Mechanics- B/Fluids, 56 (2015) 42–51.

[25]   Bilgil, H., Gürcan, F., Effect of the Reynolds number on flow bifurcations and eddy genesis in a lid-driven sectorial cavity, Japan Journal of Industrial and Applied Mathematics, 33(2) (2016) 343–360.

[26]   Deliceoğlu, A., Aydin, S. H., Flow bifurcation and eddy genesis in an L-shaped cavity, Computers and Fluids, 73 (2013) 24-46.

[27]   E.B. Becker, G.F. Carey and J.T. Oden, Finite Elements, An introduction Vol. I. Prentice-Hall, 1981, New Jersey.

[28]   Aydın, S. H., The Finite Element Method Over a Simple Stabilizing Grid Applied to Fluid Flow Problems, PhD Thesis (2008).

Determination of the annual effective dose distribution due to cosmic ray exposure of the Eastern Black Sea Region, Turkey

Cafer Mert YEŞİLKANAT (iD)

Science Teaching Department, Artvin Çoruh University, Artvin, Turkey

Abstract. In this study, annual effective dose rate distribution due to cosmic radiation, which constitutes an important part of natural radiation, was mapped in $200 \times 200 m^2$ spatial pixels for three provinces in the Eastern Black Sea region (Artvin, Rize and Trabzon). Cosmic ray-induced annual effective dose calculations were performed based on latitude and altitude changes with EXPACS, an excel-based program. Besides, the effect of cosmic radiation on the population living in the study area was determined. For the entire study area, it was calculated the average effective dose rate from Cosmic radiation as 0.65 *mSv y^{-1}* and range as (0.33-1.72) *mSv y^{-1}*. The average annual collective effective dose rate was determined approximately 508 *person-Sv y^{-1}*. Besides, the population-weighted average annual effective dose rates were obtained as 449 $\mu Sv\ y^{-1}$, 376 $\mu Sv\ y^{-1}$ and 370 $\mu Sv\ y^{-1}$ for Artvin, Rize and Trabzon provinces, respectively.

Keywords: Annual effective dose rate, Cosmic radiation, Eastern Black Sea Region, Mapping

Doğu Karadeniz Bölgesinde kozmik ışın kaynaklı yıllık etkin doz dağılımının belirlenmesi

Özet. Bu çalışmada doğal radyasyonun önemli bir kısmını oluşturan kozmik ışın kaynaklı yıllık etkin doz hızı dağılımı, Doğu Karadeniz Bölgesindeki üç il için (Artvin, Rize ve Trabzon) $200 \times 200 m^2$ 'lik mekânsal çözünürlükte haritalandırılmıştır. Kozmik ışın kaynaklı yıllık etkin doz oranı hesaplamaları, Excel tabanlı çalışan bir program olan EXPACS ile enlem ve rakım değişimlerine bağlı olarak gerçekleştirilmiştir. Ayrıca çalışma alanında yaşayan nüfusun kozmik radyasyondan etkilenme seviyeleri de tespit edilmiştir. Çalışma alanının tamam için, Kozmik ışından kaynaklanan yıllık etkin doz oranının ortalaması 0.65 *mSv y^{-1}* ve değişim aralığı (0.33-1.72) *mSv y^{-1}* olarak hesaplanmıştır. Çalışma alanının geneli için yıllık kollektif etkin doz hızı ise yaklaşık 508 *insan-Sv y^{-1}* olarak belirlenmiştir. Ayrıca kozmik radyasyondan kaynaklanan kişi başı yıllık etkin doz, sırasıyla Artvin, Rize ve Trabzon için 449 $\mu Sv\ y^{-1}$, 376 $\mu Sv\ y^{-1}$ ve 370 $\mu Sv\ y^{-1}$ olarak tespit edilmiştir.

Anahtar Kelimeler: Yıllık etkin doz hızı, Kozmik radyasyon, Doğu Karadeniz Bölgesi, Haritalama

1. INTRODUCTION

People are constantly exposed to natural radiation sources throughout their lives. These natural radiation sources are evaluated under two main groups [1]. The first group is terrestrial radionuclide induced radiation connected to geological rock structures. The second group is cosmic radiation from extraterrestrial sources. Approximate 14% of the annual effective dose is caused by Cosmic radiation [2,3]. The large amount of cosmic rays are stopped by the atmosphere before it reaches the ground. Cosmic

rays that can pass through the atmosphere have significant effects in areas above sea level [4]. The effective dose due to cosmic ray exposure averaged over the world's population was assessed to be 0.38 *mSv y*$^{-1}$ [2].

Cosmic radiation is an ionizing radiation produced by the collision of atoms in the Earth's atmosphere with extraterrestrial photons and *α* particles [5]. In addition, charged particles released from solar flares are an important source of cosmic radiation. [6].

The effect of the cosmic ray increases with the increase of latitude and altitude [7]. Due to the geomagnetic latitude effect, it has been reported that the dose rate of Cosmic radiation increases at higher latitudes (in Arctic), while the dose rate decreases at lower latitudes (in Equator) [4]. The earth's magnetic field shows a shield effect against cosmic rays. In addition, the increase in altitude causes the components of the dose equivalent from Cosmic radiation to change [2]. The greatest contribution to the equivalent dose at the sea level comes from muon, but due to the increase in height, the neutrons, protons, photons, electrons and positrons also take into account the dose rate caused by the Cosmic ray [8]. The direct dependence of the cosmic rays on both latitude and altitude has led to the exploration of new approaches in the prediction of cosmic ray-induced dose distribution. One of the studies in recent years is PARMA/EXPACS model which was created by Sato et al.[4,9–11]. EXPACS (EXcel-based Program for calculating Atmospheric Cosmic-ray Spectrum) is a sophisticated model for calculating cosmic ray doses, taking into account factors such as latitude, longitude, altitude, solar activity, atmospheric depth and cut-off rigidity [12]. It is based on the PARMA model (PHITS based Analytical Radiation Model in the Atmosphere) [4,10]

In recent years, many studies have been conducted to determine the efective dose distribution caused by cosmic radiation. Cinelli et al. [13] calculated the cosmic ray-induced effective dose rate for the whole of Europe based on the height factor and created a distribution map. Sato et al. [14] mapped the effective dose distribution of population-weighted cosmic radiation from the entire world with the EXPACS model. In both studies, local changes could not be determined with appropriate sensitivity due to the calculation of very large areas.

The purpose of this study is to create a map of cosmic radiation dose distribution for the eastern Black Sea region where have most rugged terrain of Turkey, and to determine the total dose values which is exposure of the population living in this region. Thus, it is aimed to define some of the previously obtained global results in a more detailed way.

2. MATERIAL AND METHOD

2.1. Study Area

The study area is the three provinces (Artvin, Rize and Trabzon) in the eastern Black Sea Region of Turkey. Figure 1a shows the study area. These provinces represent an important part of the Eastern Black Sea Region in terms of population and surface area. The average altitude of the study area is approximately 800*m* for Trabzon and Rize, and about 1600*m* for Artvin [15]. Elevation changes are in the range of (0-3700) *m* for Artvin, (0-3200) *m* for Trabzon and (0-3400) *m* for Rize. These rapid elevation changes lead to sudden changes in cosmic radiation dose. In addition, the intense solar radiation effect at high locations increases the Cosmic Ray Fluxes [16].

Figure 1b shows the population distribution map for the study area in 2018 [17]. This map was created by estimating population values for $100 \times 100 \ m^2$ regular grid (1 pixel) with random forest machine learning algorithm [18]. Moreover, Each pixel in the present study area was updated with current population

information provided by Turkey Statistical Institute [19], and this level of resolution (100×100 m^2 cells) was decreased to 200×200 m^2 .
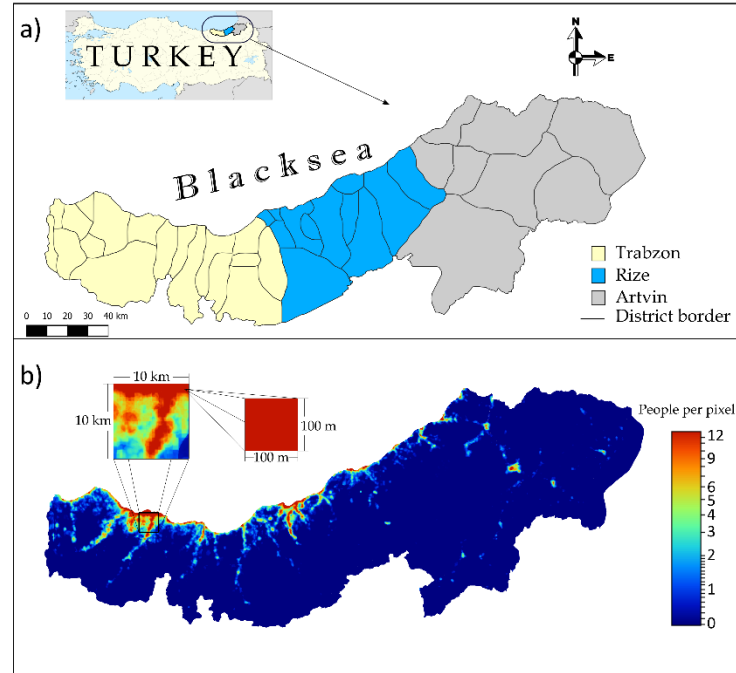
Figure 1. a) Study area, b) Population distribution map determined by 100×100 m^2 pixel for study area [17].

2.2. Dose Calculation

The dose calculations in this study were calculated with EXPACS (EXcel-based Program for calculating Atmospheric Cosmic-ray Spectrum) [4,9,12]. This program is based on the PARMA model [9] which is named PHITS (Particle and Heavy Ion Transport code System) -based Analytical Radiation Model in the Atmosphere (PARMA) [10,11]. EXPACS model can calculate terrestrial cosmic ray fluxes of protons, neutrons, muons, electrons, positrons, ions with charge up to 28 (Ni) and photons nearly in the Earth's atmosphere. it can also calculate the effective dose from the obtained cosmic ray fluxes [12].

2.3. Components of Cosmic Radiation

Typically, Cosmic rays are examined as primary and secondary cosmic rays. The primary cosmic rays are very high energy cosmic rays that reach the earth directly. They consist of protons (87%), particles (11%), nuclei with low atomic numbers (1%) and high-energy electrons (1%) [20]. Secondary cosmic rays are formed by the collision with gas atoms in the atmosphere of primary cosmic rays. The energy of such rays is lower than the primary cosmic rays. Secondary cosmic rays are divided into two classes as the directly and indirectly ionizing component [21]. Directly ionizing components of cosmic radiation are two class as muonic component (muons) and electromagnetic component (photons. electrons and positrons). Indirectly ionizing components of cosmic radiation are neutrons and protons [22]. Although muons constitute the most important component at sea level of the effective dose rate from secondary cosmic rays, neutrons, electrons, photons, positrons and protons also affect the effective dose rate with the increase in altitude [8].

2.4. Software Sources

All analyzes and calculations in this study were performed by R programming [23]. All maps used and prepared in the study were created with Quantum Geographic Information System (QGIS) version 2.18.23

[24]. In addition, regular grid analysis and estimation data were combined with SAGA-GIS version 2.3.2 [25].

3. RESULTS AND DISCUSSIONS
3.1. Mapping of Cosmic Ray Dose

All the study area was defined by a regular grid area of 200×200 m^2 pixels. Figure 2 shows the structure of the regular grid created for this study. Each pixel in this regular grid was represented by latitude, longitude, altitude and population information. In particular, by taking into account the latitude and altitude effects, it was calculated with the EXPACS model the effective dose rate from the cosmic ray for each grid pixel. Later, all results obtained were indicated by a color scale and mapped. In Figure 3 shows the cosmic ray-induced annual effective dose rate distribution map and statistical summary values for all the study area. According to the results, it was determined that Artvin is affected by cosmic rays more than Rize and Trabzon. The main reason for this is thought to be due to high altitude areas in Artvin province. For the overall study area, the mean and range of the effective annual dose from Cosmic radiation was calculated 0.65 *mSv y*[-1] and (0.33-1.72) *mSv y*[-1], respectively. According to the UNSCEAR report, the average annual dose from Cosmic radiation is approximately 0.46 *mSv y*[-1] (the directly ionizing and photon component the average value is 0.34 *mSv y*[-1] and the neutron component, the average value is 12 *mSv y*[-1]) [2]. In addition, the study conducted by Cinelli et al. reported that the annual average effective dose rate from Cosmic radiation was about 0.39 *mSv y*[-1] for the whole of Europe [13] . The average annual effective dose rate obtained from the study was found to be higher than in Europe and the world averages.
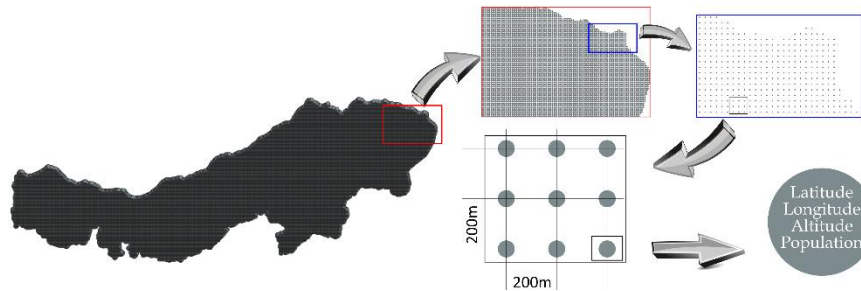
Figure 2. Grid structure of study area
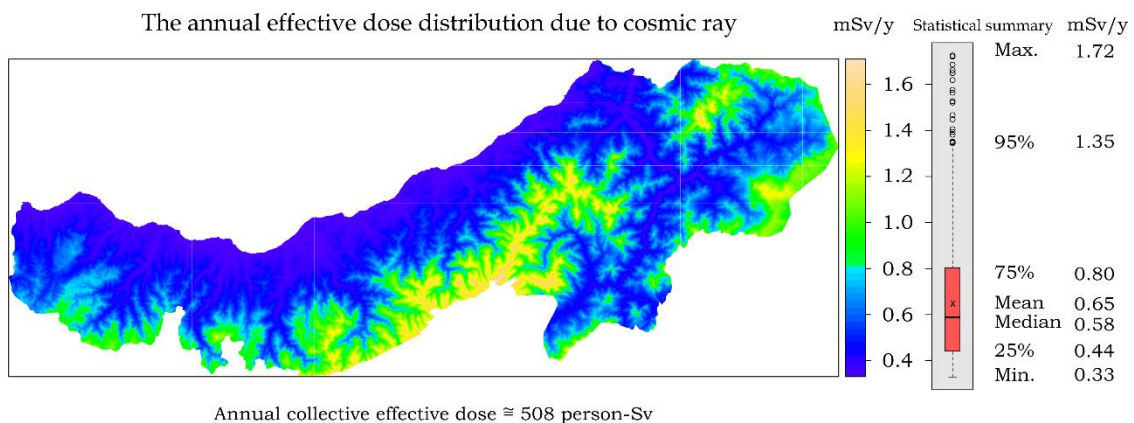
Figure 3. Distribution map of annual effective dose rate from cosmic radiation for study area

3.2. Determination of Population Exposure

Based on the total population data of the study area for 2018, Annual cosmic-ray collective effective dose was determined to be approximately 508 *person-Sv y*[-1]. The collective dose was calculated for each grid

node ($200 \times 200 \ m^2$) by multiplying the annual effective dose value with the number of population per pixel. This calculated dose rate is higher than European countries such as Estonia (400 *person-Sv y⁻¹*), Montenegro (200 *person-Sv y⁻¹*), Luxembourg (200 *person-Sv y⁻¹*) ve Iceland (200 *person-Sv y⁻¹*) [13]. Figure 4 show Annual collective effective dose (*person-Sv y⁻¹*) and the average annual effective dose per capita ($\mu Sv \ y^{-1}$) due to cosmic rays for each province in the study area. The annual collective effective dose rate vary depending on the population of the provinces and have been calculated as 79 *person-Sv y⁻¹*, 135 *person-Sv y⁻¹* and 295 *person-Sv y⁻¹* for Artvin, Rize and Trabzon, respectively. In addition, average the population-weighted (per person) annual effective dose rate due to cosmic radiation was computed as 449 $\mu Sv \ y^{-1}$ for Artvin, 376 $\mu Sv \ y^{-1}$ for Rize and 370 $\mu Sv \ y^{-1}$ for Trabzon. In only Artvin was determined a value above the world mean value (390 $\mu Sv \ y^{-1}$) of per person annual effective dose rate reported by UNSCEAR [2]. In addition, the average effective dose per capita for the whole study area was calculated 382 $\mu Sv \ y^{-1}$. This dose rate are quite close to the per capita average annual effective dose of Turkey (about 400 $\mu Sv \ y^{-1}$) [13].
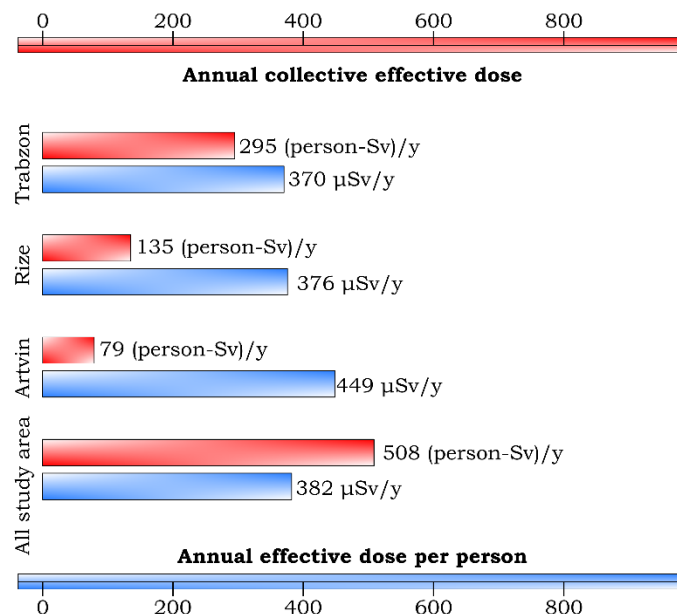
Figure 4. Annual collective effective dose (*person-Sv y⁻¹*) and the average annual effective dose per person ($\mu Sv \ y^{-1}$) due to cosmic rays for each province in the study area.

4. CONCLUSION

In this study, the effective dose rate distribution due to cosmic radiation in the Eastern Black Sea Region of Turkey was mapped and the effect levels from this cosmic rays of the population were determined. The maps were created in $200 \times 200 \ m^2$ pixels and latitude, longitude, altitude and population information were defined in each pixel. Dose calculations were calculated with EXPACS, which is an Excel-based program based on the PARMA model. The dose calculations were separately performed for each pixel, and then the annual effective dose rate distributions were mapped by representing the calculated results on a color scale. At the end of the study, the mean and range of the annual effective dose rate due to cosmic radiation was computed 0.65 *mSv y⁻¹* and (0.33-1.72) *mSv y⁻¹*, respectively. The average annual collective effective dose rate and the population-weighted average annual effective dose rate were obtained 79 *person-Sv y⁻¹* and 449 $\mu Sv \ y^{-1}$ for Artvin, 135 *person-Sv y⁻¹* and 376 $\mu Sv \ y^{-1}$ for Rize and 295 *person-Sv y⁻¹* and 370 $\mu Sv \ y^{-1}$ for Trabzon. In addition, the average annual per capita effective dose for all the study area was calculated as 382 $\mu Sv \ y^{-1}$ closely to average of Turkey (about 400 $\mu Sv \ y^{-1}$).

REFERENCES

[1]   Yeşilkanat C.M., Kobya Y., Taskin H., Çevik U., Dose rate estimates and spatial interpolation maps of outdoor gamma dose rate with geostatistical methods; A case study from Artvin, Turkey, J. Environ. Radioact. 150 (2015) 132–144. doi:10.1016/j.jenvrad.2015.08.011.

[2]   UNSCEAR, Source and effects of ionizing radiation, United Nations Scientific Committee on the Effects of Atomic Radiation, Report to the General Assembly with Annex B, United Nations, New York, 2000.

[3]   Zeyrek C.T., İyonize Radyasyon Uygulamaları İçin Güvenlik ve Korunmaya Yönelik Genel Kavramlar. (In Turkish), Süleyman Demirel Üniversitesi Fen Bilim. Enstitüsü Derg. 17 (2013) 1–9.

[4]   Sato T., Analytical model for estimating the zenith angle dependence of terrestrial cosmic ray fluxes, PLoS One. 11 (2016) 1–22. doi:10.1371/journal.pone.0160390.

[5]   Bagshaw M., Illig P., The Aircraft Cabin Environment, Fourth Edi, Elsevier Inc., 2018. doi:10.1016/b978-0-323-54696-6.00047-1.

[6]   Wilson B.G., Nehra C.P., Cosmic Ray Increases Associated with Solar Flares, J. Phys. Soc. Japan Suppl. 17 (1962) 269. https://ui.adsabs.harvard.edu/abs/1962JPSJS..17B.269W/abstract (accessed July 5, 2019).

[7]   Neher H. V., Cosmic rays at high latitudes and altitudes covering four solar maxima, J. Geophys. Res. 76 (1971) 1637–1651. doi:10.1029/JA076i007p01637.

[8]   O'Brien K., Friedberg W., Sauer H.H., Smart D.F., Atmospheric cosmic rays and solar energetic particles at aircraft altitudes., Environ. Int. 22 (1996) 9–44. http://www.ncbi.nlm.nih.gov/pubmed/11542509.

[9]   Sato T., Analytical model for estimating terrestrial cosmic ray fluxes nearly anytime and anywhere in the world: Extension of PARMA/EXPACS, PLoS One. 10 (2015) 1–33. doi:10.1371/journal.pone.0144679.

[10]   Sato T., Niita K., Matsuda N., Hashimoto S., Iwamoto Y., Noda S., Ogawa T., Iwase H., Nakashima H., Fukahori T., Okumura K., Kai T., S. Chiba, T. Furuta, L. Sihver, Particle and heavy ion transport code system, PHITS, version 2.52, J. Nucl. Sci. Technol. 50 (2013) 913–923. doi:10.1080/00223131.2013.814553.

[11]   Sato T., Niita K., Matsuda N., Hashimoto S., Iwamoto Y., Furuta T., Noda S., Ogawa T., Iwase H., Nakashima,H., Fukahori T., Okumura K., Kai T., Chiba S., Sihver L., Overview of particle and heavy ion transport code system PHITS, Ann. Nucl. Energy. 82 (2015) 110–115. doi:10.1016/J.ANUCENE.2014.08.023.

[12]   EXPACS, EXcel-based Program for calculating Atmospheric Cosmic-ray Spectrum (EXPACS),URL: https://phits.jaea.go.jp/expacs/, (2016).

[13]   Cinelli G., Gruber V., De Felice L., Bossew P., Hernandez-Ceballos M.A., Tollefsen T., Mundigl S., De Cort M., European annual cosmic-ray dose: Estimation of population exposure, J. Maps. 13 (2017) 812–821. doi:10.1080/17445647.2017.1384934.

[14]   Sato T., Evaluation of world population-weighted effective dose due to cosmic ray exposure, Sci. Rep. 6 (2016) 6–12. doi:10.1038/srep33932.

[15]   USGS, Digital elevation maps (DEM) data sets, http://earthexplorer.usgs.gov/ (Available date: 11.01.2015), (2013). http://earthexplorer.usgs.gov/.

[16]   YEGM, Yenilenebilier Enerji Genel Müdrlüğü (YEGM), Tükiye Güneş Enerjisi Potansiyel Atlası (GEPA), URL: http://www.yegm.gov.tr/MyCalculator/, (2019).

[17]   WorldPop, WorldPop (www.worldpop.org) and Center for International Earth Science Information Network (CIESIN), Columbia University, (2018). doi:https://dx.doi.org/10.5258/SOTON/WP00645.

[18]   Stevens F.R., Gaughan A.E., Linard C., Tatem A.J., Disaggregating census data for population mapping using Random forests with remotely-sensed and ancillary data, PLoS One. 10 (2015) 1–22. doi:10.1371/journal.pone.0107042.

[19]   Turkish Statistical Institute (TurkStat), Population Statistics, URL: http://www.turkstat.gov.tr/UstMenu.do?metod=temelist. Date Accessed: 14.02.2019, (2019).

[20]   Eisenbud M., Gesell T., Enviromental Radioactivity, 4. edition, Academic Press, 1997.

[21]   Rasolonjatovo D.A.H., Suzuki H., Hirabayashi N., Nunomiya T., Nakamura T., Nakao N., Measurement for the dose-rates of the cosmic-ray components on the ground., J. Radiat. Res. 43 Suppl (2002) S27-33. doi:10.1269/jrr.43.s27.

[22]   Schlickeiser R., Direct Observations of Cosmic Rays, in: 2002: pp. 25–71. doi:10.1007/978-3-662-04814-6_3.

[23]   Ihaka R., Gentleman R., R: A Language for Data Analysis and Graphics, J. Comput. Graph. Stat. 5 (1996) 299–314. doi:10.1080/10618600.1996.10474713.

[24]   Quantum GIS Development Team, Quantum GIS Geographic Information System. Open Source Geospatial Foundation Project, (2018). https://qgis.org/en/site/index.html (date accessed: 10.12.2018).

[25]   Böhner J., Bock M., Wichmann V., Fischer E., Wehberg J., Conrad O., Bechtel B., Dietrich H., Gerlitz L., System for Automated Geoscientific Analyses (SAGA) v. 2.1.4, Geosci. Model Dev. 8 (2015) 1991–2007. doi:10.5194/gmd-8-1991-2015.

Structural and Optical Properties of Indium Selenide (InSe) Thin Films Deposited on Glass and GaSe Single Crystal Substrates by SILAR Method

Hüseyin ERTAP[1]* iD *, Mustafa YÜKSEK[2]* iD *, Mevlüt KARABULUT[3]* iD

[1] Department of Physics, Science and Letters Faculty, Kafkas University, 36100 Kars, Turkey

[2] Department of Electrical-Electronics Engineering, Faculty of Engineering, Kafkas University, 36100 Kars, Turkey

[3]Department of Physics, Faculty of Science, Gebze Technical University, 41400 Kocaeli, Turkey

Abstract. Structural, morphological and optical properties of undoped and boron doped Indium Selenide (InSe) thin films grown on glass and layered Gallium Selenide (GaSe) single crystal substrates with SILAR method have been investigated by XRD, AFM and UV-Vis spectrophotometer techniques**.** XRD measurements showed that the crystal structure of InSe thin films grown on glass substrates were hexagonal P61 γ-In$_2$Se$_3$ with lattice parameters a=7.1286 Å, c=19.382 Å and z=6 while the InSe thin films grew as hexagonal P63/mmc InSe with lattice parameters a=4.005 Å, c=16.640 Å and z=4 on GaSe single crystal substrates. The AFM images showed that average particle sizes of undoped and boron doped InSe thin films were found to be varying between 26.5-60.2 nm and 30.9-101.5 nm grown on glass and GaSe single crystal substrates, respectively. The optical absorption spectra of undoped and boron doped InSe thin films grown on both glass and GaSe single crystal substrates showed absorption maxima around the 2.00 and 2.24 eV, respectively. The calculated Urbach energies of the InSe thin films grown on glass substrates were found bigger than those of the InSe thin films grown on GaSe single crystal substrates.

*Keywords***:** Indium Selenide, SILAR, thin film, GaSe single crystal substrate, Boron.

SILAR Metodu ile Cam ve GaSe Tek Kristal Alt Tabanlar Üzerinde Büyütülen İndiyum Selenit (InSe) İnce Filmlerinin Yapısal ve Optik Özellikleri

Özet. SILAR metodu ile cam ve tabakalı Galyum Selenit (GaSe) tek kristal alt tabanlar üzerinde büyütülen saf ve bor katkılı İndiyum Selenit (InSe) ince filmlerinin yapısal, morfolojik ve optik özellikleri XRD, AFM ve UV-Vis spektrofotometre teknikleri ile araştırıldı. XRD ölçümlerinden cam alt tabanlar üzerinde büyütülen InSe ince filmlerinin örgü parametrelerinin a=7.1286 Å, c=19.382 Å ve z=6 olan hekzagonal P61 γ-In$_2$Se$_3$ iken GaSe tek kristal alt tabanlar üzerinde büyütülen InSe ince filmlerinin örgü parametrelerinin a=4.005 Å, c=16.640 Å ve z=4 olan hekzagonal P63/mmc InSe olduğu görüldü. AFM görüntülerinden cam ve GaSe tek kristal alt tabanlar üzerinde büyütülen saf ve bor katkılı InSe ince filmlerinin ortalama parçacık boyutlarının sırasıyla 26.5-60.2 nm ve 30.9-101.5 nm aralığında değiştiği bulundu. Hem cam hem de GaSe tek kristal alt tabanlar üzerinde büyütülen saf ve bor katkılı InSe ince filmlerinin optik soğurma spektrumlarında sırasıyla 2.00 ve 2.24 eV civarında soğurma maksimumları gösterdi. Cam alt tabanlar üzerinde büyütülen InSe ince filmlerinin Urbach enerjilerinin GaSe tek kristal alt tabanlar üzerinde büyütülen InSe ince filmlerinin Urbach enerjilerinden daha büyük olduğu bulundu.

*Anahtar Kelimeler***:** İndiyum Selenit, SILAR, ince film, GaSe tek kristal alt taban, Bor.

* Corresponding author. *Email address:*   huseyinertap@gmail.com and huseyinertap@kafkas.edu.tr

1. INTRODUCTION

Indium Selenide (InSe) is a member of $A^{III}B^{VI}$ layered semiconductor crystals family, which also includes Gallium Selenide (GaSe), Gallium Tellurit (GaTe) and Gallium Sulphide (GaS) semiconductor crystals. These layered semiconductor crystals have strong anisotropies in chemical bonds between and within the layers as the layers are bonded together by the weak van der Waals forces while within the layers strong covalent bonds dominate. Absence of dangling bonds on the cleaved surfaces makes these crystals appropriate for the formation of heterojunctions [1-8]. InSe crystallizes in the stacking type of layers, each monolayer consist of two indium and two selenium closed-packed sublayers in the stacking sequence of Se-In-In-Se along the c axis [3, 9]. InSe single crystal has a band gap around 1.3 eV [9] and this property makes it desired material for solar cell applications [5, 10, 11]. Stoichiometric InSe is an n-type semiconductor, on the other hand, when it doped with any atoms the conductivity may change to p-type. There are four defined compounds in the phase diagram of In-Se denoted by InSe, α-In$_2$Se$_3$, α-In$_3$Se$_8$ and In$_2$Se [12]. InSe thin films have been studied for solar cell applications [5]. Nonlinear refraction index of InSe thin films deposited by thermal evaporation has been studied recently [13]. Deposition techniques, starting materials and preparation conditions are important because of the possibility of different phases for InSe thin films. In addition, deposition techniques may affect the structures, optical and electrical properties of thin films.

Several deposition techniques have been used in the growth of thin films. These methods include vacuum evaporation, microwave glow discharge, chemical vapor deposition, modulated flux deposition, Molecular Beam Epitaxy, Chemical Bath Deposition (CBD), electrodeposition, thermal evaporation and modified chemical bath deposition (M-CBD) [12-19]. The M-CBD method is also known as SILAR. SILAR method is a relatively simple and inexpensive method, however suitable for large area deposition of different configurations. The SILAR method is based on sequential reactions of cationic and anionic constituents at the substrate surface. It is a stepwise process of chemical deposition of thin films. Because of the Van der Waals bonds between the layers, the (0001) surfaces of the GaSe layers do not have dangling bonds. For this reason, InSe thin films grown on these substrates bind via Van der Waals bonds. Since the surface density of the states of naturally mirror faced GaSe layer is low (less than 10^6 cm^{-2}) [20], the density of states of heterojunctions formed by the InSe-GaSe junctions may have low density of states.

In the present study, as well known that the ion radii of the substituted atoms change the lattice parameters of the crystal structure and alter the band gaps of the crystals. For these reasons, we preferred the boron doping to InSe to investigate the changes in the lattice parameters and band gaps of the crystals. Undoped and boron doped InSe thin films have been prepared by the SILAR method on glass and GaSe single crystal substrates and their structural, morphological, optical properties were investigated by XRD, AFM and UV-Vis absorption measurements.

2. EXPERIMENTAL

The GaSe single crystal substrates were cleaved from the GaSe single crystal ingots grown by Bridgman method [6, 21] by using a razor blade. The substrates were prepared at 1cmx3cmx80μm sizes. No chemical process was applied to these naturally mirror faced GaSe single crystals prior to growth process. In addition, InSe thin films were also grown on glass substrates. The glass substrates were cleaned thoroughly before the deposition process. In order to obtained In and Se source solutions, which are $In_2(SO_4)_3$ and Na_2SeSO_3, In particles and Se powders were dissolved in H_2SO_4 and $NaSO_3$ solvents, respectively. The $Na_2B_4O_7.10H_2O$ solution was added to the cationic solution for the deposition of boron doped InSe thin films. The pH of the solutions was fixed to ~3 by addition of tartaric acid to the solvents. Four glass beakers were named as 1, 2, 3 and 4. Then, 20 ml $In_2(SO_4)_3$ and 20 ml Na_2SeSO_3 were added to 1 and 3 glass beakers, respectively, and glass beakers which are named as 2 and 4 were filled with distilled water. The substrates were immersed vertically into the 1, 2, 3 and 4 glass beakers, respectively. The substrates were stood up into the 1, 2, 3 and 4 glass beakers as 30 s, 70 s, 10 s and 70 s, respectively, and each of this process named as a cycle. Cycles were carried out 75 and 50 times for the deposition of InSe thin films on the glass and the GaSe single crystal substrates, respectively. The thicknesses of InSe thin films were estimated by the amount of films deposited, the surface area and the density [22]. The thickness of InSe thin films grown on glass substrates were calculated as ~ 110 nm.

The surface morphology of undoped and boron doped InSe thin films grown on glass and GaSe single crystal substrates were studied with help of a PSIAXE-100E model Atomic Force Microscopy (AFM). The structures of the thin films were characterized by using a X-ray diffractometer (XRD) (Rigaku D/max-2200). The optical absorption spectra of the thin films were recorded with help of a UV-Vis spectrophotometer (Perkin-Elmer Lambda 25).

3. RESULT AND DISCUSSION

The XRD spectra of undoped and boron doped InSe thin films grown on glass substrates are given in Fig. 1 a-b, respectively.
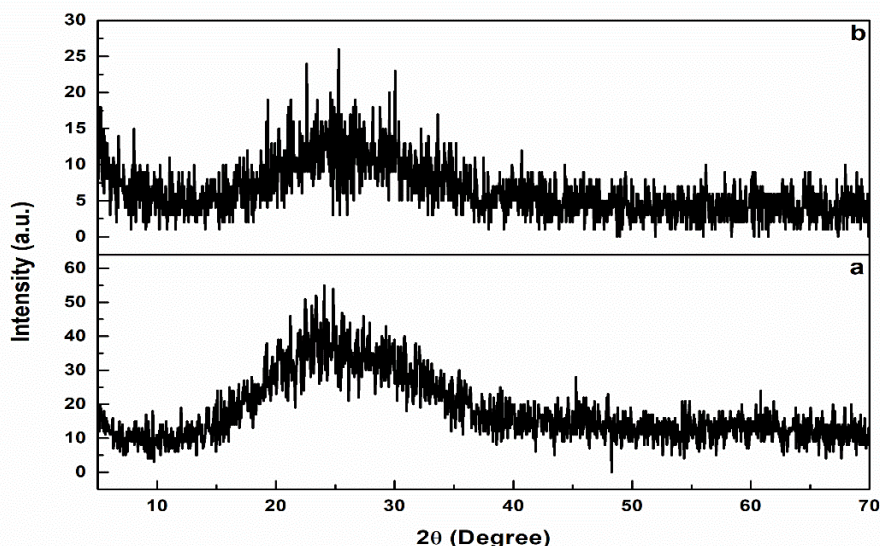
Figure 1. The XRD spectra of **(a)** undoped, **(b)** boron doped InSe thin films grown on glass substrates.

As seen from Fig. 1 a-b, undoped and boron doped InSe thin films grew in crystalline form on glass substrate. The structure of InSe thin films are determined as hexagonal (γ-In$_2$Se$_3$) with a = 7.128 Å, c = 19.382 Å, z = 6 lattice parameters and P61 space group (JCPDS Card No: 40-1407) [23]. The obtained crystallographic data is in accordance with the data given in the literature for In$_2$Se$_3$ crystal [23, 24]. The broad hump in the spectra of undoped and boron doped InSe thin films is due to the glass substrates. The XRD spectra values of undoped and boron doped InSe thin films, which are grown on glass substrates are found similar. The XRD spectra peaks of boron doped InSe thin films a little broad and the crystallization seems to be more prominent according to the undoped InSe thin films. It is clearly seen from the Fig. 1 a-b that the peak intensities of the InSe thin films decrease with the boron addition. Peak positions of undoped and boron doped InSe thin films grown on glass substrates are given in Table 1 a-b, respevtively.

Table 1: Peak position of **(a)** undoped, **(b)** boron doped InSe thin films grown on glass substrates.

Thin Film	2θ(Degree)		Planes(hkl)	Thin Film	2θ(Degree)		Planes(hkl)
	Observed	PDF File			Observed	PDF File	
a) γ-In₂Se₃ JCPDS Card No: 40-1407	23.249	23.338	1 0 4	**b) γ-In₂Se₃** JCPDS Card No: 40-1407	22.359	23.338	1 0 4
	24.764	24.968	1 1 0		24.704	24.968	1 1 0
	25.437	25.377	1 1 1		25.640	25.377	1 1 1
	29.430	29.274	2 0 1		29.546	29.274	2 0 1
	43.763	43.973	3 0 0		30.171	30.365	2 0 2
	45.353	45.337	2 1 5		33.871	34.156	1 1 5
	47.947	47.667	2 0 8		35.653	35.504	1 0 7
	59.304	59.137	2 2 6		38.517	38.843	2 1 1
					43.272	43.973	3 0 0
					47.971	47.677	2 0 8
					56.156	56.982	0 0 12
					59.653	59.137	2 2 6

The XRD spectra of GaSe single crystal, undoped and boron doped InSe thin films grown on GaSe single crystal substrates are given in Fig. 2 a-c, respectively. Fig. 2 a is showing the XRD spectra of GaSe single

crystal, grown by Bridgman method, which has a = 3.750 Å, c= 15.950 Å, z = 4 lattice parameters and P63/mmc space group (JCPDS Card No: 37-0931) [25].

Figure 2. The XRD spectra of **(a)** GaSe single crystal substrate, **(b)** undoped, **(c)** boron doped InSe thin films grown on GaSe

single crystal substrates.

X-ray diffraction analysis showed that peak intensities are decreasing and peak positions shifting to higher angles for undoped and boron doped InSe thin films compared to the GaSe single crystal substrate peaks. GaSe single crystal substrate has (0 0 2), (0 0 4), (0 0 6), (0 0 8) and (2 0 2) difraction peaks (Fig. 2 a). By the deposition of undoped and boron doped InSe thin films on this substrates the (0 0 6), (0 0 8) and (2 0 2) diffraction peaks quenched. There are some observable changes in the XRD spectra of both undoped and boron doped InSe thin films grown on GaSe single crystal substrates. Compared to the undoped InSe thin film, the XRD peak intensity of boron doped InSe thin film decrease and peak positions shift to higher degrees with boron addition. As a result, as noted before [12, 23, 24, 26-28], we have demonstrated that the thin film structures depend on the used substrate structures.

The surface morphology of undoped and boron doped InSe thin films grown on glass and GaSe single crystal substrates were investigated by AFM technique. The AFM images taken from different areas of undoped and boron doped InSe thin films grown on glass and GaSe single crystal substrates are given in Fig. 3 a-b and Fig. 4 a-b, respectively.

Figüre 3. The AFM images of **(a)** undoped, **(b)** boron doped InSe thin films grown on glass substrates in different areas.
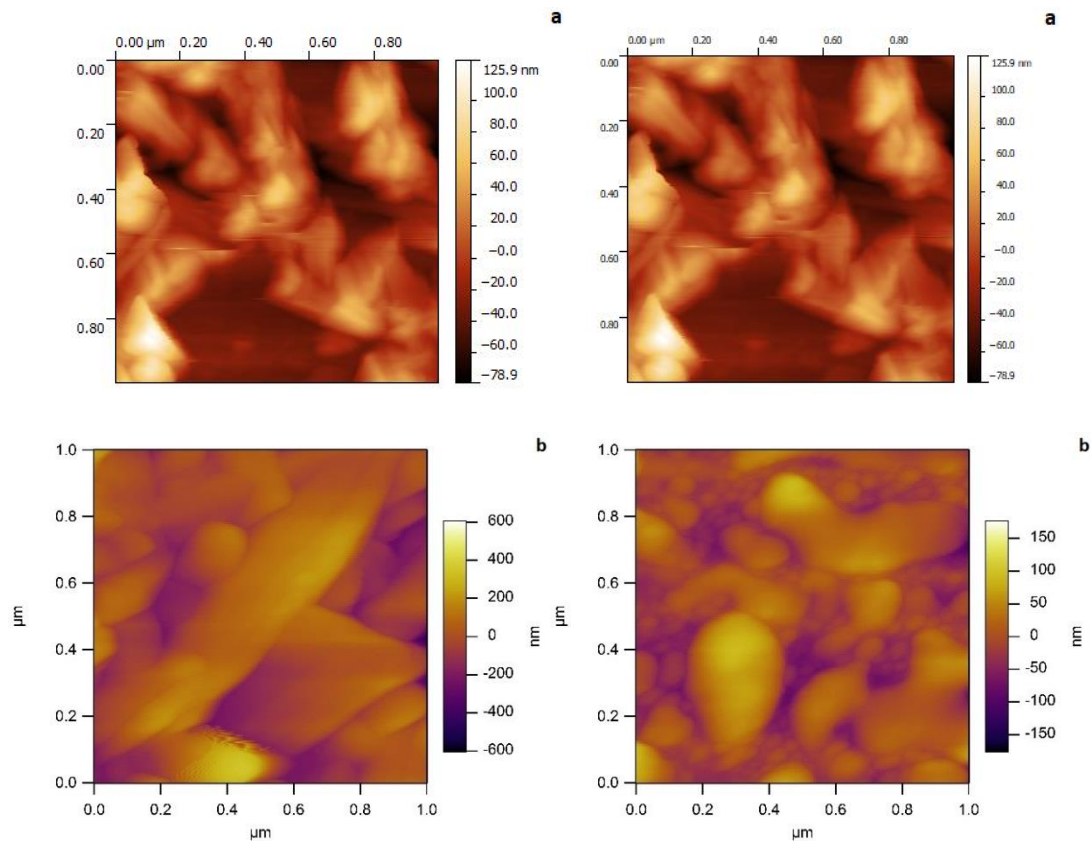
Figure 4. The AFM images of **(a)** undoped, **(b)** boron doped InSe thin films grown on GaSe single crystal substrates in different areas.

The particle sizes of all thin films were determined from Fig. 3 and Fig. 4 images by using XEI 1.6.1 software. The obtained average particle sizes were estimated between 26.5-60.2 nm and 30.9-101.5 nm for undoped and boron doped InSe thin films deposited upon glass and GaSe single crystal substrates, respectively. Similar average particle sizes of the InSe thin film grown on glass substrate were found [16]. It is clearly seen from the estimated particle sizes that the average particle sizes of undoped and boron doped InSe thin films depend on substrate types. The effect of annealing on these thin films was studied previously and it was found that particle sizes increased as a result of the annealing [16].

The optical absorption spectra of undoped and boron doped InSe thin films grown on glass substrates are given in Figure 5 a-b, respectively.
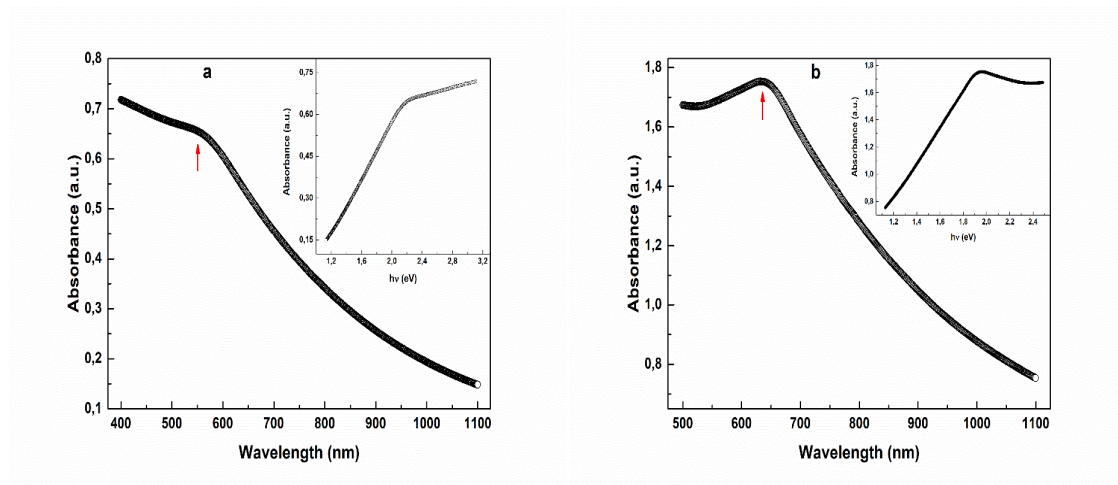
Figure 5. The optical absorption spectra of **(a)** undoped, **(b)** boron doped InSe thin films grown on glass substrates.

The slight increase at the absorption edge indicates the presence of the defect and dopant states at the band gap**.** The absorption tail of the InSe thin film grown on glass substrate starts at 1.13 eV. The absorption spectra of undoped InSe thin film have an exponential region, starting from 1.36 eV and show a maximum at 2.24 eV. The absorption tail of boron doped InSe thin film is also starting from 1.13 eV, but the absorption maximum is ending at 1.96 eV. The absorption tail shows an exponential dependence on the energy according to the Urbach rule. Steepness of the exponential absorption tail is determined from the absorption spectra as:

$$\alpha = \alpha_0 \, exp\left[(\frac{\sigma(T)}{k_B T})(h\vartheta - E_g)\right]$$

where k_B is the Boltzman constant, T is the temperature and υ is the frequency of the incident photons. The Urbach energy is also determined with the steepness of the tail, $E_u = k_B T / \sigma$ [29-31]. The Urbach energies were calculated as 513 meV and 792 meV for undoped and boron d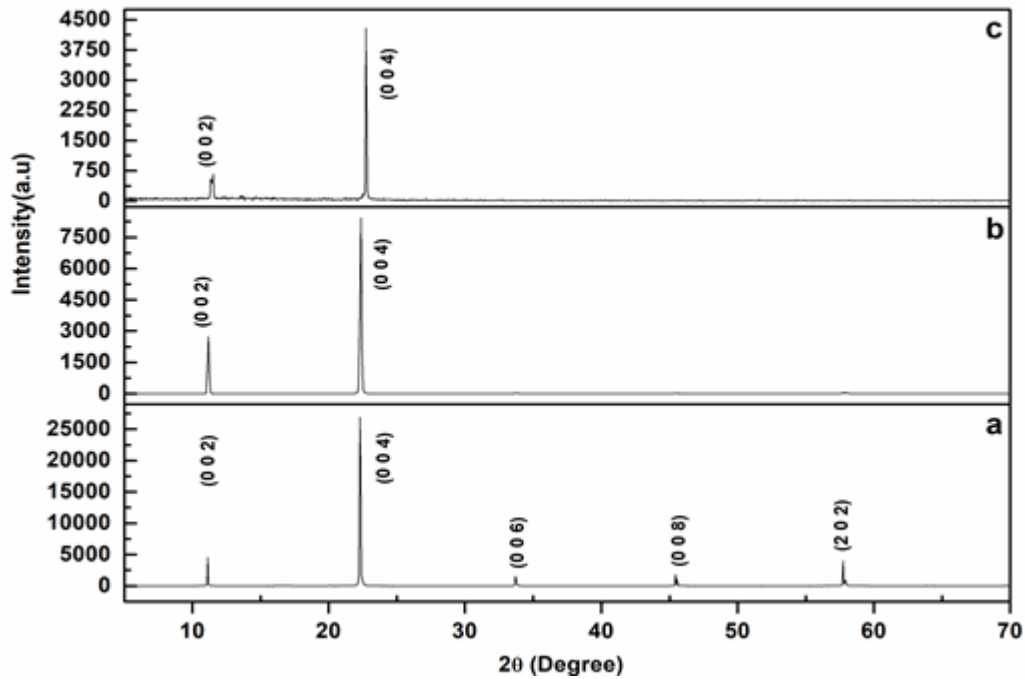oped InSe thin films grown on glass substrates, respectively. The optical absorption spectra of the GaSe single crystal substrate, undoped and boron doped InSe thin films grown on GaSe single crystal substrates are given in Figure 6 a-c, respectively.

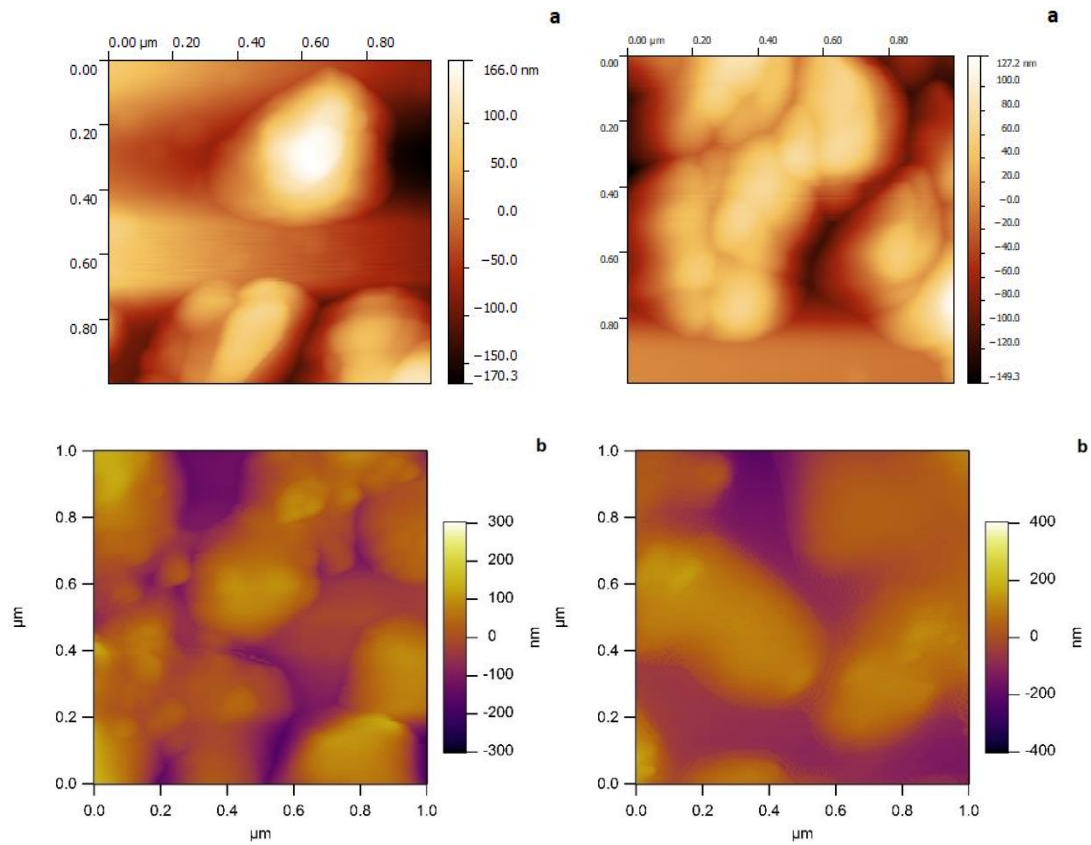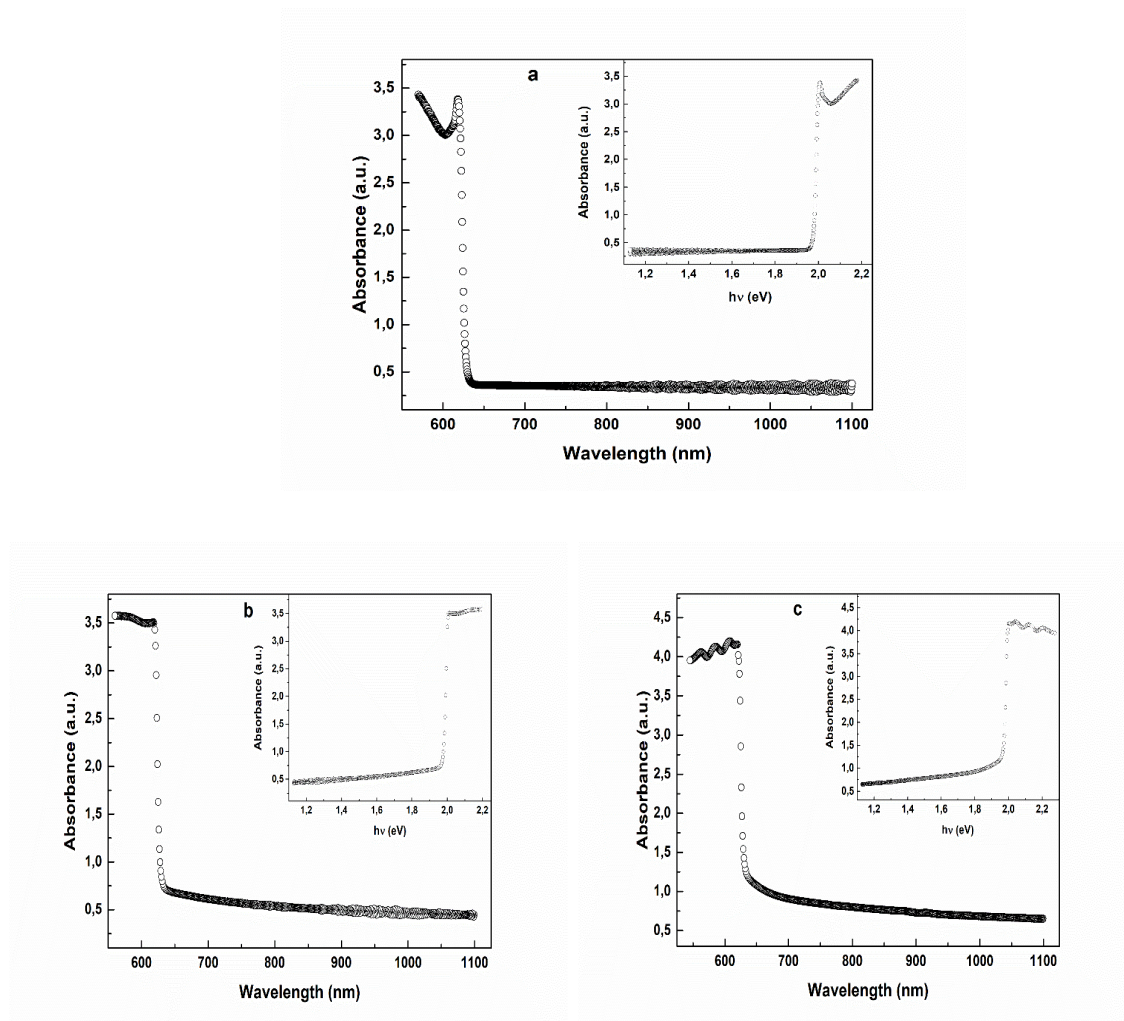**Figure 6.** The optical absorption spectra of **(a)** GaSe single crystal substrate, **(b)** undoped, **(c)** boron doped InSe thin films grown on GaSe single crystal substrates.

From the absorption spectra of the GaSe single crystal, it is seen that a sharp increasing is observed at 2.01 eV wavelength, which is attributed to optical absorption of free excitons. Similar peaks are also observed in the absorption spectra of undoped and boron doped InSe thin films grown on GaSe single crystal substrates at 2.00 eV and 1.99 eV wavelengths, respectively (Fig. 6 b-c). These decreases at the band gap energy can be attributed to the defect and dopant states absorptions. However, this should be checked with other experiments. Also, Urbach energies of GaSe single crystal substrate, undoped and boron doped InSe thin films grown on GaSe single crystal substrates were calculated to be 14.02 meV, 19.98 meV and 32.17 meV, respectively. It is seen that calculated Urbach energies of undoped and boron doped InSe thin films grown on glass substrates are found bigger than undoped and boron doped InSe thin films which are grown on GaSe single crystal substrates.

4. CONCLUSION

Undoped and boron doped InSe thin films were grown on glass and GaSe single crystal substrates by SILAR technique. The structural, morphological and optical properties of these thin films were studied by using XRD, AFM and UV-Vis measurements. The structure of the InSe thin films grown on glass substrates were hexagonal with P61 space group while the InSe thin films grown on GaSe single crystal substrates were hexagonal with P63/mmc space group. The average particle sizes of InSe thin films grown on glass and GaSe single crystal substrates were found between 26.5-60.2 nm and 30.9-101.5 nm, respectively. The optical absorption spectra of InSe thin films grown on both glass and GaSe single crystal substrates showed absorption maxima around 2.00 and 2.24 eV, respectively. Here we demonstrated that at the thin film deposition processes the used substrate types effect the structures and other physical properties of thin films.

REFERENCES

[1] Ertap H., Karabulut M., Structural and electrical properties of boron doped InSe single crystals, Materials Research Express, 6 (2019) 035901.

[2] Duman S., Gürbulak B., Doğan S., Türüt A., Electrical characteristics and inhomogeneous barrier analysis of Au–Be/p-InSe: Cd Schottky barrier diodes, Microelectronic Engineering, 86 (2009) 106-110.

[3] De Blasi C., Micocci G., Mongelli S., Tepore A., Large InSe single crystals grown from stoichiometric and non-stoichiometric melts, Journal of Crystal Growth, 57-3 (1982) 482-486.

[4] Savchyn V. P., Kytsai V. B., Photoelectric properties of heterostructures based on thermo-oxidated GaSe and InSe crystals, Thin Solid Films, 361 (2000) 123-125.

[5] Kobbi B., Kesri N., Physico-chemical and electrical properties of InSe films, Vacuum, 75 (2004) 177-182.

[6] Ertap H., Mamedov G. M., Karabulut M., Bacıoglu A., Pool–Frenkel thermoelectric modulation of exciton photoluminescence in GaSe crystals, Journal of Luminescence, 13 (2011) 1376-1379.

[7] Yüksek M., Ertap H., Elmali A., Yaglioglu H. G., Mamedov G. M., Karabulut M., Özturk M. K., Two photon absorption characteristics of bulk GaTe crystal, Optics& Laser Technology, 44 (2012) 2178-2181.

[8] Gamal G. A., Azad M. I., Photoelectric studies of gallium monosulfide single crystals Journal of Phys. Chem. Solids, 66 (2005) 5-10.

[9] Ertap H., Bacıoğlu A., Karabulut M., Photoluminescence properties of boron doped InSe single crystals, Journal of Luminescence, 167 (2015) 227-232.

[10] Cuculescu E., Evtodiev I., Caraman I., Leontie L., Nedeff V., Rusu D., Transport and generation–recombination mechanisms of nonequilibrium charge carriers in ZnO/In$_2$O$_3$/InSe:Cd heterojunctions, Thin Solid Films, 519 (2011) 7356-7359.

[11] Segura A., Chevy A., Guedson J. P., Besson J. M., Photovoltaic efficiency of InSe solar cells, Solar Energy Materials, 2 (1979) 159-165.

[12] Pathan H. M., Kulkarni S. S., Mane R. S., Lokhande C. D., Preparation and characterization of indium selenide thin films from a chemical route, Materials Chemistry and Physics, 93 (2005) 16-20.

[13] Yüksek M., Nonlinear refraction effects of amorphous semiconductor InSe thin films according to film thicknesses and/or pulse durations, Optic Communications, 285 (2012) 5472-5474.

[14] Sen S. S., Biswas N. N., Khan K. A., Temperature effect on the electrical and optical properties of indium-selenide thin-films, Applied Energy, 65 (2000) 51-58.

[15] Gopal S., Viswanathan C., Karunagaran B., Narayandass S. K., Mangalaraj D., Yi J., Preparation and characterization of electrodeposited indium selenide thin films, Crystal Research Technology, 40 (2005) 557-562.

[16] Matheswaran P., Kumar R. S., Sathyamoorthy R., Effect of annealing on the structural and optical properties of InSe bilayer thin films, Vacuum, 85 (2011) 820-826.

[17] Chen X., Hou X., Cao X., Ding X., Chen L., Zhao G., Wang X., Gallium sulfide thin film grown on GaAs (1 0 0) by microwave glow discharge, J. Cryst. Growth, 173 (1997) 51-56.

[18] Suh S., Hoffman D. M., Chemical vapor deposition of gallium sulfide thin films, Chemistry of Materials, 12 (2000) 2794-2797.

[19] Sanz C., Guillen C., Gutierrez M. T., Influence of the synthesis conditions on gallium sulfide thin films prepared by modulated flux deposition, J. Phys. D: Appl. Phys., 42 (2009) 085108.

[20] Guseinov G. D., Ramazanzade A. M., Visualization of dislocations on basal planes of GaSe single crystals, Phys. Stat. Sol. (b), 23 (1967) 461-465.

[21] Mamedov G. M., Karabulut M., Ertap H., Kodolbaş O., Öktü Ö., Bacıoğlu A., Exciton photoluminescence, photoconductivity and absorption in $GaSe_{0.9}Te_{0.1}$ alloy crystals, Journal of Luminescence, 129 (2009) 226–230.

[22] Mane R. S., Sankapal B. R., Lokhande C. D., A chemical method for the deposition of Bi2S3 thin films from a non-aqueous bath, Thin Solid Films, 359 (2000) 136-140.

[23] Lutz, H. *Private Communication* 1989.

[24] Asabe M. R., Chate P. A., Delekar S. D., Garadkar K. M., Mulla I. S., Hankare P. P., Synthesis, characterization of chemically deposited indium selenide thin films at room temperature, Journal of Physics and Chemistry of Solids, 69 (2008) 249-254.

[25] Anis M. K., Nazar F. M., X-ray and electron diffraction analysis of GaSe crystals, J. Mater. Sci. Lett., 2 (1983) 471-474.

[26] Blasi C. De., Manno D., Rizzo A., Study of the polytypism in melt grown InSe single crystals by convergent beam electron diffraction, Journal of Crystal Growth, 100 (1990) 347-353.

[27] Fotsing J., Julien C., Balkanski M., Annealing and doping effects in layered In2Se3 compounds, Material Science and Engineering, B1 (1988) 139-145.

[28] Cenzual K., Gelato L. M., Penzo M., Parthe E., Inorganic structure types with revised space groups. I., Acta Crystallographica Section B: Structural Science, 47 (1991) 433-439.

[29] Urbach F., The long-wavelength edge of photographic sensitivity and of the electronic absorption of solids, Phys. Rev., 92 (1953) 1324.

[30] Mamedov G. M., Karabulut M., Kodolbaş O. A., Öktü Ö., Exciton photoconductivity in Ge-doped GaSe crystals, Phys. Stat. Sol. (b), 242 (2005) 2885-2891.

[31] Ertap H., Baydar T., Yüksek M., Karabulut M., Structural and optical properties of gallium sulfide thin film, Turkish Journal of Physics, 40-3 (2016) 297-303.

Double Actions of Groups

Mustafa Habil GÜRSOY (iD)

İnönü University, Faculty of Arts Sciences, Department of Mathematics, Malatya-44280, TURKEY

Abstract. In this work, we present the concept of double action of a group G on a set X as a new concept in literature, which opens up the way for applying rich amount of algebraic topological facts and methods in the algebraic topology. Besides of this, we give some expository examples of this new concept. We also express the definition of a double action via permutations as similar to the definition of an action on a set of groups via permutations. We investigate some characterizations about the double actions. Also we prove an adaptation of Cayley's theorem in the case of the double action.

*Keywords***:** Group; action; double action.

Grupların Çift Etkileri

Özet. Bu çalışmada, literatürde yeni bir kavram olarak bir G grubunun bir X kümesi üzerine çift etkisi kavramını sunuyoruz, ki bu kavram cebirsel topolojide cebirsel topolojik gerçeklerin ve metotların zengin bir uygulama yolunu açacaktır. Bunun yanısıra, bu yeni kavramın bazı açıklayıcı örneklerini veriyoruz. Ayrıca permütasyonlar yardımıyla grupların bir küme üzerine etkisi tanımına benzer olarak permütasyonlar yardımıyla bir çift etkinin tanımını ifade ediyoruz. Çift etkiler hakkında bazı karakterizasyonları inceliyoruz. Ayrıca çift etki durumunda Cayley's teoreminin bir uyarlamasını ispatlıyoruz.

Anahtar Kelimeler: Grup; etki; çift etki.

1.   INTRODUCTION

The concept of action is an important tool in many area of mathematics, especially in algebraic topology. For instance, some categorical equivalences have been shown using the action of groupoid [2, 4]. Besides of the group actions, the actions of other algebraic structures such as algebra, ring, algebroid and groupoid are also studied [1, 5].

An action of a group G on a set X is a map $\cdot: G \times X \to X$ satisfying the conditions $e \cdot x = x$ and $g \cdot (h \cdot x) = (gh) \cdot x$ for all $g, h \in G$ and $x \in X$, where e is the identity of G. On the other hand, we can also define the action by using the concept of permutation, namely, an action of a group G with identity e on a set X is the choice of a permutation $\tau_g: X \to X$ for each $g \in G$ such that τ_e is the identity and, $\tau_g \circ \tau_h = \tau_{gh}$ for all $g, h \in G$. Furthermore, two basic concepts come to mind when dealing with group action: orbit and stabilizer. If there exists an action of G on X, then the set $Orb_G x = \{g \cdot x \mid g \in G\}$ is called the orbit of x. The stabilizer of x is the set $G_x = \{g \in G \mid g \cdot x = x\}$ which is a subgroup of G.

In this work, we deal with double actions of groups on sets. We investigate double situations of the concepts mentioned above. For this aim, we give definition of double action of a group on a set. In more

---

detail, we define the double action as follows: Let us suppose that a group G has two actions on a set X on the left as " $\cdot$ " and " $\circ$ ". Then, for every $g, h \in G$ and $x \in X$, if $g \cdot (h \circ x) = h \circ (g \cdot x)$ holds, then we say that G acts doubly on X on the left by means of " $\cdot$ " and " $\circ$ ". Using the concept of permutation, we can redefine the double action as follows. We say that G acts doubly on X, if it is possible to correspond a permutation η_g^h of $X \times X$ to each pair of elements $(g, h) \in G \times G$ such that $\eta_g^h \circ \eta_k^m = \eta_{gk}^{hm}$ for every $(g, h), (k, m) \in G \times G$. Also, we present the concepts of double orbit and stabilizer for double actions. Let G be a group doubly acting on a set X by means of " $\cdot$ " and " $\circ$ " and let $x \in X$. Then, the double orbit of x is the set $DOrb_G(x) = \{y \in X : g \cdot x = y = h \circ x, g, h \in G\}$, and the stabilizer of x is the set $G_x = \{(g, h) \in G \times G : g \cdot x = h \circ x = x, \ g, h \in G\}$ which is the subgroup of the product group $G \times G$. Furthermore, we present the equivalence of two double actions, namely, we say that double actions of G on sets X and X' are equivalent if there is a bijection $\phi : X \to X'$ such that $\phi(g \cdot x) = g \cdot (\phi(x))$ and $\phi(h \circ x) = h \circ (\phi(x))$ for every $g, h \in G$ and $x \in X$. Additionally, we define the concepts of transitive, effective, free and regular double actions. Besides of these, we prove an adaptation of Cayley's theorem in the case of double action of groups.

We consider that the concept of double action as a new concept will bring a new look to problems particularly those in algebraic topology. Moreover, the concept of double action for the above mentioned algebraic structures can be also defined.

2.PRELIMINARIES

This section of the paper is devoted to give basic facts related to the actions of groups on sets.

Definition 1. Let G be a group and X a nonempty set. A left action of G on X is a map $\cdot : G \times X \to X$ written as $(g, x) \mapsto g \cdot x$ satisfying

i) $e \cdot x = x$ for all $x \in X$, where "e" denotes the identity element of the group G.

ii) $g \cdot (h \cdot x) = (gh) \cdot x$ for all $g, h \in G$ and $x \in X$ [2].

Given an action of G on X, we call X a $G - set$. We denote the action by $(G, \cdot, X)$. Similarly, a right action of G on X is defined. In this case, the group elements are written on the right instead of the left. Namely, the first condition is written by $x \cdot g = x$, and the second condition is written by $(x \cdot g) \cdot h = x \cdot (gh)$. But, we will use the left action throughout the paper.

Example 1. Let G be a group and $X = G$. Then G acts on itself by left multiplication [2].

Example 2. Let G be a group and $X = G$. Then G acts on itself by conjugation [2].

Example 3. The trivial action of any group G on any set X is defined by $g \cdot x = x$ for all $g \in G$ and all $x \in X$ [2].

Another way to think about an action of a group on a set is via the concept of symmetric group, which this alternative definition will give us a very important theorem related to the group action: Cayley's theorem. For this aim, let us first recall the concept of symmetric group.

Let X be any set. A permutation of X is a function $\tau : X \to X$ which is invertible (i.e. it is both injective and surjective). The set of permutations of X forms a group under composition of functions, called the *symmetric group* on X. We denote it by $Sym(X)$. Indeed, since the identity function Id_X on X is a bijection

from X to X, we have $Id_X \in Sym(X)$, and so $Sym(X) \neq \emptyset$. For any $\tau, \phi \in Sym(X)$, since the composition $\tau \circ \phi$ is a bijection from X to X, we have $\tau \circ \phi \in Sym(X)$. Also, it is clear that the operation $\circ$ has associative property. For all $\tau \in Sym(X)$, we have $\tau^{-1} \in Sym(X)$. It follows $\tau \circ \tau^{-1} = Id_X = \tau^{-1} \circ \tau$. Thus, $(Sym(X), \circ)$ is a group.

It is clear that if we take a group G instead of the set X, then we obtain group of the automorphisms of G.

Now let us again define the action of a group G on a set X via the concept of permutation.

Definition 2. An action of a group G on a set X is the choice of a permutation $\tau_g : X \to X$ for each $g \in G$ such that the following two conditions hold:

i) τ_e is the identity, namely $\tau_e(x) = x$ *for each* $x \in X$,

ii) for every $g, h \in G$, $\tau_g \circ \tau_h = \tau_{gh}$ [3].

If we consider together the Definitions 1. and 2., then we can state the following proposition which is give the relation between the group G and the symmetric group $Sym(X)$ of the permutations of X via the concept of action of the group G on the set X:

Proposition 1. An action of a group G on a set X is the same as a group homomorphism from G to $Sym(X)$ [3].

By this proposition, we can easily say that there is no difference between an action of a group G on a set X and a homomorphism $f : G \to Sym(X)$.

We can now state Cayley's theorem.

Theorem 1. Every group G is isomorphic to a group of permutations [3].

Definition 3. Let G be a group acting on a set X. If $x \in X$, then the set $Orb_G x = \{g \cdot x \mid g \in G\}$ is called the orbit of x or the orbit through x [2].

The set of orbits under the action of G forms a partition of X. Because they are the equivalence classes of the equivalence relation given by

$$y \sim x \Leftrightarrow y = g \cdot x \text{ for some } g \in G.$$

The set of all orbits of X under the action of G is written as X/G.

Definition 4. Let X be a $G - set$. Let $x \in X$. The stabilizer of x is the set $G_x = \{g \in G \mid g \cdot x = x\}$ [2].

Proposition 2. The stabilizer G_x of x is a subgroup of G [2].

Definition 5. Let X be a $G - set$. Then

i) the action is transitive if $X \neq \emptyset$ and if for any $x, y \in X$, there exists $g \in G$ such that $g \cdot x = y$.

ii) the action is faithful if for any $g, h \in G$, there exists $x \in X$ such that $g \cdot x \neq h \cdot x$.

iii) the action is free if for $g, h \in G$, if there exists $x \in X$ such that $g \cdot x = h \cdot x$ implies $g = h$.

iv) the action is regular if it is both free and transitive. Equivalently, we have that for any $x, y \in X$ there exists a unique $g \in G$ such that $g \cdot x = y$ [2].

3.DOUBLE ACTIONS OF GROUPS

Definition 6. Let G be a group and X be a nonempty set. Let us suppose that G has two actions on X on the left as " $\cdot$ " and " $\circ$ ". For every $g, h \in G$ and $x \in X$, if the interchange law

$$g \cdot (h \circ x) = h \circ (g \cdot x) \tag{*}$$

holds, then we say that G acts doubly on X on the left by means of " $\cdot$ " and " $\circ$". The action of G on X defined by this way is called *left double action*. Then, the set X is called a left $double\ G - set$. We denote the left double action of G on X by $(G, \cdot, \circ, X)$.

Let's state that there is no need in the above definition for a condition similar to condition (i) related to the identity element given in Definition.1. Namely, since we have already had two actions such as "$\cdot$" and " $\circ$ ", the equalities $e \cdot x = x$ and $e \circ x = x$ are satisfied by themselves. And, when we take identity element "e" in the interchange law (*), it is obvious that the interchange law is satisfied.

Example 4. Let us define two different actions of a group G on itself on the left as follows:

$$\cdot : G \times G \to G$$

$$(g, x) \mapsto g \cdot x = gx,$$

and

$$\circ : G \times G \to G$$

$$(h, x) \mapsto h \circ x = xh^{-1}$$

Then, the group G acts doubly on itself on the left by means of " $\cdot$ " and " $\circ$". Namely, for all $g, h, x \in G$, we have the equality

$$g \cdot (h \circ x) = g \cdot (xh^{-1}) = g(xh^{-1}) = (gx)h^{-1} = h \circ (gx) = h \circ (g \cdot x).$$

That is, the condition (*) in Definition. 6 holds. Consequently, $(G, \cdot, \circ, G)$ is a left double action.

Example 5. Let us consider the following two actions of a group G on itself on the left.

$$\cdot : G \times G \to G$$

$$(g, x) \mapsto g \cdot x = gxg^{-1},$$

and

$$\circ : G \times G \to G$$

$$(h, x) \mapsto h \circ x = x$$

Then, for every $g, h, x \in G$, since

$$g \cdot (h°x) = g \cdot (x) = gxg^{-1} = h°(gxg^{-1}) = h°(g \cdot x)$$

the group G acts doubly on itself on the left by means of " · " and " °". Thus, $(G, \cdot, °, G)$ is a left double action.

Proposition 3. If a group G is abelian, every left action of G on the set X is a left double action.

Proof. The proof follows easily from that the second condition of the action and the commutativity of the group. Namely, let G be an abelian group and G acts on a nonempty set X on the left. Let us denote the action by $\cdot : G \times X \to X, (g, x) \mapsto g \cdot x$. Then, for every $g, h \in G$ and $x \in X$, we have

$$g \cdot (h \cdot x) = (gh) \cdot x = (hg) \cdot x = h \cdot (g \cdot x).$$

Thus, the abelian group G acts doubly on X on the left by the action " · ", which completes the proof.

Now, our current aim is to define double actions via permutations just as we have defined group actions via permutations.

If $(G, \cdot, X)$ is an action, then we have a homomorphism

$$\theta : G \to Sym(X)$$

$$g \mapsto \theta(g) = \varphi_g : X \to X$$

$$x \mapsto \varphi_g(x) = g \cdot x$$

such that $\theta(gh) = \varphi_{gh} = \varphi_g \circ \varphi_h = \theta(g) \circ \theta(h)$.

Similarly, if $(G, °, X)$ is another action, then we have also a homomorphism

$$\Gamma : G \to Sym(X)$$

$$h \mapsto \Gamma(h) = \psi^h : X \to X$$

$$x \mapsto \psi^h(x) = h°x$$

such that $\Gamma(gh) = \psi^{gh} = \psi^g \circ \psi^h = \Gamma(g) \circ \Gamma(h)$.

After all, let $(G, \cdot, °, X)$ be a double action. Then, let us define

$$\Phi : G \times G \to Sym(X \times X)$$

$$(g, h) \mapsto \Phi(g, h) = \eta_g^h : X \times X \to X \times X$$

$$(x, y) \mapsto \eta_g^h(x, y) = (\varphi_g(x), \psi^h(y))$$

$$= (g \cdot x, h°y).$$

Unlike the homomorphisms θ and Γ just mentioned above, it is not so difficult to understand that Φ is defined on $G \times G$ because of its double state.

It is obvious that the $Sym(X \times X)$ is a group. Namely, since $\eta_e^e(x,y) = (e\cdot x, e°y) = (x,y)$ for all $(x,y) \in X \times X$, then η_e^e is the identity element of $Sym(X \times X)$, where (e,e) is the identity of $G \times G$. Also the multiplication of $Sym(X \times X)$ is defined by

$$\eta_g^h \circ \eta_k^m (x,y) = \eta_g^h \left(\eta_k^m (x,y) \right)$$

$$= \eta_g^h (k\cdot x, m°y)$$

$$= (g\cdot(k\cdot x), h°(m°y))$$

$$= ((gk)\cdot x, (hm)°y)$$

$$= \eta_{gk}^{hm} (x,y)$$

for all $(g,h),(k,m) \in G \times G$ and $(x,y) \in X \times X$.

The inverse of η_g^h is defined by $\eta_{g^{-1}}^{h^{-1}}$ for any $(g,h) \in G \times G$.

Now let us show that Φ defined above is a homomorphism.

For any $(g,h),(k,m) \in G \times G$ and $(x,y) \in X \times X$,

$$\Phi((g,h)(k,m))(x,y) = \Phi(gk,hm)(x,y)$$

$$= \eta_{gk}^{hm} (x,y)$$

$$= ((gk)\cdot x, (hm)°y)$$

$$= (g\cdot(k\cdot x), h°(m°y))$$

$$= \eta_g^h (k\cdot x, m°y)$$

$$= \eta_g^h (\eta_k^m (x,y))$$

$$= \Phi(g,h)\Phi(k,m)(x,y). \tag{1}$$

Hence, Φ is a homomorphism.

Considering all of these, we can also give a new definition of a double action of G on X as follows, equivalently to the Definition 6:

Definition 7. Let X be a set and G a group. Then, we say that G acts doubly on X, if it is possible to correspond a permutation η_g^h of $X \times X$ to each pair of elements $(g,h) \in G \times G$ such $that\ \eta_g^h \circ \eta_k^m = \eta_{gk}^{hm}$ for every $(g,h),(k,m) \in G \times G$.

In other words, if there exists a homomorphism from $G \times G$ to $Sym(X \times X)$, then it is called "*G acts doubly on X*".

After this definition, we state the Cayley's theorem in case of the double action.

Theorem 2. Given a group G, the group $G \times G$ is isomorphic to a group of permutations.

Proof. For the proof, just as in the Theorem 1., we are going to utilize the advantage of the idea that the left-multiplication is a permutation in the light of the above explanations for the group $G \times G$.

Define a map

$$\Phi : G \times G \to Sym(G \times G)$$

$$(g, h) \mapsto \Phi(g, h) = l_g^h ,$$

where l_g^h is defined by $l_g^h (k, m) = (l_g(k), l^h(m)) = (gk, hm)$ for all $(k, m) \in G \times G$. It can easily shown that l_g^h is a permutation.

We want to show that Φ is an injective homomorphism.

First, suppose that $\Phi(g, h) = \Phi(k, m)$, then $l_g^h = l_k^m$ as functions mapping $G \times G$ to $G \times G$. For functions to be equal they must equal at every point, and hence $l_g^h (e, e) = l_k^m (e, e)$ implying $(g, h) = (ge, he) = (ke, me) = (k, m)$, and hence Φ is injective.

It is easily seen that Φ is a homomorphism just as similar to that one in the equation (1).

Thus, we have an embedding of $G \times G$ into the group of all permutations of the set $G \times G$.

Definition 8. Let G be a group doubly acting on a set X by means of $" \cdot "$ and $" \circ "$ and let $x \in X$. Then, the double orbit of x or the double orbit through x, written $DOrb_G(x)$, is the set

$$DOrb_G(x) = Orb_{(G, \cdot)} x \cap Orb_{(G, \circ)} x = \{y \in X : g \cdot x = y = h \circ x, g, h \in G\}.$$

Example 6. Let us consider the double action $(G, \cdot, \circ, G)$ in the Example 5. with the symmetric group $G = S_3$. Then we have the orbits $Orb_{(S_3, \cdot)}(e) = \{e\}$, $Orb_{(S_3, \cdot)}((12)) = Orb_{(S_3, \cdot)}((13)) = Orb_{(S_3, \cdot)}((23)) = \{(12), (13), (23)\}$, $Orb_{(S_3, \cdot)}((123)) = Orb_{(S_3, \cdot)}((132)) = \{(123), (132)\}$ and $Orb_{(S_3, \circ)}(e) = \{e\}$, $Orb_{(S_3, \circ)}((12)) = \{(12)\}$, $Orb_{(S_3, \circ)}((13)) = \{(13)\}$, $Orb_{(S_3, \circ)}((23)) = \{(23)\}$, $Orb_{(S_3, \circ)}((123)) = \{(123)\}$, $Orb_{(S_3, \circ)}((132)) = \{(132)\}$. Hence the double orbits of double action $(S_3, \cdot, \circ, S_3)$ are the sets of $DOrb_{S_3}(e) = \{e\}$, $DOrb_{S_3}((12)) = \{(12)\}$, $DOrb_{S_3}((13)) = \{(13)\}$, $DOrb_{S_3}((23)) = \{(23)\}$, $DOrb_{S_3}((123)) = \{(123)\}$, $DOrb_{S_3}((132)) = \{(132)\}$.

Example 7. Let us consider the double action $(G, \cdot, \circ, G)$ in the Example 4. with the symmetric group $G = S_3$. In this case, with a standard calculation it is easily seen that all double orbits of S_3 for each $x \in S_3$ will be S_3.

Proposition 4. Let G be a group and X a *double $G - set$*. Then, for every $x, y, z \in X$

i) x is in the double orbit through x.

ii) if y is in the double orbit through x, then x is in the double orbit through y.

iii) if y is in the double orbit through x and z is in the double orbit through y, then z is also in the double orbit through x.

Proof. i) For any elements $g, h \in G$ and $x \in X$, we have $g \cdot x = x \Rightarrow g = e$ and $h \circ x = x \Rightarrow h = e$. Since $e \in G$, x is in the double orbit through x.

ii) If y is in the double orbit through x, then we have $g \cdot x = y$ and $h \circ x = y$ for some $g, h \in G$. Hence

$$g \cdot x = y \Rightarrow (g^{-1}) \cdot (g \cdot x) = (g^{-1}) \cdot y$$

$$\Rightarrow (g^{-1} g) \cdot x = (g^{-1}) \cdot y$$

$$\Rightarrow e \cdot x = (g^{-1}) \cdot y$$

$$\Rightarrow x = (g^{-1}) \cdot y \tag{2}$$

and

$$h \circ x = y \Rightarrow (h^{-1}) \circ (h \circ x) = (h^{-1}) \circ y$$

$$\Rightarrow (h^{-1} h) \circ x = (h^{-1}) \circ y$$

$$\Rightarrow e \circ x = (h^{-1}) \circ y$$

$$\Rightarrow x = (h^{-1}) \circ y. \tag{3}$$

From the equations (2) and (3), x is also in the double orbit through y.

iii) If y is in the double orbit through x, then we have

$$y = g \cdot x = h \circ x \; for \; \exists g, h \in G,$$

and z is in the double orbit through y, then we have

$$z = m \cdot y = n \circ y \; for \; \exists m, n \in G.$$

Hence

$$z = m \cdot y \Rightarrow z = m \cdot (g \cdot x) \Rightarrow z = (mg) \cdot x$$

and

$$z = n \circ y \Rightarrow z = n \circ (h \circ x) \Rightarrow z = (nh) \circ x.$$

Since $mg, nh \in G$, z is in the double orbit through x. Hence, the proof is completed.

Thus, we obtain a relation on X defined by

$$y \sim x \iff y \text{ is in the double orbit through } x.$$

Corollary 1. The above relation is an equivalence relation.

The equivalence classes under this equivalence relation are called *double orbits*.

Proposition 5. Let G be a group and X a *double $G - set$*. The disjoint double orbits under the above equivalence relation form a partition of X.

Proof. From Proposition.4 (i), we have $x \in DOrb_G x$, namely, for $e \in G$ $e \cdot x = x = e°x$. So it is obvious that $X \subset \bigcup_{x \in X} DOrb_G x$. Hence, we suppose that $DOrb_G x \cap DOrb_G y \neq \emptyset$. Then, for at least one element $z \in DOrb_G x \cap DOrb_G y$, there exist $g_1, g_2, h_1, h_2 \in G$ such that

$$z = g_1 \cdot x = h_1 °x \text{ and } z = g_2 \cdot y = h_2 °y.$$

We want to show that $DOrb_G x = DOrb_G y$. For this, it suffices to show that $DOrb_G x \subset DOrb_G y$. Thus, we conclude that $DOrb_G x = DOrb_G y$ by symmetry.

From the hypothesis, for any element $u \in DOrb_G x$, there exist $g, h \in G$ such that $u = g \cdot x = h°x$. Since $x = (g_1^{-1}) \cdot z = (h_1^{-1})°z$, we have

$$u = g \cdot x \Rightarrow u = g \cdot ((g_1^{-1}) \cdot z) = (gg_1^{-1}) \cdot z = (gg_1^{-1}) \cdot (g_2 \cdot y) = (gg_1^{-1} g_2) \cdot y$$

and

$$u = h°x \Rightarrow u = h°((h_1^{-1})°z) = (hh_1^{-1})°z = (hh_1^{-1})°(h_2° y) = (hh_1^{-1} h_2)°y$$

This means that $u \in DOrb_G y$. Thus, we obtain $DOrb_G x \subset DOrb_G y$.

By symmetry, we obtain $DOrb_G x = DOrb_G y$. Consequently, if the double orbits $DOrb_G x$ and $DOrb_G y$ share even one point in common, then they are equal and thus a partition.

Definition 9. Let X be a *double $G - set$*. Let $x \in X$. The stabilizer, denoted G_x, of x is the set

$$G_x = \{(g, h) \in G \times G : g \cdot x = h°x = x, \qquad g, h \in G\}$$

which is the subset of the product group $G \times G$.

Proposition 6. The stabilizer G_x of x is the subgroup of the product group $G \times G$.

Proof. G_x is nonempty, since $(e, e) \in G_x$. Also, if $(g_1, h_1), (g_2, h_2) \in G_x$, then we have

$$g_1 \cdot x = h_1° x = x \text{ and } g_2 \cdot x = h_2°x = x.$$

Hence

$$g_1 \cdot x = x \Rightarrow g_1 \cdot (g_2 \cdot x) = x \Rightarrow (g_1 g_2) \cdot x = x$$

and

$$h_1° x = x \Rightarrow h_1°(h_2°x) = x \Rightarrow (h_1 h_2)°x = x.$$

Thus, $(g_1 g_2, h_1 h_2) \in G_x \subset G \times G$. It is obvious that the multiplication in $G \times G$ is defined by

$$(g_1, h_1)(g_2, h_2) = (g_1 g_2, h_1 h_2), \qquad \text{for all } (g_1, h_1), (g_2, h_2) \in G \times G.$$

Thus, G_x is closed under the multiplication.

On the other hand, if $(g_1, h_1) \in G_x$, then we have $g_1 \cdot x = h_1 {}^{\circ} x = x$. Hence,

$$g_1 \cdot x = x \Rightarrow (g_1{}^{-1}) \cdot (g_1 \cdot x) = (g_1{}^{-1}) \cdot x$$

$$\Rightarrow (g_1{}^{-1} g_1) \cdot x = (g_1{}^{-1}) \cdot x$$

$$\Rightarrow e \cdot x = (g_1{}^{-1}) \cdot x$$

$$\Rightarrow x = (g_1{}^{-1}) \cdot x$$

and

$$h_1{}^{\circ} x = x \Rightarrow (h_1{}^{-1}){}^{\circ} (h_1{}^{\circ} x) = (h_1{}^{-1}){}^{\circ} x$$

$$\Rightarrow (h_1{}^{-1} h_1){}^{\circ} x = (h_1{}^{-1}){}^{\circ} x$$

$$\Rightarrow e {}^{\circ} x = (h_1{}^{-1}){}^{\circ} x$$

$$\Rightarrow x = (h_1{}^{-1}){}^{\circ} x.$$

So, it follows $(g_1{}^{-1}, h_1{}^{-1}) \in G_x$. Thus, G_x is closed under the inversion.

Consequently, the stabilizer G_x is the subgroup of $G \times G$.

Example 8. Let us consider the double action $(G, \cdot, \circ, G)$ in the Example 5. with the symmetric group $G = S_3$. Then, we obtain the stabilizer groups $(S_3)_e = \{(e, e)\}$, $(S_3)_{(12)} = \{((12), (12))\}$, $(S_3)_{(13)} = \{((13), (13))\}$, $(S_3)_{(23)} = \{((23), (23))\}$, $(S_3)_{(123)} = \{((123), (123))\}$, $(S_3)_{(132)} = \{((132), (132))\}$

Proposition 7. Let G be a group doubly acting on a set X by means of $" \cdot "$ and $" \circ "$. Then, for every $(g_1, h_1), (g_2, h_2) \in G_x$

$$g_1 \cdot x = g_2 \cdot x \text{ and } h_1{}^{\circ} x = h_2{}^{\circ} x$$

$$\Longleftrightarrow$$

(g_1, h_1) and (g_2, h_2) lie in the same left coset of G_x.

Proof. The conditions $g_1 \cdot x = g_2 \cdot x$ and $h_1{}^{\circ} x = h_2{}^{\circ} x$ are equivalent to $x = (g_1{}^{-1} g_2) \cdot x = (h_1{}^{-1} h_2){}^{\circ} x$, which means $(g_1{}^{-1} g_2, h_1{}^{-1} h_2) \in G_x$. Therefore, (g_1, h_1) and (g_2, h_2) act doubly in the same way on x if and only if (g_1, h_1) and (g_2, h_2) lie in the same left coset of G_x.

Definition 10. Double actions of G on sets X and X' are called equivalent if there is a bijection $\phi \colon X \to X'$ such that

$$\phi(g \cdot x) = g \cdot (\phi(x)) \text{ and } \phi(h \circ x) = h \circ (\phi(x))$$

for every $g, h \in G$ and $x \in X$.

Let us now give some types of the double actions.

Definition 11. The double action of a group G on a set X by means of the actions $"\cdot"$ and $"\circ"$ is called *transitive* if there is an element $(g, h) \in G \times G$ such that

$$g \cdot x = y = h \circ x \text{ for any } x, y \in X.$$

Example 9. Let us consider the double action $(G, \cdot, \circ, G)$ in the Example 4. with the symmetric group $G = S_3$. By the Example 7., the double action $(S_3, \cdot, \circ, S_3)$ has unique orbit, so this double action is transitive.

Definition 12. The double action of a group G on a set X by means of the actions $"\cdot"$ and $"\circ"$ is called *faithful* (or *effective*) if there is a point $x \in X$ such that

$$g_1 \cdot x \neq g_2 \cdot x \text{ and } h_1 \circ x \neq h_2 \circ x \text{ for any } (g_1, h_1), (g_2, h_2) \in G \times G.$$

Definition 13. The double action of a group G on a set X by means of the actions $"\cdot"$ and $"\circ"$ is called *free* if for $(g_1, h_1), (g_2, h_2) \in G \times G$ if there exists $x \in X$ such that $g_1 \cdot x = g_2 \cdot x$ and $h_1 \circ x = h_2 \circ x$ imply $(g_1, h_1) = (g_2, h_2)$.

Definition 14. The double action of a group G on a set X by means of the actions $"\cdot"$ and $"\circ"$ is called *regular* if it is both free and transitive. Equivalently, for any $x, y \in X$ there exists a unique $(g, h) \in G \times G$ such that $g \cdot x = y = h \circ x$.

Example 10. The double action in Example 4. is faithful. Indeed, let us consider the actions

$$\cdot : G \times G \to G$$

$$(g, x) \mapsto g \cdot x = gx,$$

and

$$\circ : G \times G \to G$$

$$(h, x) \mapsto h \circ x = xh^{-1}.$$

There is a need to show that there exists an $x \in X$ such that

$$g_1 \cdot x \neq g_2 \cdot x \text{ and } h_1 \circ x \neq h_2 \circ x,$$

when $(g_1, h_1) \neq (g_2, h_2)$.

Let $g_1 \neq g_2$. Then

$$\left. \begin{array}{c} g_1 \cdot x = g_1 x \\ g_2 \cdot x = g_2 x \end{array} \right\} \Rightarrow g_1 x \overset{?}{=} g_2 x \Rightarrow g_1 x x^{-1} \overset{?}{=} g_2 x x^{-1} \Rightarrow g_1 e \overset{?}{=} g_2 e \Rightarrow g_1 \neq g_2$$

and

$$\left.\begin{array}{l} h_1{}^\circ x = xh_1^{-1} \\ h_2{}^\circ x = xh_2^{-1} \end{array}\right\} \Rightarrow xh_1^{-1} \overset{?}{=} xh_2^{-1} \Rightarrow x^{-1}xh_1^{-1} \overset{?}{=} x^{-1}xh_2^{-1} \Rightarrow eh_1^{-1} \overset{?}{=} eh_2^{-1} \Rightarrow h_1^{-1} \overset{?}{=} h_2^{-1} \Rightarrow h_1 \neq h_2$$

Therefore, the double action is faithful.

Example 11. Let G be a group and $H \subset G$ a subgroup. Let $G/H = \{xH : x \in G\}$ be set of the left cosets. There is a natural action of G on G/H with the left multiplication:

$$\cdot : G \times G/H \rightarrow G/H$$

$$(g, xH) \mapsto g\cdot(xH) = (gx)H.$$

Let us define another action as trivial action:

$$\circ : G \times G/H \rightarrow G/H$$

$$(k, xH) \mapsto k^\circ(xH) = xH.$$

Then, we have

$$g\cdot(k^\circ(xH)) = g\cdot(xH) = (gx)H = k^\circ((gx)H) = k^\circ(g\cdot(xH)).$$

Thus, G acts doubly on G/H by means of the actions $" \cdot "$ and $" \circ "$.

REFERENCES

[1] Alp M., Pullback Crossed Modules of Algebroids, Iran. J. Sci. Technol. Trans. A Sci., No.A1, 32 (2008) 1-5.

[2] Brown R., Topology and Groupoids, BookSurge LLC, Deganwy, United Kingdom, (2006).

[3] Derek J.S.R., A Course in the Theory of Groups, Springer-Verlag, New York, USA, (1996).

[4] Gürsoy M.H., Actions of Vector Groupoids, Bull. Iranian Math. Soc., 40-3 (2014) 565-582.

[5] Norrie K., Actions and Automorphisms of Crossed Modules, Bull. Soc. Math. France, 118 (1990) 129-146.

Evaluation of radioactive pollution in sediment samples of Borçka Dam Lake, Turkey

Murat SİRİN iD

Recep Tayyip Erdoğan University, Department of Physics, 53100, Rize, Turkey

Abstract. In this research, the concentrations of natural (226Ra, 232Th and 40K) and anthropogenic (137Cs) radionuclides were measured in sediment samples collected from the Borçka Dam Lake using a high purity germanium detector (HPGe). The activity values ranged from 4.79-21.46, 9.36–20.65, 238.01–721.26 and 0.79–6.81 Bq kg-1 for 226Ra, 232Th, 40K and 137Cs respectively. The average 226Ra, 232Th and 40K activity concentrations calculated for the sediment samples were found to be lower compared to world average values reported by UNSCEAR. In addition, radiological hazard indices were determined and compared with the international permissible values. The results of this study revealed that there is no significant health risk for people exposed to sediment samples in this region.

*Keywords***:** Borçka Dam Lake, Radioactivity, Sediment, Lifetime cancer risk.

Türkiye'de Borçka Baraj Gölünün Sediment Örneklerinde Radyoaktif Kirliliğin Değerlendirmesi

Özet. Bu araştırmada, Borçka Baraj Gölü'nden toplanan sediment örneklerinde doğal (226Ra, 232Th ve 40K) ve yapay (137Cs) radyonüklidlerin konsantrasyonları yüksek saflıkta germanyum dedektörü (HPGe) kullanılarak ölçülmüştür. Aktivite değerleri 226Ra, 232Th, 40K ve 137Cs için sırasıyla 4.79-21.46, 9.36–20.65, 238.01–721.26 ve 0.79–6.81 Bq kg-1 aralığında değişmiştir. Sediment örnekleri için hesaplanan ortalama 226Ra, 232Th ve 40K aktivite konsantrasyonları UNSCEAR tarafından rapor edilen dünya ortalaması değerlerinden daha düşük bulunmuştur. Ayrıca, radyolojik tehlike indisleri belirlenmiş ve uluslararası izin verilen değerlerle karşılaştırılmıştır. Bu çalışmanın sonuçları, bu bölgedeki sediment örneklerine maruz kalan insanlar için önemli bir sağlık riski olmadığını ortaya çıkarmıştır.

*Anahtar Kelimeler***:** Borçka Baraj Gölü, Radyoaktivite, Sediment, Yaşam boyu kanser riski.

1.   INTRODUCTION

Naturally radioisotopes (226Ra, 232Th, and 40K) are connected with rock, sand, soil and sediments in an environment. The man-made radionuclides left in our environment come from anthropogenic sources such as nuclear weapons tests and nuclear accidents [1]. Human source radionuclides, accidents in nuclear reactors, and fission products resulting from nuclear tests or industrial activities are also sources of pollution that may have a significant impact on the water environment [2]. Natural and anthropogenic radioisotopes can be transported to different

distances after different processes and finally accumulate in sediment particles [3-4]. Due to the Chernobyl nuclear power plant accident, the Marmara and the Black Sea region of Turkey was contaminated with high artificial radioisotopes [5]. After the Chernobyl accident, the north-eastern of Turkey in particular has been contaminated by artificial radionuclides. The radioactive cloud resulting from the nuclear accident arrived the territory of Turkey on 5 May 1986 and the country's different regions and ecosystems significantly polluted [6]. Therefore, the determination of the distribution of natural and anthropogenic radionuclides in the environmental environment is extremely important for environmental monitoring, nuclear protection and nuclear forensic studies [5].

It is stated that the river sediments are the wear products of the rocks and they have mineralogical properties of the original rock formation. Sediments play an important role in aquatic radioecology, because they carry and accumulate pollutants (radioactivity, heavy metal, etc.) in the environmental area. Therefore, the investigation of radioactivity levels in sediments in rivers and lakes provides useful information related to environmental pollution. For these reasons, monitoring and determining the activity concentrations and gamma-dose ratios of radionuclides is an important issue for humanity [7].

Rivers play an important role in transporting sedimental particles and organic matter from land to seas, but man-made obstacles such as dams prevent the transporting of these substances to marine environment and so these particulate matters accumulate at the bottom of the Dam lakes.

In time, sediments deposited at the bottom of the lake are an important component for monitoring the change of radioactive pollution in the region. In addition, radionuclides accumulating in the lake contaminate the water environment in which they are in contact. Dam waters are frequently used to irrigate agricultural lands located in the nearby area and therefore the determination of radioactive pollution in sediment samples in lake environment shows the importance of this research study [8].

To determine radioactivity levels at the dam lake and river sediments, some investigations have been carried out in Turkey [1, 8-11]. However, the studies conducted to determine the radioactivity levels of the sediment samples of the Dam lakes are limited in Turkey. Therefore, in the present study, the activity concentrations of natural (^{226}Ra, ^{232}Th and ^{40}K) and anthropogenic (^{137}Cs) radionuclides in sediment samples collected from Borçka Dam Lake have been surveyed. Besides, radiological hazard indices such as the radium equivalent activity (Ra$_{eq}$), the external hazard index (H$_{ex}$), the absorbed dose rate in air (D), the annual effective dose equivalent (AEDE) and the excess lifetime cancer risk (ELCR) were calculated and compared with the international permissible values.

2. MATERIALS AND METHODS

2.1. Study area and sampling
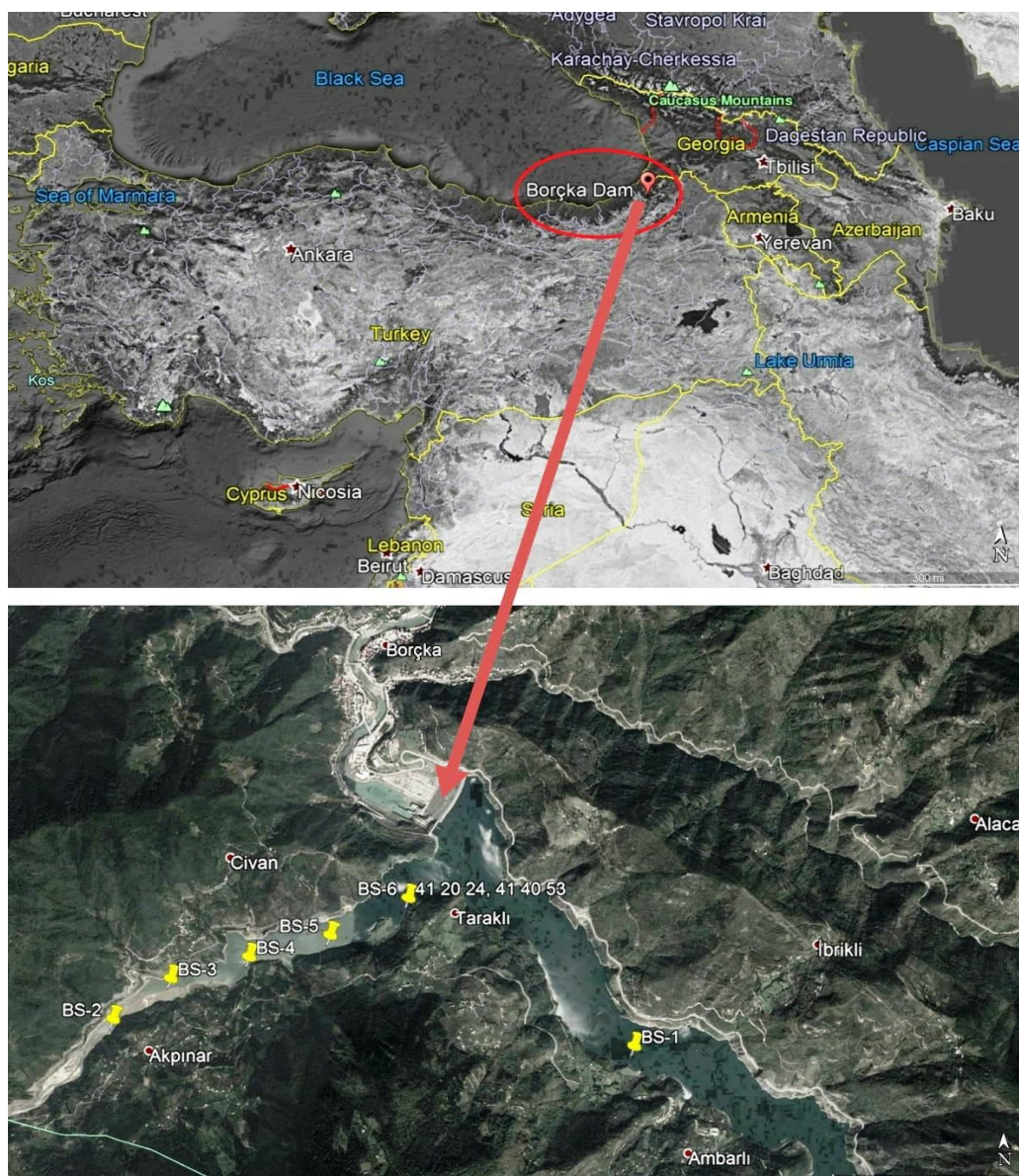
Figure 1. The sampling stations in the Borçka Dam Lake (Gedik et al., 2018)

Borçka Dam is a dam built on the Çoruh River in Artvin between 1998 and 2005 to produce energy. Turkey's Northeast Anatolia region is located on the Coruh River Basin is located in the lower Coruh basin. It is producing hydroelectric power. The body volume of the dam, which is the type of the soil trunk filling, is 7.785.000 m^3, the height from the stream bed is 86,00 m, the lake volume is 419,00 hm^3 in the normal water level, and the water area in the normal water level is 10.84 km^2. The dam produces energy of 1.039 GWh per year with 300 MW power.

In this research, three lake sediment samples were collected from each of the six sampling points determined in Borçka Dam Lake in April 2016. The sampling stations in the Borçka Dam Lake are presented in Figure 1 and the coordinates of the sampling points and some physico-chemical properties of the sediment samples collected from Borçka Dam Lake are given in Table 1. The coordinates of all sampling points were recorded using a GPS tool. Approximately 1-2 kg of sediment samples were collected from each sampling point by means of an Ekman-Birge sampler; then the collected samples were transferred to nylon bags and the bags were tightly sealed by labeling them to prevent mixing and contamination of the samples. Subsequently, all samples were transferred to the cold chain box and transported to the laboratory for the necessary analyses. [12-13].

Table 1. The coordinates of sampling points and some physico-chemical properties in sediment samples collected from Borçka Dam Lake.

Sampling location	North latitude	East longitude	Sampling depth (m)	pH	Sand (%)	Silt+Clay (%)	Total organic carbon (TOC) (%)
BS-1	41° 19′ 36″ N	41° 42′ 28″ E	35	7.36	87.45	12.55	1.84
BS-2	41° 19′ 45″ N	41° 38′ 49″ E	1.3	8.17	98.13	1.87	0.79
BS-3	41° 19′ 58″ N	41° 39′ 13″ E	3.8	8.01	92.68	7.32	1.24
BS-4	41° 20′ 05″ N	41° 39′ 46″ E	7.6	7.90	21.57	78.43	1.62
BS-5	41° 20′ 12″ N	41° 40′ 20″ E	22.4	7.89	31.22	68.78	1.67
BS-6	41° 20′ 24″ N	41° 40′ 53″ E	33.7	7.90	89.92	10.08	1.19

2.2. Characterization of sediments

Granulometric analysis of the samples was performed with the help of Retsch brand (Germany) AS 200 model vibratory sieve shaker. After Granulometric analysis, sediments were classified as sand (0.063-2 mm) and silt + clay (<0.063 mm) based on grain size. To determine the pH values of the sediment samples, the samples were sieved by a 2 mm sieve and then left to dry in the oven at 105 °C. Then 10 g of sediment sample was placed in the flask and 50 mL of deionized water (1 sediment: 5 water) was added. After the prepared mixture is stirred for about 1 hour, measurements were made with the pH probe in the YSI brand multi-parameter probe [13]. A Shimadzu SSM5000A Total Organic Carbon Analyzer device was used to measure the total organic carbon (TOC) level of the sediment samples. The TOC content in the samples was determined by the difference between total carbon (TC) and inorganic carbon (IC) values [14].

2.3. Sample preparation for activity measurements

After the sediment samples were transferred to the laboratory, the first stone particles and visible impurities were removed. Each sample of the sediment was then homogenized in a mortar and allowed to dry in an oven at 105 °C for 24 hours to remove moisture. Dried samples were sieved with a 400 mesh (63 μm) sieve. Approximately 118 g of each sample was placed in polyethylene containers with cylindrical screw cap (5.5 cm diameter and 5 cm height) for gamma measurement and sealed tightly [15]. Before starting the gamma activity analysis, the vessels were kept closed for four weeks to achieve a balance between ^{226}Ra and the short-lived generation [16].

2.4. Gamma spectrometry measurement

The activity levels of ^{226}Ra, ^{232}Th, ^{40}K and ^{137}Cs in all samples were measured using a coaxial HPGe detector (Ortec, GEM55P4-95 model). Detailed explanations about the measurement system are previously presented elsewhere [12, 16].

The gamma-energy lines of 351.9 keV (^{214}Pb) and 609.3 keV (^{214}Bi) were used to represent the ^{226}Ra series, while 911.1 keV (^{228}Ac) and 583.1 keV (^{208}Tl) were used to represent the ^{232}Th series. The activity values of of ^{40}K and ^{137}Cs were determined using their peaks at 1460.8 keV and 661.6 keV, respectively. In the calculation of activity, dry weight (dw) was taken into account for all samples [12, 17].

The activity concentrations of the studied radionuclides (^{226}Ra, ^{232}Th, ^{40}K and ^{137}Cs) in the samples measured by utilizing the equation given below were determined:

$$C = \frac{N}{\varepsilon.P_\gamma.t.m} \ (Bq \ kg^{-1}) \tag{1}$$

where N is the net count rate of the gamma ray; ε is the photo peak yield of the detector, Pγ is the absolute transition of gamma decay, t is the counting time in seconds, and m, the mass of the sample from the kilogram unit.

The MDA of the current gamma system was determined using the equation presented below [18]:

$$MDA = \frac{\sigma\sqrt{B}}{\varepsilon.I_\gamma.t.w} \qquad (2)$$

where MDA is in Bq kg^{-1}, σ is the statistical coverage factor, which is equal to 1.645 (confidence level 95%), and B is the background value for a certain radionuclide [12]. The MDA for the studied radionuclides was calculated as 0.16, 0.24, 1.69 and 0.02 Bq kg^{-1} for ^{226}Ra, ^{232}Th, ^{137}Cs and ^{40}K, respectively. In order to determine the accuracy of the measurement system, an example of the certified reference material IAEA-447 was read in the system in triplicate in a similar manner to the samples. In the reference sample, the concentrations of ^{226}Ra, ^{232}Th, ^{137}Cs and ^{40}K were given as 25.04, 37.3, 371.11 and 550 Bq kg^{-1}, respectively. For the measurement system, ^{226}Ra, ^{232}Th, ^{137}Cs and ^{40}K values were calculated as 23.96, 35.7, 362.55 and 521 Bq kg^{-1}, respectively. Accuracy, expressed as recovery of the reference substance, was found in the range of 95-98 % for all radionuclides.

3. RESULTS AND DISCUSSION

3.1. Physiochemical properties of sediments

The physico-chemical parameters determined in sediment samples are presented in Table 1. In the current study, it was found that the values of pH, Sand, Silt+Clay, and TOC ranged between 7.36–8.17, 21.57–98.13%, 1.87–78.43%, and 0.79–1.84%, respectively. The lowest pH and highest TOC content were determined at the BS-1 location. It is known that this station is under the influence of water culture and causes high organic substances due to uneaten feed, decayed plants and live wastes and feces in such areas [13].

3.2. Natural radioactivity in sediment

The activity concentrations of ^{226}Ra, ^{232}Th and ^{40}K radionuclides detected in sediment samples gathered from Borçka Dam Lake are shown in Table 2. It was observed that the concentrations determined in this study ranged from 4.79 to 21.46 Bq kg^{-1} (the mean concentration of 12.19 Bq kg^{-1}) for ^{226}Ra, from 9.36 to 20.65 Bq kg^{-1} the mean concentration of 14.05 Bq kg^{-1}) for ^{232}Th, and from 238.01 to 721.26 Bq kg^{-1} (the mean concentration of 396.41 Bq kg^{-1}) for ^{40}K. Also, the highest ^{226}Ra and ^{40}K concentration were detected in the BS-6 station, while the highest ^{232}Th concentration was detected in the BS-1 station

Table 2. The activity concentrations of [226]Ra, [232]Th, ^{137}Cs and [40]K in sediment samples of Borçka Dam Lake.

Sampling location (N = 18)	[226]Ra	[232]Th	[137]Cs	[40]K
BS-1	14.01 ± 0.49	20.65 ± 0.83	6.81 ± 0.34	464.79 ± 23.24
BS-2	8.94 ± 0.36	9.36 ± 0.56	0.79 ± 0.05	238.01 ± 9.52
BS-3	4.79 ± 0.24	10.78 ± 0.54	1.03 ± 0.06	244.96 ± 11.76
BS-4	11.80 ± 0.50	14.14 ± 0.57	5.69 ± 0.20	343.58 ± 13.03
BS-5	12.16 ± 0.61	14.96 ± 0.48	5.76 ± 0.26	365.84 ± 21.95
BS-6	21.46 ± 1.07	14.40 ± 0.94	5.10 ± 0.19	721.26 ± 46.88
Range	**4.79-21.46**	**9.36-20.65**	**0.79-6.81**	**238.01-721.26**
Mean	**12.19**	**14.05**	**4.20**	**396.41**

(N= Sampling size)

Moreover, the comparison of mean activity concentrations of the present study with published results in sediment samples is shown in Table 3. The [226]Ra activity concentrations reported in the Van Lake [1], the Metiterranean Central Basin [19], the Altınkaya Dam Lake [8], the Derbent Dam Lake [8], the Kızılırmak Delta [11] and the Yangtze Estuary [20] are higher than our values, but those for the Deriner, Borçka and Muratlı Dam Lakes [10] and the Vaigai River [21] are not.

The [232]Th levels reported in the in the Van Lake [1], the Metiterranean Central Basin [19], the Altınkaya Dam Lake [8], the Derbent Dam Lake [8], the Deriner, Borçka and Muratlı Dam Lakes [10], the Vaigai River [21], the Kızılırmak Delta [11] and the Yangtze Estuary [20] are higher than our values.

The [40]K levels reported in the Van Lake [1], the Metiterranean Central Basin [19], the Altınkaya Dam Lake [8], the Derbent Dam Lake [8], the Deriner, Borçka and Muratlı Dam Lakes [10], the Vaigai River [21] and the Yangtze Estuary [20] are higher than our values, but those for the the Kızılırmak Delta [11] are not.

Consequently, the average values of [226]Ra, [232]Th and [40]K found in Borçka Dam Lake are lower than the values recommended by UNSCEAR [22].

3.3. Artificial radioactivity in sediment

[137]Cs activity concentrations determined in this study were presented in Table 2. The mean activity concentrations of ^{137}Cs in sediment samples ranged from 0.79 to 6.81 Bq kg^{-1} (with a mean value of 4.20 Bq kg^{-1}). When the mean activity concentrations were compared according to the sampling

stations, the highest concentration (6.81 Bq kg^{-1}) was detected in BS-1 and the lowest concentration (0.79 Bq kg^{-1}) in the BS-2 station.

Furthermore, the results obtained in this study are compared with the results published in many studies in the literature as shown in Table 3. As shown in Table 3, the values reported in all previous studies for ^{137}Cs were higher than those of this study.

Table 3. Comparison of mean activity concentrations of the present study with published results in sediment samples.

Location	^{226}Ra (Bq $^{-1}$)	^{232}Th Bqkg^{-1})	^{137}Cs (Bq kg^{-1})	^{40}K (Bq kg^{-1})	References
Turkey (Van Lake)	47.48	57.87	4.37	524	[1]
Italy (Mediterranean Central Basin)	25.1	28.1		809.8	[19]
Turkey (Altınkaya Dam Lake)	19.5*	27.7		460	[8]
Turkey (Derbent Dam Lake)	18.8*	25.5		365	[8]
Turkey (Deriner, Borçka and Muratlı Dam Lakes)	11.4*	18.3	13.5	510.2	[10]
Indian (Tamilnadu, Vaigai River)	7.45*	33.81		448.24	[21]
Turkey (Kızılırmak Delta)	27.898*	14.184	9.890	62.372	[11]
China (Yangtze Estuary)	24.3	40.9		628	[20]
Worldwide	35	30		400	[22]
Turkey (Borçka Dam Lake)	**12.19**	**14.05**	**4.20**	**396.41**	**Present Study**

*^{238}U

3.4. Radiological hazard indices

3.4.1. Radium equivalent activity (Ra$_{eq}$):

Radium equivalent activity is calculated using the equation given below [23].

$$Ra_{eq} = C_{Ra} + 1.43C_{Th} + 0.077C_K \tag{3}$$

where, C$_{Ra}$, C$_{Th}$ and C$_K$ were the activities of ^{226}Ra, ^{232}Th and ^{40}K (Bq kg^{-1}), respectively. The results of radium equivalent activities (Ra$_{eq}$) for sediment are presented in Table 4. As noted in Table 4, the radium equivalent activity value varied from 39.07 Bq kg^{-1} to 97.59 Bq kg^{-1} with the average of 62.81 Bq kg^{-1}. The determined average value were found to be less than the recommended maximum permissible value of 370 Bq kg^{-1} [24].

3.4.2. External Hazard İndex (H$_{ex}$)

The main aim of this index is to limit the radiation dose to dose equivalent limit of 1 mSvy^{-1} [25]. H$_{ex}$ should not exceed the unity limit in order to ensure that the level of risk generated by the radiation is negligible. H$_{ex}$ was determined using the formula described below [26].

$$H_{ex} = \frac{C_{Ra}}{370} + \frac{C_{Th}}{259} + \frac{C_K}{4810} \leq 1 \tag{4}$$

Table 4 showed that the average hazard index values for all samples were less than unity, which revealed that there was no harm to the farmers and populations living in the area studied.

3.4.3. Absorbed dose rate in air (D)

The gamma dose rate absorbed in outdoor air exposed at 1 meter above the surface by knowing the activity concentrations of ^{226}Ra, ^{232}Th, ^{40}K and ^{137}Cs in the sediment can be determined using the formula defined below [22, 27]:

$$D\ (nGyh^{-1}) = 0.461 \times C_{Ra} + 0.623 \times C_{Th} + 0.0417 \times C_K + 0.1243 \times C_{CS} \tag{5}$$

where C_{Ra}, C_{Th}, C_K and C_{Cs} are the activity concentration values (in Bq kg^{-1}) of ^{226}Ra, ^{232}Th, ^{40}K and ^{137}Cs, respectively, in the sediment samples. The detected activity concentrations were converted into doses using dose conversion factors of 0.461, 0.623, 0.0417 and 0.1243 for ^{226}Ra, ^{232}Th, ^{40}K and ^{137}Cs, respectively [22]. Looking at Table 4, the determined values of absorbed gamma dose rate for the sediment samples ranged from 19.27 to 49.57 nGyh^{-1} with an average value of 31.43 nGyh^{-1}. The determined average doses for all samples is lower than the world average value of 60 nGy h^{-1} [28].

3.4.4. Annual effective dose equivalent (AEDE)

The annual effective dose equivalent (AEDE) was determined using the equation given below [22]:

$$AEDE\ (mSv\ y^{-1}) = D\ (nGyh^{-1}) \times 8760\ h \times 0.7\ SvGy^{-1} \times 0.2\ x\ 10^{-6} \tag{6}$$

According to Table 4, the determined values of the annual effective dose for the sediment samples ranged from 0.024 and 0.061 mSvy^{-1}, with a mean value of 0.039 mSvy^{-1} [22]. However, the determined mean dose values for all samples was lower than the recommended limit value of 0.080 mSvy^{-1}.

3.4.5. Excess lifetime cancer risk (ELCR)

The excess lifetime cancer risk (ELCR) values were determined with the help of the relation given below [22]:

$$ELCR = AEDE \times DL \times RF \tag{7}$$

DL Here is the average life expectancy (about 78 years in Turkey) [15] and RF are factors indicating the probability of a deadly carcinogen per sievert (Sv^{-1}). Because of stochastic effects, ICRP 60 considers 0.05 for public [29]. When Table 4 was examined, it was seen that the ELCR values ranged from 0.09 x 10^{-3} to 0.24 x 10^{-3} (with a mean value 0.15 × 10^{-3}). This average value of ELCR is less than the world average (0.29 × 10^{-3}) [27].

In addition, looking at Table 4, the average lifetime total dose rate was determined as 3.01 mSv. This determined mean value is lower than recommended maximum permissible value of 4.90 mSv [22].

Table 4. Radiological parameters of the sediment samples collected from the Borçka Dam Lake.

Sampling location	Ra_{eq} (Bq kg^{-1})	H_{ex}	D (nGy h^{-1})	AEDE (mSv y^{-1})	Lifetime total dose (mSv)	ELCR (×10^{-3})
BS-1	79.33	0.21	39.55	0.049	3.78	0.19
BS-2	40.65	0.11	19.98	0.024	1.91	0.10
BS-3	39.07	0.11	19.27	0.024	1.84	0.09
BS-4	58.48	0.16	29.28	0.036	2.80	0.14
BS-5	61.72	0.17	30.90	0.038	2.96	0.15
BS-6	97.59	0.26	49.57	0.061	4.74	0.24
Min	**39.07**	**0.11**	**19.27**	**0.024**	**1.84**	**0.09**
Max	**97.59**	**0.26**	**49.57**	**0.061**	**4.74**	**0.24**
Mean	**62.81**	**0.17**	**31.43**	**0.039**	**3.01**	**0.15**

3.5. Statistical Analyses

Pearson's correlation coefficients were determined to evaluate the relationship between radionuclides and some physico-chemical parameters in sediment samples and given in Table 5. The correlation analysis revealed that 40K was substantially correlated with 226Ra (r = 0.957, p<0.01), pH was substantially correlated with 232Th (r = -0.970, p<0.01) and Silt + Clay was substantially correlated with Sand (r = -1.000, p<0.01). Besides, TOC was moderately correlated with 232Th (r = 0.848, p<0.05) and 137Cs (r = 0.849, p<0.05), Depth was moderately correlated with 232Th (r = 0.827, p<0.05) and 40K (r = 0.844, p<0.05) and 137Cs was moderately correlated with 232Th (r = 0.888, p<0.05). The strong relationship between 226Ra and 40K shows that their origin and behavior in the lake is the same, while the weak positive relationship between 232Th and the other two radionuclides (226Ra and 40K) indicates that they may have the same origin but their behavior in the lake environment differ [30]. It seems that there is no clear relationship between pH and the activity concentrations of 226Ra, 40K and 137Cs in the sediment of the dam lake, while there is a considerable negative relationship between pH of the sediment and the activity of 232Th. For these relationships can be said that the radionuclides extracted from a leached sediment into the water in neutral and alkaline media could decrease and weaken the fixation of nuclides in the sediment [31]. The similar results of this study were consistent with the

finding of literature [31-32] concerning about the effect of soil properties. In light of this information, it can be said that the activity levels of artificial and natural radionuclides decrease in sediment samples with increasing pH. Although no significant correlation was found between 137Cs and depth, a positive correlation was found between the two parameters. This can be explained by the fact that 137Cs is correlated with the depth of the sediment, as expressed by Szarlowicz et al. (2018) [33]. The concentration of 137Cs varies depending on the particle size of the sediment, mineral composition, organic matter and total organic carbon content. The amount of total organic carbon was found to be important in the deposition of 137Cs radionuclides in sediments [14] and a significant relationship between the amount of total organic matter and 137Cs was reported in some studies in the literature [14, 34-35]. In this study, a positive correlation was found between the amount of total organic carbon and 137Cs radioisotope in accordance with the literature.

Table 5. Pearson correlation coefficients between radionuclides and some physico-chemical parameters in sediment samples.

	^{226}Ra	^{232}Th	^{137}Cs	^{40}K	pH	Sand	Silt+Clay	TOC	Depth
^{226}Ra	1								
^{232}Th	0.500	1							
^{137}Cs	0.649	**0.888**[*]	1						
^{40}K	**0.957**[**]	0.501	0.582	1					
pH	-0.352	**-0.970**[**]	-0.758	-0.391	1				
Sand	-0.024	-0.184	-0.532	0.114	0.023	1			
Silt+Clay	0.024	0.184	0.532	-0.114	-0.023	**-1.000**[**]	1		
TOC	0.181	**0.848**[*]	**0.849**[*]	0.184	-0.800	-.0577	0.577	1	
Depth	0.809	**0.827**[*]	0.771	**0.844**[*]	-0.748	0.059	-0.059	0.530	1

Correlation is significant at the 0.01 level (two-tailed).
Correlation is significant at the 0.05 level (two-tailed).

4. CONCLUSION

The activity values of ^{226}Ra, ^{232}Th, ^{137}Cs and ^{40}K were determined in sediment samples collected from the Borçka Dam Lake using gamma ray spectroscopy. The mean activity concentrations of ^{226}Ra, ^{232}Th, ^{137}Cs and ^{40}K were found to be 12.19 Bq kg^{-1}, 14.05 Bq kg^{-1}, 4.20 Bq kg^{-1} and 396.41 Bq kg^{-1}, respectively. The results show that the mean activity concentration values of ^{226}Ra, ^{232}Th and ^{40}K in the Borçka Dam Lake were lower than the world average values suggested by UNSCEAR. Also, the mean activity concentration of ^{137}Cs is lower than the results of previous studies in the literature. Additionally, the radiological hazard

indices (Ra_{eq}, H_{ex}, D, AEDE, and ELCR) were determined and compared with international permissible values, and the results were lower than the limit values. The data obtained can be used by the researchers as reference data for monitoring possible radioactive contamination of the Borçka Dam Lake in the future.

Acknowledgments

REFERENCES

[1] Zorer Ö.S., Evaluations of environmental hazard parameters of natural and some artificial radionuclides in river water and sediments, Microchem. J., 145 (2019) 762–766.

[2] Papaefthymiou H., Athanasopoulos D., Papatheodorou G., Iatrou M., Geraga M., Christodoulou D., Kordella S., Fakiris E. and Tsikouras B., Uranium and other natural radionuclides in the sediments of a Mediterranean fjord-like embayment, Amvrakikos Gulf (Ionian Sea), Greece, J. Environ. Radioact., 122 (2013) 43–54.

[3] Ergül H.A., Belivermiş M., Kılıç Ö., Topcuoğlu S. and Çotuk Y., Natural and artificial radionuclide activity concentrations in surface sediments of Izmit Bay, Turkey, J. Environ. Radioact., 126 (2013) 125–132.

[4] El-Taher A. and Madkour H.A., Distribution and environmental impacts of metals and natural radionuclides in marine sediments in-front of different wadies mouth along the Egyptian Red Sea Coast, Appl. Radiat. Isot., 69 (2011) 550–558.

[5] Otansev P., Taşkın H., Başsarı A. and Varinlioğlu A., Distribution and environmental impacts of heavy metals and radioactivity in sediment and seawater samples of the Marmara Sea, Chemosphere, 154 (2016) 266–275.

[6] Celik N., Cevik U., Celik A. and Koz B., Natural and artificial radioactivity measurements in Eastern Black Sea region of Turkey, J. Hazard. Mater., 162 (2009) 146–153.

[7] Aytas S., Yusan S., Aslani M.A., Karali T., Turkozu D.A., Gok C., Erenturk S., Gokce M. and Oguz K.F., Natural radioactivity of riverbank sediments of the Maritza and Tundja Rivers in Turkey, J. Environ. Sci. Heal. Part A, 47 (2012) 2163–2172.

[8] Eroğlu, H. and Kabadayi, Ö., Natural radioactivity levels in lake sediment samples, Radiat. Prot. Dosimetry, 156 (2013) 331–335.

[9] Kulahci F. and Doğru M., Physical and chemical investigation of water and sediment of the Keban Dam Lake, Turkey Part 1: Iso-curves of radioactivity, J. Radioanal. Nucl. Chem., 268 (2006) 517–528.

[10] Kobya Y., Taşkın H., Yeşilkanat C.M., Varinlioğlu A. and Korcak S., Natural and artificial radioactivity assessment of dam lakes sediments in Çoruh River, Turkey, J. Radioanal. Nucl. Chem., 303 (2015) 287–295.

[11] Arıman S. and Gümüş H., Radioactivity levels and health risks due to radionuclides in the soil and sediment of mid-Black Sea: Kızılırmak Deltas-Turkey, Radiochim. Acta, 106 (2018) 927–937.

[12] Baltas H., Sirin M., Dalgic G. and Cevik U., An overview of the ecological half-life of the ^{137}Cs radioisotope and a determination of radioactivity levels in sediment samples after Chernobyl in the Eastern Black Sea, Turkey, J. Mar. Syst., 177 (2018) 21–27.

[13] Gedik K., Terzi E. and Yesilcicek T., Biomonitoring of metal (oid)s in mining-affected Borcka Dam Lake coupled with public health outcomes, Hum. Ecol. Risk Assess. An Int. J., 24 (2018) 1–18.

[14] Kim Y., Kim K., Kang H.D., Kim W., Doh S.H., Kim D.S. and Kim B.K., The accumulation of radiocesium in coarse marine sediment: effects of mineralogy and organic matter, Mar. Pollut. Bull., 54 (2007) 1341–1350.

[15] Baltas H., Kiris E., Dalgic G. and Cevik U., Distribution of ^{137}Cs in the Mediterranean mussel (Mytilus galloprovincialis) in Eastern Black Sea Coast of Turkey, Mar. Pollut. Bull., 107 (2016) 402–407.

[16] Baltas H., Kiris E., Ustabas I., Yilmaz E., Sirin M., Kuloglu E. and Gunes B.E., Determination of natural radioactivity levels of some concretes and mineral admixtures in Turkey, Asian J. Chem., 26 (2014) 3946–3952.

[17] Baltas, H., Kiris, E. and Sirin M., Determination of radioactivity levels and heavy metal concentrations in seawater, sediment and anchovy (*Engraulis encrasicolus*) from the Black Sea in Rize, Turkey, Mar. Pollut. Bull., 116 (2017) 528-533.

[18] Currie L.A., Limits for qualitative detection and quantitative determination. Application to radiochemistry, Anal. Chem., 40 (1968) 586–593.

[19] Caridi F., Marguccio S., Belvedere A. and Belmusto G., Measurements of gamma radioactivity in river sediment samples of the Mediterranean Central Basin, Am. J. Condens. Matter Phys., 5 (2015) 61–68.

[20] Wang J., Du J. and Bi Q., Natural radioactivity assessment of surface sediments in the Yangtze Estuary, Mar. Pollut. Bull., 114 (2017) 602–608.

[21] Ramasamy V., Paramasivam K., Suresh G. and Jose M.T., Role of sediment characteristics on natural radiation level of the Vaigai river sediment, Tamilnadu, India, J. Environ. Radioact., 127 (2014) 64–74.

[22] U.N.S.C. on the E. of A. Radiation, Sources and effects of ionizing radiation UNSCEAR 2000 report to the General Assembly, with scientific annexes Volume I: Sources, (2000).

[23] Elsaman R., Omer M.A.A., Seleem E.M.M. and El-Taher A., Natural Radioactivity Levels and Radiological Hazards in Soil Samples Around Abu Karqas Sugar Factory, J. Environ. Sci. Technol., 11 (2018) 28–38.

[24] Beretka J. and Matthew P.J., Natural radioactivity of Australian building materials, industrial wastes and by-products, Health Phys., 48 (1985) 87–95.

[25] (ICRP) I.C. on R. Protection, Protection against radon-222 at home and at work, International Commission on Radiological Protection, (1992).

[26] SureshGandhi M., Ravisankar R., Rajalakshmi A., Sivakumar S., Chandrasekaran A. and Anand D.P., Measurements of natural gamma radiation in beach sediments of north east coast of Tamilnadu, India by gamma ray spectrometry with multivariate statistical approach, J. Radiat. Res. Appl. Sci., 7 (2014) 7–17.

[27] Taskin H., Karavus M., Ay P., Topuzoglu A., Hidiroglu S. and Karahan G., Radionuclide concentrations in soil and lifetime cancer risk due to gamma radioactivity in Kirklareli, Turkey, J. Environ. Radioact., 100 (2009) 49–53.

[28] Kayakökü H. and Doğru M., Radioactivity analysis of soil samples taken from the western and northern shores of Lake Van, Turkey, Appl. Radiat. Isot., 128 (2017) 231–236.

[29] I.C. on R. Protection, ICRP Publication 60: 1990 Recommendations of the International Commission on Radiological Protection, Elsevier Health Sciences, (1991).

[30] Isinkaye M.O. and Emelue H.U., Natural radioactivity measurements and evaluation of radiological hazards in sediment of Oguta Lake, South East Nigeria, J. Radiat. Res. Appl. Sci., 8 (2015) 459–469.

[31] Tsai T.L., Liu C.C., Chuang C.Y., Wei H.J. and Men L.C., The effects of physico-chemical properties on natural radioactivity levels, associated dose rate and evaluation of radiation hazard in the soil of Taiwan using statistical analysis, J. Radioanal. Nucl. Chem., 288 (2011) 927-936.

[32] Skarlou V., Papanicolaou E.P. and Nobeli C., Soil to plant transfer of radioactive cesium and its relation to soil and plant properties, Geoderma, 72 (1996) 53-63.

[33] Szarlowicz K., Reczynski W., Czajka A., Spyt B. and Szacilowski G., Comprehensive study of the mountainous lake sediments in relation to natural and anthropogenic processes and time (Mały Staw Lake, Poland), Environ. Sci. Pollut. Res., 25 (2018) 3335–3347.

[34] Park G., Lin X.J., Kim W., Kang H.D., Lee H.L., Kim Y., Doh S.H., Kim D.S., Yun S.G. and Kim C.K., Properties of ^{137}Cs in marine sediments off Yangnam, Korea, J. Environ. Radioact., 77 (2004) 285–299.

[35] Kim Y., Cho S., Kang H.D., Kim W., Lee H.R., Doh S.H., Kim K., Yun S.G., Kim D.S. and Jeong G.Y., Radiocesium reaction with illite and organic matter in marine sediment, Mar. Pollut. Bull., 52 (2006) 659–665.

Linear And Nonlinear Intersubband Optical Absorptions In Multiple Quantum Wells Under The External Fields

Rana ÖZBAKIR iD

Cumhuriyet University, Physics Department, 58140 Sivas, Turkey

Abstract. In this study, the effects of the external fields (electric and tilted magnetic fields) and well parameters on the optical absorption coefficients in GaAs/GaAlAs multiple (five) quantum wells under the applied electric and tilted magnetic fields has been investigated theoretically. Firstly, the energy eigenvalues and eigen functions of an electron confined in multiple quantum wells are calculated by analytically from Schrödinger equation using the transfer matrix method within the effective mass approximation, Secondly, the linear, nonlinear and total intersubband optical absorptions in GaAs/GaAlAs multiple quantum wells system are studied within the compact density-matrix approach. It is shown that the parameters such as strenghts of the external fields and θ-tilted angle values not only shift the peak positions in absorption spectrum but also considerably modify their potential heights. In generally, electronic and optical properties of the quantum wells are very sensitive to the applied external fields and well parameters. Therefore, we can conclude that the effect of the external fields can be used to tune and control the optical properties of interest in the range of the far-infrared electromagnetic spectrum.

Keywords: Multiple Quantum Wells, Optical Properties, Electric Field, Tilted Magnetic Field.

DIŞ ALANLAR ALTINDAKİ ÇOKLU KUANTUM KUYULARINDA LİNEER VE LİNEER OLMAYAN BAND İÇİ OPTİK SOĞURMA

Özet. Bu çalışmada, elektrik ve eğik manyetik alan altında GaAs/GaAlAs çoklu (beş kuantum kuyusu) kuantum kuyusunda dış alanların (elektrik ve eğik manyetik alan) ve kuyu parametrelerinin optik soğurma katsayısı üzerindeki etkileri teorik olarak incelenmiştir. İlk olarak, çoklu kuantum kuyularında kuşatılmış bir elektronun özdeğer ve özfonksiyonları, etkin-kütle yaklaşımı ile transfer-matris metodu kullanılarak Schrödinger denkleminden analitik olarak hesaplanmıştır. İkinci aşamada, GaAs/GaAlAs çoklu kuantum kuyu sisteminde doğrudan, dolaylı ve toplam bandiçi optik soğurma çalışılmış ve optik geçişler için kompakt yoğunluk matris yaklaşımı kullanılmıştır. Dış alan şiddetleri ve θ-eğiklik açıları gibi parametrelerin sadece soğurma spektrumdaki pik pozisyonlarını kaydırmakla kalmayıp, aynı zamanda yüksekliklerini de önemli ölçüde değiştirdiği gösterilmiştir. Genellikle, kuantum kuyularının elektronik ve optik özellikleri, uygulanan dış alanlara ve kuyu parametrelerine oldukça duyarlıdır. Bu nedenle, dış alanların etkisini, uzak kızılötesi elektromanyetik spektrum aralığında ilgili optik özellikleri ayarlamak ve kontrol etmek için kullanılabileceği sonucuna varabiliriz.

Anahtar Kelimeler: Çoklu Kuantum Kuyusu, Optik Özellikler, Elektrik Alan, Eğik Manyetik Alan.

1. INTRODUCTION

In recent years, with great advances in semiconductor growth technology, semiconductor quantum wells (QW) with different geometries such as square, parabolic, semiparabolic, rectangular have been grown and due to their superior electronic and optical properties have considerably attracted great deal of attention. In addition to the well-known square and parabolic quantum wells, such as semi-parabolic, graded, V-shaped, inverse parabolic, PoschTeller, Tietz-Hua have been intensively studied also [1-13]. The electronic and optical properties of the QWs are very sensitive to the applied external fields. These and quantum confinement effects leads to the formation of discrete energy levels within the well, which results in significant optical properties in the semiconductor QW system compared with that in the bulk material [14,15]. Optical properties of these semiconductor QWs have the potential for device applications such as far-infrared laser amplifiers, high-speed electro-optical modulators, photodetectors, etc.[16-18].

In a parabolic potential well eigenenergies of two-dimensional electrons subjected to a tilted magnetic field have been solved analytically by Maan [19]. İ.Sökmen at all. have completely solve the Schrödinger equation using a square multiple quantum wells as the confinement potential and it has obtained analytical solutions with applying an orthogonal transformation to two-dimensional semiconductor heterostructures under externally tilted magnetic field [20]. They have made the Hamiltonian of the system separable in terms of the new coordinates after implementation of successive transformations [20-23]. In this manuscript, It have been completely solved the Schrödinger equation using multiple square wells potentials as the confining potential and obtained analytical solutions without making any approximations as in Refs [20-23] for two dimensional semiconductor heterostructures under externally applied electric and tilted magnetic fields. In this system, the electric field is applied along the growth direction (z-direction) of the multiple square quantum wells whereas the magnetic field is applied to the (x-z) in-plane. θ is the tilt angle between the direction of magnetic field and x-axis. After solving the Hamiltonian of the system, the multiple quantum wells become narrower (wider) when the θ-tilted angle increases (decreases) because the multiple quantum well widths are proportional with Lcos θ. Furthermore, potential heights of the multiple quantum wells are proportional with VoCos2 θ so their potential heights decrease when the θ-tilted angle increases.

In recent years, several theoretical studies have been made on linear and nonlinear intersubband optical absorption (AC) and refractive index changes(RIC) in single QWs and multi-quantum wells under applied electric and magnetic fields [24-32]. In this study, the effects of the electric and magnetic field strength, different tilt angles (i.e. direction of the magnetic field) on total absorption coefficient including the linear and third order nonlinear terms for the transitions between the ground and other excited states of an electron in multiple (five) quantum wells are investigated.

2.THEORY

Within the framework of an effective mass approximation, the electron Hamiltonian for the multiple (five) quantum wells in the presence of magnetic field $\vec{B}$ applied in x-z plane and electric field $\vec{F}$ applied in the z-direction (perpendicular to the growth direction), is given by:

$$H = \frac{1}{2m^*}\left(\vec{p} + e\vec{A}\right)^2 + V(z). \tag{1}$$

where m*, $\vec{p}$ and e are the effective mass, momentum vector and charge of the electron, respectively. The magnetic field can be described by the vector potential $\vec{A}$ =(0,x B sin θ – z B cos θ,0) which is applied in the (x–z) plane and where θ is the angle between the magnetic field and the x-axis. The magnetic field have been defined as $\vec{B}$ =(Bcos θ,0,B sin θ) by using vector potential in Coulomb gauge. V(z) is the confinement potential of the electron and its functional form is defined by

$$V(z) = V_0 \sum_{i=1}^N \left[S\left(z_{L_i} - z\right) + S\left(z - z_{R_i}\right) - (N-1)\right] - eFz, \tag{2}$$

where S(z) is the step function, for i.th quantum well z=zLi and z=zRi are the left and right well boundaries, respectively. N is the total number of quantum well. The wave function of the system by using the translation symmetry in the y direction can be defined as

$$\psi(r) = Exp\left(ik_y y\right)\varphi(x,z) \tag{3}$$

After using the successive transformations which are proposed by Refs.[20-23], Hamiltonian can be separable in terms of the new coordinates and the Schrödinger equation of the system taken into consideration without making any approximation for the heterostructures subject to the electric and tilted magnetic field can be solved. After these transformations, Hamiltonian in the z^'-direction is obtained as follows

$$H = \frac{p_{z'}^2}{2m^*} + \frac{1}{2}m^*\varpi^2(z_0' - z')^2 + V(z') \tag{4}$$

where $\varpi\ (= eB/m^*)$ is the cyclotron frequency, $z_0'(= \hbar k_y/eB = a_H^2 k_y)$ is the position of the orbit center, $a_H(= (\hbar/m^*\varpi)^{1/2})$ is the magnetic length,

$$V(z') = V_0 \cos^2\theta \sum_{i=1}^N \left[S\left(z_{L_i}' - z'\right) + S\left(z' - z_{R_i}'\right) - (N-1)\right] + eF\cos\theta z' \tag{5}$$

is the confinement potential in z'-direction. And eigenfunction of the system is obtained

$$\psi(r) = Exp\left(ik_y y'\right)\chi(x')\phi(z') \tag{6}$$

If we define $\tilde{\xi} = \tilde{u} - 2\tilde{\beta}$ together with the dimensionless variables- $\tilde{u} = \left(\frac{\sqrt{2}}{a_H}\right)(z_0' - z')$, $\tilde{E}_{z'} = E_{z'}/\hbar\varpi$ and $\tilde{V}_0 = V_0/\hbar\varpi$ for z'-direction, Schrödinger equation in the new coordinate system is written as follows

$$\frac{d^2\phi(\tilde{\xi})}{d\tilde{\xi}^2} + \left\{ \left(m + \frac{1}{2}\right) - \frac{1}{4}\,\tilde{\xi}^2 \right\} \phi(\tilde{\xi}) = 0, \tag{7}$$

where m is the quantum number and the solution of this equation which corresponds to the motion in the z'-direction is the Weber functions.

After the eigenvalues and their corresponding wave functions for the Hamiltonian in the Eq. (4) are obtained, the expressions including the linear, third order nonlinear and total absorption coefficient (AC) can be define clearly as follows [23-31 and references therein], respectively:

$$\alpha^{(1)}(\omega) = \omega \sqrt{\frac{\mu}{\varepsilon_R}} \frac{|M_{ji}|^2 \sigma_V \hbar \Gamma_{ij}}{(\Delta E - \hbar \omega)^2 + (\hbar \Gamma_{ij})^2} \tag{8}$$

$$\alpha^{(3)}(\omega, I) = -2\omega \sqrt{\frac{\mu}{\varepsilon_R}} \left(\frac{I}{\varepsilon_0 n_r c}\right) \frac{|M_{ji}|^4 \sigma_V \hbar \Gamma_{ij}}{\left[(\Delta E - \hbar \omega)^2 + (\hbar \Gamma_{ij})^2\right]^2} \tag{9}$$

$$\times \left(1 - \frac{|M_{jj} - M_{ii}|^2}{|2M_{ji}|^2} \frac{(\Delta E - \hbar \omega)^2 - (\hbar \Gamma_{ij})^2 + 2(\Delta E)(\Delta E - \hbar \omega)}{(\Delta E)^2 + (\hbar \Gamma_{ij})^2} \right),$$

$$\alpha(\omega, I) = \alpha^{(1)}(\omega) + \alpha^{(3)}(\omega, I) \tag{10}$$

In these equations, n_r is the refractive index, μ is the permeability of the system, σ_V is electron density, ε_0 is the permittivity of free space, Γ_{12} is the relaxation rate which is equals to the inverse relaxation time T_{12}, c is the speed of the light in free space, I $(= \frac{2n_r}{\mu c}|E(\omega)|^2)$ is the optical intensity of the incident electromagnetic wave with an angular frequency ω which leads to the intersubband optical transitions, ε_R is the real part of the permittivity, $\Delta E = E_j - E_i$ is the energy difference between the ground and first excited levels, $M_{ij} = \left| \left\langle \phi(\tilde{\xi})_i \middle| \tilde{\xi} \middle| \phi(\tilde{\xi})_j \right\rangle \right|$ (i=1 and j=2) is the dimensionless electric dipole moment matrix element.

3.RESULTS AND DISCUSSIONS

The values of the using parameters in calculations are: $\varepsilon_0 = 12.58$, $m^* = 0.067\, m_0$ (where m_0 is the free electron mass), $V_0 = 228\,[meV]$ (which corresponding to x=0.3 for Aluminum concentration), $n_r = 3.2$, $T_{12} = 0.148\,[ps]$, $I = 2.0 \times 10^9\,[W/m^2]$, $\Gamma_{12} = 1/T_{12}$, $\mu_0 = 4\pi \times 10^{-7}\,[Hm^{-1}]$, $\sigma_v = 3.0 \times 10^{22}\,[m^{-3}]$. Effective well width, effective barrier height and the orbit center are chosen as $L_T = \frac{\sqrt{2}}{a_H}(L_w + L_b)\cos\theta$ (where L_w is well width, L_b is barrier width), $V_{eff} = \frac{V_0}{\hbar\omega}\cos^2\theta$ and $z_0' = [2L_T + \frac{\sqrt{2}L_w}{2a_H}\cos\theta]$. All results are for $L_w = 80\,[\text{Å}]$ and $L_b = 15\,[\text{Å}]$.

The schematic diagram of the multiple (five) quantum wells and squared wavefunctions of the electron in the ground and first excited level for F=0 (blackline) and F=30kV/cm (redline) is seen in Fig.1. In addition, effect of the θ -tilted angle on the system is also clearly seen. The energy levels are quantized by the combined effects of the magnetic field and barriers of the multiple quantum wells. The second energy level is in an extended state in which is dominant effect of the magnetic confinement as seen in θ>60 (in Fig.1(c)). When the electric field is applied, electron becomes localize in the right side of the well (triangle region, (please see Figs.1(a), (b) and(c)).
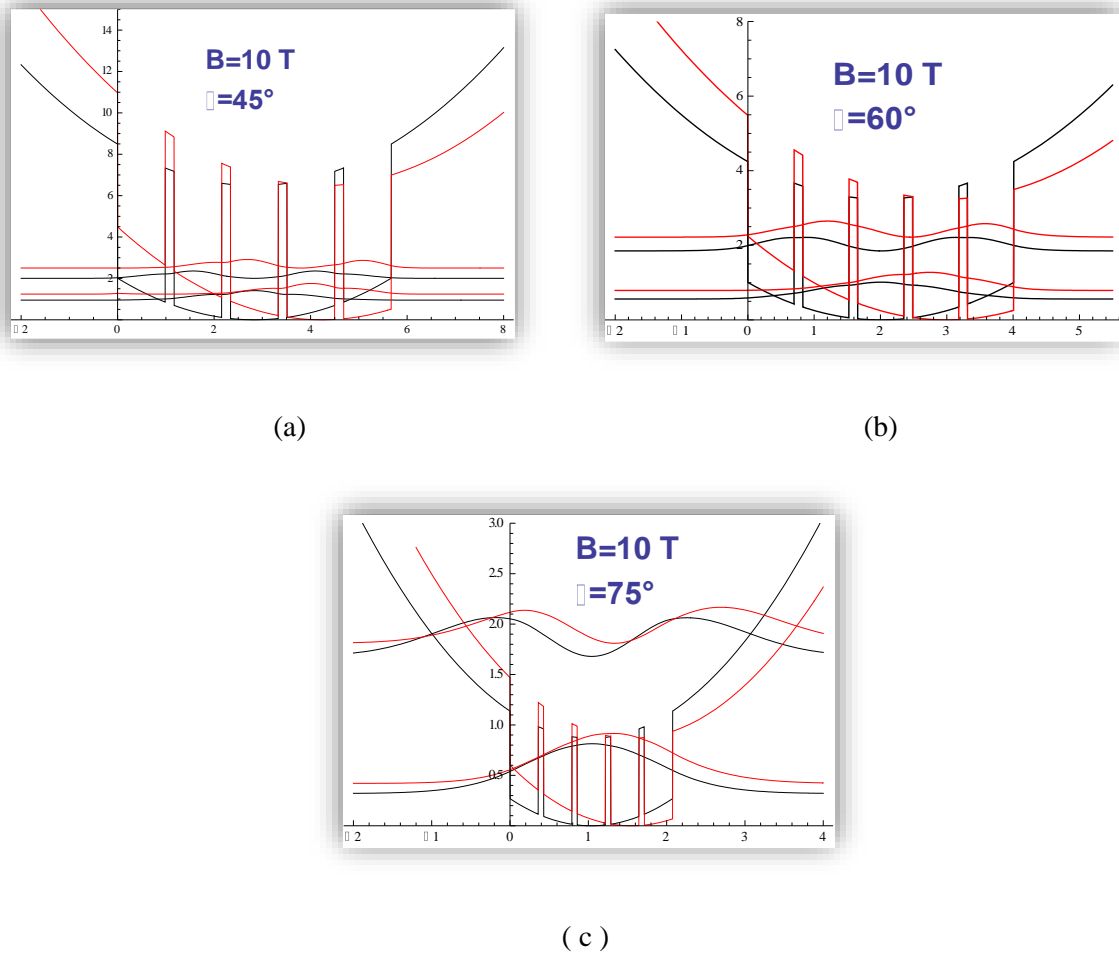

(a)

(b)

(c)

Figure1. The schematic diagram of the multiple (five) quantum wells and squared wavefunctions of the electron in the ground and first excited level for F=0 (blackline) and F=30kV/cm (redline) a) θ = 45º b) θ = 60º c) θ = 75º

In Fig.2, it's plotted the first six electronic energy levels of the multiple quantum wells system as a function of the z' for three different tilt angles for F=0 (in a, b, c) and F=30kV/cm (in d,e,f). These results clearly show that there are two different types of the energy states; the states confined in multiple quantum wells (the lowest states in Fig 2 (a, b and c)) and extended states (the higher states in Fig.2 (a, b and c)). The energies of the lower states are less than effective potential height in small θ-tilt angle degrees (see Fig.2(a, b, c)). The effective potential heights decrease as θ-tilt angle degree increases. Because the effective potential height is proportional with $\cos^2 \theta$. Electronic energy levels are located at Landau levels as they move away from the center of multiple quantum wells (i.e. in larger z' values).
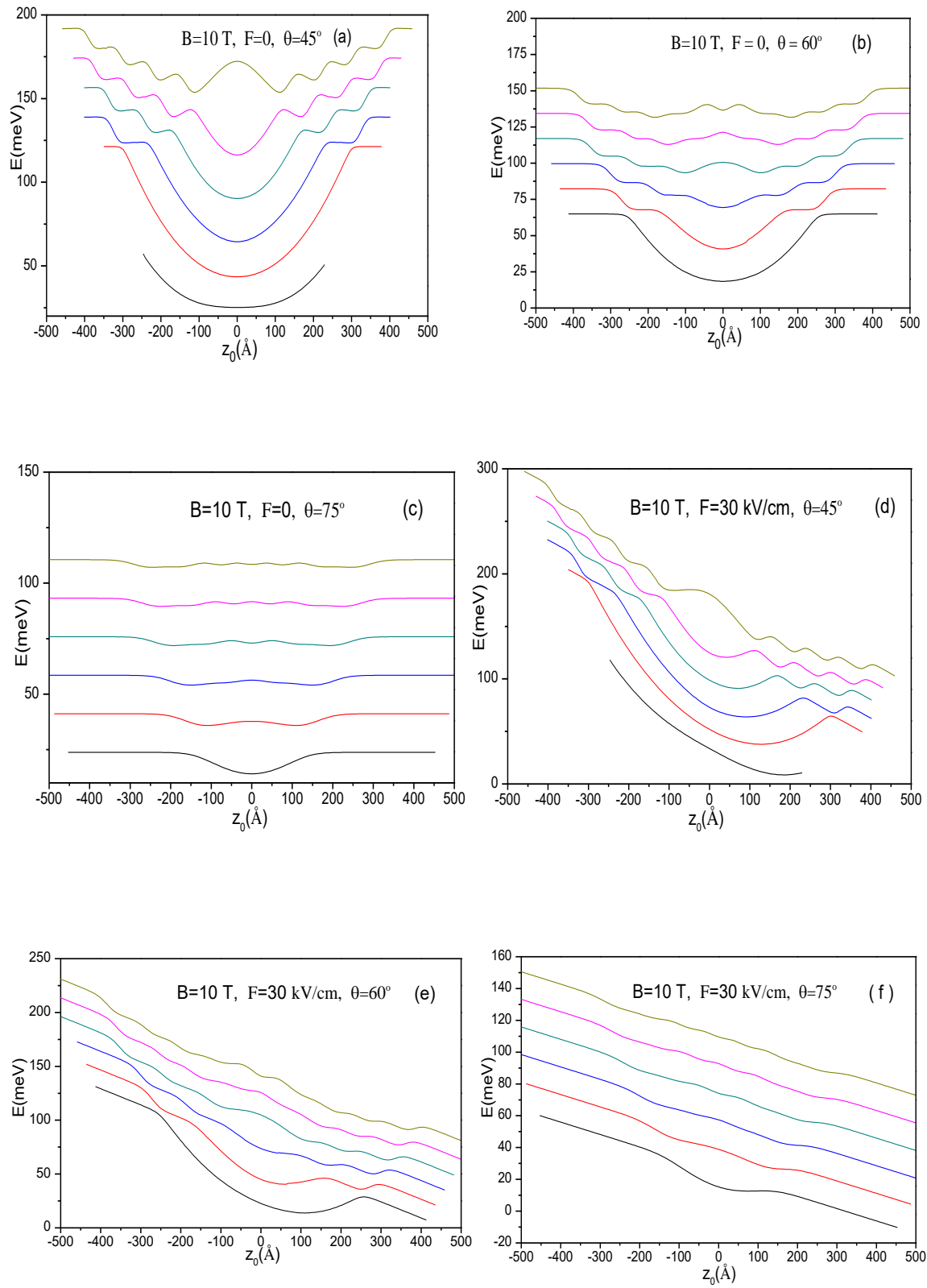
Figure2. The first six electronic energy levels of the multiple quantum wells system as a function of the z' for three different tilt angles for F=0 (in a,b,c) and F=30kV/cm (in d,e,f).

It shows the variations of linear, nonlinear and total ACs as a function of the incident photon energy for different tilt angles that are given in Fig. 3: a) F=0 b) F=30kV/cm electric field values.

As the tilt angles increases, ΔE energy difference between the related energy levels increases and thus the total AC shifts to the blue and this behavior is seen clearly in Fig.3(a).

(a)

(b)

(c)
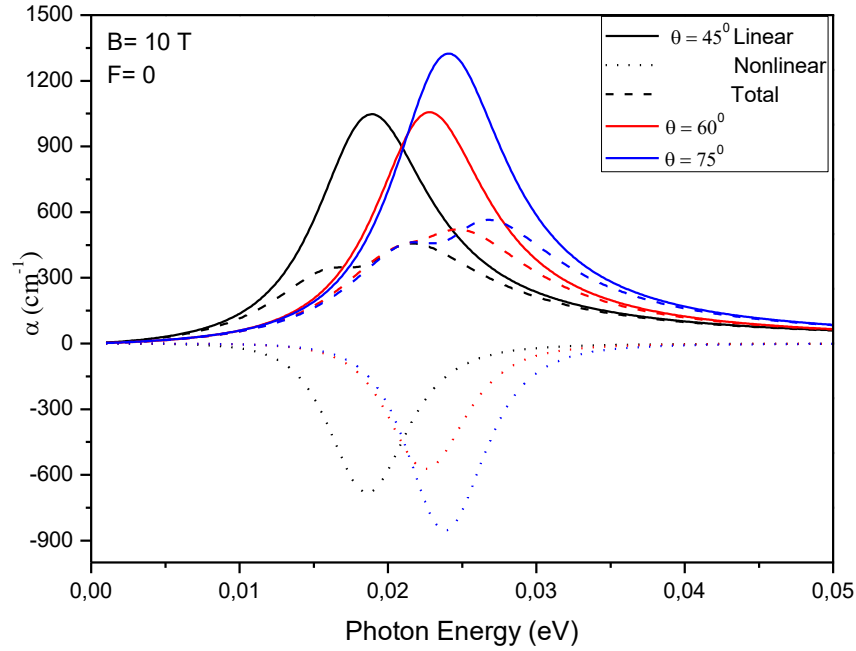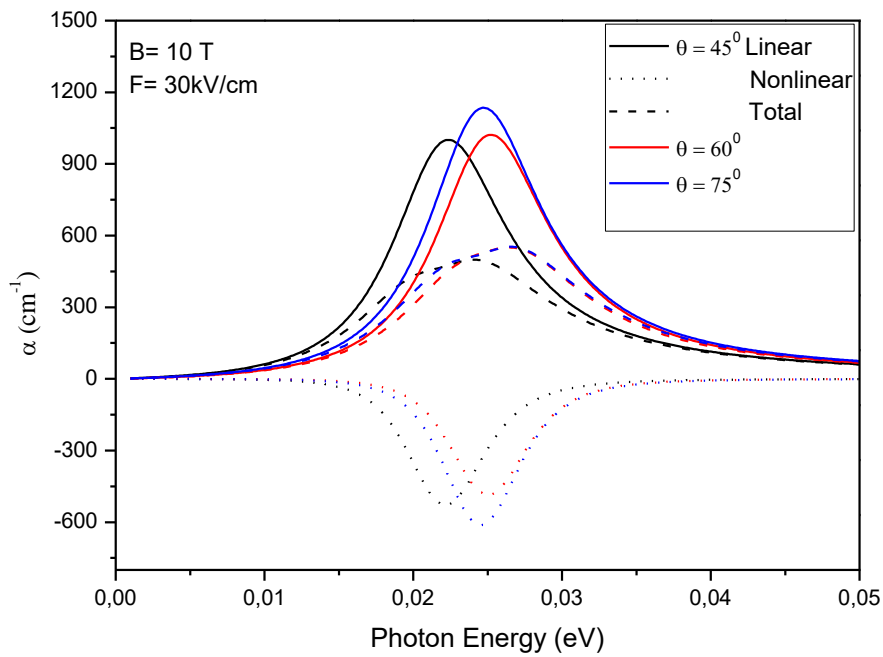
Figure3. The variation of linear, nonlinear and total absorption coefficients as a function of the photon energy for different tilt angles and **a)** F=0 **b)** F=30kV/cm electric field values. **c)** The variation of the energy differences between the related energy levels- ΔE as a function of the tilt angles for two different electric field values.

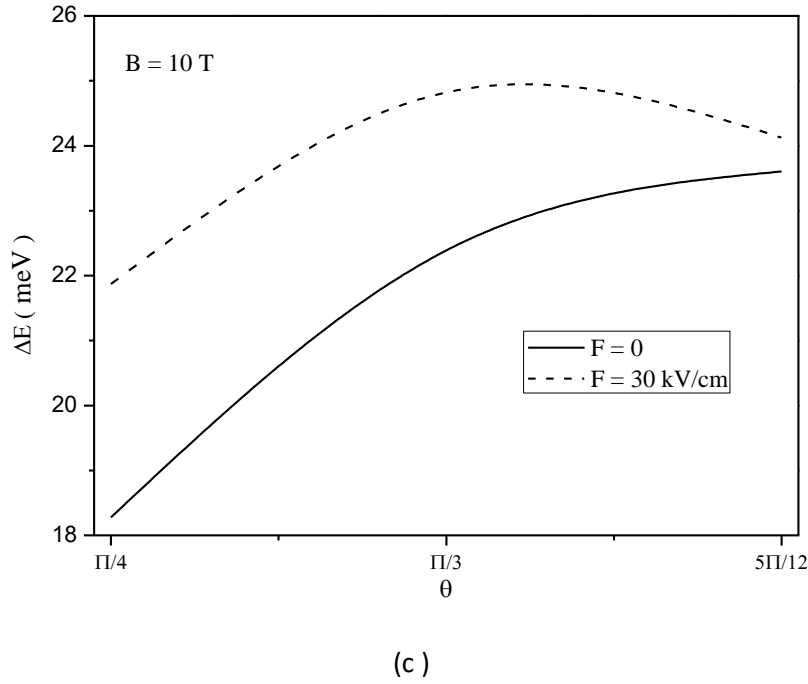When the electric field is applied, electron becomes localize in the right side of the well (Figs.1(a), (b) and(c) redline) since QWs bend in the opposite direction to the electric field and thus the peak positions of the ACs shifts towards to higher photon energies since ΔE increases with the electric field (Figs.3 (b)). It's seen that in Fig.3 (c) at F=30kV/cm, as the tilt angle increases from θ=45º to θ=60º ΔE increases and thus total AC shifts to the blue. For further angle values (θ>60º), the peak of the total AC slows down shift to the blue since ΔE decreases. This behavior of total AC spectra is a direct consequence of the increment or decrement in the energy differences between the ground and first excited levels with increasing angle values, respectively. In addition, the presence of the electric field is eliminated saturation when θ tilt angle value increases (see Fig.3(b)). In order see better the effects of the electric field strength on the AC spectrum, it is plotted the variation of the energy differences between the related energy levels- ΔE as a function of the tilt angle for two different electric field values in Fig. 3 (c). This is expected, effective well width and effective potential height ($L_{eff} = \frac{\sqrt{2}L_w}{2a_H}\cos\theta$, $V_{eff} = \frac{V_o}{\hbar\omega}\cos^2\theta$) decrease with increasing angle values and this behavior is pronounced for θ > 30º. In this case, electron in the ground and first excited level is localized in the bottom part of the well in θ ≤ 60 angle values, whereas for

θ > 60 electron in the first excited level is localized in the upper part (magnetic confinement) while its ground level is in the bottom part of the well as seen in Figs. 1(a) and (b).

As a result, it is investigated the effect of the electric field on total absorption coefficient including the linear and third order nonlinear terms in the multiple GaAs/GaAlAs quantum wells for a constant tilted

magnetic field. Furthermore, electric field strength as well as the effects of the magnetic field direction (i.e. different tilt angles) and the well parameters on the optical properties have been investigated.

4. CONCLUSION

In this study, it is investigated the effects of the electric field strength and direction of the magnetic field on total absorption coefficient including the linear and third order nonlinear terms in the GaAs/GaAlAs multiple quantum wells under the external electric and magnetic field. The obtained results show that absorption coefficient change is sensitive to the electric field and direction of the magnetic field. By changing the direction of the magnetic field and existence of the electric field, we can obtain a blue or red shift, without the need for the growth of different samples. This also gives a new degree of freedom in various device applications based on the intersubband transition of electrons.

Acknowledgements

References

[1] Karabulut İ., Atav Ü., Şafak H., Tomak M., Eur. Phys. J. B 55 (2007) 283-288.

[2] C. Mailhiot, Y.C. Chang, T.C. McGill, Phys. Rev. B 26 (1982) 4449–4457.

[3] Q. Guo, Y.P. Feng, H.C. Poon, C.K. Ong, Eur. Phys. J. B 9 (1999) 29–36.

[4] F.Q. Zhao, X.X. Liang, S.L. Ban, Eur. Phys. J. B 33 (2003) 3–8.

[5] Z.P. Wang, X.X. Liang, X. Wang, Eur. Phys. J. B 59 (2007) 41–46.

[6] Y.B. Yu, S.N. Zhu, K.X. Guo, Phys. Lett. A 335 (2005) 175–181.

[7] E. Kasapoglu, H. Sari, I. Sökmen, Surf. Rev. Lett. 13 (2006) 397–401.

[8] E. Kasapoglu, I. Sökmen, Physica E 27 (2005) 198–203.

[9] O. Aytekin, S. Turgut, M. Tomak, Physica E 44 (2012) 1612–1616.

[10] E. Kasapoglu, S. Sakiroglu, F. Ungan, U. Yesilgul, C.A. Duque, I.Sökmen, Physica B 526 (2017) 127-131.

[11] S. Baskoutas, A.F. Terzis, Physica E 40 (2008) 1367–1370.

[12] S. Baskoutas, C. Garoufalis, A.F. Terzis, Eur. Phys. J. B 84 (2011) 241–247.

[13] F. Ungan, E. Kasapoglu, I. Sökmen, Solid State Commun. 151 (2011) 1415–1419.

[14] E. Rosencher, Ph. Bois, Phys. Rev. B 44, 11315 (1991).

[15] M.K. Gurnick and T.A. Detemple, IEEE J. Quantum Electron. QE-19, 791 (1983).

[16] İ. Karabulut, S. Baskoutas, J. Appl. Phys. 103, 073512 (2008).

[17] C.H. Liu, B.R. Xu, Phys. Lett. A 372, 888 (2008). DOI: 10.1016/j.physleta.2007.08.046

[18] B. Chen, K.X. Guo, Z.L. Liu, R.Z. Wang, Y.B. Zheng, B. Li, J. Phys.: Condens. Matter 20, 255214 (2008).

[19] J.C. Maan,Solid-State Sciences,53,edited by G.Bauer, F.Kuchar, H.Heinrich (1984).

[20] I. Sökmen, H. Sari, S. Elagöz, Y. Ergün, S. Erzin, Superlattices Microstruct. 17, 3 (1995).

[21] Y. Ergün, I. Sökmen, H. Sari, S. Elagoz, M.C. Arıkan, Semicond. Sci. Technol. 12, 802 (1997).

[22] R Amca, Y Ergun, I Sökmen, H Sari, Semicond. Sci. Technol. 15, 1087 (2000).

[23] R. Özbakır, Can. J. Phys. 96, (9), 999–1003 (2018)

[24] E.M. Goldys, J.J. Shi,Phys. Status Solidi (b), 210, 237 (1998).

[25] S. Ünlü, İ. Karabulut, H. Safak, Physica E 33, 319 (2006).

[26] F. Ungan, M. E. Mora-Ramos, C. A. Duque, E. Kasapoglu, H. Sari, I. Sökmen, Superlattices Microstruct. 66, 129 (2014).

[27] E. Kasapoglu, C. A. Duque, H. Sari, I. Sökmen, The European Physical Journal B, 82, 13 (2011).

[28] İ. Karabulut, Ü. Atav, H. Safak, M. Tomak, Eur. Phys. J. B 55, 283 (2007).

[29] B. Chen, K.X. Guo, R.Z. Wang, Z.H. Zhang, Z.L. Liu, Solid State Commun. 149, 310 (2009).

[30] D. Ahn, S.L. Chuang, IEEE J. Quantum Electron 23, 2196 (1987).

[31] I. Karabulut, C.A. Duque, Physica E 43, 1405 (2011).

[32] M.J. Karimi, A. Keshavarz, Superlatt. Microstruct. 50, 572 (2011).

Comparison of Remote Sensing Classification Techniques for Water Body Detection: A Case Study in Atikhisar Dam Lake (Çanakkale)

Emre ÖZELKAN 🆔

Çanakkale Onsekiz Mart University, Faculty of Architecture & Design, Department of Urban & Regional Planning, Çanakkale, TURKEY.

Abstract. Water resources management is one of the most important issues of today. Satellite remote sensing have been successfully used to detect the presence of water bodies. In this study, four remote sensing methods: (1) normalized difference water index (NDWI), (2) support vector machine (SVM), (3) geographic object-based image analysis (GEOBIA) and (4) NDWI supported GEOBIA (GEOBIA_NDWI) were examined for water body area detection. For this purpose, Atikhisar Dam Lake, the only water source of Çanakkale central district of Turkey was selected as study area. As remote sensing data nine multitemporal Landsat-8 Operational Land Imager (OLI) multispectral satellite images between 2013 and 2017 were used. For the accuracy assessment, area values extracted from the used methods were tested with in-situ measurement lake area values. The main issues discussed in this study can be specified as follows: (i) Is pixel-based classification SVM or object-based image classification GEOBIA more successful in the water body detection?, (ii) Are the image classification methods (SVM and GEOBIA) or the water index (NDWI) more successful in the water body detection? and (iii) What is the contribution of NDWI to GEOBIA_NDWI (GEOBIA_NDWI) classification in the water body detection? The results show that meteorological factors and irrigation were influential in lake area variations. NDWI was found to be superior to other methods in determining water body and allowed for better detection of the lake boundary. Additionally, NDWI made a better separation of the land cover classes adjacent to water at the border. The object based GEOBIA was better than the pixel based SVM for distinguishing water and other land cover classes adjacent to border. GEOBIA_NDWI lake area results were more accurate than the standard object-based classification. Mixed pixels out of the lake area was determined less in the NDWI and GEOBIA_NDWI results.

*Keywords***:** Water body detection, NDWI, SVM, GEOBIA, GEOBIA_NDWI.

Su Kütlesi Belirlemede Farklı Sınıflandırma Yöntemlerinin Karşılaştırılması: Atikhisar Barajı (Çanakkale) Örneği

Özet. Su kaynakları yönetimi günümüzün en önemli konularının başında gelmektedir. Su kütlelerinin varlığının tespitinde uydudan uzaktan algılama başarı ile kullanılmaktadır. Bu çalışmada, (1) normalize edilmiş fark su indisi (NDWI), (2) destek vektör makinaları (DVM), (3) coğrafi nesne-tabanlı görüntü analizi (GEOBIA) ve NDWI destekli GEOBIA (GEOBIA_NDWI) uzaktan algılama yöntemleri su kütlesini belirleyebilmek için incelenmiştir. Bu amaçla, Türkiye'nin Çanakkale İl'inin Merkez İlçe'sinin tek su kaynağı olan Atikhisar Baraj Gölü çalışma alanı olarak tercih edilmiştir. Uzaktan algılama verisi olarak, 2013 ve 2017 yılları arasında temin edilmiş, dokuz adet çok zamanlı Landsat-8 Operational Land Imager (OLI) multispektral uydu görüntüsü kullanılmıştır. Kullanılan yöntemlerden elde edilen sonuçların doğruluk analizi için, yerinde ölçülen göl alanı değerleri kullanılmıştır. Bu çalışmada ele alınan ana konular şu şekilde sıralanabilir: (i) Piksel tabanlı sınıflandırma DVM mi yoksa nesne tabanlı sınıflandırma GEOBIA mı su kütlesi belirlemede daha başarılıdır?, (ii) Görüntü sınıflandırma yöntemleri mi (DVM ve GEOBIA) yoksa su indisi mi (NDWI) su kütlesi belirlemede daha başarılıdır? ve (iii) NDWI'ın GEOBIA_NDWI sınıflandırmasına su kütlesi belirlemede katkısı nedir?

Sonuçlar meteorolojik etkenlerin ve sulamanın göldeki değişimlerde etkili olduğunu göstermektedir. NDWI göl alanı belirlemede daha başarılı bulunmuştur ve göl sınırı belirlemede daha iyi sonuç vermektedir. Ek olarak, NDWI göl kenarında su ile temas eden sınıfları daha iyi ayırabilmektedir. Nesne tabanlı GEOBIA suyla temas eden arazi örtüsü sınıflarını piksel tabanlı DVM'den daha iyi ayırabilmektedir. GEOBIA_NDWI sonuçları standart nesne tabanlı sınıflandırmadan daha doğrudur. NDWI ve GEOBIA_NDWI sonuçlarında göl alanı dışında su olarak atanmış piksel sayısı daha azdır.

Anahtar Kelimeler: Su kütlesi belirleme, NDWI, DVM, GEOBIA, GEOBIA_NDWI.

1. INTRODUCTION

Water is the most vital resource for the continuity of all life on earth. Water resources management is the most important issue of today due to the decreasing water resources and increasing water demand [1]. Moreover, global warming and climate change that continually increase their destructive effect makes the precision water resources management important more than ever in the management of the agricultural irrigation [2, 3]. Since the lack of water adversely affects whole life, water resources need to be managed in the most accurate and effective manner [4, 5].

The most basic and known way to detect the location, size and content of the water bodies is to make in situ measurements and observations. However, these measurements and observations are not effective as time and cost. Continuity of observations and measurements is extremely important especially in arid and semi-arid climates, where monthly and seasonal changes are significant. Remote sensing is widely used efficiently in the management of water resources [6, 7]. Remote sensing from the satellite provides a great advantage in monitoring water bodies owing to the ability to extract information about large areas at once [7]. In other words, satellite remote sensing makes continuous monitoring of water resources possible in a time- and cost-effective way [4, 6].

There are several remote sensing methods for detecting water bodies, and image classification and water indices are some of the most preferred methods [8-11]. The methods of image classification are generally divided into supervised and unsupervised, and, however, supervised classification is most preferred in terms of accuracy and reliability [12]. Some of the popular supervised classification methods are Maximum Likelihood, Spectral Angle Mapper, Neural Network and Support Vector Machine (SVM) [12, 13]. On the other hand, image classification methods are divided into pixel and object-based [14]. While the pixel-based classification classifies the pixels according to the spectral characteristics of the image, the basic approach in the object-based classification is to create homogeneous image objects from image pixels with similar spectral properties and to classify these objects by taking into account the spectral, statistical, texture and geometric characteristics defined for these objects [15, 16]. The most commonly used object-based classification method is eCognition's geographic object–based image analysis (GEOBIA) software system [17].

Water indices are the most effective and easy way to detect water bodies with remote sensing. Water indices are composed of simple algorithms performed by spectral bands considering the

spectral properties of water that are high reflectance in visible and low reflectance in infrared regions such as normalized difference water index (NDWI) [18] and modified NDWI [19]. In spite of their simple structures and working principles, water indices can produce faster and more accurate information than other methods [9]. There are many successful studies conducted with SVM [20], GEOBIA [21] and NDWI [22] methods for determining the water body. On the other hand, the water body extraction studies, where GEOBIA is supported by indices such as NDWI comprising the most basic and useful band arithmetic, are also increasing [23-25].

In this study, the water body area detection capability of four methods: (1) normalized difference water index (NDWI), (2) support vector machine (SVM) – a supervised classification method, (3) geographic object-based image analysis (GEOBIA) and (4) NDWI supported GEOBIA (GEOBIA_NDWI) were investigated. As a study area Atikhisar Dam Lake in Çanakkale province of Turkey was selected and as remote sensing data nine multitemporal Landsat-8 Operational Land Imager (OLI) multispectral satellite images between 2013 and 2017 were used. Contrary to the classical approach in accuracy assessment such as using high spatial resolution images, maps, ground control points with GPS, etc., the extracted lake area values using remote sensing methods were verified by in-situ measured lake area values. Considering the above assessments and approaches, the main issues discussed in this study can be specified as follows: (i) Is pixel-based classification (SVM) or object-based image classification (GEOBIA) more

successful in the water body detection?, (ii) Are the image classification methods (SVM and GEOBIA) or the water index (NDWI) more successful in the water body detection? and (iii) What is the contribution of NDWI to GEOBIA (GEOBIA_NDWI) classification in the water body detection?

2. MATERIALS AND METHODS

2.1 Study Area

The study area is Atikhisar Dam Lake located between 26°31'2.22" - 26°33'10.30" eastern meridians and 40°7'36.31" - 40°3'49.67" northern parallels within the borders of Canakkale city established in the west of the Turkey (Figure 1). Atikhisar Dam is crucial for the region since it is the only water source of the central district and serves as a multi-purpose dam providing drinking water, irrigation, flood protection, etc [4]. The study area is located in the Marmara climate, which is a regional transition zone between the Black Sea and Mediterranean climates [26]. According to Turkish State Meteorological Service long term data: (a) The rainiest and driest months are December with 106.8 mm and August with 6.4 mm, respectively and (b) The hottest and the coldest months are July with 25oC and January with 6.1oC, respectively.

2.2 Field Data

In the study area, all water level measurements are performed by the General Directorate of State Hydraulic Works (DSİ) on the first day of the month. Field data from DSİ observation and measurement station were acquired between 2013 and 2017. The remote sensing water body detection methods' results were verified by in-situ water area measurement values. As explained in the next

section, only nine in-situ measurement data could be used because of the atmospheric constraints (fog, haze and cloud) in obtaining satellite images (Table 1). Additionally, the meteorological data

(only precipitation for this study) from Turkish State Meteorological Service (MGM) was used to interpret results.
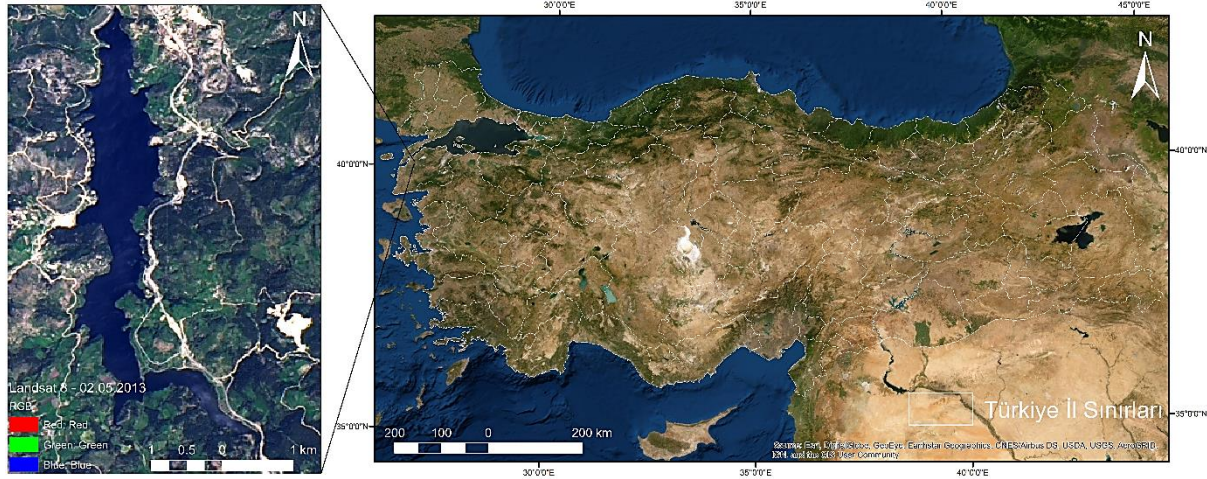

Figure 1: Study area.

Table 1: List of used images and difference from in-situ measurement day of image acquisition date.

No	Image Acquisition Date	Path/Row	Difference from In-situ Measurement Day
1	02.05.2013	181/32	1
2	30.09.2013	182/32	1
3	02.07.2015	182/32	1
4	02.06.2016	182/32	1
5	01.10.2016	181/32	0
6	02.11.2016	181/32	1
7	02.04.2017	182/32	1
8	30.06.2017	181/32	1
9	02.09.2017	181/32	1

2.3 Remote Sensing Data and Processing

The dates and numbers of the images used were determined by considering the dates of in-situ water level measurements performed on the first day of the month. Satellite images are procured on the same day as the local data or with a maximum difference of one day. On the other hand, during the selection of the images, attention was given to ensure that the study area is not covered by fog, haze and cloud. A total of nine Landsat 8

Operational Land Imager (OLI) multitemporal satellite images over the study area between 2013 and 2017 were utilized in this study (Table 1). In the process of preprocessing the remote sensing data, 15m spatial resolution surface reflectance images were produced by using ENVI software's Quick Atmospheric Correction (QUAC) and nearest-neighbor diffusion-based (NNDiffuse) pan-sharpening algorithms.

In this study, the water body area detection capability of four methods: **(1) NDWI, (2) SVM** – a supervised classification, **(3) GEOBIA** and **(4) GEOBIA_NDWI** were investigated and these classification methods can be explained as follows:

(1) NDWI is one of the most commonly-used indices to detect water bodies, and was composed of the green (high reflectance of water) and near-infrared (NIR) (low reflectance of water) spectral bands of Landsat initially [18] and then used for different remote sensing data [22]. The results of the NDWI formula NDWI = (Green - NIR)/(Green + NIR) range from -1 and 1. In the study of McFeeters, NDWI's values greater than 0 are considered as water and values below 0 mean other land use/cover classes [18].

(2) SVM is a supervised classification algorithm based on statistical learning theory [12]. The working principle of SVM is based on the principle of defining the most appropriate decision function which can distinguish classes, in other words, defining the hyper-plane that separates the classes in the most accurate way [12, 16]. In the SVM classification, the default set of parameters (Kernel Type: Radial Basis Function, Gamma in the Kernel Function: 0.143, Penalty Parameter: 100, Pyramid Levels: 0, and Classification Probability Threshold: 0) were employed by training region of interest values of land cover classes (water, vegetation and others).

(3) The basic approach in **GEOBIA** is to create homogeneous image objects (i.e. segmentation) from image pixels with similar spectral properties/signatures and then to classify these objects by considering the spectral, statistical, texture and geometric characteristics defined for

these objects [15, 17]. In this context, the GEOBIA method of eCognition software was applied for object-based image classification. For the purpose of consistency, the same set of parameters (image layer weights: 1 for visible bands and 2 for infrared bands for better discrimination between water and other classes, scale parameter: 10, shape: 0.1 and compactness: 0.5) were utilized in segmentation process. The next stage after the segmentation is the classification of the segments, and in this study two options (methods 3 and 4) were preferred at this stage. The first is standard **GEOBIA** the implementation of the maximum likelihood classification algorithm to objects training by the samples from each land cover classes (water, vegetation and others), which is basically similar to the supervised classification [14, 27].

(4) The second approach in **GEOBIA** is to classify the objects according to the threshold values of another data set that may be bands of the satellite image from which the objects/segments are generated, or index images generated from this image [25, 28]. In the **GEOBIA_NDWI** classification, water class assignment was done according to the acceptance that the objects' NDWI values greater than 0 are considered as water.

2.4 Data Analysis

The capability of the four methods (NDWI, SVM, GEOBIA, and GEOBIA_NDWI) was examined employing root mean square error (RMSE) and Pearson's correlation coefficients (R) to correlate the computed data from remote sensing methods with validation data (i.e. field data).

3. RESULTS AND DISCUSSION

NDWI, SVM, GEOBIA, and GEOBIA_NDWI methods' water body detection performances were investigated to examine the superiority between the pixel-based and the object-based classification, the superiority between the NDWI and the image classification methods and the contribution of the NDWI to the object-based classification.

The in-situ values showed that the lake generally reaches its largest and narrowest limits at the end of the rainy (between September and May) and the dry (between June and August) periods, respectively. According to the used data set, the average lake area value is 2.917 km^2 and standard deviation is 0.546 km^2 (Table 2). The lake area was narrowest on November 02, 2016 with 2.156 km^2 (Figure 2). Under normal conditions, November is in the rainy season, however the main reason why

the lake is narrowest on November 02, 2016 was the precipitation in September and October declined by 92% compared to the long-term average data that was a severe meteorological drought. On the other hand, the second reason of lack of water in lake area was agricultural irrigation in September. On the other side, although it was not the end of the rainy season, the lake reached its largest area on May 2, 2013 with 3.692 km^2 (Figure 2). The extreme precipitation in January, February and April being almost twice the long-term average is the main reason of this early formation before the end of the rainy season. In addition, although July 2, 2017 was in the dry period, 3.434 km^2 of lake area was formed, and the biggest reason for this is excessive precipitation (65 mm) that is more than twice the long-term average precipitation occurred in June 2017.

Table 2: Average, standard deviation, RMSE and average of deleted mixed pixels out of the lake area values of NDWI, SVM, GEOBIA and GEOBIA_NDWI (NDWI supported GEOBIA).

	NDWI	SVM	GEOBIA	GEOBIA_NDWI	In-situ Measurement
Average lake areas (km^2)	2.908	3.068	3.050	2.939	2.917
Standard Deviation (km^2)	0.490	0.631	0.654	0.507	0.546
RMSE (km^2)	0.067	0.177	0.179	0.083	-
Average of deleted mixed pixels out of the lake area (km^2)	0.010	0.037	0.032	0.010	-

All water body extraction methods produced minimum and maximum values on the same dates as in-situ lake measurements. When the average of the lake area values produced by the methods is examined, it is determined that the average of the lake area values produced by NDWI is the closest to the in-situ measurement values (Table 2). The second one is GEOBIA_NDWI and the worst is SVM. According to standard deviation value of the

results the closest method to the in-situ values is GEOBIA_NDWI, the second is NDWI and the worst GEOBIA. In addition, the best results for the RMSE values are NDWI, followed by GEOBIA_NDWI, SVM and GEOBIA from low RMSE to high. On the other hand, pixels or objects remaining outside the lake area and mixed with other land use/cover classes were determined and deleted manually. Table 2 shows the mean of the

deleted mixed pixel areas (i.e. assignment of water to non-water classes) resulting from the application of each method. The results show that NDWI and GEOBIA_NDWI methods produced the least mixed pixels. While the maximum mixing with other classes was occurred by SVM, there is only 0.25 km^2 difference between the best and worst method. Each data set from investigated four methods have a high positive correlation over 0.990 with the data set composed of in-situ measured area values, and only 0.007 difference is available between the lowest (GEOBIA_NDWI) and highest (NDWI and SVM) correlation values (Figure 3). As a result of the evaluations, a scoring was performed using RMSE, deleted mixed areas and correlations. The methods generated smaller RMSE and mixed area were evaluated as more successful. On the other hand, for positive correlation, the greater the correlation value means that the R value is close to 1, i.e. the lower the value of 1 minus R (1 - R), the higher the correlation.

When the simple evaluation equation = (RMSE + Deleted Mixed Pixels + (1 - R)) was applied, success ranking of the methods is as follows: NDWI > GEOBIA_NDWI > GEOBIA > SVM.

Additionally, it was determined that the borders of the lake area could be determined more successfully with NDWI that use the advantage of high reflectance in visible and low reflectance in near infrared of water. Due to the positive effect of NDWI, GEOBIA_NDWI was found to be second. However, mixing with classes in contact with water at the boundary line was found to be less with GEOBIA compared to SVM. Although all the methods tested in this study produced reasonable results, the results produced with NDWI were superior to others. When all findings were evaluated together, it was concluded that all the methods tested in this study produce reasonable results, but the results produced with NDWI are superior to others.
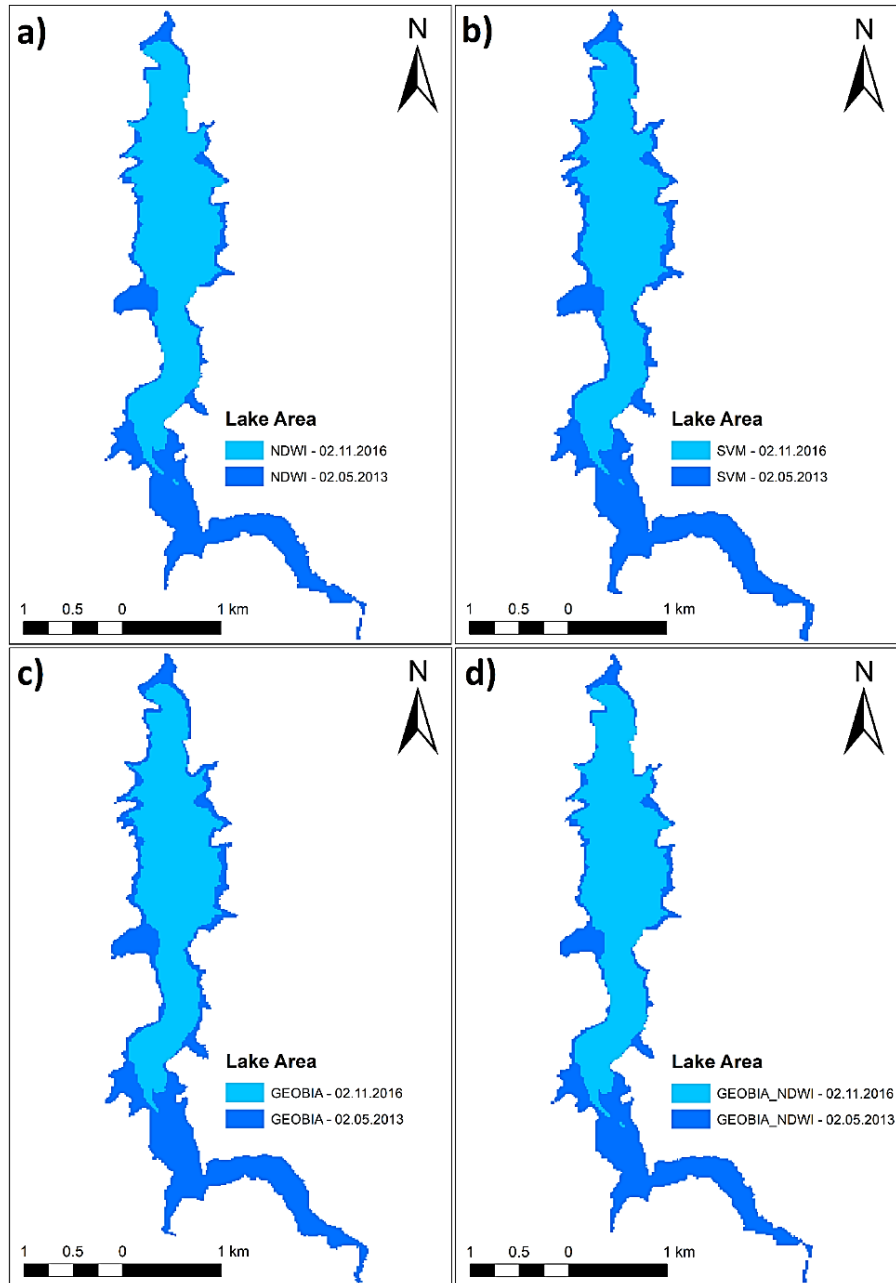
Figure 2: Lake area results from 02.05.2013 (maximum) and 02.11.2016 (minimum): a) NDWI, b) SVM, c) GEOBIA and d) GEOBIA_NDWI (NDWI supported GEOBIA).
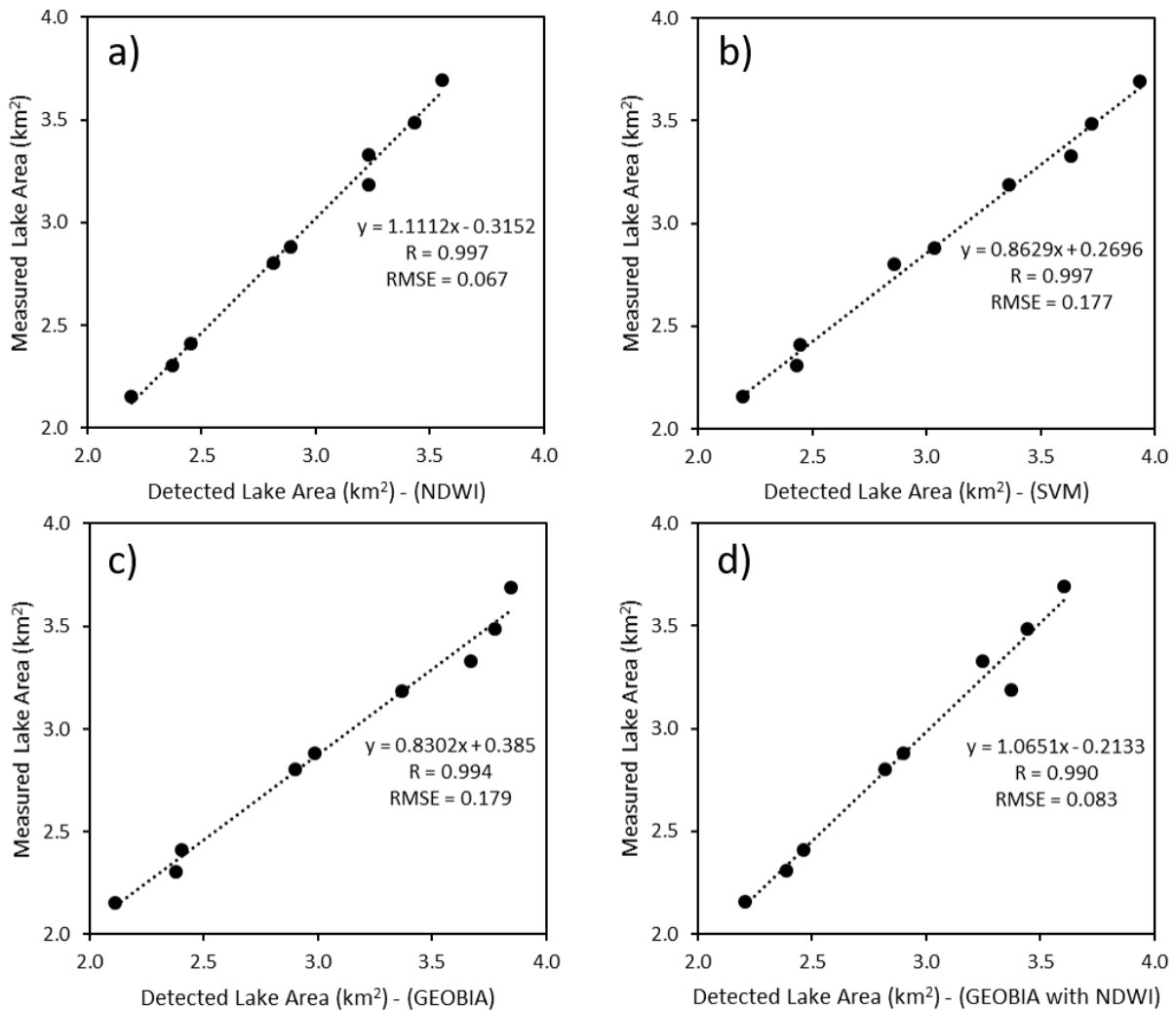
Figure 3: Correlations between in-situ and investigated methods' values: a) NDWI, b) SVM, c) GEOBIA and d) GEOBIA_NDWI (NDWI supported GEOBIA).

4. CONCLUSION

Increasing of human population, decreasing of sources, global warming and climate change are all the vital problems that cause most vital problem lack of water. Water resource management must be the most prominent issue today and future especially for arid and semi-arid climate regions. In this context, satellite technologies and remote sensing methods, which allow time- and cost-effective analyze of wide areas, should be used in the most efficient way in water resources management.

In this study, the capability of the four remote sensing methods (NDWI, SVM, GEOBIA and GEOBIA_NDWI) was examined for water body extraction. By using these four methods, the superiority between the pixel-based and the object-based classification, the superiority between the NDWI and the image classification methods and the contribution of the NDWI to the object-based classification were tested. The main findings of this study can be listed as follows:

- Meteorological factors and irrigation were found to be effective in lake area variations.

- Sophisticated image classification methods tested in this study rely on human expertise and contain high computation, but simple NDWI water index could detect water bodies more accurate, faster and easier than others.

- NDWI allowed for better identification of the lake boundary and a better separation of the land cover classes adjacent to water at the border.

- The object-based classification was better than the pixel-based classification for distinguishing water and other land cover classes adjacent to border.

- GEOBIA supported by NDWI (GEOBIA_NDWI) produced better results than the standard object-based classification.

- Deleted mixed pixels out of the lake area was determined less in the results of NDWI and GEOBIA_NDWI.

This study demonstrates the role and importance of remote sensing in natural resources management, and specifically the results clearly show that the practical, easy and fast NDWI water index, which is created according to the spectral features of water, provides great advantages in the management of water resources. Future research will include more classification methods, different parameter values of the classification methods and the effect of other meteorological parameters such as evaporation on the water body change.

REFERENCES

[1] Demirel K. and Kavdır Y., Effect of Soil Water Retention Barriers on Turfgrass Growth and Soil Water Content, Irrigation Science, 31-4 (2013) 689-700.

[2] Genç L., Demirel K., Çamoglu G., Asık S. and Smith S. Determination of plant water stress using spectral reflectance measurements in watermelon (citrullus vulgaris), American-Eurasian Journal of Agricultural & Environmental Sciences, 11-2 (2011) 296-304.

[3] Çamoğlu G., Demirel K., Genc L. Use of infrared thermography and hyperspectral data to detect effects of water stress on pepper, Quantitative InfraRed Thermography Journal, 15-1 (2018) 81-94.

[4] Özelkan E. and Karaman M., The Analysis of the Effect of Meteorological and Hydrological Drought on Dam Lake via Multitemporal Satellite Images: A Case Study in Atikhisar Dam Lake (Çanakkale), Omer Halisdemir University Journal of Engineering Sciences, 7-2 (2018) 1023-1037.

[5] Karaman M., Budakoglu M., Uca Avci Z.D., Özelkan E., Bülbül A., Civas M. and Tasdelen S., Determination of Seasonal Changes in Wetlands Using CHRIS/Proba Hyperspectral Satellite Images: A Case Study from Acigöl (Denizli), Turkey, Journal of Environmental Biology, 36 (2015) 73-83.

[6] Liu Z., Yao Z. and Wang R., Assessing Methods of Identifying Open Water Bodies Using Landsat 8 OLI Imagery, Environmental Earth Sciences, 75-10 (2016) 1-13.

[7] Karaman M., Özelkan E. and Tasdelen S., Influence of Basin Hydrogeology in the Detectability of Narrow Rivers by Sentinel2-A Satellite Images: A Case Study in Karamenderes (Çanakkale), Journal of Natural Hazards and Environment, 4 (2018) 140-155.

[8] Ji L., Zhang L. and Wylie B., Analysis of Dynamic Thresholds for the Normalized Difference Water Index, Photogrammetric Engineering & Remote Sensing, 75-11 (2009) 1307–1317.

[9] Du Z., Li W., Zhou D., Tian L., Ling F., Wang H., Gui Y. and Sun B., Analysis of Landsat-8 OLI Imagery for Land Surface Water Mapping, Remote Sensing Letters, 5-7 (2014) 672-681.

[10] Gürsoy Ö., Atun R. Investigating surface water pollution by integrated remotely sensed and field spectral measurement data: A case study, Polish Journal of Environmental Studies, 28-4 (2019) 2139-2144.

[11] Gürsoy Ö., Birdal A., Özyonar F., Kasaka E. Determining and monitoring the water quality of Kizilirmak River of Turkey: First results, ISPRS - International Archives of the Photogrammetry, Remote Sensing and Spatial Information Sciences, XL-7/W3 (2015) 1469-1474.

[12] Kavzoğlu T. and Çölkesen İ., Destek Vektör Makineleri ile Uydu Görüntülerinin Sınıflandırılmasında Kernel Fonksiyonlarının Etkilerinin İncelenmesi, Harita Dergisi, 144 (2010) 73-82.

[13] Gürsoy Ö and Altun R., Comparison of Spectral Classification Methods in Water Quality, Cumhuriyet Science Journal, 39-2 (2018) 543-549.

[14] Kalkan K. and Maktav D., Nesne Tabanlı ve Piksel Tabanlı Sınıflandırma Yöntemlerinin Karşılaştırılması (IKONOS Örneği). In: III. Uzaktan Algılama ve Coğrafi Bilgi Sistemleri Sempozyumu, 12-15 October, Gebze – Kocaeli, Türkiye, 2010.

[15] Belgiu M. and Drăguţ L., Comparing Supervised and Unsupervised Multiresolution Segmentation Approaches for Extracting Buildings from Very High Resolution Imagery, ISPRS Journal of Photogrammetry and Remote Sensing, 96 (2014) 67-75.

[16] Çölkesen İ., Yomralıoğlu T. and Kavzoğlu T., Obje Tabanlı Sınıflandırmada Bölgeleme Esasına Dayalı Ölçek Parametresi Tespiti: WorldView-2 Uydu Görüntüsü Örneği, Harita Dergisi., 154, (2015) 9-18.

[17] Blaschke T., Object Based Image Analysis for Remote Sensing, ISPRS Journal of Photogrammetry and Remote Sensing, 65 (2010) 2–16.

[18] McFeeters S.K., The Use of Normalized Difference Water Index (NDWI) in the Delineation of Open Water Features, International Journal of Remote Sensing, 17 (1996) 1425–1432.

[19] Xu H., Modification of Normalised Difference Water Index (NDWI) to Enhance Open Water Features in Remotely Sensed Imagery, International Journal of Remote Sensing, 27-14 (2006) 3025-3033.

[20] Pôssa E.M. and Maillard P., Precise Delineation of Small Water Bodies from Sentinel-1 Data using Support Vector Machine Classification, Canadian Journal of Remote Sensing, 44-3 (2018) 179-190.

[21] Uca Avci Z.D., Karaman M., Ozelkan E., Kumral M., Budakoglu M., OBIA Based Hierarchical Image Classification for Industrial Lake Water, Science of the Total Environment, 487 (2014) 565-573.

[22] Karaman M., Budakoglu M., Uca Avci D.U., Ozelkan E., Bulbul A., Civas M., Tasdelen S., Determination of Seasonal Changes in Wetlands Using CHRIS/Proba Hyperspectral Satellite Images: A Case Study from Acigöl (Denizli), Turkey, Journal of Environmental Biology, 36-1 (2015) 73.

[23] Korzeniowska K. and Korup O., Object-Based Detection of Lakes Prone to Seasonal Ice Cover on the Tibetan Plateau, Remote Sensing, 9-4 (2017) 339.

[24] Olmanson L.G. and Bauer M.E., Land cover Classification of the Lake of the Woods/Rainy River Basin by Object-Based Image Analysis of Landsat and Lidar Data, Lake and Reservoir Management, 33-4 (2017) 335-346.

[25] Kaplan G. and Avdan U., Object-based Water Body Extraction Model Using Sentinel-2 Satellite Imagery, European Journal of Remote Sensing, 50-1 (2017) 137-143.

[26] Şensoy S., Demircan M., Ulupınar Y. and Balta Z., Türkiye İklimi, Turkish State Meteorological Service Report. URL: https://www.mgm.gov.tr/FILES/genel/makal

e/13_turkiye_iklimi.pdf Retrieved February 10, 2019.

[27] Chen G., Özelkan E., Singh K.K., Zhou J., Brown M.R. and Meentemeyer R.K., Uncertainties in Mapping Forest Carbon in Urban Ecosystems, Journal of Environmental Management, 187 (2017) 229-238.

[28] Özelkan E., Sağlık A., Sümer S.K., Bedir M. and Kelkit A., Kentleşmenin Tarım Alanları Üzerine Etkisinin Uzaktan Algılama ile İncelenmesi–Çanakkale Örneği, Çanakkale Onsekiz Mart Üniversitesi Ziraat Fakültesi Dergisi, 6 (2018) 123-134.

The Oxidation of 4-(4-Formylphenoxy) Phthalonitrile to 4-(4-Carboxylphenoxy) Phthalonitrile at Ambient Conditions

Pinar SEN [1], ⓘD *, Güneş DEMİRTAŞ [2]* ⓘD *, Necmi DENGE [2]* ⓘD *, Davut AVCI [3]* ⓘD *, Salih Zeki YİLDİZ [4]* ⓘD

[1] *Centre for Nanotechnology Innovation, Department of Chemistry, Rhodes University, Grahamstown, 6140, South Africa*
[2] *Ondokuz Mayıs University, Faculty of Arts and Sciences, Department of Physics, 55139 Samsun, Turkey*
[3] *Sakarya University, Faculty of Arts and Sciences, Department of Physics, 54187, Serdivan, Sakarya, Turkey*
[4] *Sakarya University, Faculty of Arts and Sciences, Department of Chemistry, 54187, Sakarya, Turkey*

Abstract. The substituted phthalonitriles have been used to prepare soluble phthalocyanine species in recent years. One of the most used phthalonitrile derivatives for the target product is 4-nitrophthalonitrile. In this study 4-(4-formylphenoxy) phthalonitrile was prepared as the substituted phthalonitrile derivative by the nucleophilic substitution reaction of para-hydroxybenzaldehyde with 4-nitrophthalonitrile. During the crystallization of the product by slow evaporation technique, it readily self-oxidized to 4-(4-carboxylphenoxy) phthalonitrile at ambient condition open to air. The crystal structure of the molecule was determined by XRD technique. The molecule crystalizes at triclinic space group P-1 and the unit cell parameters of crystal are a=6.3591 (10) Å, b=7.5464 (11) Å, c=13.819 (2) Å, α=88.434 (11)°, β=87.942 (12)°, γ=80.111 (12)° and Z=2. The crystal structure has intermolecular O—H···O, C—H···N and C—H···O hydrogen bonds. In addition to these hydrogen bonds, C—N···Cg and Cg···Cg interactions are present between molecules. In the crystal, intermolecular O—H···O hydrogen bonds occur between molecular units in a dimeric molecular form. Molecular structure, vibrational frequencies and ^{1}H and ^{13}C NMR chemical shifts of the target compound have been calculated by using B3LYP method with 6-311++G(d, p) basis set, as well.

Keywords: Substituted phthalonitrile, Crystal structure, Oxidation, Theoretical calculation.

4- (4-formilfenoksi) ftalonitrilin 4- (4-karboksilfenoksi) ftalonitril'e Ortam Koşullarında Oksidasyonu

Özet. Sübstitüe ftalonitriller, son yıllarda çözünür ftalosiyanin türlerini hazırlamak için kullanılmaktadır. Hedef ürün için en çok kullanılan ftalonitril türevlerinden biri, 4-nitroftalonitrildir. Bu çalışmada, 4-(4-formilfenoksi) ftalonitril, para-hidroksibenzaldehidin 4-nitroftalonitril ile nükleofilik yerdeğiştirme reaksiyonu ile sübstitüe ftalonitril türevi olarak hazırlanmıştır. Ürün yavaş buharlaştırma tekniği ile kristallendirilmesi sırasında, havaya açık ortam koşullarında, 4- (4-karboksilfenoksi) ftalonitril'e kendiliğinden oksitlenmiştir. Molekülün kristal yapısı XRD tekniği ile belirlendi. Molekül, triklinik uzay grubu P-1'de kristallenmiştir ve kristalin birim hücre parametreleri a = 6.3591 (10) Å, b = 7.5464 (11) Å, c = 13.819 (2) Å, a = 88.434 (11) °, 87 = 87.942 (12) °, γ = 80.111 (12) ° ve Z = 2' dir. Kristal yapı moleküllerarası O — H ··· O, C — H ··· N ve C — H ··· O hidrojen bağlarına sahiptir. Bu hidrojen bağlarına ek olarak, moleküller arasında C — N ··· Cg ve Cg ··· Cg etkileşimleri mevcuttur. Kristalde moleküllerarası O — H ··· O hidrojen bağları, bir dimerik yapı içinde moleküler birimler arasında meydana gelir. Hedef bileşiğin, moleküler yapısı, titreşim frekansları ve ^{1}H ve ^{13}C NMR kimyasal kaymaları da 6-311 ++ G (d, p) temel seti ile B3LYP metodu kullanılarak hesaplanmıştır.

Anahtar Kelimeler: Sübstitüe ftalonitril, Kristal yapı, oksidasyon, teorik hesaplama.

---

* Corresponding author. *Email address: sen_pinar@hotmail.com*

1.   INTRODUCTION

Phthalonitriles are known a starting material in the synthesis of symmetrically and unsymmetrically phthalocyanines [1]. Substituted phthalonitriles are the most important phthalocyanine precursors due to the substituent effect on the phthalocyanine properties. Synthesis of phthalonitriles carrying functional groups leads to functionalized phthalocyanines which are of great importance for the targeted applications such as catalysis [2], liquid crystals [3], photosensitizers for PDT [4], non-linear optics [5], nanotechnology [6] and dye-sensitized solar cell [7]. Tetra-substituted phthalocyanines are generally obtained from mono-substituted phthalonitriles [8].

Phthalocyanines (Pcs) carrying purposive groups such as carboxyl, amines and hydroxyl groups are attractive target for chemists due to phthalocyanine-based multicomponent systems as new molecular materials [9-12].

Schif bases are one of the parts of used chelate compounds for the advancement of coordination chemistry since it could generate complexes with most transitions metals. The imine formation *via* aldehyde groups is a complementary system with excellent building block potential for further applications. It is very important to produce Pcs containing the aldehyde group from the corresponding phthalonitrile since they may carry out further chemical reactions on the macrocycle rings to prepare Schiff's base metal complex substituted phthalocyanines. Therefore, we have recently described a model study; the synthesis, characterization and fluorescence properties of two salicyhydrazon Zn complexes substituted zinc-phthalocyanine as a new functionalized material. It was obtained the reaction of the metal salt with imine group achieved from aldehyde group on Pc [13].

In this study, we have presented the self-oxidation of 4-(4-formylphenoxy) phthalonitrile to 4-(4-carboxylphenoxy) phthalonitrile which was observed during the experimental procedure. The synthesis and characterization of 4-(4-formylphenoxy) phthalonitrile have been performed to prepare an alternative starting material for the synthesis of different aldehyde substituted phthalonitriles. During the crystallization process of the aldehyde substituted phenoxy phthalonitrile prepared as the starting material, it was determined that the target product self-oxidized to the acid form by air oxygen at ambient condition. So the obtained results were decided to present. The structural crystallographic characterization of oxidized form is studied. The theoretical calculations were also performed for both the aldehyde and acidic forms.

2.   EXPERIMENTAL AND THEORETICAL PROCEDURE

2.1. Materials and measurements

4-Hydroxybenzaldehyde, deutorated chloroform, dimethylformamide (DMF), dichloromethane (DCM), hexane and chloroform were obtained from Sigma-Aldrich. The drying and cleaning of all solvents were performed as determined by Perrin and Armarego [14]. The reported literature was followed for the preparation of 4-nitrophthalonitrile [15]. Thin-Layer chromatography (TLC) containing silica gel 60 HF$_{254}$ as an adsorbent was used to check the progress of the reaction. Column chromatography with silica gel (Merck grade 60) was applied to provide the purification. Melting points (m.p.) were found out with the Barnstad-Electrotermel 9200. Infrared spectra were obtained by using Perkin Elmer Spectrum two FT-IR spectrophotometer existed with Perkin Elmer UATR-TWO diamond ATR. ^{1}H ve ^{13}C NMR spectra were gained with Varian Mercury Plus 300 MHz spectrometer.

2.2. Computational Details

The ground state geometry of 4-(4-formylphenoxy)phthalonitrile was taken into account by using density functional theory (DFT) with B3LYP (Becke's three-parameter hybrid functional using the LYP correlation functional) at 6-311++G(d,p) level [16,17]. In this work, Gaussian 09W program package [17] and Gauss-View molecular visualization program [18] were used to find out the optimized geometry of the structure, IR spectra, ^{1}H and ^{13}C NMR chemical

shifts of 4-(4-formylphenoxy) phthalonitrile. Furthermore, the theoretical harmonic vibrations of the molecule were scaled by 0.9608 and these frequencies were compared with the experimental results.

2.3. Synthesis

2.3.1. 4-(4-formylphenoxy)phthalonitrile, 1

The expected compound (**1**) was obtained as a cream colored powder according to published procedure [19]. The purification of the compound was achieved with the column chromatography on silica-gel by using chloroform as mobile phase. Yield 1.3 g, 90.0 %. m.p: 154 °C. FT-IR (PIKE MIRacle™ ATR) ν max/cm^{-1}: 3104-3043 (Ar,C-H), 2858, 2746 (Aldehyde C-H), 2238 (C≡N), 1691 (C=O), 1606-1502 (Ar, C=C), 1489-1309 (Ar C-C), 1255 (Ar-O-Ar), 1209, 1155, 1111, 1087, 950, 858, 839, 821. ^{1}H-NMR (CDCl$_3$) δ (ppm) : 10.03 (s, 1H), 8.01 (d, 2H), 7.81 (d, 1H), 7.40 (d, 1H), 7.35(d, 1H), 7.23 (d, 2H). ^{13}C-NMR (CDCl$_3$) δ (ppm): 190.68, 160.34, 159.10, 135.94, 134.09, 132.64, 123.03, 122.89, 120.59, 118.21, 115.32, 114.90, 110.56.

2.3.2. 4-(4-carboxylphenoxy)phthalonitrile, 2

4-(4-formylphenoxy)phthalonitrile (1) was attempted to crystallize in chloroform by slow evaporation technique to obtain single-crystal. Single-crystal X-ray studies showed that during the crystallization of this compound, it oxidized to 4-(4-carboxylphenoxy) phthalonitrile by exposing the air oxygen at ambient condition. FT-IR (PIKE MIRacleTM ATR) □ max/cm-1: 3400-2552 (O-H), 3087-3039 (Ar,C-H), 2231 (C≡N), 1673 (C=O), 1603-1503 (Ar, C=C), 1487-1421 (Ar C-C), 1250 (Ar-O-Ar), 1210, 951, 845.1H-NMR (CDCl3) δ (ppm): 8.15 (d, 1H), 8.02 (d, 1H), 7.93 (s, 1H), 7.54 (d 1H), 7.25 (d, 2H).13C-NMR (CDCl3) δ (ppm): 224.16, 167.25, 162.14, 134.42, 130.13, 123.54, 122.53, 120.50, 117.27, 115.78, 114.58, 113.82, 108.27.

2.4. X-Ray Crystal Structure Determination

Single crystal X-ray data were picked up with a Stoe IPDS II [20] single crystal diffractometer at 296 K and were used monochromated MoK$_\alpha$ radiation. Cell refinement and data reduction were performed with X-AREA [20] and X-RED [20] programs. It was used SHELXS-97 [21] program to solve structure and SHELXL-97 [21] program to refine structure. ORTEP-3 for Windows [22] to obtain figures, WinGX [23] and PLATON [24] software to prepare material for publication were used.

All hydrogen atoms were positioned geometrically (C-H=0.930 Å, O-H=0.820 Å) and treated as riding with U$_{iso}$(H)=1.2U$_{eq}$(C), U$_{iso}$(H)=1.5U$_{eq}$(O). The crystal data and refinement of the compound **2** are shown in Table 1.

Table 1. Crystal data and structure refinements of the title compound

Formula	C$_{15}$H$_8$N$_2$O$_3$
Crystal System	Triclinic
Color / Shape	Colorless / Plate
Crystal size	0.64×0.29×0.05 mm
Temperature	296 K
Space Group	P-1
Unit Cell Dimensions	
a	6.3591 (10) Å
b	7.5464 (11) Å
c	13.819 (2)Å
α	88.434 (11)°
β	87.942 (12)°
γ	80.111 (12)°
h / k / l	-7, 7 / -9, 9 / -17, 17
Volume	652.70 (17) Å^3
Z	2
Density (calculated)	1.344 mg/m^3
Radiation	MoKα (λ=0.71073 Å)
Absorption coefficient (*μ*)	0.10 mm^{-1}
Absorption correction	Integration X-RED
F(000)	272
θ Ranges	2.7° / 26.5°
Observed reflections, I>2σ(I)	721
Independent Reflections	1460 (Rint=0.100)
Measured Reflections	5818
Data / Restrains / Parameters	1463 / 0 / 182
Maximum shift / error	0.00
S	1.04
Final R indices [I>2σ(I)]	R1=0.055, *w*R(*F*^{2})=0.111
Largest diff. Peak and hole	0.09 eÅ^{-3}, -0.11 eÅ^{-3}

3. RESULT AND DISCUSSION

3.1. Synthesis and Spectroscopic Characterization

The synthetic pathway to obtain 4-(4-carboxylphenoxy) phthalonitrile can be presented as seen in Scheme 1.
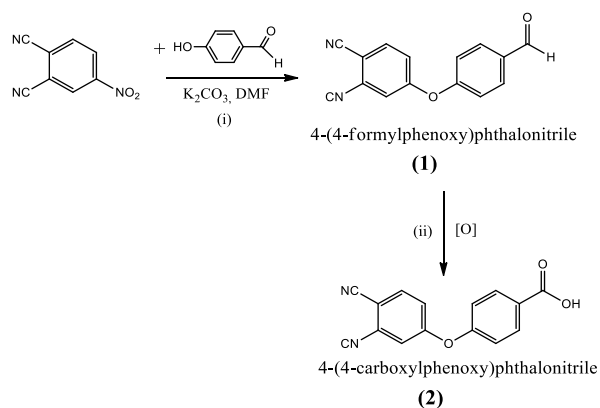
Scheme 1. *Reagent and conditions*: (i). 4-hydroxybenzaldehyde, DMF, K_2CO_3, (90%); (ii) in air at room temperature

The 4-(4-formylphenoxy)phthalonitrile (**1**) was obtained as powder from the reaction of 4-hydroxybenzaldehyde and 4-nitrophthalonitrile in presence of K_2CO_3 in DMF by keeping on stirring at ambient temperature for 24h. 4-(4-carboxylphenoxy)phthalonitrile (**2**) was obtained with the oxidation of 4-(4-formylphenoxy) phthalonitrile at ambient condition by air during the slow evaporation crystallization process of compound **1**.

The verification of the obtained products was provided by spectroscopic methods including ^{1}H NMR, ^{13}C NMR, FT-IR, and melting point. All spectral data confirm the proposed structures.

When the results of **1** to p-hydroxybenzaldehyde are compared, the replacement of the –OH peak with new bands at 1691 cm^{-1}, 1255 cm^{-1}, and 2237 cm^{-1}, belonging to the -C=O, Ar-O-Ar and -C≡N vibrations respectively clearly indicate the formation of **1**. The aldehyde C-H vibrations were detected as the Fermi resonance in between 2858 cm^{-1} and 2746 cm^1 at the FT-IR spectrum of **1**, supporting this event, as well.

In the FT-IR spectrum of **2**, the oxidation of **1** was confirmed by the shifting of C=O stretching vibration from 1691 cm^{-1} to 1673 cm^{-1} due to resonance of carboxyl group with the phenyl ring and the C=O band was calculated at: 1746 cm^{-1} using B3LYP method with 6-311++G(d, p) basis set. The O-H vibration appeared at 3400-2552 cm^{-1} as the broad and distorted typical organic acid vibrations due to the strong inter and intramolecular hydrogen bond formation, and the O-H vibration bands were calculated at; 3662 cm^{-1} using B3LYP method with 6-311++G(d, p) basis set. Furthermore, the disappearances of bands at 2858-2746 cm^{-1} region, which are arised from the Fermi resonance, confirm the conversion of the aldehyde group, as well. The shifting of the significant C≡N vibration of **1** at 2239 cm^{-1} to 2231 cm^{-1} for **2** supports the proposed conversion as shown in Fig. 1. The aromatic C-H vibrations of both molecules are also appeared at different wavelengths at 3104-3043 cm^{-1} for **1** and at 3087-3039 cm^{-1} for **2,** as expected. The C-H vibration bands were calculated at; 3216-3195 cm^{-1} for **2** using B3LYP method with 6-311++G(d, p) basis set.
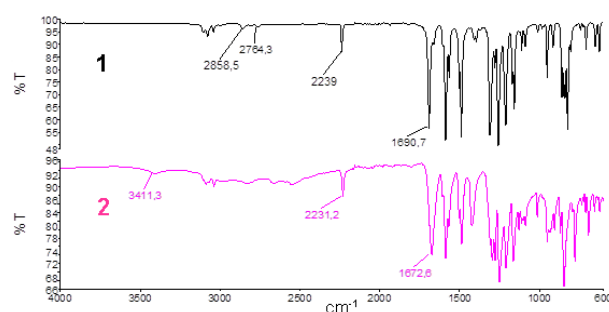

Figure 1. FT-IR spectra of **1** and **2**

The ^{1}H NMR and ^{13}C NMR data gave satisfactory information about the obtained molecules *via* the proposed conversions. In the ^{1}H NMR spectra of **1**, the disappearances of OH peak of p-hydroxybenzaldehyde and the appearance of new peaks in aromatic region (8.01-7.23 ppm) are the proof for the formation of **1**. The aldehyde proton signal was predicted as 10.03 ppm which was different from the starting material. Also in this study, the aldehyde proton signal and the aromatic region were calculated as 10.05 ppm and 7.77-

7.01 ppm respectively at the ^{1}H NMR spectrum of **1** using B3LYP method with 6-311++G(d, p) basis set. In the ^{13}C NMR spectrum of **1** the appearance of the signal at 115.32 and 114.90 ppm (that calculated at; 119.02 and118.74 ppm using DFT) belonging to the nitrile carbon atom is the clearly different from p-hydroxy benzaldehyde.

In the ^{1}H NMR spectra of **2**, the expected O-H proton of carboxylic acid group was not observed in the region. It has shifted strongly to the upper field and disappeared which was the evidence of the strong hydrogen bond formation between the acid molecules which caused to dimeric molecular form determined by the crystallographic studies. The other signals belonging to the acid form (**2**) were determined in the aromatic region which was totally different from the aldehyde form (**1**). In the ^{13}C NMR spectra of **2**, the expected carbon signal of carboxylic acid group was observed at 224.16 ppm which differs from compound **1**.

In this study, the total energy of the molecules (**1**) and (**2**) were calculated as -836.54 and -911.80 a.u. respectively using B3LYP method with 6-311++G(d, p) basis set. According to the above results it can be said that molecule **2** is more stable from molecule **1** which obviously illustrates why the aldehyde form of the prepared molecules (**1**) easily self-oxidize the acid form (**2**) by air oxygen during the crystallization process.

3.2. Synthesis and Spectroscopic Characterization

The asymmetric unit of the title compound is given in the Fig. 2. The molecule has two cyano groups and the triple C—N bond distances belong to these groups are 1.138 (6) Å for C1—N2 and .147 (6) Å for C8—N1.These bond distances were calculated 1.155 Å for C1—N2 and 1.154 Å for C8—N1. These triple C—N bond distances agree with the literature [25, 26]. The N2—C1—C2 and N1—C8—C7 bond angles are 178.7 (6)° and 179.0 (5)° and these angles were calculated at; 178.4° and 178.3° respectively. These bond angles deviate a small amount from linearity, because of the intermolecular hydrogen bonds. The C—C aromatic bond distances range from 1.411 (5) Å to

1.368 (6) Å. Two aromatic rings are present in the molecule and these rings are almost planar (r.m.s. deviations are 0.0061 Å for C2/C7, 0.0035 Å for C9/C14) and dihedral angle between these rings is 67.19 (15)°. The aromatic rings are linked *via* oxygen atom and C5—O3—C11 bond angle is 119.3 (4)°. Some selected bond distances, bond angles and torsion angles are given in Table 2.
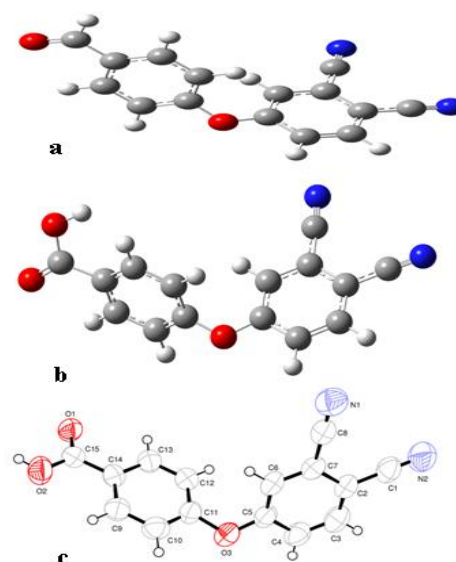

Figure 2. (a) Optimized molecular structure (with B3LYP/6-311++G(d,p) level) of acid form (**2**), (b) Optimized molecular structure (with B3LYP/6-311++G(d,p) level) of aldehyde form (**1**), (c) The experimental geometric structure of the title compound.
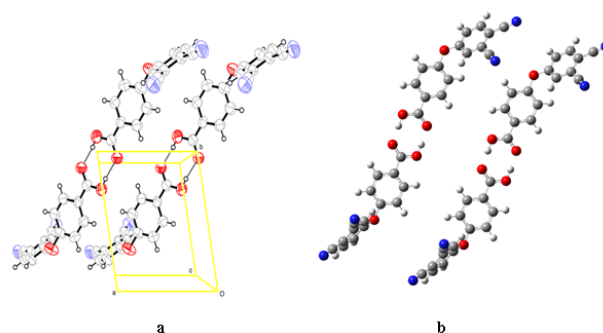

Figure 3. (a) Experimental and (b) theoretical dimer structure of the title compound

Table 2. Some selected bond distances, bond angles and torsion angles of the title compound (Å, °)

Atoms	Experimental	B3LYP	Atoms	Experimental	B3LYP
C1—N2	1.138 (6)	1.155	C8—N1	1.147 (6)	1.154
O1—C15	1.249 (5)	1.200	O2—C15	1.299 (5)	1.359
O3—C5	1.373 (5)	1.367	O3—C11	1.398 (6)	1.387
N1—C8—C7	179.0 (5)	178.3	N2—C1—C2	178.7 (6)	178.4
O1—C15—O2	121.0 (5)	119.9	C5—O3—C11	119.3 (4)	121.2
O1—C15—C14	122.5 (5)	123.1			
C6—C7—C8—N1	−107 (31)	105.651	N2—C1—C2—C3	41 (24)	42.295
C13—C14—C15—O1	4.0 (7)	4.101			

Table 3. Hydrogen-bond geometry (Å,°)

D—$H \cdots A$	D—H	$H \cdots A$	$D \cdots A$	D—$H \cdots A$
O2—H2$\cdots$O1[i]	0.82	1.82	2.632 (5)	171
C3—H3$\cdots$N2[ii]	0.93	2.55	3.477 (6)	178
C4—H4$\cdots$O1[iii]	0.93	2.57	3.475 (6)	163
C6—H6$\cdots$N1[iv]	0.93	2.53	3.450 (5)	170

Symmetry codes: (i) −x, −y+2, −z; (ii) −x+3, −y, −z+1; (iii) x+1, y−1, z; (iv) −x+1, −y+1, −z+1.

The crystal structure has intermolecular O—H$\cdots$O, C—H$\cdots$N and C—H$\cdots$O hydrogen bonds. While the carboxyl groups of the molecules establish $R_2^2(8)$ dimers *via* intermolecular O—H$\cdots$O hydrogen bonds belong to graph set notation in the crystal structure, the cyano groups of the molecules create $R_2^2(10)$ motifs *via* intermolecular C—H$\cdots$N hydrogen bonds. The C—H$\cdots$N hydrogen bonds create a hydrogen-bonded chain running parallel to the [-110] direction. The geometric parameters of O—H$\cdots$O hydrogen bond are 0.82 Å, 1.82 Å, 2.632 (5) Å and 171°. The O—H$\cdots$O hydrogen bond are calculated at; 1.014 Å, 1.608 Å, 2.622 Å and 1.039 Å, 1.608 Å, 2.2.647 Å, respectively, using B3LYP-6-311++G(d, p) basis level as seen Fig. 3. In addition to these hydrogen bonds, C—N$\cdots$Cg and Cg$\cdots$Cg interactions are present in the crystal structure. The geometric parameters of hydrogen bonds are given in Table 3.

4. CONCLUSION

We have reported the synthesis of 4-(4-formylphenoxy)phthalonitrile (**1**) as an aldehyde-substituted phthalonitrile playing a key component in the chemistry of phthalocyanine. It

is crucial to obtain phthalocyanines containing reactive functional groups in this way in order to be able to further chemical reactions on Pc macrocycles. During the crystallization process of the compound (**1**), we observed that aldehyde groups oxidized easily to carboxyl group even with air O_2. The new carboxyl phthalonitrile derivative obtained by self-oxidation of aldehyde group has been characterized by FT-IR, ^{1}H-NMR, ^{13}C-NMR. The crystal structure of the molecule (**2**) was determined by XRD technique and also, theoretical calculations were performed. X-ray diffraction data show that the crystal structure has O—H$\cdots$O, C—H$\cdots$N, C—H$\cdots$O hydrogen bonds. In addition to these hydrogen bonds, the crystal structure has also C—N$\cdots$Cg and Cg$\cdots$Cg interactions. Hydrogen bonds together with these interactions are effective in crystal packaging. The molecule (**2**) is more stable than compound (**1**) with respect to the calculated total energies of the molecules. Furthermore, all crystallographic data agree with the theoretical bond lengths, angles, dihedral angles of the compound **2**.

APPENDIX A. SUPPLEMENTARY DATA

CCDC 1041091 contains the supplementary crystallographic data for this paper. This data can

be obtained free of charge *via* https://www.ccdc.cam.ac.uk/services/structure_de posit/, or from the Cambridge Crystallographic Data Centre, 12 Union Road, Cambridge CB2 1EZ, UK; fax: (+44) 1223 336 033; or e-mail: deposit@ccdc.cam.ac.uk.

REFERENCES

[1] McKeown N.B., Phthalocyanine Materials: Synthesis, Structure and Function. United Kingdom, Cambridge, 1998.

[2] McKeown N.B. and Budd P.M., Polymers of intrinsic microporosity (PIMs): organic materials for membrane separations, heterogeneous catalysis and hydrogen storage, Chem. Soc. Rev., 35 (2006) 675-683.

[3] Van der Pol J.F., Neeleman E., Zwikker J.W., Nolte R.J.M., Drenth W., Aerths J., Visser R. and Picken S., Homologous series of liquid-crystalline metal free and copper octa-n-alkoxyphthalocyanines, J. Liq. Cryst., 6 (1989) 577-592.

[4] Bonnett R., Chemical Aspects of Photodynamic Therapy. Gordon and Breach, Sci Pub, 2000.

[5] Torre G., Vazquez P., Agullo-Lopez F. and Torres T., Role of Structural Factors in the Nonlinear Optical Properties of Phthalocyanines and Related Compounds, Chem. Rev., 104 (2004) 3723-3750.

[6] Elemans J.A.A.W., Hameren R.V., Nolte R.J.M. and Rowan A.E., Molecular Materials by Self-Assembly of Porphyrins, Phthalocyanines and Perylenes, Adv. Mater., 18 (2006) 1251-1266.

[7] Martinez-Diaz M.V., Ince M. and Torres T., Phthalocyanines: colorful macroheterocyclic sensitizers for dye-sensitized solar cells,

[8] Leznoff C.C. and Lever A.B.P., Phthalocyanines: Properties and Applications. Cambridge, 1989, 1993, 1996.

[9] Bekaroglu O., Phthalocyanines containing macrocycles, Appl. Organometal. Chem., 10 (1996) 605-622.

[10] Beall L.S., Mani N.S., White A.J.P., Williams D.J., Barrett A.G.M. and Hoffman B.M., Porphyrazines and Norphthalocyanines Bearing Nitrogen Donor Pockets: Metal Sensor Properties, J. Org. Chem., 63 (1998) 5806-5817.

[11] Camur M. and Bulut M., Phthalocyanines prepared from 4-chloro-/4-hexylthio-5-(4-phenyloxyacetic acid)phthalonitriles and functionalization of the related phthalocyanines with hydroxymethylferrocene, J. Organomet. Chem., 695 (2010) 45-52.

[12] Akkurt B. and Hamuryudan E., Enhancement of solubility *via* esterification: Synthesis and characterization of octakis (ester)-substituted phthalocyanines, Dyes and Pigments, 79 (2008) 153-158.

[13] Sen P., Yildiz S.Z., Tuna M. and Canlica M., Preparation of aldehyde substituted phthalocyanines with improved yield and their use for Schiff base metal complex formation, J. Organomet. Chem., 769 (2014) 38-45.

[14] Perrin D.D., Armarego W.L.F. and Perrin D.R., Purification of Laboratory Chemicals. New York, Pergamon Press, 1985.

[15] Young J.G. and Onnebuagu W., Synthesis and characterization of di-disubstituted phthalocyanines, J. Org. Chem., 55 (1990) 2155-2159.

[16] Becke A.D., Density-functional thermochemistry. III. The role of exact exchange, J. Chem. Phys., 98 (1993) 5648.

[17] Lee C., Yang W. and Parr R.G., Development of the Colle-Salvetti correlation-energy formula into a functional of the electron density, Phys. Rev. B, 37 (1988) 785-789.

[18] Gaussian 09, Revision A.1, Frisch M.J., Trucks G.W., Schlegel H.B., Scuseria G.E., Robb

M.A., Cheeseman J.R., Scalmani G., Barone V., Mennucci B., Petersson G.A., Nakatsuji H., Caricato M., Li X., Hratchian H.P., Izmaylov A.F., Bloino J., Zheng G., Sonnenberg J.L., Hada M., Ehara M., Toyota K., Fukuda R., Hasegawa J., Ishida M., Nakajima T., Honda Y., Kitao O., Nakai H., Vreven T., Montgomery J.A., Peralta J.E., Ogliaro F., Bearpark M., Heyd J.J., Brothers E., Kudin K.N., Staroverov V.N., Kobayashi R., Normand J., Raghavachari K., Rendell A., Burant J.C., Iyengar S.S., Tomasi J., Cossi M., Rega N., Millam J.M., Klene M., Knox J.E., Cross J.B., Bakken V., Adamo C., Jaramillo J., Gomperts R., Stratmann R.E., Yazyev O., Austin A.J., Cammi R., Pomelli C., Ochterski J.W., Martin R.L., Morokuma K., Zakrzewski V.G., Voth G.A., Salvador P., Dannenberg J.J., Dapprich S., Daniels A.D., Farkas O., Foresman J.B., Ortiz J.V., Cioslowski J. and Fox D.J., Gaussian, Inc., Wallingford CT, 2009.

[19] Sen P., Atmaca G.Y., Erdoğmuş A., Dege N., Genç H., Atalay Y. and Yildiz S.Z., The synthesis, characterization, crystal structure and photophysical properties of a new meso-BODIPY substituted phthalonitrile, J. Fluoresc., 25 (2015) 1225-1234

[20] Stoe & Cie, X-AREA (Version 1.18) and X-RED32 (Version 1.04) Stoe & Cie, Darmstadt, Germany, 2002

[21] Sheldrick G.M., Crystal structure refinement with SHELXL, Acta Crystallogr. A 64 (2008) 112-122.

[22] Farrugia L.J., ORTEP-3 for Windows - a version of ORTEP-III with a Graphical User Interface (GUI), J. Appl. Cryst., 30 (1997) 565.

[23] Farrugia L.J., WinGX program features, J. Appl. Cryst., 32 (1999) 837-838.

[24] Spek A.L., Single-crystal structure validation with the program PLATON, J. Appl. Cryst., 36 (2003) 7-13.

[25] Tanak H., Köysal Y., Işık Ş., Yaman H. and Ahsen V., Experimental and computational approaches to the molecular structure of 3-(2-Mercaptopyridine) phthalonitrile, Bull. Korean Chem. Soc., 32 (2011) 673-679.

[26] Jan C.Y., Shamsudin N.B.H., Tan A.L., Young D.J., Ng S.W. and Tiekink E.R.T., 4-Nitro-phthalonitrile, Acta Cryst. E 70 (2014) 323.

Cumhuriyet Science Journal

CSJ

Hermite-Hadamard Type Inequalities For Two Times Differentiable Arithmetic-Harmonically Convex Functions

Huriye KADAKAL [iD]

Ministry of Education, Hamdi Bozbağ Anatolian High School, Giresun, TURKEY

Abstract. In this work, by using both an integral identity and the Hölder, the power-mean integral inequalities it is established several new inequalities for two times differentiable arithmetic-harmonically-convex function. Also, a few applications are given for some means of real numbers.

***Keywords*:** Convex function, Arithmetic-harmonically-convex function, Hermite-Hadamard's inequality.

İki Kez Türevlenebilen Aritmetik-Harmonik Konveks Fonksiyonlar İçin Hermite-Hadamard Tip Eşitsizlikler

Özet. Bu çalışmada, hem bir integral özdeşlik hem de Hölder ve power-mean integral eşitsizlikleri kullanılarak iki kez türevlenebilen aritmetik-harmonik konveks fonksiyonlar için birkaç yeni eşitsizlik elde edilmiştir.

***Anahtar Kelimeler*:** Konveks fonksiyon, Aritmetik-harmonik konveks fonksiyon, Hermite-Hadamard eşitsizliği.

1. INTRODUCTION

Theory of convex sets and convex functions play an important role in mathematics and the other pure and applied sciences. Convexity theory has appeared as a powerful technique to study a wide class of unrelated problems in pure and applied sciences.

Definition 1.1 A function $f: I \subseteq \mathbb{R} \to \mathbb{R}$ is said to be convex if the inequality

$$f(tx + (1 - t)y) \leq tf(x) + (1 - t)f(y)$$

valid for all $x, y \in I$ and $t \in [0,1]$. If this inequality reverses, then f is said to be concave on the interval $I \neq \varnothing$. This definition is well known in the literature.

Theorem 1.2 Let $f: I \subseteq \mathbb{R} \to \mathbb{R}$ be a convex function defined on the interval I of real numbers and $a, b \in I$ with $a < b$. The following inequality holds:

$$f\left(\frac{a + b}{2}\right) \leq \frac{1}{b - a} \int_a^b f(x)dx \leq \frac{f(a) + f(b)}{2} \tag{1}$$

This double inequality is known in the literature as Hermite-Hadamard integral inequality for convex functions. See [2, 4], for the results of the generalization, improvement and extension of the famous integral inequality (1).

Definition 1.3 [5] A function $f: I \subset \mathbb{R} \to (0, \infty)$ is said to be arithmetic-harmonically (AH) convex function if for all $x, y \in I$ and $t \in [0,1]$ the equality

$$f(tx + (1 - t)y) \leq \frac{f(x)f(y)}{tf(y) + (1 - t)f(x)} \tag{2}$$

holds. If the inequality (2) is reversed then the function $f(x)$ is said to be arithmetic-harmonically (AH) concave function.

In this study, in order to establish some new inequalities of Hermite-Hadamard type inequalities for arithmetic harmonically convex functions, we will use the following lemma obtained in the specials case of identity given in [3].

Lemma 1.4 Let $f: I \subseteq \mathbb{R} \to \mathbb{R}$ be two times-differentiable mapping on $I°$ and $f'' \in L[a, b]$, where $a, b \in I°$ with $a < b$, we have the identity

$$bf(b) - af(a) - \frac{b^2 f'(b) - a^2 f'(b)}{2} - \int_a^b f(x)dx = -\frac{1}{2}\int_a^b x^2 f''(x)dx. \tag{3}$$

For shortness, throughout this paper, we will use the following notations for special means of two nonnegative numbers a, b with $b > a$:

1. The arithmetic mean
$$A := A(a, b) = \frac{a + b}{2}, \quad a, b > 0,$$

2. The geometric mean
$$G := G(a, b) = \sqrt{ab}, \quad a, b \geq 0$$

3. The logarithmic mean
$$L := L(a, b) = \begin{cases} \dfrac{b - a}{\ln b - \ln a}, & a \neq b \\ a, & a = b \end{cases}; \quad a, b > 0$$

4. The p-logaritmic mean
$$L_p := L_p(a, b) = \begin{cases} \left(\dfrac{b^{p+1} - a^{p+1}}{(p + 1)(b - a)}\right)^{\frac{1}{p}}, & a \neq b, p \in \mathbb{R} \backslash \{-1, 0\} \\ a, & a = b \end{cases}; \quad a, b > 0.$$

These means are often used in numerical approximation and in other areas. However, the following simple relationships are known in the literature:

$$H \leq G \leq L \leq I \leq A.$$

It is also known that L_p is monotonically increasing over $p \in \mathbb{R}$, denoting $L_0 = I$ and $L_{-1} = L$.

2. MAIN RESULTS

Theorem 2.1 Let $f: I \subset (0, \infty) \to (0, \infty)$ be a two-times differentiable mapping on I°, and $a, b \in I^\circ$ with $a < b$. If $|f''|$ is an arithmetic-harmonically convex function on the interval $[a, b]$, then the following inequality holds:

i) If $|f''(a)| - |f''(b)| \neq 0$, then

$$\left| \frac{bf(b) - af(a)}{b-a} - \frac{b^2 f'(b) - a^2 f'(b)}{2(b-a)} - \frac{1}{b-a} \int_a^b f(x)dx \right|$$

$$\leq \frac{(b-a)|f''(a)||f''(b)|}{2} \left[\frac{1}{B_f} \left(\frac{b^2 - a^2}{2} - (b-a)C_f \right) + \frac{C_f^2}{L(|f''(a)|, |f''(b)|)} \right], \quad (4)$$

ii) If $|f''(a)| - |f''(b)| = 0$, then

$$\left| \frac{bf(b) - af(a)}{b-a} - \frac{b^2 f'(b) - a^2 f'(b)}{2(b-a)} - \frac{1}{b-a} \int_a^b f(x)dx \right| \leq \frac{|f''(b)|}{6} [2A(a^2, b^2) + G^2(a, b)],$$

where

$$B_f = B_f(a, b; n) = |f''(a)| - |f''(b)|$$

$$C_f = C_f(a, b; n) = \frac{b|f''(b)| - a|f''(a)|}{B_f}.$$

Proof. i) Let $|f''(a)| - |f''(b)| \neq 0$. If $|f''|$ is an arithmetic-harmonically convex function on the interval $[a, b]$, using Lemma 1.4 and the following inequality

$$|f''(x)| = \left| f'' \left(\frac{b-x}{b-a} a + \frac{x-a}{b-a} b \right) \right| \leq \frac{|f''(a)||f''(b)|}{\frac{b-x}{b-a}|f''(b)| + \frac{x-a}{b-a}|f''(a)|}$$

$$= \frac{(b-a)|f''(a)||f''(b)|}{(b-x)|f''(b)| + (x-a)|f''(a)|},$$

we get

$$\left| bf(b) - af(a) - \frac{b^2 f'(b) - a^2 f'(b)}{2} - \int_a^b f(x)dx \right|$$

$$\leq \frac{1}{2} \int_a^b x^2 |f''(x)| dx$$

$$\leq \frac{1}{2} \int_a^b \frac{x^2(b-a)|f''(a)||f''(b)|}{(b-x)|f''(b)| + (x-a)|f''(a)|} dx$$

$$= \frac{(b-a)|f''(a)||f''(b)|}{2} \int_a^b \frac{x^2}{(b-x)|f''(b)| + (x-a)|f''(a)|} dx. \qquad (5)$$

From here, we can write the following inequality

$$\left| bf(b) - af(a) - \frac{b^2 f'(b) - a^2 f'(b)}{2} - \int_a^b f(x)dx \right|$$

$$\leq \frac{(b-a)|f''(a)||f''(b)|}{2B_f} \int_a^b \frac{x^2}{x + C_f} dx$$

$$= \frac{(b-a)|f''(a)||f''(b)|}{2B_f} \int_a^b \left(x - C_f + \frac{C_f^2}{x + C_f} \right) dx$$

$$= \frac{(b-a)|f''(a)||f''(b)|}{2B_f} \left[\frac{x^2}{2} - xC_f + C_f^2 \ln(x + C_f) \right]\Big|_a^b$$

$$= \frac{(b-a)|f''(a)||f''(b)|}{2B_f} \left[\frac{b^2 - a^2}{2} - (b-a)C_f + C_f^2 \ln\left(\frac{b + C_f}{a + C_f} \right) \right]$$

$$= \frac{(b-a)|f''(a)||f''(b)|}{2B_f} \left[\frac{b^2 - a^2}{2} - (b-a)C_f + C_f^2 \ln\left(\frac{|f''(a)|}{|f''(b)|} \right) \right]$$

$$= \frac{(b-a)|f''(a)||f''(b)|}{2} \left[\frac{1}{B_f} \left(\frac{b^2 - a^2}{2} - (b-a)C_f \right) + \frac{C_f^2}{L(|f''(a)|, |f''(b)|)} \right].$$

So, we get the desired inequality.

ii) Let $|f''(a)| - |f''(b)| = 0$. Then, substituting $|f''(a)| = |f''(b)|$ in (5), we obtain

$$\left| \frac{bf(b) - af(a)}{b-a} - \frac{b^2 f'(b) - a^2 f'(b)}{2(b-a)} - \frac{1}{b-a} \int_a^b f(x)dx \right|$$

$$\leq \frac{f''(b)}{2} \int_a^b x^2 dx$$

$$= \frac{|f''(b)|}{6} [2A(a^2, b^2) + G^2(a, b)]. \qquad (6)$$

This completes the proof of theorem.

Theorem 2.2 Let $f: I \subset (0, \infty) \to (0, \infty)$ be two-times differentiable mapping on $I°$, and $a, b \in I°$ with $a < b$. If $|f''|^q$ is an arithmetic-harmonically convex function on the interval $[a, b]$, then the following inequality holds:

i) If $|f''(a)|^q - |f''(b)|^q \neq 0$, then

$$\left| \frac{bf(b) - af(a)}{b - a} - \frac{b^2 f'(b) - a^2 f'(b)}{2(b - a)} - \frac{1}{b - a} \int_a^b f(x)dx \right|$$

$$\leq \frac{1}{2} \frac{L_{2p}^2(a, b) G^2(|f''(a)|, |f''(b)|)}{\left[L(|f''(a)|, |f''(b)|) L_{q-1}^{q-1}(|f''(a)|, |f''(b)|) \right]^{\frac{1}{q}}}, \tag{7}$$

ii) If $|f''(a)|^q - |f''(b)|^q = 0$, then

$$\left| \frac{bf(b) - af(a)}{b - a} - \frac{b^2 f'(b) - a^2 f'(b)}{2(b - a)} - \frac{1}{b - a} \int_a^b f(x)dx \right| \leq \frac{1}{2} |f''(b)| L_{2p}^2(a, b),$$

where

$$\frac{1}{p} + \frac{1}{q} = 1.$$

Proof. i) Let $|f''(a)|^q - |f''(b)|^q \neq 0$. If $|f''|^q$ for $q > 1$ is an arithmetic-harmonically convex function on the interval $[a, b]$, then using Lemma 1.4, well known Hölder integral inequality and the following inequality

$$|f''(x)|^q = \left| f'' \left(\frac{b - x}{b - a} a + \frac{x - a}{b - a} b \right) \right|^q \leq \frac{(b - a)|f''(a)|^q |f''(b)|^q}{(b - x)|f''(b)|^q + (x - a)|f''(a)|^q},$$

we can write,

$$\left| bf(b) - af(a) - \frac{b^2 f'(b) - a^2 f'(b)}{2} - \int_a^b f(x)dx \right|$$

$$\leq \frac{1}{2} \left(\int_a^b x^{2p}dx \right)^{\frac{1}{p}} \left(\int_a^b |f''(x)|^q dx \right)^{\frac{1}{q}}$$

$$\leq \frac{1}{2} \left((b - a)L_{2p}^{2p}(a, b) \right)^{\frac{1}{p}} \left(\int_a^b \frac{(b - a)|f''(a)|^q |f''(b)|^q}{(b - x)|f''(b)|^q + (x - a)|f''(a)|^q} dx \right)^{\frac{1}{q}}. \tag{8}$$

From here, we get

$$\left| bf(b) - af(a) - \frac{b^2 f'(b) - a^2 f'(b)}{2} - \int_a^b f(x)dx \right|$$

$$\leq \frac{1}{2} (b - a)^{\frac{1}{p}} L_{2p}^2(a, b)(b - a)^{\frac{1}{q}} \frac{|f''(a)||f''(b)|}{[|f''(b)|^q - |f''(a)|^q]^{\frac{1}{q}}} \left(\int_{(b-a)|f''(a)|^q}^{(b-a)|f''(b)|^q} \frac{1}{u} du \right)^{\frac{1}{q}}$$

$$= \frac{1}{2} (b - a) L_{2p}^2(a, b) \frac{|f''(a)||f''(b)|}{[|f''(b)|^q - |f''(a)|^q]^{\frac{1}{q}}} \left(\ln u \Big|_{(b-a)|f''(a)|^q}^{(b-a)|f''(b)|^q} \right)^{\frac{1}{q}}$$

$$= \frac{1}{2}(b-a)L_{2p}^2(a,b)|f''(a)||f''(b)| \left(\frac{\ln(b-a)|f''(b)|^q - \ln(b-a)|f''(a)|^q}{|f''(b)|^q - |f''(a)|^q} \right)^{\frac{1}{q}}$$

$$= \frac{1}{2}(b-a)L_{2p}^2(a,b)|f''(a)||f''(b)| \left(\frac{\ln|f''(b)|^q - \ln|f''(a)|^q}{|f''(b)|^q - |f''(a)|^q} \right)^{\frac{1}{q}}$$

$$= \frac{1}{2}(b-a)\frac{L_{2p}^2(a,b)G^2(|f''(a)|,|f''(b)|)}{\left[L(|f''(a)|,|f''(b)|)L_{q-1}^{q-1}(|f''(a)|,|f''(b)|) \right]^{\frac{1}{q}}},$$

where

$$\int_a^b x^{2p}dx = (b-a)L_{2p}^{2p}(a,b),$$

$$\frac{\ln|f''(b)|^q - \ln|f''(a)|^q}{|f''(b)|^q - |f''(a)|^q} = \frac{\ln|f''(b)| - \ln|f''(a)|}{|f''(b)| - |f''(a)|} \frac{q[|f''(b)| - |f''(a)|]}{|f''(b)|^q - |f''(a)|^q}$$

$$= \left[L(|f''(a)|,|f''(b)|)L_{q-1}^{q-1}(|f''(a)|,|f''(b)|) \right]^{-1}.$$

Therefore, the required result is obtained.

    ii) Let $|f''(a)|^q - |f''(b)|^q = 0$. Then, from (8) we obtain the following:

$$\left| \frac{bf(b) - af(a)}{b-a} - \frac{b^2f'(b) - a^2f'(a)}{2(b-a)} - \frac{1}{b-a}\int_a^b f(x)dx \right| \le \frac{1}{2}|f''(b)|L_{2p}^2(a,b). \quad (9)$$

This completes the proof of the Theorem.

Theorem 2.3 *Let* $f: I \subset (0,\infty) \to (0,\infty)$ *be two-times differentiable mapping on* I°, *and* $a, b \in I^\circ$ *with* $a < b$. *If* $|f''|^q, q \ge 1$ *is an arithmetic-harmonically convex function on the interval* $[a,b]$, *then the following inequality holds:*

    i) If $|f''(a)|^q - |f''(b)|^q \neq 0$, then

$$\left| \frac{bf(b) - af(a)}{b-a} - \frac{b^2f'(b) - a^2f'(a)}{2(b-a)} - \frac{1}{b-a}\int_a^b f(x)dx \right| \le \frac{b-a}{2}|f''(a)||f''(b)|L_2^{2\left(1-\frac{1}{q}\right)}(a,b)$$

$$\times \left[\frac{1}{B_f}\left(\frac{b^2-a^2}{2} - (b-a)C_f \right) + \frac{C_f^2}{L(|f''(a)|^q,|f''(b)|^q)} \right]^{\frac{1}{q}}, \quad (10)$$

    ii) If $|f''(a)|^q - |f''(b)|^q = 0$, then

$$\left| \frac{bf(b) - af(a)}{b-a} - \frac{b^2f'(b) - a^2f'(a)}{2(b-a)} - \frac{1}{b-a}\int_a^b f(x)dx \right|$$

$$\le \frac{1}{6}|f''(b)|[2A(a^2,b^2) + G^2(a,b)],$$

where

$$B_{q,f} = B_{q,f}(a,b;n) = |f''(a)|^q - |f''(b)|^q$$

$$C_{q,f} = C_{q,f}(a,b;n) = \frac{b|f''(b)|^q - a|f''(a)|^q}{B_{q,f}}.$$

Proof. i) Let $|f''(a)|^q - |f''(b)|^q \neq 0$. If $|f''|^q$ for $q \geq 1$ is an AH-convex function on $[a,b]$, then using Lemma 1.4 and well known power-mean integral inequality, we have

$$\left| bf(b) - af(a) - \frac{b^2 f'(b) - a^2 f'(b)}{2} - \int_a^b f(x)dx \right| \tag{11}$$

$$\leq \frac{1}{2} \left(\int_a^b x^2 dx \right)^{1-\frac{1}{q}} \left(\int_a^b x^2 |f''(x)|^q dx \right)^{\frac{1}{q}}$$

$$\leq \frac{1}{2} \left(\int_a^b x^2 dx \right)^{1-\frac{1}{q}} \left(\int_a^b \frac{x^2(b-a)|f''(a)|^q|f''(b)|^q}{(b-x)|f''(b)|^q + (x-a)|f''(a)|^q} dx \right)^{\frac{1}{q}}$$

$$= \frac{b-a}{2} |f''(a)||f''(b)|L_2^{2\left(1-\frac{1}{q}\right)}(a,b) \left(\int_a^b \frac{x^2}{(b-x)|f''(b)|^q + (x-a)|f''(a)|^q} dx \right)^{\frac{1}{q}}$$

$$= \frac{b-a}{2} |f''(a)||f''(b)|L_2^{2\left(1-\frac{1}{q}\right)}(a,b) \left[\frac{1}{B_{q,f}} \int_a^b \left(x - C_{q,f} + \frac{C_{q,f}^2}{x + C_{q,f}} \right) dx \right]^{\frac{1}{q}}$$

$$= \frac{b-a}{2} |f''(a)||f''(b)|L_2^{2\left(1-\frac{1}{q}\right)}(a,b) \left[\frac{1}{B_{q,f}} \left(\frac{b^2 - a^2}{2} - (b-a)C_{q,f} + C_{q,f}^2 \ln\left(\frac{b + C_{q,f}}{a + C_{q,f}} \right) \right) \right]^{\frac{1}{q}}$$

$$= \frac{b-a}{2} |f''(a)||f''(b)|L_2^{2\left(1-\frac{1}{q}\right)}(a,b) \left[\frac{1}{B_{q,f}} \left(\frac{b^2 - a^2}{2} - (b-a)C_{q,f} \right) + \frac{C_{q,f}^2}{L(|f''(a)|^q, |f''(b)|^q)} \right]^{\frac{1}{q}}.$$

Therefore, we get the following inequality:

$$\left| \frac{bf(b) - af(a)}{b-a} - \frac{b^2 f'(b) - a^2 f'(b)}{2(b-a)} - \frac{1}{b-a} \int_a^b f(x)dx \right|$$

$$\leq \frac{b-a}{2} |f''(a)||f''(b)|L_2^{2\left(1-\frac{1}{q}\right)}(a,b)$$

$$\times \left[\frac{1}{B_f} \left(\frac{b^2 - a^2}{2} - (b-a)C_f \right) + \frac{C_f^2}{L(|f''(a)|^q, |f''(b)|^q)} \right]^{\frac{1}{q}}$$

ii) Let $|f''(a)|^q - |f''(b)|^q = 0$. By using the inequality (2.8), we have

$$\left| \frac{bf(b) - af(a)}{b-a} - \frac{b^2 f'(b) - a^2 f'(b)}{2(b-a)} - \frac{1}{b-a} \int_a^b f(x)dx \right|$$

$$\leq \frac{1}{6} |f''(b)|[2A(a^2, b^2) + G^2(a,b)]. \tag{12}$$

This completes the proof of the Theorem.

Corollary 2.4 If we take $q = 1$ in the inequality (10), we get the following inequality:

$$\left| \frac{bf(b) - af(a)}{b - a} - \frac{b^2 f'(b) - a^2 f'(b)}{2(b - a)} - \frac{1}{b - a} \int_a^b f(x)dx \right|$$

$$\leq \frac{1}{2} |f''(a)||f''(b)| \left[\frac{1}{B_f} \left(\frac{b^2 - a^2}{2} - (b - a)C_f \right) + \frac{C_f^2}{L(|f''(a)|, |f''(b)|)} \right].$$

3. APPLICATIONS FOR SPECIAL MEANS

If $p \in (-1,0)$ then the function $f(x) = x^p, x > 0$ is an arithmetic harmonically-convex function [1]. Using this function we obtain following propositions related to means:

Proposition 3.1 Let $0 < a < b$ and $p \in (-1,0)$. Then we have the following inequalities:

$$L_{p+2}^{p+2}(a, b) \leq \left(\frac{G^p(a, b)}{pL_{p-1}^{p-1}(a, b)} \right)^2 \left[\frac{(p+1)L_p^{2p}(a, b)}{L_{p-1}^{p-1}(a, b)L(a, b)} - pA(a, b)L_{p-1}^{p-1}(a, b) - (p+1)L_p^p(a, b) \right]$$

Proof. Let $p \in (-1,0)$. Then we consider the function $f(x) = \frac{x^{p+2}}{(p+1)(p+2)}, x > 0$. Under the assumption of the Proposition

$$|f''(x)| = x^p$$

is an arithmetic harmonically-convex function. Therefore, the assertion follows from the inequality (4) in the Theorem 2.1, for $f: (0, \infty) \to \mathbb{R}$, $f(x) = \frac{x^{p+2}}{(p+1)(p+2)}$.

Proposition 3.2 Let $a, b \in (0, \infty)$ with $a < b$, $q > 1$ and $m \in (-1,0)$. Then, we have the following inequality:

$$L_{\frac{m}{q}+2}^{\frac{m}{q}+2}(a, b) \leq \frac{L_{2p}^2(a, b)G^{\frac{2m}{q}}(a, b)}{L^{\frac{1}{q}}(a, b)L_{m-1}^{\frac{m-1}{q}}(a, b)}.$$

Proof. The assertion follows from the inequality (6) in the Theorem 2.2. Let

$$f(x) = \frac{1}{\left(\frac{m}{q} + 1 \right) \left(\frac{m}{q} + 2 \right)} x^{\frac{m}{q}+2}, \qquad x \in (0, \infty).$$

Then $|f''(x)|^q = x^m$ is an arithmetic harmonically-convex on $(0, \infty)$ and the result follows directly from Theorem 2.2.

Proposition 3.3 Let $a, b \in (0, \infty)$ with $a < b$, $q > 1$ and $m \in (-1,0)$. Then, we have the following inequality:

$$L_{\frac{m}{q}+2}^{\frac{m}{q}+2}(a,b) \leq \left[\frac{G^m(a,b)}{mL_{m-1}^{m-1}(a,b)}\right]^{\frac{2}{q}} L_2^{2\left(1-\frac{1}{q}\right)}(a,b)$$

$$\times \left\{\frac{(m+1)^2 L_m^{2m}(a,b)}{L(a,b)L_{m-1}^{m-1}(a,b)} - (m+1)L_m^m(a,b) - mA(a,b)L_{m-1}^{m-1}(a,b)\right\}^{\frac{1}{q}}. \qquad (13)$$

Proof. The assertion follows from the inequality (8) in the Theorem 2.3. Let

$$f(x) = \frac{1}{\left(\frac{m}{q}+1\right)\left(\frac{m}{q}+2\right)} x^{\frac{m}{q}+2}, \qquad x \in (0,\infty).$$

Then $|f''(x)|^q = x^m$ is an arithmetic harmonically-convex on $(0,\infty)$ and the result follows directly from Theorem 2.3.

Corollary 3.4 If we take $q = 1$ in the inequality (13), we get the following inequality:

$$L_{m+2}^{m+2}(a,b) \leq \frac{G^{2m}(a,b)}{m^2 L_{m-1}^{2(m-1)}(a,b)}\left[\frac{(m+1)^2 L_m^{2m}(a,b)}{L(a,b)L_{m-1}^{m-1}(a,b)} - (m+1)L_m^m(a,b) - mA(a,b)L_{m-1}^{m-1}(a,b)\right].$$

REFERENCES

[1] Dragomir, S.S., Inequalities of Hermite-Hadamard type for AH-convex functions, Stud. Univ. Babeş-Bolyai Math., 61-4 (2016) 489-502.

[2] Dragomir S.S. and Pearce, C.E.M., Selected Topics on Hermite-Hadamard Inequalities and Applications, RGMIA Monographs, Victoria University, 2000.

[3] Maden, S., Kadakal, H., Kadakal M. and İşcan, İ., Some new integral inequalities for n-times differentiable convex and concave functions. J. Nonlinear Sci. Appl., 10 (2017) 6141-6148.

[4] Sarikaya, M.Z. and Aktan, N., On the generalization of some integral inequalities and their applications, Mathematical and Computer Modelling, 54 (2011) 2175-2182.

[5] Zhang, T.Y. and Qi, F., Integral Inequalities of Hermite-Hadamard Type for m-AH Convex Functions, Turkish Journal of Analysis and Number Theory, 2-3 (2014) 60-64.

The Comparison of Primary, Secondary and Tertiary Amine Ligands on Palladium (II) Complex Ion on Thermo-Physical, Chemical Reactivity, and Biological Properties: A DFT Study

Mohammad Jahidul ISLAM [1] iD *, Md. Nuruzzaman SARKER* [1] iD *, Ajoy KUMER* [2,*] iD *, Sunanda PAUL* [3,*] iD

[1] *Department of Physics, European University of Bangladesh, Dhaka-1216, Bangladesh*
[2] *Department of Chemistry, European University of Bangladesh, Dhaka-1216, Bangladesh*
[3] *Department of Biochemistry and Molecular Biology, University of Chittagong, Chittagong, Hathazari-4334, Bangladesh*

Abstract. The Palladium is considered as the catalyst for coupling reaction and useful metal in industry. The thermo-physical, chemical reactivity and biological interaction are considered the most expected parameters for use in any area of the chemical industry, the pharmaceutical industry, and academia. The palladium (II) complex ion with different amine ligands are considered under theoretical study by the method of density functional theory (DFT). Some thermo-physical parameters such as free energy, entropy, dipole moment, binding energy, nuclear energy, electronics energy, heat of formation, reactivity properties of molecule like Highest Occupied Molecular Orbital (HOMO), Lowest Unoccupied Molecular Orbital (LUMO), HOMO-LUMO gap, ionization potential, electronegativity, hardness, softness and electron affinity, and biological properties of molecules like charge density, surface area grid, volume, LogP, polarizibility, refractivity, molecular mass, PIC50 were calculated using the computational program of DFT method. The value of HOMO LUMO gap is 10.78, 0.59, 0.50, and 10.73 and PIC50 is -20.41, -8.46, -1.69, and 1.83 for L01, L02, L03, and L04 respectively while the chemical stability is same for L02, and L03, similarly L01 and L04. The QSAR study provides information about their correlation and biological activity as drugs whereas the biological activity was increased with increasing methyl groups. The four palladium (II) complex ions with amine ligands have strong biological activity for L03 and L04, and occur the correlation on thermophysical, chemical reactivity.

*Keywords***:** Palladium, alkylamine, QSAR, HOMO, LUMO, vibrational spectroscopy and PIC50

Palladium (II) Kompleks İyondaki Primer, Sekonder ve Tersiyer Amin Ligandlarının Termo-Fiziksel, Kimyasal Reaktivite ve Biyolojik Özelliklerle Karşılaştırılması: DFT Çalışması

Özet. Palladyum kenetlenme reaksiyonları için katalizör olarak dikkate alınır ve sanayide kullanışlı bir metaldir. Termo-fiziksel, kimyasal reaktivite ve biyolojik etkileşim, kimya endüstrisi, ilaç endüstrisi ve akademi de en çok dikkate alınan parametrelerdir. Farklı amin ligandları içeren Pd (II) kompleks iyonu, çalışmanın teorik kısmında DFT yöntemi kullanılarak incelenmiştir. Serbest enerji, entropi, dipol moment, bağlanma enerjisi, nükleer enerji, elektronik enerji, oluşum ısısı gibi termo-fiziksel parametreler, HOMO enerjisi, LUMO enerjisi, HOMO-LUMO enerji aralığı, iyonlaşma enerjisi, elektronegatiflik, sertlik, yumuşaklık ve elektron ilgisi gibi reaktivite özellikleri, yük yoğunluğu, yüzey alanı, hacim logP, Polarlanabilirlik, refraktivite, moleküler kütle, PIC50 gibi biyolojik özellikleri DFT methodu yardımıyla hesaplanmıştır. L01, L02, L03 ve L04 için HOMO-LUMO enerji aralığı değerleri 10.78, 0.59, 0.50 ve 10.73; PIC50 değerleri sırasıyla -20.41, -8.46, -1.69 ve 1.83 tür. L02 ile L03 ün, L02 ile L04 ün kimyasal kararlılıkları hemen hemen aynıdır. QSAR çalışması moleküllerin

biyolojik aktiflikleri hakkında bilgi sağlar. Amin ligandlarını içeren dört Pd(II) kompleks iyonu L03 ve L04 için güçlü biyolojik aktiviteye sahiptir.

Anahtar Kelimeler: Palladyum, alkil amin, QSAR, HOMO, LUMO, titreşim spektroskopisi ve PIC50

1. INTRODUCTION

Palladium is a soft, rare, silvery-white metal that is valued for its catalytic properties and shares many of the characteristics common to the platinum group metal [1]. It has a face-centered cubic crystalline structure at ordinary temperatures and it is strongly resistant to corrosion in the air and to the action of an acid. The largest uses of palladium are as metal in the field of jewelry [2], dentistry, watch making, blood sugar test strips, aircraft spark plugs, surgical instruments, and electrical contacts [3]. On the other hand, these are currently attracted considerable interest because they're potentially beneficial as pharmaceutical ingredients, a bioactive molecule, pharmacological properties [4-6]. Palladium complexes have been worked against cancer cells [7-9]. However, although palladium has less cytotoxic effects than platinum, palladium has good cytotoxic effects as well for use as bioactive molecules of the area drug design [10, 11]. Palladium complexes with aromatic N-containing ligands, e.g., derivatives of amine, pyridine, quinoline, pyrazole, and 1, 10-phenanthroline has shown very promising antitumor characteristics molecules. Some of these complexes, especially the *trans* complexes with non-planar heterocyclic amine ligands have been found to overcome multifactorial *cis* platin resistance in human ovarian cell lines. On the other hand, Pd(II) complexes or complex ions have been widely explored due to their catalytic efficiency, e.g., for various carbon-carbon and carbon-nitrogen bond-forming reactions. The most palladium (0), palladium (II) on carbon makes some versatile catalyst of organic syntheses such as Heck reaction, Suzuki coupling, Tsuji-Trost reactions, Wacker process, Negishi reaction and Stille coupling, etc [12-15]. While most studies of palladium have concentrated on the reactivity of its complexes, little information about their electronic structures has been obtained.

Organometallic transition-metal complexes utilizing nitrogen ligands with ionic or polar substituent have been found to catalyze a large variety of chemical transformations in aqueous solution. Palladium is one of the most catalytically versatile transition metal. The nitrogen-containing ligand assisted palladium catalyzed Suzuki coupling reaction is the most frequently employed methods of carbon-carbon bond formation in organic synthesis [14]. In the literature, the molecular structure of a complex containing palladium atom have been studied for years, however electronic structure of this molecule have been worked out quite a bit.

Taking into account all the benefits in thermophysical, chemical reactivity, biological profile, the computational chemistry is the best tools in present time of chemistry, physics, material science, pharmaceutical science, molecular engineering, and biochemistry. To save time and cost, computational computer programming is used on making the correlation of the thermophysical, chemical and biological activity of some palladium complexes. A thermodynamic system is a definite macroscopic area or space in the universe in which one or more thermodynamic processes take place. This system has a specific volume consisting of molecules and atoms with continuous movement and concussion by the interaction with the external surrounding. The internal properties and its interaction with the surrounding determine the system behavior [16-18].

A thermodynamic system can switch from initial state through the intermediate state to the final state which is called transformation of state or thermodynamics process [17, 19]. Using the computational simulation of the examined palladium complexes, It would be calculated by the various method of computational methods. As

the anion has an effective influence on biological activity, the relationship of substituent group in benzene rings was estimated using computing parameters [20, 21]. The most beneficial of the study is the safe the money including conducting a chemical experiment in laboratory and consumption of time in the laboratory at which the most errorless method is the Density functional theory (DFT) [22, 23].

The Density functional theory (DFT) finds an increasingly broad application in the chemical and materials sciences for the interpretation and prediction of complex system behavior at an atomic scale. Specifically, DFT computational methods are applied for the study of systems to synthesis and processing parameters. The Density Functional Theory (DFT) is used to determine chemical structures of molecules and structural changes in molecules. Especially, the B3LYP method is widely used because it yields results very close to experimental results. Moreover, the DFT is a very useful method for predicting the experimental results.

In this study, the palladium (II) complex was synthesized and optimized with DFT/B3LYP. Some geometrical parameters and HOMO-LUMO energy level of the complex were calculated at B3LYP. Their molecular structural relationship, HOMO, LUMO, and quantum chemical properties and LogP plays the role of the chemical reactivity, biological activity and hydrophobicity and hydrophobicity of chemicals in relation with living cells activity and associated mechanistic interactions.

2. COMPUTING METHODS FOR SIMULATION

The molecular modeling program permits to build and analyze different molecular structures and determine the molecular, electronic, and biological properties. In order to create the spatial chemical structure of each calculated molecule, the two-dimensional structure of the molecule shall be built step-by-step by drawing. Then hydrogen atoms are automatically added from building option and chemical structure is converted into a 3D structure.

The first step in getting the main characteristic parameters of molecules is to optimize the molecular structure to obtain a configuration characterized by minimum free energy. In sitting the DFT was fixed via 6G-31G*, and B3-LYP [24-26]. After completing optimization, the theoretical properties of the studied compound such as free energy, entropy, dipole moment, binding energy, nuclear energy, electronics energy, the heat of formation, the HOMO, LUMO are recorded. The QSAR properties of molecules like charge density, surface area grid, volume, LogP, polarizability, refractivity, molecular mass, were calculated.

3. RESULTS AND DISCUSSIONS
3.1. Optimized Structure
The symmetry is a very powerful tool to establish the molecular symmetry calculation. In fig-01, Tetraamine palladium (II) complexes ion (L01), Tetra(methylamine) palladium (II) complexes ion (L02), Tetra(dimethylamine) palladium (II) complexes ion (L03) and Tetra(trimethylamine) palladium (II) complexes ion (L04) molecular orbital diagram having both of molecular symmetry and asymmetry properties are represented.
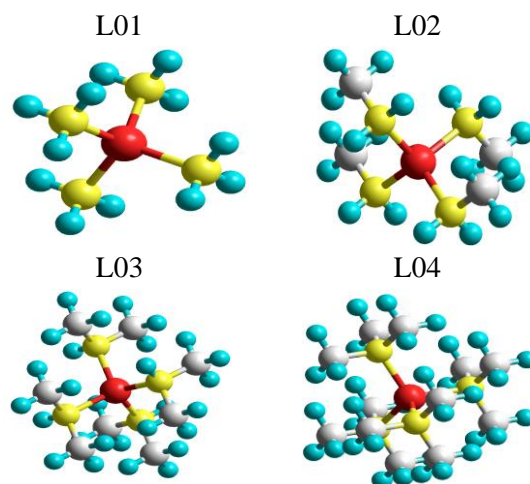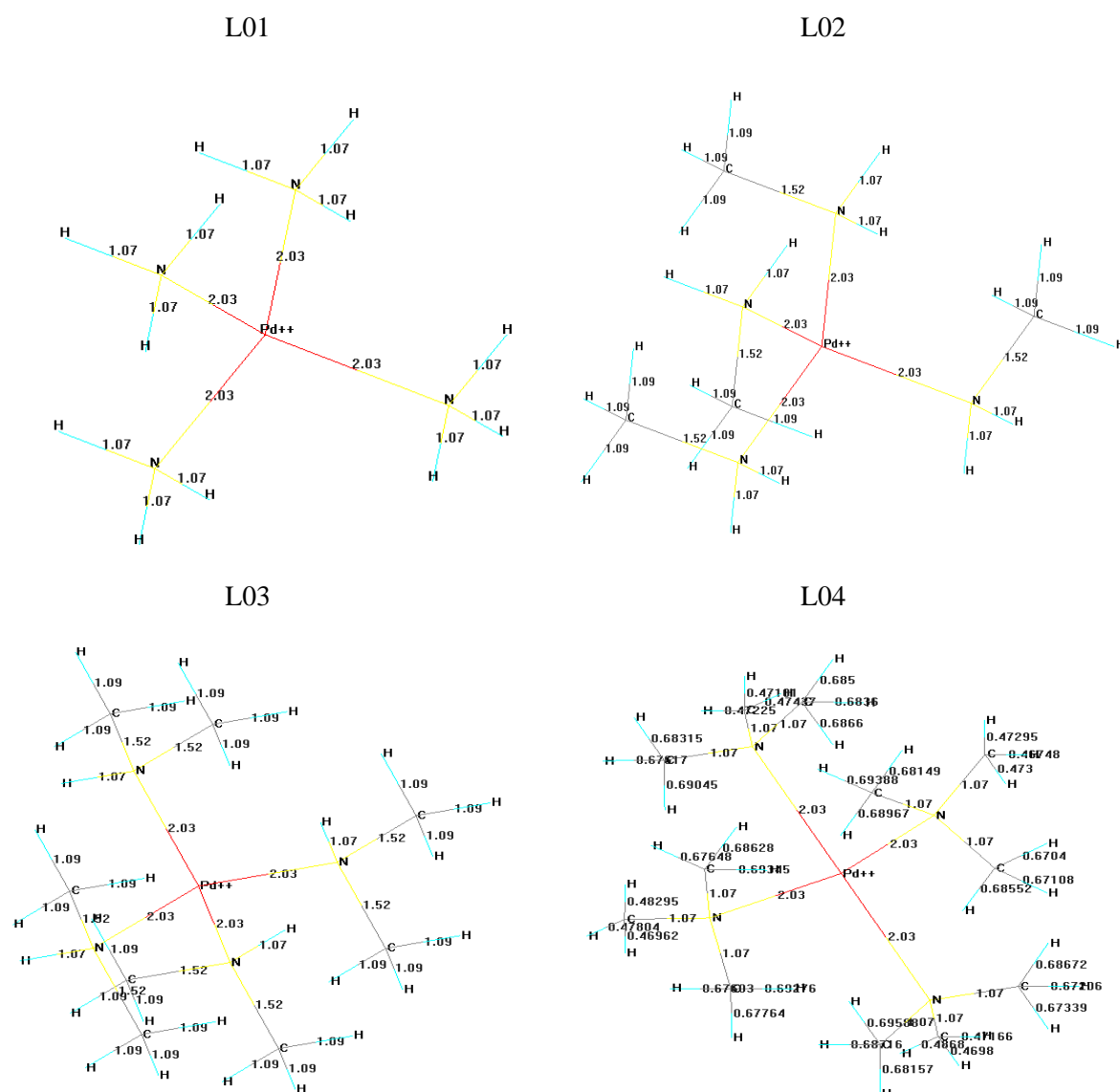

Figure 1. Optimized structure of palladium (II) complex ions with different amine ligands

3.2. Bond Length
In general, the bond length between two atoms is approximately the sum of the covalent radii of the two atoms. For covalent bonds, bond energies and bond lengths depend on many factors like electron affinities, sizes, electronegativity, chemical

reactivity, ionization potential, and chemical stability of atoms involved in the bond. The bond length of atoms in complexes ions are given in fig-02. The bond length in palladium (II) with nitrogen is 2.03 for all complexes.

Figure 2. Bond length of palladium (II) complex ions with different amine ligands

3.3. Bond Order

The bond order indicates the chemical stability. The higher the bond order indicates the stronger the pull between the two atoms and the shorter the bond length. The shorter bond length indicates the higher required energy, as a result, the rate of reaction decreases and chemical reactivity decreases [27]. From figure 03, the bond order between all atoms in a molecule is obtained in same and that is one.

3.4. The Atomic Charges

The atomic charge is the most important parameters for calculation of thermophysical properties and thermodynamics shown in fig 4. In L01, the atomic charge of palladium atom is 1.057, and a nitrogen atom in amine ligands almost 0.300 to 0.397 and carbon atom in the methyl group is 3.96 to 3.99.
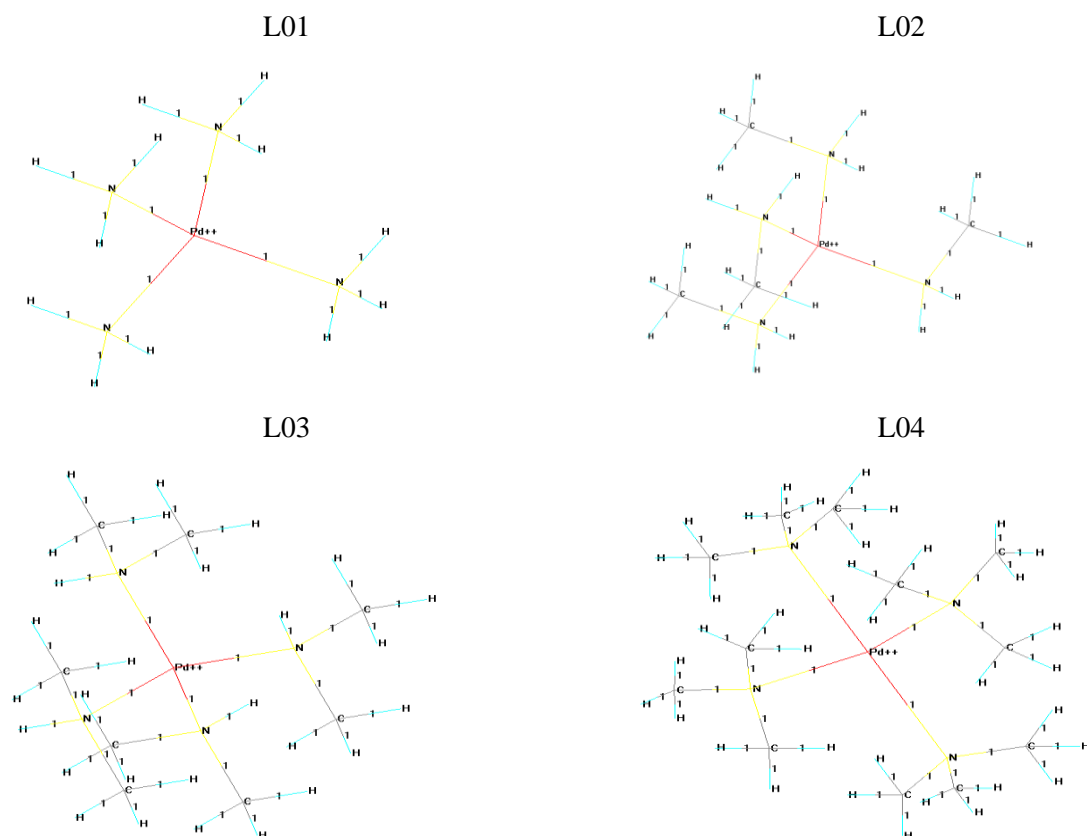
Figure 3. Bond order of palladium (II) complex ions with different amine ligands

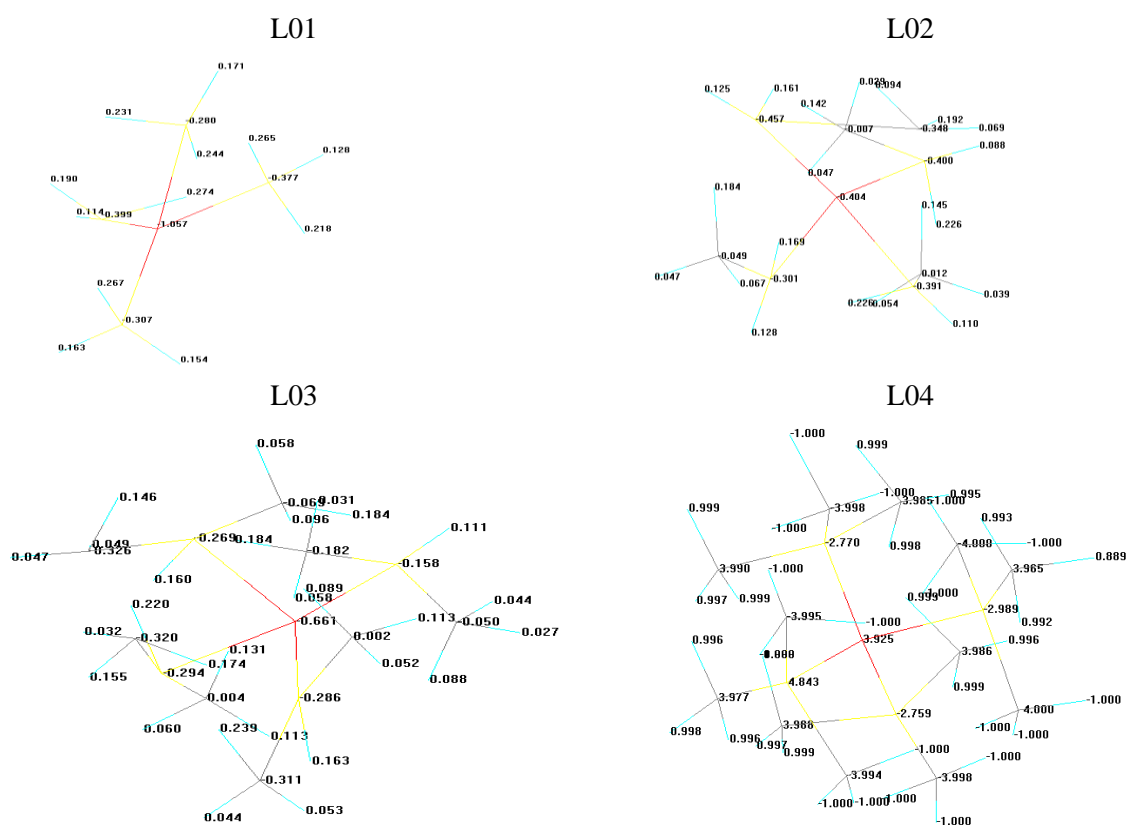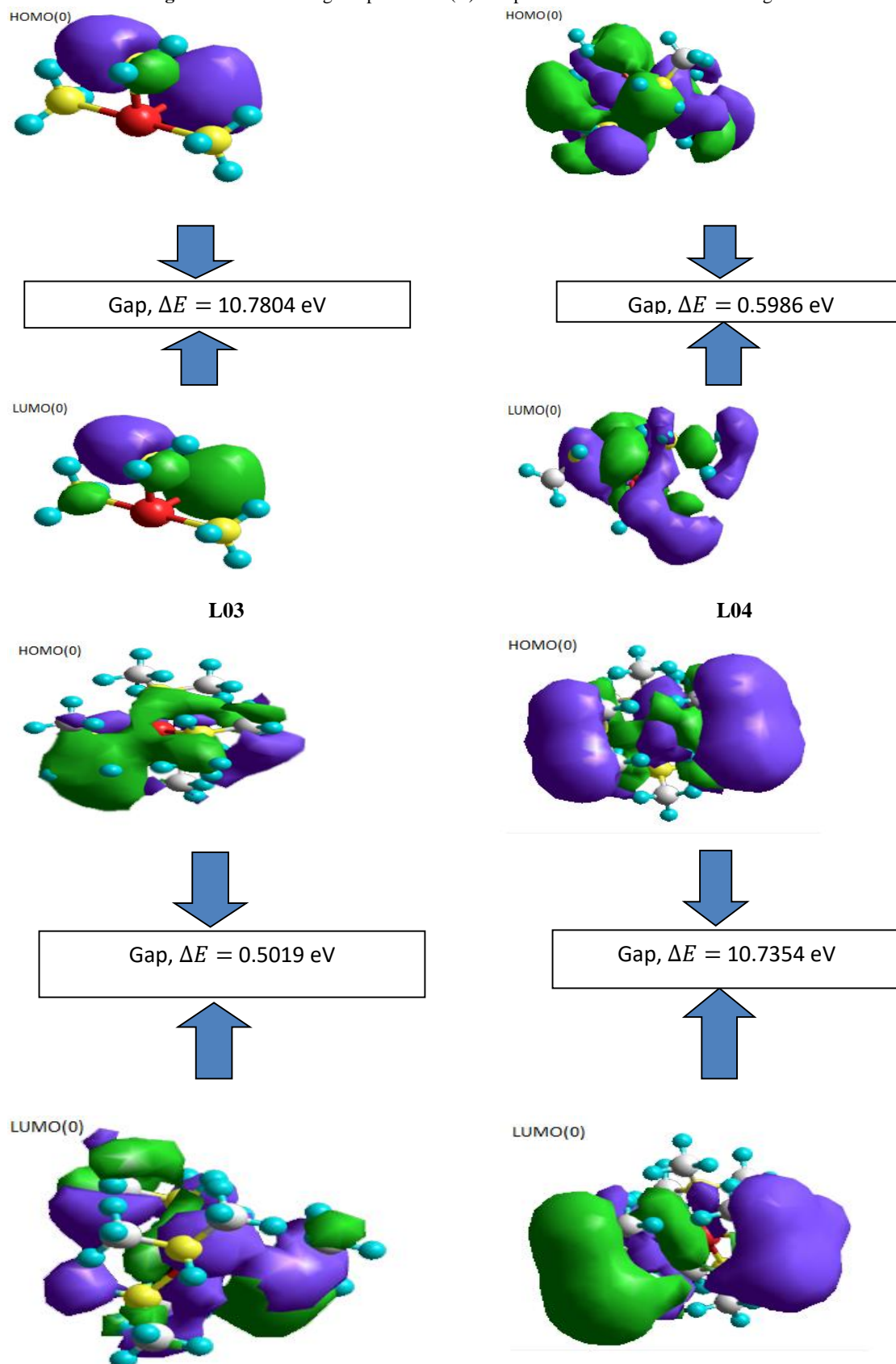**Figure 4.** Atomic charge of palladium (II) complex ions with different amine ligands

Figure 5: Orbital picture of HOMO and LUMO palladium (II) complex ions with different amine ligands

3.5. HOMO-LUMO

The energy levels of the molecular orbitals order HOMO and LUMO for palladium (II) complexes ion with different amine ligands give information on the possible electronic transition and chemical stability. The HOMO and LUMO also indicate the electrophilic and nucleophilic attraction region in the molecule. The LUMO-HOMO gap is the most important parameter for chemical reactivity [28].

The shorter LUMO- HOMO gap is considered as the high reactivity, they are highlighted in figure 5 (color: green is a positive value and blue is a negative value). The HOMO can be through the outermost orbital containing electrons tends to give these electrons such as an electron donor. On the other hand, LUMO can be through the innermost orbital containing free places to accept an electron.

Table 1. Data for HOMO LUMO in different transition state

	L01	L02	L03	L04
HOMO(0), eV	-16.1487	-18.05713	-23.64721	-37.68882
HOMO(-1), eV	-5.360071	-17.45854	-23.14531	-26.95374
HOMO(-2), eV	-4.970126	-17.22483	-21.69175	-19.8055
LUMO, (0), eV	-5.360071	-17.45854	-23.14531	-26.95374
LUMO, (-1), eV	-16.1487	-18.05713	-23.64721	-37.68882
LUMO, (-2), eV	-17.39359	-18.3907	-23.9424	-37.84376

3.6. Chemical reactivity by DFT Calculations

The Energy of the HOMO is directly related to the ionization potential and LUMO Energy is directly related to the electron affinity. The energy difference between HOMO and LUMO orbital is called an energy gap which is an important parameter that determines the stability of the structures. The energy gap is used in determining molecular electrical transport properties. In addition, according to Koopmans' theorem the energy gap, Egap, defined as the difference between HOMO and LUMO energy [29].

$$E_{gap} = (E_{LUMO} - E_{HOMO}) \approx IP - EA$$

The ionization potential (I) and electron affinity (A) can be estimated from the HOMO and LUMO energy values as following

$$I = -E_{HOMO} \quad\quad\quad\quad (1)$$
$$A = -E_{LUMO} \quad\quad\quad\quad (2)$$

Table 2: Data for HOMO, LUMO, IP, EA, and LUMO- HOMO gap, (ΔE)

	L01	L02	L03	L04
HOMO, eV	-16.1487	-18.0571	-23.6472	-37.6888
LUMO, eV	-5.3601	-17.4585	-23.1453	-26.9534
ΔE, (LUMO-HOMO gap), eV	10.7804	0.5986	0.5019	10.7354
Ionization potential (I),eV	16.1487	18.0571	23.6472	37.6888
Electron affinity (A),eV	5.3601	17.4585	23.1453	26.9534

3.7. Chemical reactivity by DFT Calculations

Entropy and enthalpy is an important part of thermodynamics, which allows physics and physical chemistry to participate in any system throughout physical and chemical change. Entropy and enthalpy are closely related to each other.

Entropy can be understood as the discharge condition of any substance, i.e., whose entropy value is greater than its distortion in the reaction

of the participant. Table 3 shows that at the zero temperature without electric field, the value of

entropy of optimized molecule is zero. On the other hand, it is found from table 4 that entropy and heat of capacity is increased with increasing temperature.

Table 3: Thermophysical properties

Properties	L01	L02	L03	L04
Total energy, (kcal/mol)	-3159536.19	-3273037.55	-3311028.49	-3015629.47
Entropy, (kcal/mol-deg)	0	0	0	0
Free energy, (kcal/mol)	-3159536.19	-3273037.55	-3311028.49	-3015629.47
Heat capacity, (kcal/mol-deg)	0	0	0	0
Dipole moment, (D)	0	0	0	0
RMS gradient, (kcal/mol)	0	0	0	0
Binding energy, (kcal/mol)	-3159536.19	-3273037.55	-3311028.49	-3015629.47
Electronic energy,(kcal/mol)	-3580683.64	-3976688.55	-4438431.58	-4654099.65
Nuclear energy, (kcal/mol)	421147.450	703650.999	1127403.091	1638470.185

Table 4: Entropy and Heat capacity in different temperature

	273 K		298 K		323 K	
	Entropy	Heat capacity, (kcal/mol-deg)	Entropy	Heat capacity, (kcal/mol-deg)	Entropy	Heat capacity, (kcal/mol-deg))
L01	0.07008	0.010338	0.0712	0.0107	0.0722	0.0112
L02	0.07046	0.007458	0.0713	0.0077	0.0721	0.0080
L03	0.07200	0.007138	0.0729	0.0074	0.0737	0.0077
L04	0.07498	0.008278	0.0758	0.0085	0.0768	0.0088

3.8. Vibrational spectrum

The vibrational spectrum is the characteristic peak of any molecule for identification similar to the FTIR peak. To optimize these molecules for vibrational peak obtain the identified peak in the different region about 0 to 5800 cm^{-1} at which the main characteristic peak of tetraamine palladium(II) complex ion is almost 4200-4300, 3825- 3900 and 3600-3550 cm^{-1} and represented in fig-06.
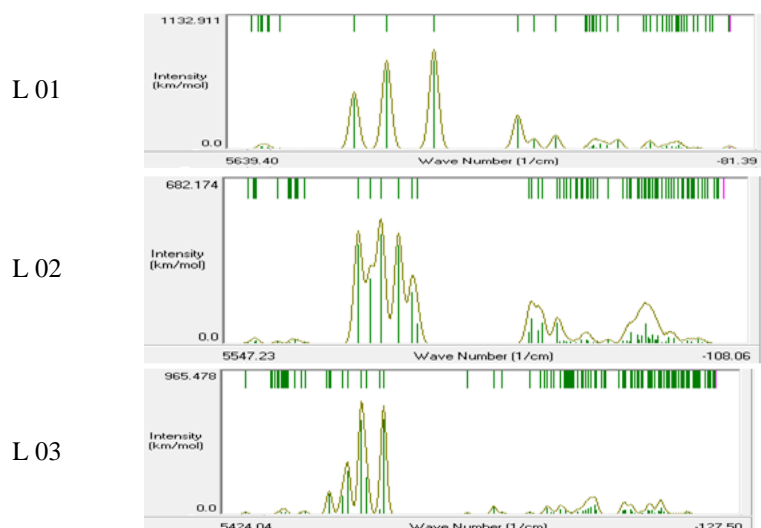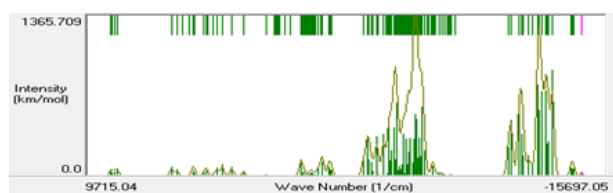
L 04

Figure 6. Vibrational spectrum

Table 5. Data for a vibrational spectrum of palladium (II) complex ions

	Normal mode	Degeneracy	Frequency	Intensity	Symmetry
L01	1	1	178.65	18.201	1 A
L02	1	1	149.0	0.994	1 A
L03	1	1	124.84	0.517	1 A
L04	1	1	-14541.96	37.383	1 A

3.9. UV-visible Spectrum

UV-visible Spectrum provides a powerful technique by which the nature of metal ligands bonding may be identified. A remarkable covalency between almost all of the upper filled molecular orbitals of the ligand cluster and the metal d orbitals of suitable symmetry can be calculated. Those interactions which arise from ligand orbitals of n symmetry primarily involve filled metal 4dxz and 4dyz orbitals and, although of importance, do not result in significant Pd (II) overlap since contributions due to filled bonding and anti-bonding levels tend to cancel one another. However, the interactions with orbitals of symmetry involve empty 4dxy and 5s metal orbitals and result in important ligand-to-metal charge transfer [30].

The UV-visible spectrum of the tetra-amine palladium (II) complex ion shows in fig 7 with table 6, a strong transition (e near 250 and 360 nm, as well as an ultraviolet band of weaker intensity near 320 nm.
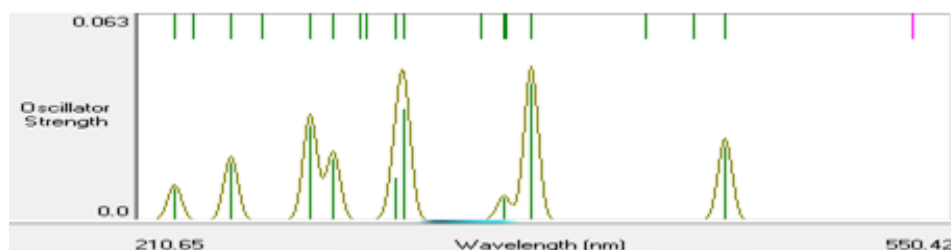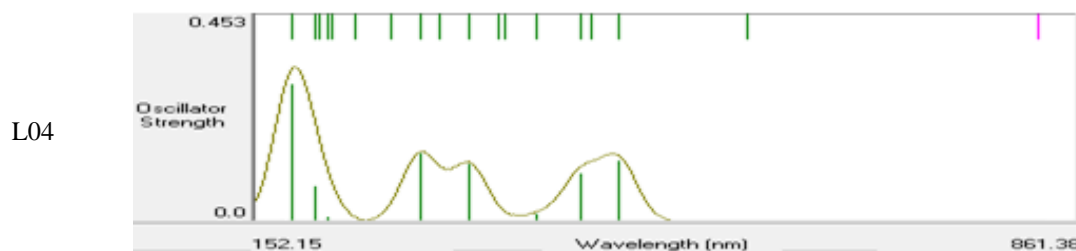
L01

L02

L03

L04
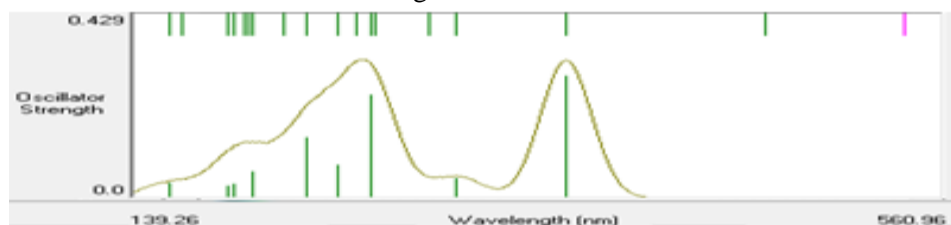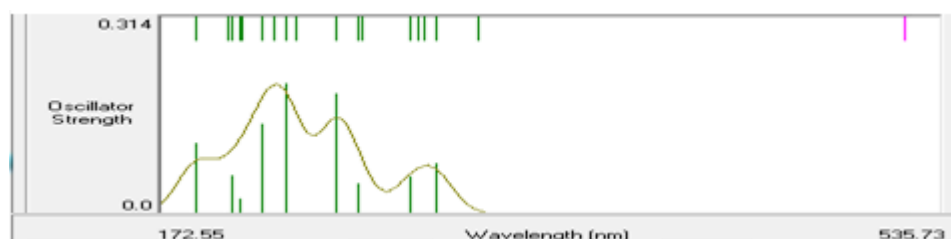
Figure 7: UV-visible Spectrum

Table 6. Data for different transition state, spin multiplicity, wavelength and oscillator strength for UV –visible spectrum

	Transition	Degeneracy	Spin Multiplicity	Wavelength	Oscillator Strength
L01	1	1	Triplet	541.79	0.0
L02	1	1	Triplet	519.22	0.0
L03	1	1	Triplet	534.98	0.0
L04	1	1	Triplet	829.14	0.0

4. THE BIOLOGICAL ACTIVITY OF OPTIMIZED MOLECULES

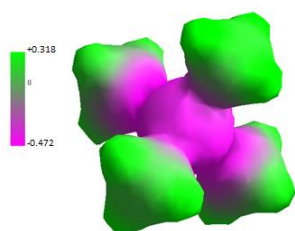### 4.1. The distribution electrostatic potential in case of 3D mapped structure

The stability of the studied molecular structure is given by the higher negative values of total energy. The biological activity of a compound can be estimated on the basis of the energy difference ΔE frontier orbitals given in table-07. This difference, ΔE represents the electronic excitation energy which is possible in a molecule. The electrostatic potential in view of the 3D mapped structure in fig 08 indicates positive and negative charge region and the charged surface area in a molecule that is considered as the best tools to estimate the biological activity parameter [31].

According to the mechanism of antimicrobial activity and antimicrobial agents of bioactive molecules, the positive charge end of molecules is responsible to damage the plasma membrane of pathogens [32]. To kill the different human pathogenic microorganism, the region of molecules was used the positive charge area of the molecule. In this case, the most important factors are explained that the higher surface area having a positive charge is considered as the high antimicrobial activity.
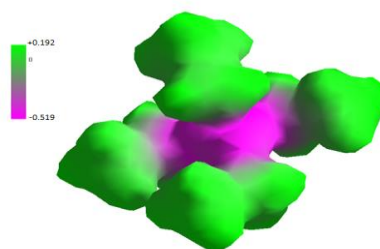
The three-dimensional geometry of molecular electrostatic potential distribution highlights the existence of three regions with increased electronegativity in the whole molecule of L01, L02 and highly positivity in L03 and L04 shown in fig-08 and which play a role in their coupling to different structures in which ions are positively charged.

L01

L02

L03

L04

Figure 8: The 3D geometry of the distribution electrostatic potential

Table 7. Data of electrostatic potential energy difference of two levels

	L01	L02	L03	L04
E1	+0.318	+0.192	+2.907	+0.754
E2	-0.472	-0.519	-4.463	-5.654
ΔE= E2-E1	-0.790	-0.711	-7.370	-6.408

Here, E1 = Electrostatic potential energy in positive value, E2 = Electrostatic potential energy in negative value and ΔE = Electrostatic potential energy difference of two level.

4.2. Chemical reactivity

The HOMO and LUMO energies are used for the determination of global reactivity descriptors. It is important that electrophilicity (ω), the chemical potential (μ), electronegativity (χ), hardness (η) and softness (S) be put into a molecular orbital's framework. We focus on the HOMO and LUMO energies in order to determine the interesting molecular/atomic properties and chemical

quantities. These are calculated as following equations, and given in table 08.

$$(\mu) = -\frac{I+A}{2} \tag{3}$$

$$(\eta) = \frac{I-A}{2} \tag{4}$$

$$(S) = \frac{1}{\eta} \tag{5}$$

$$(\chi) = \frac{I+A}{2} \tag{6}$$

$$(\omega) = \frac{\mu^2}{2\eta} \tag{7}$$

Table 8. Chemical reactivity

	L01	L02	L03	L04
Hardness, (η)	5.3943	0.2993	0.2509	5.3677
Softness, (S)	0.1854	3.3411	3.9856	0.1863
Electrophilicity (ω),	10.7203	526.7949	1090.8466	97.3092
Chemical potential, (μ)	-10.7544	-17.7578	-23.3963	-32.3211
Electronegativity, (χ)	10.7544	17.7578	23.3963	32.3211

4.3. Quantitative structure - activity relationships (QSAR)

The molecule with minimum binding energy will have the maximum binding affinity and having the maximum binding affinity, indicating as the best molecule for drug leads molecules targeting computationally. In case of the biological activity of a molecule, the surface area is considered as an

important parameter. Greater charge surface area of a molecule can be able to kill more pathogens. The greater positive charge surface area means a higher biological activity. On the other hand, a negative value of logP indicates the hydrophilicity and positive LogP indicates the hydrophobicity that plays an important role in biochemical interactions and bioactivity [33, 34].

Hydrophobic drugs tend to be more toxic because, in general, are kept

longer, have a wider distribution in the body, are somewhat less selective in their binding to molecules and finally are often extensively metabolized.

Finally, the correlation of L01, L02, L03, and L04 complexes ion are increased the biological activity as increasing the size of ligands with fine correlation showing in table 09.

4.4. Calculation of PIC50

The correlation between the biological activity and descriptor is developed by Zineb Almi et.al. 2014 [35] for the PIC50 value calculation from the Hyperchem simulation value that is given in the following equation as:

$$\begin{aligned} PIC50 = {} & 3.028 - 0.542 logP + 0.352\,HE - 1.272\,Pol \\ & + 0.863 MR - 0.038\,MV \\ & - 0.024 MW + 19.120 q01 \\ & + 0.024 SAG \end{aligned}$$

Here, HE = Hydration Energy, Pol = Polazibility, MR = Molecular Refractivity, LogP = Partition coefficient, MV = Molar Volume, MW = Molar Weight, SAG = Surface Area Grid, q01 = atomic net charges.

According to Zineb Almi et.al. 2014 [35], the biologically active molecule have PIC50 less value -200. From the table 10, the computed molecule of palladium (II) complex ion has the value of more 20 to 225 that means have biological activity and increasing length or number of methyl groups in amine ligands, the biological activity increases. In the L03 and L04 have the highest biological activity near to standard bioactive molecules.

Table 9. Data for QSAR study

	L01	L02	L03	L04
Partial charge (e)	0.00	0.00	0.00	0.00
Surface Area(grid),	286.86	365.65	412.23	439.46
Volume, Å^3	401.50	586.90	713.83	806.95
Hydration Energy kcal/mol	-43.34	-10.91	0.86	4.79
Log P	-3.91	-2.93	-1.94	-0.95
Refractivity Å^3	9.60	29.19	48.77	68.36
Polarizibility, Å^3	4.74	12.08	19.42	26.76
Mass (amu)	174.52	230.63	286.74	342.84

Table 10. Data of PIC50

	L01	L02	L03	L04
PIC50	-20.41	-8.46	-1.69	1.83

4.5. Correlation and comparison study in case of substituent groups in amine ligands

In the case of chemical reactivity, the LUMO-HOMO gap in presence of H atom in NH₃ and 3CH₃ in N-atom is 10.7804 and 10.7354 eV which is larger value meaning lower reactivity and almost the same. On the other hand, attaching one and two methyl group in amine ligand, the LUMO-HOMO gap is 0.5986 and 0.5019 eV which means that attaching two

methyl groups has higher reactivity that one methyl group.

The most important comparison in thermophysical properties is explained that with increasing the temperature, the entropy and heat capacity increases in poor amount and with increasing methyl group in amine ligand the entropy change is an amount of 0.00 0.00038, 0.00154 and 0.0029 kcal/mol. The heat capacity

is also decreased as $3CH_3 < 2CH_3 < CH_3 < H$ or
primary < secondary < tertiary.

Table 11: Correlation among all palladium (II) complex ions

	Pi, π		Refractivity, (MR)		Surface Area, (SA)	
Pi, π		Biological activity		Biological activity	SA	Biological activity
H	0.0	--	0.0	--	0.0	Correlation occurs
CH_3	-0.98	Less	+19.59	Less	+78.79	
$2CH_3$	-1.97	Less	+39.17	Less	+125.37	
$3CH_3$	-2.96	Less	+58.76	Less	+152.60	
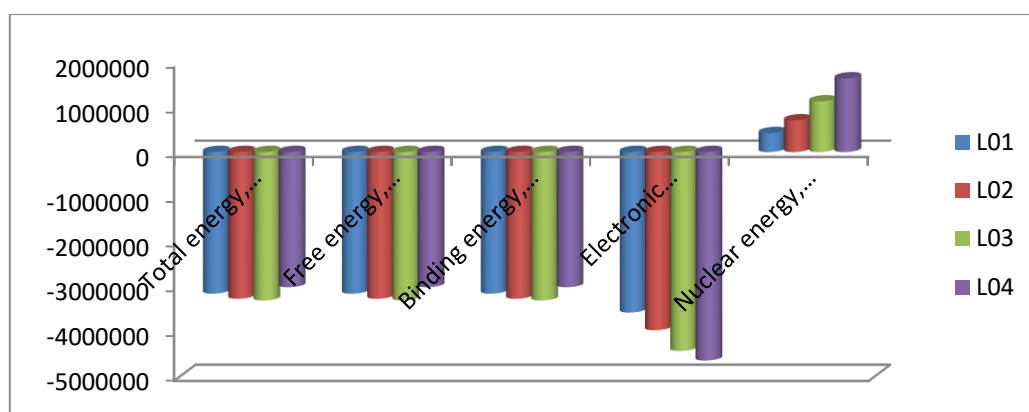
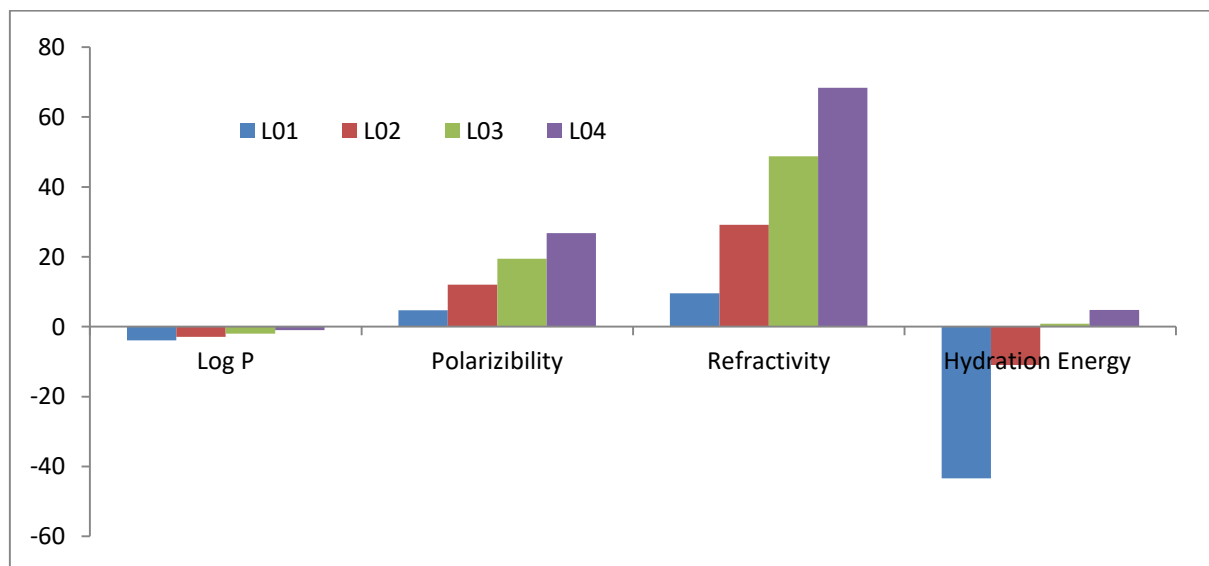**Figure 9.** Comparison of thermophysical properties
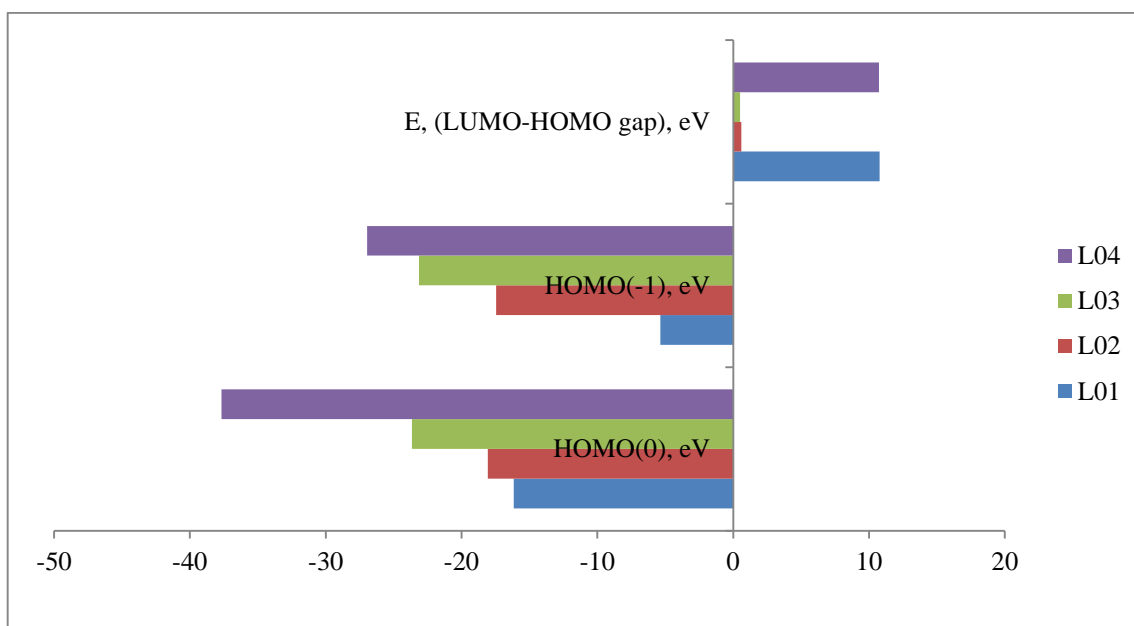

Figure 10. Comparison of QSAR

Figure 11. Comparison of the gap with chemical reactivity
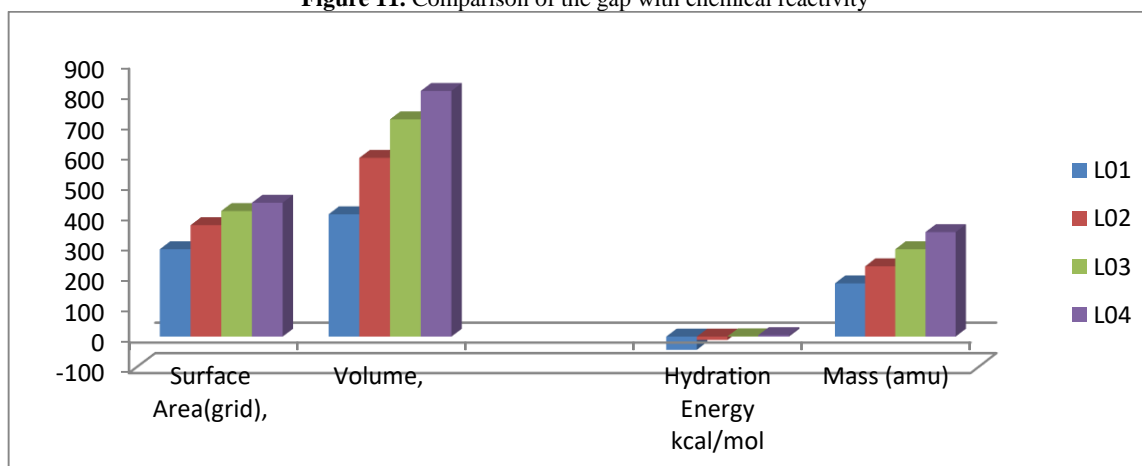

Figure12. Comparison of molecular properties

From figure 9, 10, 11, 12, it was found that biological activity increases with the increase the alkyl groups in palladium (II) complex ions.

5. CONCLUSION

The DFT method was used to characterize and optimize of palladium (II) complex ions with amine ligands and the thermophysical and chemical and biological properties were recorded. From the spectroscopy studies, the vibration, degeneracy, symmetry, and splitting of d orbitals give the information in the analytical method. In the case of HOMO, LUMO, and HOMO – LUMO gap can be informed that palladium (II) complex ions with amine ligands are chemically reactive for further uses. As the value of LogP is negative, palladium (II) complex ions with amine ligands are hydrophilic nature that is why the toxicity is very less and supports the safe uses in all areas.

REFERENCES

[1] Valderrama S., Van Roekel N., Andersson M., Goodacre C. J., Munoz C. A., A comparison of the marginal and internal adaptation of titanium and gold-platinum-palladium metal ceramic crowns, International Journal of Prosthodontics, 1995. 8(1).

[2] Atkinson R.H., A volumetric method for the rapid assay of palladium jewellery alloys, Analyst, 79-939 (1954) 368-370.

[3] Faurschou A., Kapa E. A., Metal allergen of the 21st century—a review on exposure, epidemiology and clinical manifestations of palladium allergy, Contact Dermatitis, 64-4 (2011) 185-195.

[4] Garrett C. E. P., Kapa, The art of meeting palladium specifications in active pharmaceutical ingredients produced by Pd-catalyzed reactions, Advanced Synthesis & Catalysis, 346-8 (2004) 889-900.

[5] Torborg C., Beller M., Recent applications of palladium-catalyzed coupling reactions in the pharmaceutical, agrochemical, and fine chemical industries, Advanced Synthesis & Catalysis, 351-18 (2009) 3027-3043.

[6] Doucet H. H., Jean-Cyrille, Palladium coupling catalysts for pharmaceutical applications, Current opinion in drug discovery & development, 10-6 (2007) 672-690.

[7] Ray S., Mohan R., Singh J. K., Samantaray MK, Shaikh MM., Anticancer and antimicrobial metallopharmaceutical agents based on palladium, gold, and silver N-heterocyclic carbene complexes, Journal of the American Chemical Society, 129-48 (2007) 15042-15053.

[8] Schmidt A., Molano V., Hollering M., Pöthig A., Casini A., Kühn F. E., Evaluation of new palladium cages as potential delivery systems for the anticancer drug cisplatin, Chemistry–A European Journal, 22-7 (2016) 2253-2256.

[9] Khan H., Badshah A., Murtaz G. , Said M., Rehman Z.-ur, Neuhausen C., Todorova M., Jean-Claude B. J., Butler I. S., Synthesis, characterization and anticancer studies of mixed ligand dithiocarbamate palladium (II) complexes, European journal of medicinal chemistry, 46-9 (2011) 4071-4077.

[10] Rebolledo A. P., Vieites M., Gambino D., Piro O. E., Castellano E. E., Palladium (II) complexes of 2-benzoylpyridine-derived thiosemicarbazones: spectral characterization, structural studies and cytotoxic activity, Journal of inorganic biochemistry, 99-3 (2005) 698-706.

[11] Matesanz, A. I. P., José M., Navarro P., Moreno J. M., Colacio E., Souza P., Synthesis and characterization of novel palladium (II) complexes of bis (thiosemicarbazone). Structure, cytotoxic activity and DNA binding of Pd (II)-benzyl bis (thiosemicarbazonate), Journal of inorganic biochemistry, 76-1 (1999) 29-37.

[12] Ohff M., Ohff A., van der Boom M. E., Milstein D., Highly active Pd (II) PCP-type catalysts for the Heck reaction, Journal of the American Chemical Society, 119-48 (1997) 11687-11688.

[13] Old D. W., Wolfe J. P., Buchwald S. L., A highly active catalyst for palladium-catalyzed cross-coupling reactions: room-temperature Suzuki couplings and amination of unactivated aryl chlorides, Journal of the American Chemical Society, 120-37 (1998) 9722-9723.

[14] Dai C. F., Gregory C., The first general method for palladium-catalyzed Negishi cross-coupling of aryl and vinyl chlorides: use of commercially available Pd (P (t-Bu) 3) 2 as a catalyst, Journal of the American Chemical Society, 123-12 (2001) 2719-2724.

[15] Shapiro A. H., The Dynamics and Thermodynamics of Compressible Fluid Flow: In Two Volumes. 1953: Wiley.

[16] Von Bertalanffy L., The theory of open systems in physics and biology, Science, 111-2872 (1950) 23-29.

[17] Frank H. S., Evans M. W., Free volume and entropy in condensed systems III. Entropy in binary liquid mixtures; partial molal entropy in dilute solutions; structure and thermodynamics in aqueous electrolytes, The Journal of Chemical Physics, 13-11 (1945) 507-532.

[18] Guggenheim E. A., Thermodynamics-an advanced treatment for chemists and physicists, Amsterdam, North-Holland, 414 (1985) 1985.

[19] Hossain M. I., Ajoy K., Synthesis and Characterization of Ammonium Ionic Liquids and Their Antimicrobial and Computational Overview, Asian journal of chemical science, 3-4 (2018) 1-10.

[20] Hossain M. I., Kumer A., Begum S. H., Synthesis and Characterization of Ammonium Benzoate and Its Derivative Based Ionic Liquids and Their Antimicrobial Studies, Asian

journal of physical and chemical science, 3-4 (2018) 1-9.

[21] Becke, A. D., Density-functional thermochemistry. III. The role of exact exchange, The Journal of chemical physics, 98-7 (1993) 5648-5652.

[22] Janak, J. F., Proof that $\partial E \partial n$ i= ε in density-functional theory, Physical Review, 18-12 (1978) 7165.

[23] Howard A., McIver J., Collins J., Hyperchem computational chemistry, Hypercube Inc., Waterloo, 1994.

[24] Gill P. M. J., Johnson B. G., Pople J. A., Frisch M. J, The performance of the Becke—Lee—Yang—Parr (B—LYP) density functional theory with various basis sets, Chemical Physics Letters, 197-4,5 (1992) 499-505.

[25] Miehlich B., Savin A., Stoll H., Preuss H., Results obtained with the correlation energy density functionals of Becke and Lee, Yang and Parr, Chemical Physics Letters, 157-3 (1989) 200-206.

[26] Lechner W., Dellago C., Accurate determination of crystal structures based on averaged local bond order parameters, The Journal of chemical physics, 129-11 (2008) 114707.

[27] Kumer A., Ahmed B., Sharif Md A., Al-Mamun A., A Theoretical Study of Aniline and Nitrobenzene by Computational Overview, Asian journal of physical and chemical science, 4-2 (2017) 1-12.

[28] Koopmans Y. T., Uber die zuordnung von wellenfunktionen und eigenwerten zu den,einzelnen elektronen eines atoms, Physica, 1-1,6 (1934) 104-113.

[29] Canadell E., Ravy S., Pouget J. P., Brossard L., Concerning the band structure of D (M (dmit) 2) 2 (D= TTF, Cs, NMe4); M= Ni, Pd) molecular conductors and superconductors: Role of the M (dmit) 2 Homo and Lumo, Solid State Communications, 75-8 (1990) 633-638.

[30] Böhm M., Stürzebecher J, Klebe G., Three-dimensional quantitative structure− activity relationship analyses using comparative molecular field analysis and comparative molecular similarity indices analysis to elucidate selectivity differences of inhibitors binding to trypsin, thrombin, and factor Xa, Journal of medicinal chemistry, 42-3 (1999) 458-477.

[31] Timofeeva L., Kleshcheva N., Antimicrobial polymers: mechanism of action, factors of activity, and applications, Applied microbiology and biotechnology, 89-3 (2011) 475-492.

[32] Kumer A., Sarker N., Paul S., Zannat A., The Theoretical Prediction of Thermophysical properties, HOMO, LUMO, QSAR and Biological Indics of Cannabinoids (CBD) and Tetrahhdrocannabinol (THC) by Computational Chemistry, Advanced Journal of Chemistry, 3-3 (2019) 1-13.

[33] Kumer A., Sarker M. N., Paul S., The theoretical investigation of HOMO, LUMO, thermophysical properties and QSAR study of some aromatic carboxylic acids using HyperChem programming, International Journal of Chemistry and Technology, 3-1 (2019) 26-37.

[34] Almi Z., Belaidi S., Lanez T., Tchour N., Structure Activity Relationships, QSAR Modeling and Drug-like calculations of TP inhibition of 1,3,4- oxadiazoline-2-thione Derivatives, International Letters of Chemistry, Physics and Astronomy, 37 (2014) 113-124.

Antifungal Activity of Some Benzimidazole-Hydrazones

Ulviye ACAR ÇEVİK [1,2] iD *, Derya OSMANİYE [1,2] ** iD

[1] *Department of Pharmaceutical Chemistry, Faculty of Pharmacy, Anadolu Universty, Eskişehir, Turkey*
[2] *Doping and Narcotic Compounds Analysis Laboratory, Faculty of Pharmacy, Anadolu Universty, Eskişehir, Turkey*

Abstract. In the present work, 15 4-(1-(prop-2-in-1-yl)-1*H*-benzoimidazole-2-yl)-*N*'-(substitutedmethylene)benzohydrazide derivatives (**4a**-**4o**) were re-synthesized to evaluate their antifungal activity. Structure identification of synthesized compounds was elucidated by ^{1}H-NMR, ^{13}C-NMR, and HRMS spectroscopic methods. Inhibitory potential of the re-synthesized compounds was investigated against *Candida supp*. The compounds **4e** and **4l** showed significant anti fungal activity. Consistent with the activity studies, **4e** was found to be potent derivative with its MIC_{50} value of (1.95 µg/mL) against *Candida glabrata*. And **4l** was found to be potent derivative with its MIC_{50} value of (1.95 µg/mL) against *Candida krusei*.

Keywords: Benzimidazole, Hydrazone, Antifungal activity, NMR, HRMS

Bazı Benzimidazol-Hidrazonların Antifungal Etkinliği

Özet. Mevcut çalışmada, 15 4-(1-(prop-2-in-1-il)-1*H*-benzimidazol-2-il)-*N*'-(sübstitüemetilen) benzohidrazit türevleri **(4a-4o),** antifungal aktivitelerini değerlendirmek üzere yeniden sentezlendi. Sentezlenen bileşiklerin yapı tanımlamaları ^{1}H-NMR, ^{13}C-NMR ve HRMS spektroskopik yöntemlerle açıklandı. Yeniden sentezlenen bileşiklerin antifungal etkinlikleri Candida türlerine karşı değerlendirildi. Bileşik **4e** ve **4l** önemli aktivite gösterdi. Aktivite çalışmaları ile uyumlu olarak, **4e** bileşiği *Candida glabrata*'ya karşı 1.95 µg / mL MIC_{50} değeri ile güçlü bir türev olarak bulundu. Aynı zamanda **4l** bileşiği *Candida krusei*'ye karşı 1.95 µg / mL MIC_{50} değeri ile güçlü bir türev olarak bulundu.

Anahtar Kelimeler: Benzimidazol, Hidrazon, Antifungal aktivite, NMR, HRMS

1. INTRODUCTION

Life loss depending on fungal infections are more than 1.35 million per year worldwide [1]. *Aspergillus spp*., *Cryptococcus neoformans* and *Candida spp*. are still the three main pathogens of fungal infections. Over the last few decades, the occurrence of systemic fungal infections has increased considerably in immunocompromised hosts, particularly patients who receive cancer chemotherapy or patients with AIDS and undergone organ transplantation [1-3]. Some research teams stated that *Candida albicans* (*C. albicans*) which caused severe mucosal infections with potentially fatal invasive infections was the most common fungus in these patients [4, 5]. On the other hand, only a restricted number of antifungal agents are formerly accessible to treat these life-threatening fungal infections [6]. Presently, clinical antifungal agents can be separated into four classes: Echinocandins (such as Micafungin and Caspofungin), antimetabolites (such as 5-fluorocytosine) polyenes (such as Nystatin and Amphotericin B) and azoles (such as Itraconazole and Fluconazole) [2,3].

Azoles inhibits lanosterol 14-α-demetilase enzyme; which is responsable for converting lanosterol into ergosterol. Ergosterol is the major component of fungal cytoplasmic membranes and responsable for bioregulation of membrane assymmetry [7]. Azoles are first-line drug for fungal infections due to their wide antifungal spectrum, high potency and low toxicity [8]. However, some problems remain, such as severe drug resistance, cytotoxicity. However, emergence of drug resistance, environmental hazards and other problems objectively indicate the urgent need for novel antifungal agents [2,9].

Nitrogen heterocycles are common structural motifs in compounds with antifungal activity [4]. Benzimidazole that was an important heterocyclic nucleus that has been used extensively in medicinal chemistry is a component of vitamin B12 and is related to the DNA base purine and the stimulant caffeine. Substituted benzimidazole displays a broad spectrum of potential pharmacological activities such as antiinflammatory, anti-tubercular, anticancer, antibacterial, antiviral and antifungal activity. [5-7, 9, 10-17]. In addition to benzimidazole derivatives, hydrazone based compounds, which bear an azomethine -NHN=CH- functional group, have showed antifungal activity [18,19].

Based on the above information, antifungal activities of the compounds containing benzimidazole and hydrazone residues were the subject of curiosity. For this purpose, we resynthesized some benzimidazole-hydrazone based upon the studies that reported the antifungal potentials [20].

2. MATERIALS AND METHODS
2.1. Chemistry

All chemicals used in the syntheses were purchased either from Sigma-Aldrich Chemicals (Sigma-Aldrich Corp., St. Louis, MO, USA) or Merck Chemicals (Merck KGaA, Darmstadt, Germany). Melting points of the obtained compounds were determined by MP90 digital melting point apparatus (Mettler Toledo, OH, USA) and were uncorrected. The IR spectra were obtained on a Shimadzu, IR Prestige-21 (Shimadzu, Tokyo, Japan). ^{1}H NMR and ^{13}C

NMR spectra of the synthesized compounds were registered by a Bruker 300 MHz and 75 MHz digital FT-NMR spectrometer (Bruker Bioscience, Billerica, MA, USA) in DMSO-d_6, respectively. Splitting patterns were designated as follows: s: singlet; d: doublet; t: triplet; m: multiplet in the NMR spectra. Coupling constants (J) were reported as Hertz. M+1 peaks were determined by Shimadzu LC/MS ITTOF system (Shimadzu, Tokyo, Japan). All reactions were monitored by thin-layer chromatography (TLC) using Silica Gel 60 F254 TLC plates (Merck KGaA, Darmstadt, Germany).

2.1.1. General procedure for the synthesis of target compounds (**4a-4o**)

In order to determine the antifungal activity, synthesis studies were carried out for compound **4a-4o**. Synthesis studies was performed by means of previous study reported by our research group [20].

2.2. Antifungal Activity

The *in vitro* antifungal activities of all resynthesized derivatives **4a**–**4o** were screened at between 1 mg/mL–1.95 µg/mL concentrations using various Candida strains including *C. albicans (ATCC 90030), C. glabrata (ATCC 90030) C. krusei (ATCC 6258)* and *C. parapsilopsis (ATCC 22019)* and following the protocol of the EUCAST in keeping with the previous studies reported by our research group [21, 22].

3. RESULTS AND DISCUSSIONS
3.1. Chemistry

The compounds **4a-4o** were re-synthesized as summarized in **Scheme 1**. Compound **1** was synthesized under microwave irradiation using 1,2-phenylenediamine and methyl 4-formylbenzoate. Reaction of Methyl 4-(1*H*-benzo[d]imidazol-2-yl)benzoate and propargyl bromide gave the compound **2**. Reaction of the methyl 4-(1-(prop-2-in-1-yl)-1*H*-benzo[d]imidazole-2-yl)benzoate (**2**) and hydrazine hydrate gave 4-(1-(prop-2-in-1-yl)-1*H*-benzo[d]imidazole-2-yl)benzohydrazide (**3**). Reaction of compound 3 and aldehydes afforded to the target compounds (**4a-4o**).

Structural elucidation of the synthesized compounds (**4a-4o**) was carried out by spectral analyses including IR, ^{1}H-NMR, ^{13}C-NMR and

HRMS. All the results of the analysis are in accordance with our previous report [20].
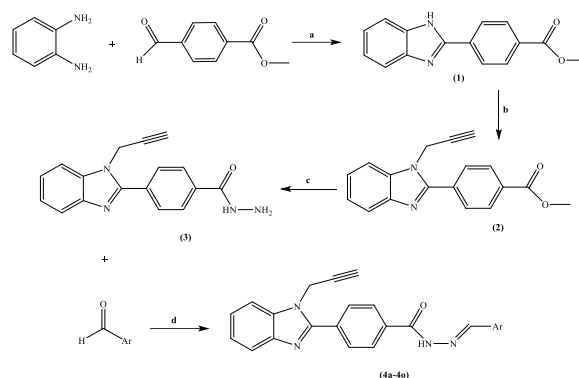
Comp.	Ar	Comp.	Ar
4a	Thiophen-2-yl	**4i**	4-Methoxyphenyl
4b	5-Nitro-thiophen-2-yl	**4j**	2-Methoxyphenyl
4c	Pyrrol-2-yl	**4k**	3-Methoxyphenyl
4d	1-Methyl-pyrrol-2-yl	**4l**	3-Hydoxyphenyl
4e	Pyridin-3-yl	**4m**	3,5-Dihydoxyphenyl
4f	4-Fluorophenyl	**4n**	3,5-Dimethoxyphenyl
4g	4-Chlorophenyl	**4o**	2,3-Dimethoxyphenyl
4h	4-Hydroxyphenyl		

Scheme 1: Synthesis way of the compounds **4a-4o**. **Reagents and Conditions: a:** Na$_2$S$_2$O$_5$ /DMF, Microwave irradiation, 240 ^{o}C, 10 bar, 5 + 5 min. **b:** NaH/DMF, propargyl bromide, r.t, 20 h. **c:** NH$_2$NH$_2$.H$_2$O (%100), Microwave irradiation, 150°C, 10 bar, 10 min. **d:** EtOH/CH$_3$COOH, reflux, 2 h.

Table 1. MIC$_{50}$ (µg/mL) values of compounds **4a**-**4o**.

Comp.	*C. albicans*	*C. glabrata*	*C. krusei*	*C. parapsilosis*
4a	>1000	>1000	62.50	>1000
4b	>1000	>1000	>1000	>1000
4c	>1000	>1000	62.50	>1000
4d	**1.95**	>1000	>1000	>1000
4e	125	**1.95**	>1000	>1000
4f	>1000	>1000	>1000	>1000
4g	>1000	>1000	>1000	>1000
4h	**1.95**	>1000	>1000	15.63
4i	>1000	>1000	>1000	>1000
4j	**1.95**	>1000	>1000	>1000
4k	>1000	>1000	>1000	>1000
4l	15.63	>1000	**1.95**	>1000
4m	>1000	125	7.81	>1000
4n	>1000	>1000	>1000	>1000
4o	>1000	>1000	31.25	>1000
Ketoconazole	0.98	1.95	1.95	1.95
Fluconazole	0.98	1.95	1.95	0.98

3.2. Antifungal Activity

According to the protocol of the EUCAST reported previously by our research group [21, 22], all obtained compounds **4a**-**4o** were screened for their *in vitro* antifungal activity against four pathogenic fungi;

C. albicans (ATCC 90030), C.glabrata (ATCC 2001), C. krusei (ATCC 6258), C. parapsilosis (ATCC 22019). Ketoconazole and fluconazole were used as reference drugs. The results of antifungal activities are listed in **Table-1**. Compounds **4d**, **4h** and **4j** were determined to have MIC$_{50}$ values of 1.95 µg/ml against *C. albicans*. On the other hand, Compounds **4e** and

4l were determined to have MIC$_{50}$ values of 1.95 µg/ml against *C. glabrata* and *C. krusei*, respectively. This MIC$_{50}$ values is the same as the MIC$_{50}$ values of reference drugs against *C. glabrata* and *C. krusei*. Compound **4e** bearing pyridin-3-yl possessed good activity against *C. glabrata* with an MIC value of 1.95 µg/mL. Compound **4l** including 3-hydroxyphenyl possessed good activity against *C. krusei* with an MIC value of 1.95 µg/mL. However compound **4m** bearing 3,5-dihydoxyphenyl had weak antifungal activity. This information suggests that the hydroxy group brought to the fifth position of phenyl ring reduces the antifungal activity. The lack of activity of the methoxy-containing derivative in the third position of phenyl (**4k**) indicates that the replacement of the hydrogen and methyl group of the hydroxyl group decreases the This information suggests that hydroxyl hydrogen in the third position of phenyl ring enhances activity propably by making hydrogen bonds.

4. CONCLUSION

In summary, a series of benzimidazole-hydrazone derivatives were re-synthesized and evaluated for their antifungal activity. The primary results indicated that obtained compounds **4a**–**4o** displayed antifungal activities within different ranges. Compounds **4e** and **4l** displayed significant activity against *C. glabrata* and *C. krusei*, respectively. Compound **4e** bearing pyridine-3-yl and compound **4l** bearing 3-hydroxyphenyl came to the fore in the series. We assume that the aromatic ring bound to the hydrazone group contributes to the antifungal activity by means of long-pair electron in third position. However, if the hydroxyl group at position third of phenyl ring is replaced by a methoxy group, the activity decreases activity. This information suggests that the steric hindrance of the methyl group abolishes the effect of the long-pair electron, or that the hydroxyl hydrogen's ability to form hydrogen bonds contributes to activity.

REFERENCES

[1] Wang S.Q., Wang Y.F., Xu Z., Tetrazole hybrids and their antifungal activities, Eur. J. Med. Chem., 170 (2019) 225-234.

[2] Zhao L., Tian L., Sun N., Chen Y., Wang X., Zhao S., Su X., Zhao D., Cheng M., Design, synthesis, and structure-activity relationship studies of l-amino alcohol derivatives as broad-spectrum antifungal agents, Eur. J. Med. Chem., 177 (2019) 374-385.

[3] Zhao S., Zhang X., Wei P., Su X., Zhao L., Wu M., Hao C., Liu C., Zhao D., Cheng M., Design, synthesis and evaluation of aromatic heterocyclic derivatives as potent antifungal agents. Eur. J. Med. Chem., 137 (2017) 96-107.

[4] Lino C.I., de Souza I.G., Borelli B.M., Silverio Matos T.T., Santos Teixeira I.N., Ramos J.P., de Souza Fagundes E.M., de Oliveira Fernandes P., Maltarollo V.G., Johann S., de Oliveira R.B., Synthesis, molecular modeling studies and evaluation of antifungal activity of a novel series of thiazole derivatives, Eur. J. Med. Chem., 151 (2018) 248-260.

[5] Shi Y., Jiang K., Zheng R., Fu J., Yan L., Gu Q., Zhang Y., Lin F., Design, Microwave-Assisted Synthesis and in Vitro Antibacterial and Antifungal Activity of 2,5-Disubstituted Benzimidazole, Chem. Biodiversity, 16 (2016) 1800510.

[6] Villa P., Arumugam N., Almansour A.I., Kumar R.S., Mahalingam S.M., Maruoka K., Thangamani S., Benzimidazole tethered pyrrolo[3,4-b]quinoline with broad-spectrum activity against fungal pathogens, Bioorg. Med. Chem. Lett., 29 (2019) 729-733.

[7] Karaburun A.C., Kaya Çavuşoğlu B., Acar Çevik U., Osmaniye D., Sağlık B.N., Levent S., Özkay Y., Atlı Ö., Koparal A.S., Kaplancıklı Z.A., Synthesis and Antifungal Potential of Some Novel Benzimidazole-1,3,4-Oxadiazole Compounds, Molecules, 24 (2019) 191.

[8] Wu J., Ni T., Chai X., Wang T., Wang H., Chen J., Jin Y., Zhang D., Yu S., Jiang Y., Molecular docking, design, synthesis and antifungal activity study of novel triazole derivatives, Eur. J. Med. Chem., 143 (2018) 1840-1846.

[9] Si W.J., Wang X.B., Chen M., Wang M.Q., Lu A.M., Yang C.L., Design, synthesis, antifungal

activity and 3D-QSAR study of novel pyrazole carboxamide and niacinamide derivatives containing benzimidazole moiety, New. J. Chem., 43 (2019) 3000.

[10] Kashid B.B., Ghanwat A.A., Khedkar V.M., Dongare B.B., Shaikh M.H., Deshpande P.P., Wakchaure Y.B., Design, Synthesis, In Vitro Antimicrobial, Antioxidant Evaluation, and Molecular Docking Study of Novel Benzimidazole and Benzoxazole Derivatives, J. Heterocycle. Chem., 56 (2019) 895.

[11] Yadav S., Lim S.M., Ramasamy K., Vasudevan M., Ali Shah S.A., Mathur A., Narasimhan B., Synthesis and evaluation of antimicrobial, antitubercular and anticancer activities of 2-(1-benzoyl-1H-benzo[d] imidazol-2-ylthio)-N-substituted acetamides, Chemistry Central Journal, 12-66 (2018) 1-14.

[12] Abdel-Wahab S.M., Abdelsamii Z.K., Abdel-Fattah H.A., El-Etrawy A.S., Dawe L.N., Swaroop T.R., Georghiou P.E., Synthesis of 2-Aryl- and 2-Haloarylbenzimidazole-N1-acetamido Conjugates and a Preliminary Evaluation of Their Antifungal Properties, ChemistrySelect, 3 (2018) 8106-8110.

[13] Chandrika N.T., Shrestha S.K., Ngo H.X., Tsodikov O.V., Howard K.C., Garneau-Tsodikova S., Alkylated Piperazines and Piperazine-Azole Hybrids as Antifungal Agents, J. Med. Chem., 61 (2018) 158-173.

[14] Vıjey Aanandhı M., Anbhule Sachın J., Synthesıs, Characterızatıon, And Evaluatıon Of Antıfungal Propertıes Of Substıtuted Benzımıdazole Analog, Asian J. Pharm. Clin. Res., 11 (2018) 66-69.

[15] Li L.X., Jiao J., Wang X.B., Chen M., Fu X.C., Si W.J., Yang C.L., Synthesis, Characterization, and Antifungal Activity of Novel Benzo[4,5]imidazo[1,2-d][1,2,4]triazine Derivatives, Molecules, 23 (2018) 746.

[16] Eren B., Yılmaz Ö., Çetin G., Darcan C., Microwave Assisted Synthesis and Potent Antimicrobial Activity of Some Novel 1,3-Dialkyl-2-arylbenzimidazolium Salts, Lett. Drug. Des. Discov., 15 (2018) 621-633.

[17] Liu H.B., Gao W.W., Tangadanchu V.K.R., Zhou C.H., Geng R.X., Novel aminopyrimidinyl benzimidazoles as potentially antimicrobial agents: Design, synthesis and biological evaluation, Eur. J. Med. Chem., 143 (2018) 66-84.

[18] Özkay Y., Tunalı Y., Karaca H., Işıkdağ İ., Antimicrobial activity and a SAR study of some novel benzimidazole derivatives bearing hydrazone moiety, Eur. J. Med. Chem., 45 (2010) 3293-3298.

[19] Küçükgüzel S.G., Mazi A., Sahin F., Öztürk S., Stables J., Synthesis and biological activities of diflunisal hydrazide_/hydrazones, Eur. J. Med. Chem., 38 (2003) 1005-1013.

[20] Can Ö.D., Osmaniye D., Demir Özkay U., Sağlık B.N., Levent S., Ilgın S., Baysal M., Özkay Y., Kaplacıklı Z.A., MAO enzymes inhibitory activity of new benzimidazole derivativesincluding hydrazone and propargyl side chains, Eur. J. Med. Chem., 131 (2017) 92-106.

[21] Rodriguez-Tudela J.L., Barchiesi F. Subcommittee on Antifungal Susceptibility Testing (AFST). EUCAST Definitive Document EDef 7.1: Method for the determination of broth dilution MICs of antifungal agents for fermentative yeast. Clin. Microbiol. Infect., 14 (2008) 398-405.

[22] Can N.Ö., Çevik U.A., Saglık B.N., Özkay Y., Atlı Ö., Baysal M., Özkay Ü.D., Can Ö.D., Pharmacological and Toxicological Screening of Novel Benzimidazole-Morpholine Derivatives as Dual-Acting Inhibitors, Molecules, 22 (2017) 1374.

Recurrence Relations for the Moments of Minimum Order Statistics from Exponential Distribution

Muhammet BEKÇİ (iD)

Sivas Cumhuriyet University, Faculty of Science, Department of Statistics and Computer Sciences, 58140, Sivas, Turkey.

Abstract. In this paper, certain recurrence relations for the moments of minimum order statistics of a random sample of size *n* arising from exponential distribution are obtained. The usefulness of these relations in evaluating the moments of exponential minimum order statistics is also discussed.

*Keywords***:** Exponential distribution, Minimum order statistics, Moments, Recurrence relations.

Üstel Dağılımdan Minimum Sıra İstatistiğinin Momentleri İçin Yinelenme İlişkileri

Özet. Bu çalışmada, üstel dağılımdan elde edilen *n* birimlik bir rasgele örneklemin minimum sıra istatistiğinin momentleri için belli yinelenme ilişkileri elde edilmiştir. Üstel minimum sıra istatistiğinin momentleri değerlendirilmesinde bu ilişkilerin yararlılığı ayrıca tartışılmıştır.

*Anahtar Kelimeler***:** Üstel dağılım, Minimum sıra istatistiği, Momentler, Yinelenme ilişkileri.

1. INTRODUCTION

The use of recurrence relations for the moments of order statistics is quite well-known in the statistical literature (see, for example [1] and [2]). For improved forms of these results, it can be seen in [3] and [4]. Balakrishnan et al. have reviewed many recurrence relations and identities for the moments of order statistics arising from several specific continuous distributions such as normal, Cauchy, logistic, gamma and exponential [5]. For some recent results on moments of the order statistics arising from some other important specific distributions [6] and [7]. David and Nagaraja have given an account of the recurrence relations for the moments of order statistics arising from arbitrary as well as some specific distributions [8]. There are other studies on this subject (see, for example, [9], [10], [11], [12], [13] and [14]). Hence the aim of this paper is to consider minimum order statistics of a random sample of size *n* drawn from exponential distribution and derive some recurrence relations for the moments of the minimum order statistics.

2. MATERIALS AND METHODS

2.1. Minimum Order Statistics from Exponential Distribution

Let X be a random variable whose distribution function (d.f.) and probability density function (p.d.f.) are $F(x)$ and $f(x)$ respectively. Let $X_1, X_2, ..., X_n$ have independent and identical d.f. $F(x)$ and p.d.f. $f(x)$. $X_{1:n} \leq X_{2:n} \leq ... \leq X_{n:n}$ denotes the order statistics of these random variables. For $1 \leq r \leq n$, the p.d.f. of $X_{r:n}$ is given by

$$f_{r:n}(x) = \frac{n!}{(r-1)!(n-r)!}[F(x)]^{r-1}[1-F(x)]^{n-r}f(x)$$

For $r = 1$, the p.d.f. of $X_{1:n}$ is given by

$$f_{1:n}(x) = n[1-F(x)]^{n-1}f(x)$$

Let $X_1, X_2, ..., X_n$ have independent and identically distributed exponential distribution with θ mean parameter. Then, d.f. and p.d.f. are $F(x)$ and $f(x)$ respectively

$$F(x) = 1 - e^{-x/\theta} \ , \ x > 0, \ \theta > 0$$

$$f(x) = \frac{1}{\theta}e^{-x/\theta} \ , \ x > 0, \ \theta > 0 \tag{1}$$

The p.d.f. of $X_{1:n}$ is given by

$$f_{1:n}(x) = n\left[e^{-x/\theta}\right]^{n-1}\frac{1}{\theta}e^{-x/\theta} = \frac{n}{\theta}e^{-nx/\theta} \tag{2}$$

$$X_{1:n} \sim Exp(\theta/n)$$

2.2. Recurrence Relations for the Moments of Exponential Minimum Order Statistics

Theorem 1. Let $X_1, X_2, ..., X_n$ have independent and identically distributed exponential distribution with θ mean parameter (i.e., if Eq. (1) then). Then, the kth ($k = 1, 2, 3, ...$) moments of minimum order statistics ($X_{1:n}$) is given by

$$\mu_{1:n}^{(k)} = E(X_{1:n}^k) = k!\left(\frac{\theta}{n}\right)^k \tag{3}$$

Proof.

$$\mu_{1:n}^{(k)} = E(X_{1:n}^k) = \int_0^\infty x^k f_{1:n}(x)dx = \int_0^\infty x^k \frac{n}{\theta}e^{-nx/\theta}dx = \frac{n}{\theta}\int_0^\infty x^k e^{-nx/\theta}dx$$

Let's remember that $\int\limits_0^\infty x^{\alpha-1}e^{-x/\beta}dx = \Gamma(\alpha)\beta^\alpha$ and $\Gamma(\alpha) = (\alpha-1)!$, $\alpha \in Z^+$. Then,

$$\mu_{1:n}^{(k)} = E(X_{1:n}^k) = \frac{n}{\theta}\int\limits_0^\infty x^k e^{-nx/\theta}dx = \frac{n}{\theta}\Gamma(k+1)\left(\frac{\theta}{n}\right)^{k+1} = k!\left(\frac{\theta}{n}\right)^k$$

Corollary 1. By Theorem 1, the expected value (1th moment), 2th moment and the variance of $X_{1:n}$ are given by

$$\mu_{1:n}^{(1)} = \mu_{1:n} = E(X_{1:n}) = \frac{\theta}{n}$$

$$\mu_{1:n}^{(2)} = E(X_{1:n}^2) = 2\left(\frac{\theta}{n}\right)^2$$

$$Var(X_{1:n}) = E(X_{1:n}^2) - E(X_{1:n})^2 = \mu_{1:n}^{(2)} - (\mu_{1:n})^2 = 2\left(\frac{\theta}{n}\right)^2 - \left(\frac{\theta}{n}\right)^2 = \left(\frac{\theta}{n}\right)^2$$

Theorem 2. If X random variables have exponential distribution with θ mean parameter (i.e., if Eq. (1) then), the $(k+1)^{th}$ moments of $X_{1:n}$ is given by

$$\mu_{1:n}^{(k+1)} = (k+1)\frac{\theta}{n}\mu_{1:n}^{(k)} \qquad (4)$$

Proof.

$$\mu_{1:n}^{(k+1)} = E(X_{1:n}^{k+1}) = (k+1)!\left(\frac{\theta}{n}\right)^{k+1} = (k+1)\frac{\theta}{n}\mu_{1:n}^{(k)}$$

Theorem 3. If X random variables have exponential distribution with θ mean parameter (i.e., if Eq. (1) then), the $(k+\ell)^{th}$ moments of $X_{1:n}$ is given by

$$\mu_{1:n}^{(k+\ell)} = (k+\ell)...(k+1)\left(\frac{\theta}{n}\right)^\ell \mu_{1:n}^{(k)} \qquad (5)$$

Proof.

$$\mu_{1:n}^{(k+\ell)} = E(X_{1:n}^{k+\ell}) = (k+\ell)!\left(\frac{\theta}{n}\right)^{k+\ell} = (k+\ell)...(k+1)\left(\frac{\theta}{n}\right)^\ell \mu_{1:n}^{(k)}$$

Theorem 4. If X random variables have exponential distribution with θ mean parameter (i.e., if Eq. (1) then), the kth moments of $X_{1:n+1}$ is given by

$$\mu_{1:n+1}^{(k)} = k! \left(\frac{\theta}{n+1} \right)^k \tag{6}$$

Proof.

$$\mu_{1:n+1}^{(k)} = E(X_{1:n+1}^k) = k! \left(\frac{\theta}{n+1} \right)^k$$

Theorem 5. If X random variables have exponential distribution with θ mean parameter (i.e., if Eq. (1) then), the $(k+1)^{\text{th}}$ moments of $X_{1:n+1}$ is given by

$$\mu_{1:n+1}^{(k+1)} = (k+1) \left(\frac{\theta}{n+1} \right) \mu_{1:n+1}^{(k)} \tag{7}$$

Proof.

$$\mu_{1:n+1}^{(k+1)} = E(X_{1:n+1}^{k+1}) = (k+1)! \left(\frac{\theta}{n+1} \right)^{k+1} = (k+1) \left(\frac{\theta}{n+1} \right) \mu_{1:n+1}^{(k)}$$

Theorem 6. If X random variables have exponential distribution with θ mean parameter (i.e., if Eq. (1) then), the $(k+\ell)^{\text{th}}$ moments of $X_{1:n+1}$ is given by

$$\mu_{1:n+1}^{(k+\ell)} = (k+\ell)...(k+1) \left(\frac{\theta}{n+1} \right)^{\ell} \mu_{1:n+1}^{(k)} \tag{8}$$

Proof.

$$\mu_{1:n+1}^{(k+\ell)} = E(X_{1:n+1}^{k+\ell}) = (k+\ell)! \left(\frac{\theta}{n+1} \right)^{k+\ell} = (k+\ell)...(k+1) \left(\frac{\theta}{n+1} \right)^{\ell} \mu_{1:n+1}^{(k)}$$

Theorem 7. If X random variables have exponential distribution with θ mean parameter (i.e., if Eq. (1) then), the kth moments of $X_{1:n+m}$ is given by

$$\mu_{1:n+m}^{(k)} = k! \left(\frac{\theta}{n+m} \right)^k \tag{9}$$

Proof.

$$\mu_{1:n+m}^{(k)} = E(X_{1:n+m}^k) = k! \left(\frac{\theta}{n+m} \right)^k$$

Theorem 8. If X random variables have exponential distribution with θ mean parameter (i.e., if Eq. (1) then), the $(k+\ell)^{th}$ moments of $X_{1:n+m}$ is given by

$$\mu_{1:n+m}^{(k+\ell)} = (k+\ell)...(k+1)\left(\frac{\theta}{n+m}\right)^{\ell} \mu_{1:n+m}^{(k)} \tag{10}$$

Proof.

$$\mu_{1:n+m}^{(k+\ell)} = E(X_{1:n+m}^{k+\ell}) = (k+\ell)!\left(\frac{\theta}{n+m}\right)^{k+\ell} = (k+\ell)...(k+1)\left(\frac{\theta}{n+m}\right)^{\ell} \mu_{1:n+m}^{(k)}$$

Theorem 9. If X random variables have exponential distribution with θ mean parameter (i.e., if Eq. (1) then), the kth moments of $X_{1:n+1}$ is given by

$$\mu_{1:n+1}^{(k)} = \left(\frac{n}{n+1}\right)^{k} \mu_{1:n}^{(k)} \tag{11}$$

Proof.

$$\mu_{1:n+1}^{(k)} = k!\left(\frac{\theta}{n+1}\right)^{k} \text{ and } \mu_{1:n}^{(k)} = k!\left(\frac{\theta}{n}\right)^{k}$$

$$\mu_{1:n+1}^{(k)} = c_1\mu_{1:n}^{(k)}$$

$$k!\left(\frac{\theta}{n+1}\right)^{k} = c_1 k!\left(\frac{\theta}{n}\right)^{k}$$

$$c_1 = \left(\frac{n}{n+1}\right)^{k}$$

Theorem 10. If X random variables have exponential distribution with θ mean parameter (i.e., if Eq. (1) then), the kth moments of $X_{1:n+m}$ is given by

$$\mu_{1:n+m}^{(k)} = \left(\frac{n}{n+m}\right)^{k} \mu_{1:n}^{(k)} \tag{12}$$

Proof.

$$\mu_{1:n+m}^{(k)} = k!\left(\frac{\theta}{n+m}\right)^{k} \text{ and } \mu_{1:n}^{(k)} = k!\left(\frac{\theta}{n}\right)^{k}$$

$$\mu_{1:n+m}^{(k)} = c_2\mu_{1:n}^{(k)}$$

$$k!\left(\frac{\theta}{n+m}\right)^k = c_2 k!\left(\frac{\theta}{n}\right)^k$$

$$c_2 = \left(\frac{n}{n+m}\right)^k$$

Theorem 11. If X random variables have exponential distribution with θ mean parameter (i.e., if Eq. (1) then), the $(k+\ell)^{th}$ moments of $X_{1:n+1}$ is given by

$$\mu_{1:n+1}^{(k+\ell)} = \left(\frac{n}{n+1}\right)^{k+\ell} \mu_{1:n}^{(k+\ell)} \tag{13}$$

Proof.

$$\mu_{1:n+1}^{(k+\ell)} = (k+\ell)!\left(\frac{\theta}{n+1}\right)^{k+\ell} \quad \text{and} \quad \mu_{1:n}^{(k+\ell)} = (k+\ell)!\left(\frac{\theta}{n}\right)^{k+\ell}$$

$$\mu_{1:n+1}^{(k+\ell)} = c_3 \mu_{1:n}^{(k+\ell)}$$

$$(k+\ell)!\left(\frac{\theta}{n+1}\right)^{k+\ell} = c_3(k+\ell)!\left(\frac{\theta}{n}\right)^{k+\ell}$$

$$c_3 = \left(\frac{n}{n+1}\right)^{k+\ell}$$

Theorem 12. If X random variables have exponential distribution with θ mean parameter (i.e., if Eq. (1) then), the $(k+\ell)^{th}$ moments of $X_{1:n+m}$ is given by

$$\mu_{1:n+m}^{(k+\ell)} = \left(\frac{n}{n+m}\right)^{k+\ell} \mu_{1:n}^{(k+\ell)} \tag{14}$$

Proof.

$$\mu_{1:n+m}^{(k+\ell)} = (k+\ell)!\left(\frac{\theta}{n+m}\right)^{k+\ell} \quad \text{and} \quad \mu_{1:n}^{(k+\ell)} = (k+\ell)!\left(\frac{\theta}{n}\right)^{k+\ell}$$

$$\mu_{1:n+m}^{(k+\ell)} = c_4 \mu_{1:n}^{(k+\ell)}$$

$$(k+\ell)!\left(\frac{\theta}{n+m}\right)^{k+\ell} = c_4(k+\ell)!\left(\frac{\theta}{n}\right)^{k+\ell}$$

$$c_4 = \left(\frac{n}{n+m}\right)^{k+\ell}$$

Theorem 13. If X random variables have exponential distribution with θ mean parameter (i.e., if Eq. (1) then), the $(k+\ell)^{\text{th}}$ moments of $X_{1:n+m}$ is given by

$$\mu_{1:n+m}^{(k+\ell)} = \frac{(k+\ell)...(k+1)}{(n+m)^{\ell}}\theta^{\ell}\left(\frac{n}{n+m}\right)^{k}\mu_{1:n}^{(k)} \tag{15}$$

Proof.

$$\mu_{1:n+m}^{(k+\ell)} = (k+\ell)!\left(\frac{\theta}{n+m}\right)^{k+\ell} \text{ and } \mu_{1:n}^{(k)} = k!\left(\frac{\theta}{n}\right)^{k}$$

$$\mu_{1:n+m}^{(k+\ell)} = c_5\mu_{1:n}^{(k)}$$

$$(k+\ell)!\left(\frac{\theta}{n+m}\right)^{k+\ell} = c_5 k!\left(\frac{\theta}{n}\right)^{k}$$

$$c_5 = \frac{(k+\ell)...(k+1)}{(n+m)^{\ell}}\theta^{\ell}\left(\frac{n}{n+m}\right)^{k}$$

Theorem 14. If X random variables have exponential distribution with θ mean parameter (i.e., if Eq. (1) then), the $(k+\ell)^{\text{th}}$ moments of $X_{1:n}$ is given by

$$\mu_{1:n}^{(k+\ell)} = (k+\ell)...(k+1)\theta^{\ell}\frac{(n+m)^{k}}{n^{k+\ell}}\mu_{1:n+m}^{(k)} \tag{16}$$

Proof.

$$\mu_{1:n}^{(k+\ell)} = (k+\ell)!\left(\frac{\theta}{n}\right)^{k+\ell} \text{ and } \mu_{1:n+m}^{(k)} = k!\left(\frac{\theta}{n+m}\right)^{k}$$

$$\mu_{1:n}^{(k+\ell)} = c_6\mu_{1:n+m}^{(k)}$$

$$(k+\ell)!\left(\frac{\theta}{n}\right)^{k+\ell} = c_6 k!\left(\frac{\theta}{n+m}\right)^{k}$$

$$c_6 = (k+\ell)...(k+1)\theta^{\ell}\frac{(n+m)^{k}}{n^{k+\ell}}$$

3. CONCLUSION

In this study, the kth moments of $X_{1:n}$ and some recurrence relations related to this k^{th} moments are presented. The recurrence relations for the moments of minimum order statistics are important in the

theory of order statistics. The moments of minimum order statistics can be obtained by some other moments of minimum order statistics.

REFERENCES

[1] Arnold B.C., Balakrishnan N. and Nagaraja H.N., A First Course in Order Statistics, John Wiley, New York, 1992.

[2] Malik H.J., Balakrishnan N. and Ahmed S.E., Recurrence Relations and Identities for Moments of Order Statistics-I: Arbitrary Continuous Distributions, Commun. Statist.–Theo. Meth., 17 (1988) 2623-2655.

[3] Samuel P. and Thomas P.Y., An Improved form of a Recurrence Relations on the Product Moments of Order Statistics, Commun. Statist.–Theo. Meth., 29 (2000) 1559-1564.

[4] Thomas P.Y. and Samuel P., A Note on Recurrence Relations for the Product Moments of Order Statistics, Statistics & Probability Letters, 29 (1996) 245-249.

[5] Balakrishnan N., Malik H.J. and Ahmed S.E., Recurrence Relations and Identities for Moments of Order Statistics-II: Specific Continuous Distributions, Commun. Statist.–Theo. Meth., 17 (1988) 2657-2694.

[6] Raqab M.Z., Generalized Exponential Distribution: Moments of Order Statistics, Statistics, 38 (2004) 29-41.

[7] Thomas P.Y., On the Moments of Extremes from Generalized Gamma Distribution, Commun. Statist.– Theo. Meth., 25 (1996) 1825-1836.

[8] David H.A. and Nagaraja H.N., Order Statistics, 3rd edn., John Wiley & Sons, New York, 2003.

[9] Bekçi M., Recurrence Relations for the Moments of Order Statistics from Uniform Distribution, Scientific Research and Essay, 4-11 (2009) 1302-1305.

[10] Khan R.U., Kumar D. and Athar H., Moments of Generalized Order Statistics from Erlang-Truncated Exponential Distribution and Its Characterization, Int. J. Stat. Syst., 5-4 (2010) 455-464.

[11] Khwaja S.K., Athar H. and Nayabuddin, Recurrence Relations for Marginal and Joint Moment Generating Function of Lower Generalized Order Statistics from Extended Type I Generalized Logistic Distribution, J. Appl. Stat. Sci., 20-1 (2012) 21-28.

[12] Ismail A.A. and Abu-Youssef S.E., Recurrence Relations for the Moments of Order Statistics from Doubly Truncated Modified Makeham Distribution and Its Characterization, Journal of King Saud University-Science, 26 (2014) 200-204.

[13] Nayabuddin and Athar H., Recurrence Relations for Single and Product Moments of Generalized Order Statistics from Marshall-Olkin Extended Pareto Distributions, Comm. Statist. Theory Methods, 46-16 (2017) 7820-7826.

[14] Zarrin S., Athar H. and Abdel-Aty Y., Relations for Moments of Generalized Order Statistics from Power Lomax Distribution, J. Stat. Appl. Pro. Lett., 6-1 (2019) 29-36.

Winter Season Analysis of Global Warming Impact on Sivas Province

Mustafa ERTURK [1]* iD , Kenan BALCI [2] iD , Can COSKUN [3] iD

[1] *Balıkesir University, Balıkesir Vocational School, Department of Electricity and Energy, Balıkesir, TURKEY*

[2] *Recep Tayyip Erdoğan University, Turgut Kıran Maritime Faculty, Rize, TURKEY*

[3] *İzmir Democracy University, Faculty of Engineering, Mechanical Engineering Department, İzmir, TURKEY*

Abstract. The climate has undergone various levels of change since the existence of the Earth. With the industrial Resolution, humankind has begun to be influential in climate change. Industrial revolution lead to unsteady greenhouse gases emissions that led to the global warming and consequent climate change impacts at different scales in various regions of the world. Accordingly, the seasonal periods started to change especially for seasons of Spring and Fall and consequently undesirable changes in the natural events started to occur such as excessive rain, outdoor temperatures above seasonal normal levels. Nowadays, global climate change is one of the most significant problems that mankind has to front with respect to its results. Due to global warming the Turkish province of Sivas is in a sensitive position because of its location. In this study, Sivas province is studied in terms of monthly and seasonal temperature trends. The temperature trends are analyzed by the use of linear regression techniques and the results indicate a significant rise in temperature trends.

Keywords: Sivas, Global climate change, Temperature, Winter seasons.

Kış Sezonunda Sivas İlinin Küresel Isınma Etkisinin İncelenmesi

Özet. Dünyanın varoluşundan günümüze iklim birçok defa değişim göstermiştir. Sanayi devrimi ile birlikte insanoğlu iklim değişikliği üzerinde etkili olmaya başlamıştır. Sanayi devrimiyle birlikte atmosferdeki sera gazı miktarının sürekli olarak artması dünyanın küresel olarak ısınmasına neden olmuştur. Bu durum geçiş mevsimleri (ilkbahar, sonbahar) sürelerinin azalttığı için yeryüzünde istenmeyen doğa olaylarına (aşırı yağmur, mevsim sıcaklıkları üzerinde görülen dış hava sıcaklıkları) neden olmaktadır. Günümüzde küresel iklim değişikliği, sonuçları itibariyle insanoğlunun karşılaştığı en önemli problemlerden biri olarak gösterilmektedir. Sivas ili'de konumu itibariyle küresel iklim değişikliğinden etkilenen hassas bir konumda yer almaktadır. Bu çalışmada, Sivas ili özelinde aylık ve mevsimlik sıcaklık trendleri incelenmiştir. Lineer regresyon teknikler kullanılarak sıcaklık trendleri analiz edilmiştir. Sonuçlar, sıcaklık trendleride anlamlı artışa işaret etmektedir.

Anahtar Kelimeler: Sivas, Küresel iklim değişikliği, Sıcaklık, Kış sezonu.

1. INTRODUCTION

Fossil fuels burnings result in the emission of carbon dioxide into the atmosphere and contributes to global climate change by causing greenhouse gas effect. Radical changes in fossil fuel based technologies are necessary in order to reduce this threat to the environment [1]. In energy systems, both improvements in energy efficiency and the use of renewable energy sources are some of the most effective means of reducing CO2 emission [2]. In the last five

years, there has been an important increase in sustainability and eco-friendly production processes and the use of renewable energy sources for the products [3].

The change in global temperature averages trend does not demonstrate an equal distribution in all geographies. The heating trend between 40º and 70º degrees north latitudes occurs at a higher level. In the countries located at middle and high latitudes, the effect of global climate change is observed at a higher level [4].

Due to its regionally different climate structure, Turkey is one of the countries, which will be highly affected from the impacts that may occur in relation to the global climate change. Different regions of Turkey are impacted by the global climate change in different ways and at various levels. Areas that will be the most affected from the global change appear to be the arid, semi-arid and sub-humid regions [5]. Thus, the central Anatolia region happens to be one of the places that will be mostly affected due to its geographical position. In the master thesis the changes and trends in the rainfall and temperature data due to the global warming process [6]. The author revealed the reality of Turkey's global climate change. Barak (2009) stated as a result of its semi-arid feature climate is the biggest factor that affects the Central Anatolia Region [7]. As known, those regions with semi-arid climate respond to climate changes rather quickly. In the thesis study, Barak (2009) determined the areas, which were locally affected from the climate change. It is stated that some regions with steppe climate have evolved into semi-desert steppe climate. In some areas, evaporation rate is found to increase

and it was stated that the greatest factor that play role in that increase is the rise in temperature. Especially, between the years 1991-2006, the impact of global climate change was identified to be at the highest level.

Sivas province constitutes the basis of this study and it is located in the Central Anatolia Region as one of the provinces sensitive to climate changes due to its location. As a result of this, vegetation and natural resources are damaged to a great extent in Sivas and Kayseri provinces. Especially, these provinces are the main areas, where environmental problems such as drought and flood may occur. Moreover, this problem leads to a great amount of pressure on water resources [8].

In this study, temperature trends are analyzed on monthly, seasonal and annual basis by using the data obtained from the meteorology stations in Turkey. An analysis is performed on what level global climate change is effective in the winter period in Sivas.

2. MATERIALS AND METHODS

In this study, outdoor temperatures data are obtained from the Meteorological Service of Turkey at meteorology stations throughout Turkey for the trend determination in the outdoor temperatures. The Thom test was used to determine the degree of homogeneity of these data series. The results of the test revealed that in general, the data had a homogeneous structure. Moreover, the non- parametric Mann and Kendall correlation coefficient is used. Subsequently, the linear trends of temperatures are calculated for Sivas province. The linear trend and Mann-Kendall results are evaluated.

Python, open source software, is used to perform the analyses. Outdoor temperature values are analyzed in different categories with this software. Overall, the analyses are carried out in the form of hourly, daily, monthly and annual bases.

2.1 Determination of Outdoor Temperature Distributions for Sivas

The distributions obtained from the software enabled the hourly, monthly, seasonal and annual analyses of outdoor temperatures as presented below. The monthly distribution of outdoor temperature of Sivas province in the winter season is given in Figure 1. It can be seen that on a monthly basis, during the period between November and June the outdoor temperatures change between - 28°C and 28°C. On the other hand, during the period between December and March the peak point is around 0°C with a rate of 7%. Furthermore, the outdoor temperature distribution in Sivas province during winter season is given in Figure 2.
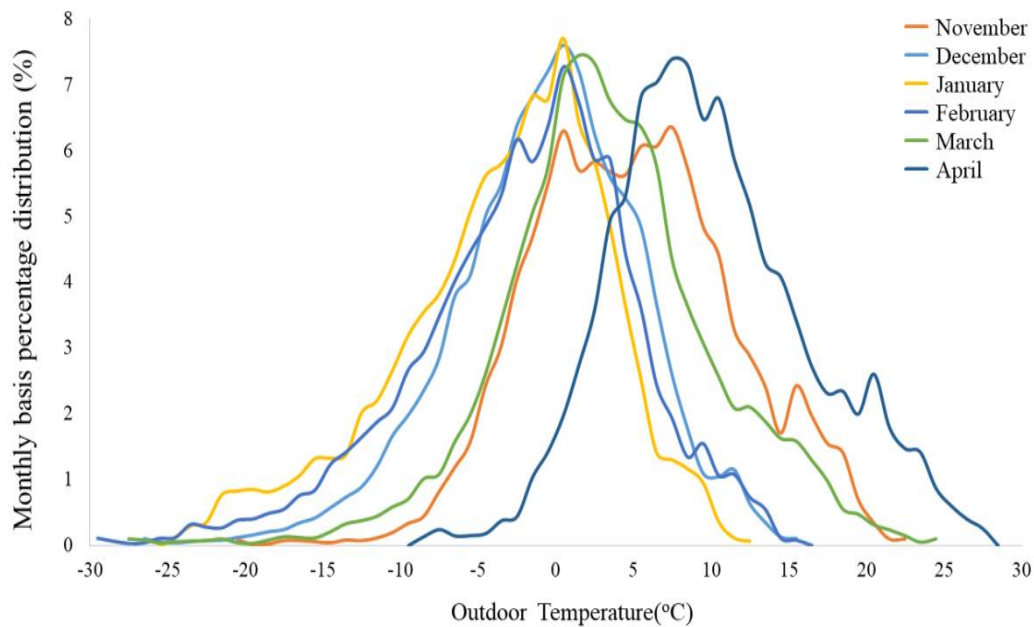
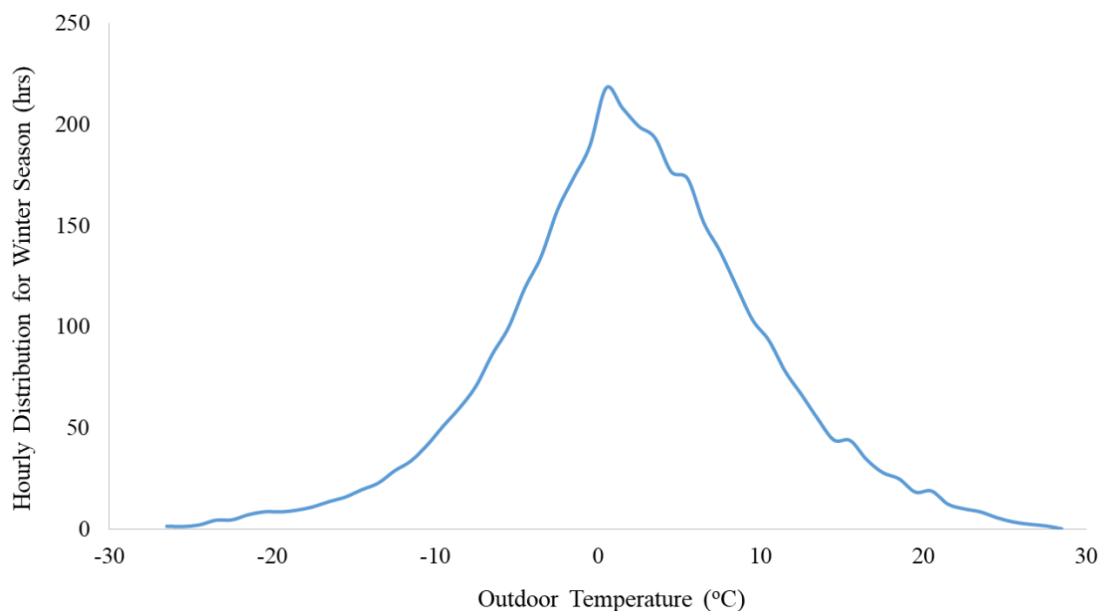**Figure 1.** The monthly distribution of outdoor temperature of Sivas province in the winter season.

Figure 2. The distribution of outdoor temperature of Sivas province in the winter season.

The average annual winter outdoor temperatures is presented in Figure 2,and it is obvious that the most common temperature range for Sivas province is from -1 °C to 0°C. During the winter period, temperature occurrence is observed on the average as 218 hours in this area. The temperature range occurrence in the winter season reaches to 56°C. When the winter period is taken into consideration, the average temperature is at a level of 4°C. In figure 3, the fluctuation in the average temperature changes for the last 32 years is demonstrated.
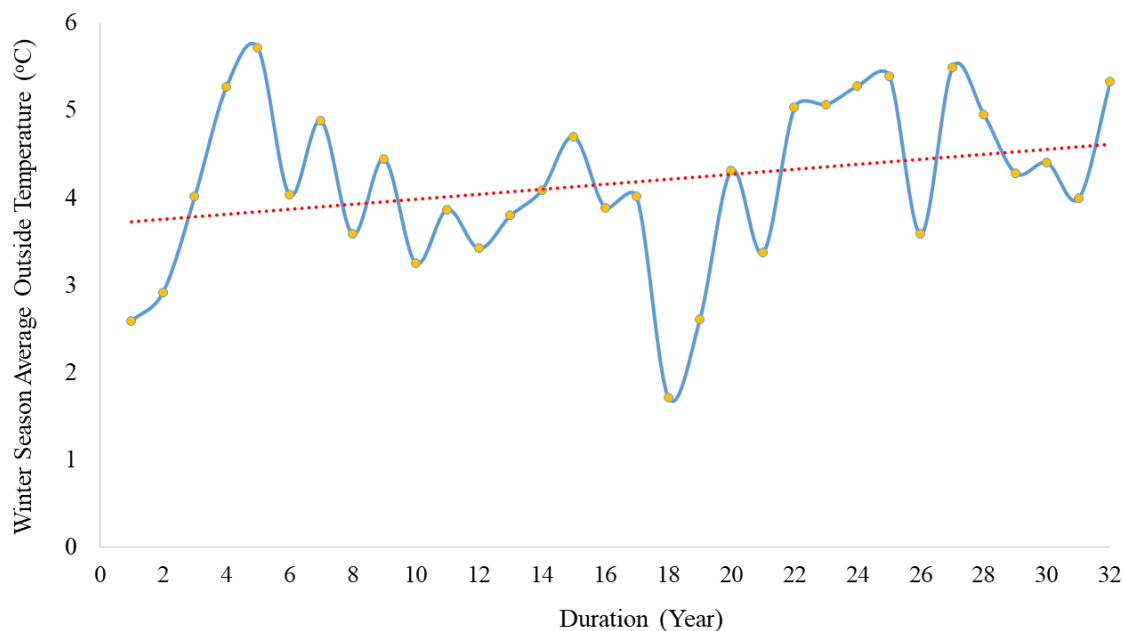
Figure 3. The global climate change effects on winter season average outside temperature

2.2 The Impact of Global Climate Change on Heating

Various methods are used for determining heating energy demand. One of these methods is Degree-Hour (DH) method. In this method, outdoor temperature data of 8760 hours is used. It is calculated in a different way for the heating season and the cooling season. The heating DH value used in this method can be obtained through the following formula:

$$DS = \sum_{j-1}^{N}(T_b - T_o)_j \qquad for \ (T_b \leq T_o)_j \qquad (1)$$

In this equation, T_o, is the outdoor temperature and T_b expresses the temperature taken as reference for heating. N stands for the number of hours below the reference temperature. Heating energy demand appears as a result when outdoor temperature falls below the reference degree. The heating DH values are determined for Sivas and presented in Figure 4. A downward trend in heating DH values can be seen and a level of 154 °C- hour is detected in the heating DH value in terms of the winter season. When a value of 100142 °C DH is taken as reference for an average of 32 years, it yields to a decrease of 0.15 % on a yearly basis. On the other hand, at a period of 100 years it is possible to forecast a 15% decrease in the need for heating energy.
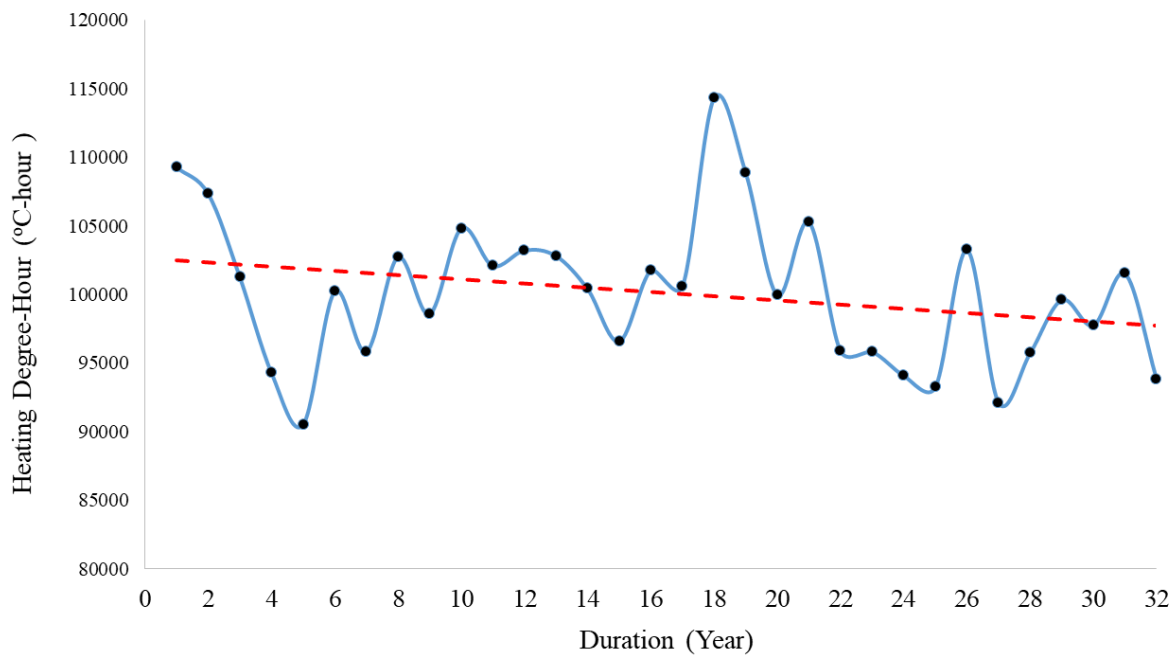

Figure 4. The change trend in heating degree-hours for the winter season

3. DISCUSSION AND RESULTS

When the data set obtained from all over Turkey is examined, the two provinces which will be impacted by the global climate change within the context of the Central Anatolia region seem to be Sivas and Kayseri. When the context of winter period is considered, Gürün district is the

most affected, in addition to Kangal, Altınyayla and Divriği counties in Sivas due to global warming. As can be seen in Figure 5, within a 100 year perspective for Sivas, it can be forecasted that the temperature rise will be between 3.1 °C and 3.9 °C during the winter season. With the impact of global climate change, the average temperature in winter is predicted to rise from 4 °C to 7°C or 8 °C in the context of counties. This temperature increase within Sivas is at a level far above the average temperature rise in winter in Turkey. In the context of the winter season, when Turkey is regarded as a whole, provinces that require precautions are Sivas, Kayseri, Malatya, and Kahramanmaraş. The governors of these four provinces may gather and form a platform and take common actions about global climate change. With this platform, a program and structure can be established that will make the most of government subsidies as the provinces that are most affected by the global climate change. Within Sivas context, detailed studies may be carried out in order to detect the effects of global climate change on economic activities.
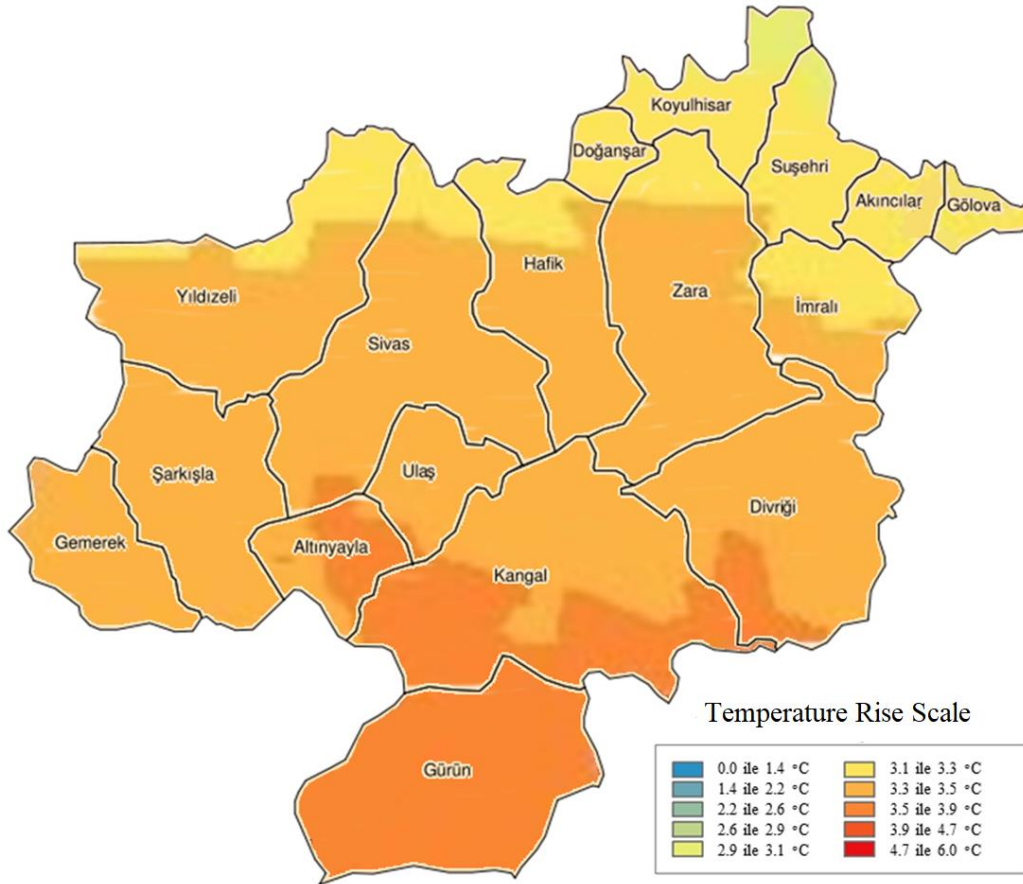

Figure 5. Map of future average outdoor temperature change over 2018-2118 period for the winter season

As known, the economic activities in Sivas are based on agriculture to a great extent. It is known that 70% of the economically active populations work in the agricultural sector. After agriculture, livestock farming comes in the second place as a source of income. In terms of agricultural production, grains and legumes are very important. The amount of cereal

products varies each year in relation to seasonal conditions and they are most affected by the global climate change. The main agricultural products are wheat, rye, beans, lentil, sugar beet and potatoes. During the last few years, there has been a decrease in the wheat production due to the rising effects of global climate change. This shortage in wheat production causes an increase in the cost of bread and this triggers food inflation. The decline in wheat production affects not only Sivas, but Turkey in general. By establishing a common platform for Sivas, Kayseri, Malatya and Kahramanmaraş cities, public and statewide awareness may be raised. After detecting the problem, action might be taken. The aim of this study is to provide a spark for these four provinces, which are the most affected ones by the negative impacts of global climate change, and hence, it is necessary, to take action and lessen from these negative effects. By the pioneering role of the universities in these aforementioned provinces, they may act together and this may inspire the state to act immediately on this issue.

REFERENCES

[1] Hoffert, M., Global warming and fuel choices. Energy and nanotechnology: Strategy for future conference report, (2011) Retrieved from ww.rice.edu/energy/publications/docs/NanoReportFeb2005.pdf

[2] Jänicke, M. Dynamic governance of clean-energy markets: how technical innovation could accelerate climate policies. Journal of Cleaner Production. 22 (2012) 50-59

[3] Narodoslawsky, M., Niederl-Schmidinger, A., Halasz, L. Utilising renewable resources economically: new challenges and chances for process development, Journal of Cleaner Production. 16 (2008) 164-170

[4] Cosun, F., Karabulut, M., Kahramanmaraş'ta Ortalama, minimum ve Maksimum Sıcaklıkların Trend Analizi. Türk Coğrafya Dergisi 53 (2009) 41-50.

[5] Türkeş, M., Sümer, U. M. ve Çetiner, G. Küresel iklim değişikliği ve olası etkileri. Çevre Bakanlığı, Birleşmiş Milletler İklim Değişikliği Çerçeve Sözleşmesi Seminer Notları (13 Nisan 2000, İstanbul Sanayi Odası): 7-24, ÇKÖK Gn. Md., Ankara. (2000).

[6] Barak, B. İç Anadolu Bölgesi'nde küresel ısınma sürecinde yağış ve sıcaklık verilerinde meydana gelen değişimler ve eğilimler. Master Thesis (2009) .

[7] Altın, B.R., Barak, B., Altın, B.N. Change in Precipitation and Temperature Amounts over Three Decades in Central Anatolia, Turkey. Atmospheric and Climate Sciences, 2 (2012) 107-125.

[8] Karabulut, M. Kayseri'de Yağış ve Sıcaklıkların Trend Analizleri. KSÜ Sosyal Bilimler Dergisi. S. 8 (1) (2010) 79-89.

The Determination of Some Qualities Parameters and Use of Strip Loin Beef (*M. Longissimus dorsi*) Powder in Bread Enrichment

Duygu BALPETEK KÜLCÜ [1],* iD *, Nurgül KOCABAŞ* [1] iD *, Sonay KUTLU* [1] iD

[1] Giresun University, Engineering Faculty, Department of Food Engineering, Giresun, Turkey

Abstract. In this study, the protein content of the bread, that is also known as rich in carbohydrate content, is enriched by using strip loin beef *(M. longissimus dorsi)* powder as the additive. In order to meet the daily protein needs of individuals, bread was prepared with the addition of certain amounts (3%, 5%, 7%, and 10%) of beef minced powder to the wheat flour. The protein content of the bread samples with the addition of strip loin beef *(M. longissimus dorsi)* powder were increased from 14.41%, 16.03%, 17.43% and 20.33% for enriched bread, respectively. The total colour darkness of the interior of the bread was increasing with the increasing level of strip loin beef *(M. longissimus dorsi)* powder. Extensograph analysis, amylograph analysis, gluten, gluten index, sedimentation, delayed sedimentation, moisture (%) and ash (%) analysis were performed in enriched bread flours. As a result of physico-chemical, rheological and microbiological analysis, it has been determined that protein content increases due to the enrichment rate of meat powdered bread. Sensory analysis questionnaire was conducted to determine the acceptability of the breads by consumers. According to the survey; Questions were asked about the external properties of the bread (crust texture, crust color, form in general), and internal properties (texture, color, chewability, pore structure, taste and odor). The aim of this research is to increase the protein content of bread and to develop an alternative new product that can be consumed by consumers.

Keywords: Bread, strip loin beef, microbial quality, protein.

Ekmek Zenginleştirmede Dana Kontrfile (*M. Longissimus dorsi*) Tozunun Kullanımı ve Bazı Kalite Parametrelerinin Belirlenmesi

Özet. Bu çalışmada, karbonhidrat içeriği bakımından zengin olarak bilinen ekmeğin protein içeriği, katkı maddesi olarak kıyma haline getirilmiş kontrfile (*M. longissimus dorsi*) tozu kullanılarak zenginleştirilmiştir. Bireylerin günlük protein ihtiyacını karşılamak için, buğday ununa belirli miktarlarda (%3, %5, %7 ve %10) kıyma tozu ilavesiyle ekmek hazırlanmıştır. Dana kontrfile (*M. longissimus dorsi*) tozu ilavesi ile ekmek numunelerinin protein içeriği, sırasıyla %14.41, %16.03, %17.43 ve %20.33 arttırılmıştır. Ekmeğin iç kısmındaki toplam renk koyuluğu, dana kontrfile kıyma (*M. longissimus dorsi*) tozu ile artmıştır. Ekstensograf analizi, amylograph analizi, glüten, glüten indeks, sedimantasyon, gecikmeli sedimantasyon, nem (%) ve kül (%) analizleri zenginleştirilmiş ekmek unlarında yapılmıştır. Fiziko-kimyasal, reolojik ve mikrobiyolojik analizler neticesinde kıyma tozlu ekmeğin, zenginleşme oranına bağlı olarak protein içeriğinin arttığı belirlenmiştir. Üretilen ekmeklerin, tüketiciler tarafından kabul edilebilirliğini tesbit etmek amacıyla duyusal analiz anketi yapılmıştır. Ankete göre; ekmeğin dış özellikleri (kabuk tekstürü, kabuk rengi, genel olarak şekli), ve iç özellikleri (tekstür, renk, çiğnenebilirlik, gözenek yapısı, tat ve koku) ile ilgili sorular sorulmuştur. Bu araştırma ile ekmeğin protein oranı arttırılarak, tüketiciler tarafından tüketilebilecek alternatif bir yeni ürün geliştirilmesi amaçlanmıştır.

Anahtar Kelimeler: Ekmek, kontrfile, mikrobiyolojik kalite, protein.

1. INTRODUCTION

Nutrient intake of the individual is influenced by the nutrient consumption that is used in connection with the habit of eating, economic reasons, mental state, cultural structure, climate condition, appetite and diseases [1]. Nutrition is very important for the individual's body, soul and mental health to be good and to maintain this condition. A balanced diet is known as the consumption of food components by the appropriate amount and type. People are required to take the basic compounds they need regularly with their food. Otherwise, the human body has to meet the missing compounds from the stores in the body. Nutrients must be consumed in a sufficient and balanced way with the basic condition of healthy living. This will reduce disability, premature death and diseases that may occur with nutritional deficiencies [2.3].

All of the countries in the world consume nutrients of vegetable origin more than the animal origin for calorie consumption. In developed countries, nutrients from animal origin are consumed more to meet protein needs. In our country, a large part of the daily energy need is obtained by bread consumption [4].

In bread making, wheat flour, yeast, salt and water in a certain ratio are mixed, kneaded and the resulting dough is cooked after fermentation [5]. The bread has nutritious and satisfying properties as well as being easily supplied and cheap. In addition, the fact that the bread has a unique neutral flavor allows it to be consumed together with other foodstuffs [3].

Bread with a high energy level and carbohydrate content cannot meet the body's need for vitamins, proteins and minerals. However, cereals are not sufficient in terms of essential amino acids, compared to animal nutrients [6].

Meat proteins with more nutritive value than vegetable proteins contain a balanced and sufficient amount of exogenous amino acids that the organism cannot synthesize and must be taken with foodstuffs. It also contains mineral substances such as vitamin B12, phosphorus, sodium, potassium, iron, magnesium and zinc. In terms of healthy nutrition, it is important to provide at least 40-50% of the daily protein requirement with animal proteins [7].

In this study, it is aimed to increase the protein content of the bread that can be consumed every meal and investigate some chemical and microbiological properties of bread produced using wheat flour and strip loin beef powder. In addition, the effects of strip loin beef powder, which is used at different rates during bread production, on the quality changes caused by the storage period were also investigated. In the literature, bread experiments were made by using different the enrichment components [8-16]. However, there is no study on using strip loin beef in the enrichment bread.

2. MATERIALS AND METHODS

2.1. Materials

In this study, the sample of beef loin meat obtained from butchers and grocery stores in Giresun province was brought to the laboratory by protecting the cold chain. After the meat sample was minced in a meat grinder, the beef loin sample was dried at 150 °C in the drying cabinet for 2 hours. The dried minced meat samples were powdered by blender. In the study, the reason for the use of beef loin is to minimize the fat content and to minimize the quality losses of the minced meat. In addition, wheat flour obtained from Ulusoy Un A.Ş. (Samsun) and instant dry yeast, salt, sugar, oil (riviera olive oil), water (packaged) are used in bread production. No additives were used in bread production. Fakir Pane Deluxe bread baking machine, 500 g program and dark color setting were used for bread baking experiments.

Table 1. Dough formulations prepared for bread production

Enrichment Rate	Flour (g)	Water (ml)	Salt (g)	Yeast (g)	Sugar (g)	Oil (ml)	Strip Loin Beef Powder (%)
0%	463	330	6	3	28	10	0
3%	448	330	6	3	28	10	15
5%	438	330	6	3	28	10	25
7%	428	330	6	3	28	10	35
10%	413	330	6	3	28	10	50

2.2. Methods

The ash [17] and moisture [18], gluten [19], gluten index [20], sedimentation [21] value of flour samples were determined according to ICC Standard Methods. The amylograph [22] and extensograph [23] analysis were conducted to examine the rheological properties of dough.

The protein content of the whole bread samples was measured according to the AACC method [24].

Bread made from bread-baking machine, was analyzed in terms of pH [6], water activity (a_w) (Aqua Lab Dew Point Water Aktivity Meter, 4TE,USA), moisture [6], protein [6], color (HunterLab, Reston, Virginia, USA) and microbiological (yeast-mold) [25] qualities. After being divided into slices (2 cm thickness), the bread was packed in a room conditions (+18ºC-(+24 ºC) for 3 days. Bread was analyzed on the 1st, 2nd, 3rd, and 4th days of the preservation and quality changes were examined day by day. The study was carried out in three parallel with two replications.

2.3. Sensory analyses

Control and meat powdered bread were scored on the first day of production by 9 different panelists according to sensory ratio scale. In the questionnaire, control group and meat powdered bread; questions were asked about crust texture, crust color, general form and inner texture, inner color, chewability, pore structure, taste, odor and overall acceptability. Survey of the questionnaire is numbered as 1 (poor), 4 (excellent). The survey panel group consisted of 9 randomly selected participants.

2.4. Statistical analysis

Data were analyzed using One way ANOVA and Duncan's post hoc tests by using IBM SPSS 24 software (SPSS Inc., Chicago, IL, USA) with a significance level of 5%.

3. RESULT AND DISCUSSION
3.1. Results

Table 2. Analysis results of wheat flour enriched with strip loin beef powder

Strip Loin Beef Powder Additive Rates	Gluten	Gluten Index	Sedimentation	Moisture (%)	Ash (%)
0%	28,96±0,58[a]	88 ±1	42 ±2[a]	13,45±0,24[a]	0,54±0,05[a]
3%	30,75±0,96[ab]	90 ±2	38 ±2[ab]	13,11±0,17[ab]	0,61±0,03[ab]
5%	31,12±1,6[ab]	93 ±5	36 ±1[bc]	13,07±0,16[abc]	0,68±0,04[bc]
7%	33,63±1,78[b]	93 ±1	33 ±1[c]	12,80±0,22[bc]	0,72±0,04[cd]
10%	34,55±2,61[b]	94 ±4	32 ±1[d]	12,59±0,05[c]	0,80±0,09[d]
P	0,013	0,196	0,000	0,002	0,000

*: The difference between the averages (±; standard deviation) is significant indicated in different letters in the same column (p<0.05).

Table 3. The results of extensograph analysis of wheat flour enriched with strip loin beef powder

Mincer Powder Additive Rates	Energy (cm²)	Elongation Resistance (BU)	Elongation (mm)	Max. Resistance (BU)	Ratio	Max. Ratio
0%	109,±3[a]	571,±34[a]	134,±9	666,50±15,5[ab]	4,45±0,35	5,20±0,2
3%	107,50±2,5[a]	521,±47[a]	128,50±1,5	651,±19[a]	3,90±0,6	4,90±0,5
5%	100,50±5,5[b]	501,±9[ab]	128,50±6,5	611,±9[bc]	3,95±0,25	4,75±0,15
7%	94,50±2,5[b]	478,±14[b]	128,±1	592,50±25,5[c]	3,85±0,15	4,75±0,25
10%	94,±6[ab]	472,50±38,5[ab]	125,50±1,5	585,±37[abc]	3,70±0,3	4,55±0,35
P	0.003	0.022	0.397	0,005	0,197	0,214

* The difference between the averages (±; standard deviation) is significant indicated in different letters in the same column (p<0.05).

Table 4. Results of amylograph trials of strip loin beef powder additional wheat flour

	0%	3%	5%	7%	10%	P
Max. gelatinization (AU)	906±11[a]	775±2.5[b]	706±3[c]	666±12.5[d]	608±3.5[e]	0.000

*: The difference between the averages (±; standard deviation) is significant indicated in different letters in the same row (p<0.05).

Table 5. Ash and protein content of bread enriched with strip loin beef powder at different rates

Addition Rate (%)	Ash content (%)	Protein content (%)
0%	0,69 ± 0,015[a]	13,87 ± 0,05[a]
3%	0,83 ± 0,003[b]	14,41 ± 0,41[a]
5%	0,88 ± 0,007[c]	16,03 ± 0,15[b]
7%	0,92 ± 0,009 [c]	17,43 ± 0,15[c]
10%	1,06 ± 0,030 [d]	20,33 ± 0,25[d]

a, b, c, d : The difference between the averages (±; standard deviation) is significant indicated in different letters in the same column (p<0.05).

Table 6. pH, moisture and a_w values of bread enriched with different addition rate

Property	Storage Period (days)	Rate 0%	Rate 3%	Rate 5%	Rate 7%	Rate 10%
pH	0	4,59 ± 0,03[a]	4,63 ± 0,02[ab]	4,67 ± 0,07[bc]	4,80 ± 0,08[c]	4,83 ±0,02[c]
	1	4,50 ± 0,10[a]	4,74 ± 0,05[b]	4,73 ± 0,11[b]	4,81 ± 0,04[b]	4,79 ± 0,05[b]
	2	4,52 ± 0,41[a]	4,81 ± 0,11[b]	4,81 ± 0,10[b]	4,81 ± 0,03[b]	4,89 ± 0,05[b]
	3	4,12 ± 0,05[a]	4,62 ± 0,16[b]	4,91 ± 0,08[b]	4,74 ± 0,07[bc]	4,92 ± 0,05[c]
Moisture	0	36,57±0,36[Aa]	37,80±0,30[Ab]	39,52±0,36[Ac]	40,32±0,16[Ad]	40,99±0,12[Ad]
	1	37,45±0,24[Ba]	38,80±0,23[Bb]	39,39±0,21[Ac]	40,97±0,15[Bd]	41,28±0,21[Ad]
	2	38,52±0,36[Ca]	39,25±0,15[Bb]	40,39±0,22[Bc]	41,77±0,21[Cd]	42,81±017[Be]
	3	40,50±0,04[Da]	41,51±0,47[Cb]	42,37±0,23[Cc]	43,67±0,19[Dd]	45,30±0,21[Ce]
a_w	0	0,96 ± 0,002	0,97 ± 0,003	0,97 ± 0,005	0,98 ± 0,003	0,98 ± 0,002
	1	0,98 ± 0,004	0,98 ± 0,005	0,99 ± 0,004	0,98 ± 0,005	0,99 ± 0,010
	2	0,98 ± 0,008	0,98 ± 0,002	0,99 ± 0,003	0,99 ± 0,005	0,99 ± 0,005
	3	0,998 ± 0,001	0,998 ± 0,001	0,998 ± 0,001	0,998 ± 0,001	0,998 ± 0,001

A, B, C, D; The difference between the averages (±; standard deviation) is significant indicated in different letters in the same column (P<0.05).
a, b, c, d, e; The difference between the averages (±; standard deviation) is significant indicated in different letters in the same row (P<0.05).

Table 7. L *, a *, b * values of the inside of bread enriched with different addition rate

Property	Storage Period (days)	Rate 0%	Rate 3%	Rate 5%	Rate 7%	Rate 10%
L*	0	77,44 ±0,75[Aa]	70,58±0,07[Ab]	68,64 ±0,40[Ac]	66,18±1,96[Ad]	67,53±0,33[Ae]
	1	75,67 ±1,09[Ba]	69,32±2,40[Bb]	65,71 ±0,52[Bc]	63,14±1,87[Bd]	62,79 ±1,80[Be]
	2	72,26 ±0,18[Ca]	67,20±2,04[Ca]	64,38±0,51[Bb]	62,62 ±2,31[Cc]	62,44±1,70[Bd]
	3	70,22 ±1,47[Da]	67,48±2,47[Db]	65,53 ±0,71[Cc]	64,31±2,17[Dd]	60,27 ±2,21[Ce]
a*	0	2,02 ± 0,31[Aa]	3,54 ± 0,16[Ab]	4,36 ± 0,07[Ac]	5,49 ± 0,08[Ad]	6,67 ± 0,19[Ae]
	1	1,62 ± 0,57[Aa]	3,24 ± 0,55[Ab]	3,88 ±0,29[ABc]	5,23 ± 0,33[Ad]	6,19 ± 0,23[Ae]
	2	1,70 ± 0,15[Aa]	2,55 ± 0,12[Bb]	3,69 ± 0,32[Bc]	5,02 ± 0,39[Bd]	6,03 ± 0,26[Ae]
	3	1,53 ± 0,16[Ba]	2,56 ± 0,07[Cb]	3,63 ± 0,10[Cc]	4,96 ± 0,57[Cd]	6,05 ± 0,56[Be]
b*	0	22,18 ±0,48[Aa]	24,39±0,54[Ab]	25,50 ±0,55[Ac]	25,94 ±0,80[Ac]	25,65±0,29[Ad]
	1	21,22 ±1,90[Ba]	23,03±1,74[Bb]	23,72 ±0,27[Bc]	23,27±1,33[Ad]	24,44 ±1,24[Be]
	2	21,66 ±2,25[Ca]	23,18±1,66[Bb]	23,53 ±1,08[Bc]	23,69 ±0,58[Bc]	24,10±0,21[Bd]
	3	20,96 ±0,12[Da]	22,29±0,81[Cb]	23,09 ±0,30[Cc]	23,10 ±0,29[Cc]	24,35±0,77[Cd]

A, B, C, D; The difference between the averages (±; standard deviation) is significant indicated in different letters in the same column (P<0.05).
a, b, c, d, e; The difference between the averages (±; standard deviation) is significant indicated in different letters in the same row (P<0.05).
b * values with the increase of the enrichment rate of bread samples.

Table 8. Yeast-mold values of bread enriched with different addition rate (cfu/gr)

Property	Storage Period (days)	Rate				
		0%	3%	5%	7%	10%
Yeast - Mold	0	NG	NG	NG	NG	NG
	1	NG	NG	$2,49 \pm 0,07^{Ab}$	$2,42 \pm 0,05^{Ac}$	$3,11 \pm 0,03^{Ad}$
	2	$2,13 \pm 0,05^{Aa}$	$2,99 \pm 0,06^{Ab}$	$3,12 \pm 0,07^{Bc}$	$3,56 \pm 0,02^{Bc}$	$3,69 \pm 0,09^{Bc}$
	3	$3,32 \pm 0,05^{B}$	$4,35 \pm 0,07^{B}$	$4,45 \pm 0,05^{C}$	$4,46 \pm 0,03^{C}$	$4,72 \pm 0,07^{C}$

A, B, C, D; The difference between the averages (±; standard deviation) is significant indicated in different letters in the same column (P<0.05).
a, b, c, d, e; The difference between the averages (±; standard deviation) is significant indicated in different letters in the same row (P<0.05).
NG; Not Growing

Table 9. Sensory properties of bread samples

Sensorial Properties	Additional Rate				
	0%	3%	5%	7%	10%
Crust texture	$3,11 \pm 0,6^{a}$	$3,56 \pm 0,53^{ab}$	$3,78 \pm 0,44^{b}$	$3,33 \pm 0,5^{ab}$	$3,44 \pm 0,53^{ab}$
Crust color	$3,22 \pm 0,67^{a}$	$3,44 \pm 0,53^{a}$	$3,56 \pm 0,73^{a}$	$3,11 \pm 0,78^{a}$	$3,56 \pm 0,53^{a}$
General form	$3,56 \pm 0,53^{ab}$	$3,89 \pm 0,33^{b}$	$3,67 \pm 0,5^{b}$	$3,33 \pm 0,5^{ab}$	$3 \pm 0,5^{a}$
Inner texture	$3,44 \pm 0,53^{a}$	$3,56 \pm 0,53^{a}$	$3,56 \pm 0,53^{a}$	$3 \pm 1,12^{a}$	$2,89 \pm 0,6^{a}$
Inner color	$3,67 \pm 0,5^{a}$	$3,89 \pm 0,33^{a}$	$3,78 \pm 0,44^{a}$	$3,67 \pm 0,5^{a}$	$2,44 \pm 0,53^{b}$
Chewability	$3,67 \pm 0,5^{a}$	$3,67 \pm 0,5^{a}$	$3,33 \pm 0,5^{a}$	$3 \pm 0,5^{ab}$	$2,33 \pm 0,5^{b}$
Pore structure	$3,67 \pm 0,5^{a}$	$3,44 \pm 0,53^{a}$	$3,11 \pm 0,93^{ab}$	$3,33 \pm 0,5^{ab}$	$2,56 \pm 0,53^{b}$
Taste and odor	$3,56 \pm 0,53^{a}$	$3,44 \pm 0,53^{a}$	$2,89 \pm 0,6^{ab}$	$3,11 \pm 1,17^{ab}$	$2,67 \pm 0,5^{b}$
Overall acceptability	$3,78 \pm 0,44^{a}$	$3,56 \pm 0,53^{ab}$	$3,33 \pm 0,5^{bc}$	3 ± 0^{c}	$2 \pm 0,5^{d}$

a, b, c, d, e; The difference between the averages (±; standard deviation) is significant indicated in different letters in the same row (P<0.05).

3.2. Discussion

As a result of gluten index analysis, it was observed that gluten content increased as the percentage of minced meat increased. This can be explained by the fact that powder particles are large enough to pass through the gluten sieves during analysis. However, if only the gluten content was increased due to this situation, the gluten of 3% strip loin beef powder dough should be 30.75. As a result of the analysis, a high result such as 34.55 can be explained by the possibility that the meat proteins cannot dissolve in salt water and even increase the rate of gluten by binding to water, or another component that is insoluble in salt water. This result may also be due to the fact that the minced meat pieces absorb water due to having very low moisture content.

Extensograph results showed that there was a decrease of 1% in dough samples in water lifting capacity. According to the result of the analysis, the excess of water that was bound by gluten during the washing was not shown here. This may be due to the fact that the minced meat used in the enrichment can remove as much water as the water removed by the flour it replaces. In addition, although the protein content has increased, it is possible to say that the loss of starch may be caused by such a loss.

In addition, according to the extensograph results, it can be stated that the rheological quality of the dough decreases as the rate of fortification increases. In all of the dough with strip loin beef powder, extensibility is lower than the extensibility of the control group dough. Thus, it was observed that resistance, elasticity and total energy have decreased gradually.

When the amylograph results of the enriched dough samples were examined, it was observed that the maximum level was gradually decreasing, which could be explained not by the increase of alpha amylase enzyme, but by the decrease of the starch ratio as the rate of minced meat increased. In addition, it was observed that the peak levels decreased as the starch ratio decreased. Viscosity increases were determined before gelling in 10% minced meat dough sample.

In the dough samples, the moisture content has decreased as the percentage of the enrichment

increases, which can be explained by the fact that the dried minced meat sample has very low moisture content.

The amount of ash increased as the percentage of additives increased, which could be related to the fact that the presence of mineral material in the wheat flour with dried strip loin beef powder was higher than the content of wheat flour.

As the fortification percentage increased, the sedimentation values gradually decreased. It can be stated that the worsening of the rheological properties due to the enrichment rate in the extensograph analysis is also confirmed by the sedimentation.

As the amount of the strip loin beef powder added increased, protein content of the enrichment bread increased. The protein ratio of the bread in the control group (0%) was 13,87%, while the protein content of the bread with 10% strip loin beef powder was increased to the highest value with 20,33%. These results show parallelism with Dursun et al. [26] that uses mined fish as additive. Mohammed et al. [27] determined that the increase in the amount of ash in the samples of the additive bread depending on the addition rate.

In addition, Mohammed et al. [27] found an increase in the amount of protein depending on the rate of addition. These results are in parallel with our study.

Dursun et al. [28] stated that the amount of protein increased due to the rate of minced fish addition bread. Çakmak et al. [29] stated that the amount of protein increased due to the contribution rate of white and whole wheat bread with chicken meat added. Accordingly, the increase in protein value of bread as a result of the addition of animal protein shows parallelism with our results.

Çakmak et al. [29] observed that the increase in the amount of moisture content and water activity of both bread varieties increased as the amount of wheat and whole wheat flour breads increased in different ratios. The results of our study are in parallel with the results of the researchers.

Found values in Dursun [30] for the simple bread study shows parallelism with the control group of our study for the protein content, but the ash ratio

and pH value were found lower as a result of our analysis.

Mohammed et al. [30] stated that the L* color of the chickpea flour bread decreased due to the increasing contribution rates, the product got a darker color and the a* and b* values increased. The results obtained by the researchers are in parallel with our study.

Dursun [26] stated that L* value decreased and the inner color was darker than the control bread with the increase of the substitution rate of the inner color of the bread samples enriched with fish meal. It can be stated that there is a decrease in L *, a * according to the addition ratio and that yeast-mold growth was not detected in all bread samples on the first day of bread production (first day of storage, 0th day).While the number of yeast-molds was not determined on the 1st day 0% and 3% added bread, an increase was observed depending on the enrichment rate and storage time. According to Turkish Food Codex Microbiological Criteria Regulation [31] 0% and 3% dough bread 0., 1. and on the second day yeast-mold value was found to be suitable for consumption. According to the same regulation, 5% and 7% enriched bread was suitable for consumption in terms of yeast and mold values on day 0 and day 1, while bread with 10% added was found to be suitable for consumption only on day 0. On other days of storage, bread cannot be consumed in terms of yeast and mold. This case may be related to the use of strip loin beef powder as an enriching agent. In the questionnaire, control group and meat powdered bread; questions were asked about crust texture, crust color, general form and inner texture, inner color, chewability, pore structure, taste, odor and overall acceptability. Survey of the questionnaire is numbered as 1 (poor), 4 (excellent). The sensory parameter scores are shown in Table 9. Significant differences were observed between bread samples in terms of sensory properties (P <0.05). The most admired by the panelists was bread with 3% meat powdered and the least liked bread with 10% meat powdered. It is more appreciated than additive-free bread. This can be explained by the fact that as the meat additives rate increases, the taste of

minced meat is more perceived as a result of the loss of traditional taste.

4. CONCLUSION

It can be stated that the addition of strip loin beef powder with the wheat flour does not improve the rheological properties of the dough as desired and the dough lost their processing properties as the fortification rate increases. If different methods can be used to bring the dough rheology to the appropriate condition in the bread to be used as the additive, the negative factors resulting from the fortification can be prevented and thus the high dough quality can be ensured. However, different amounts of strip loin beef powder added to the bread dough provided the production of bread with high protein content. It can be stated that the nutritional value of bread will increase with increasing protein content. These properties must be further improved for consumer acceptability. An alternative product rich in protein content has emerged by using red meat and wheat flour which has a very important place for human nutrition. Strip loin beef powder bread can be used as an alternative product that provides the protein and energy requirements of the individual by closing inadequate protein deficit of wheat flour with red meat that has high protein value and utilization rate.

The literature on using this study is limited and further research is needed. This study will contribute to further studies on this subject.

REFERENCES

[1] Pekcan, G., Beslenme Durumunun Saptanması, Sağlık Bakanlığı Yayınları, Klasmat Matbaacılık, Ankara, 2008.

[2] Tayar, M., Kokmaz, N.H. and Özkeleş, H.E., Beslenme İlkeleri, Dora Yayıncılık, Bursa, 2015.

[3] Elgün, A. and Ertugay, Z., Tahıl İşleme Teknolojisi. Erzurum, 1995.

[4] Kotancılar, G., Çelik, İ. and Ertugay, Z., Ekmeğin Besin Değeri ve Beslenmedeki Önemi, Erzurum, 1995.

[5] Bulduk, S., Gıda Teknolojisi, Detay Yayıncılık, Ankara, 2013.

[6] Elgün, A., Türker, S., and Bilgiçli, N., Tahıl ve Ürünlerinde Analitik Kalite Kontrolü. S.Ü. Ziraat Fakültesi Gıda Mühendisliği Ders Notları. Konya,Turkey, 2005.

[7] Gürbüz, Ü., Mezbaha Bilgisi Ve Pratik Et Muayenesi, Konya, 2009.

[8] Kucerova, J., Sottnikova, V. and Nedomova, S., Influence of Dietary Fiber Addition on The Rheological and Sensory Properties of Dough and Bakery Products, Czech J. Food Sci., 31-4 (2013) 340-346.

[9] Noorfarahzilah, M., Lee, J.S., Sharifudin, M.S., Mohd Fadzelly, A.B. and Hasmadi, M., Applications of Composite Flour in Development of Food Products, International Food Research Journal, 21-6 (2014) 2061-2074.

[10] Bhol, S. and Don Bosco, S. J., Influence of Malted Finger Millet and Red Kidney Bean Flour on Quality Characteristics of Developed Bread, Food Science and Technology, 55 (2014) 294-300.

[11] Mondor, M., Guevremont E. and Villeneuve, S., Processing, Characterization and Bread-Making Potential of Malted Yellow Peas, Food Bioscience, 7 (2014) 11-18.

[12] Villarino, C.B.J., Jayasena, V., Coorey, R., Chakrabarti-Bell, S., Foley, R., Fanning, K. and Johnson, S.K., The Effects of Lupin (Lupinus Angustifolius) Addition to Wheat Bread on Its Nutritional, Phytochemical and Bioactive Composition and Protein Quality, Food Research International, 76-1 (2015) 58-65.

[13] Rizzello, C.G., Calasso, M., Campanella, D., De Angelis, M. and Gobbetti, M., Use of Sourdough Fermentation and Mixture of Wheat, Chickpea, Lentil and Bean Flours For Enhancing The Nutritional, Texture and Sensory Characteristics of White Bread. International Journal of Food Microbiology, 180 (2014) 78-87.

[14] Ajo, R.Y., Characteristics of Thick Kmaj Bread Enrichment With Faba Bean (Vicia Faba) Flour, Quality Assurance and Safety of Crops & Foods, 5-4 (2013) 369-374.

[15] Serventia, L., Vittadini, E., and Vodovotza, Y., Effect of Chickpea Protein Concentrate on The Loaf Quality of Composite Soy-Wheat Bread, LWT-Food Science and Technology, 89 (2018) 400–402.

[16] Erdemir, Z.Ş., Isıl Işlem Görmüş Bakla Ezme Tozunun Ekmek Yapımında Kullanımı ve Kalite Kriterleri Üzerine Etkisinin Belirlenmesi, Pamukkale Üniversitesi Fen Bilimleri Enstitüsü, Yüksek Lisans Tezi. Denizli. 2015

[17] International Association for Cereal Science and Technology (I.C.C.). Determination of Ash in Cereals and Cereal Products. 104/1, Vienna. (1990).

[18] International Association for Cereal Science and Technology (I.C.C.). Determination of the Moisture Content of Cereals and Cereal Products (Practical method) 110/1, Vienna, (1976).

[19] International Association for Cereal Science and Technology (I.C.C.) Mechanical Determination of the Wet Gluten Content of Wheat Flour (Perten Glutomatic), 137/1,Vienna. (1994).

[20] International Association for Cereal Science and Technology (I.C.C.) Determination of Wet Gluten Quantity and Quality (Gluten Index ac. to Perten) of Whole Wheat Meal and Wheat Flour (Triticum aestivum), 155, Vienna. (1994).

[21] International Association for Cereal Science and Technology (I.C.C.) Determination of the Sedimentation Value (according to Zeleny) as an Approximate Measure of Baking Quality116/1, Vienna. (1994).

[22] International Association for Cereal Science and Technology (I.C.C.) Method for using the Brabender Amylograph, vol 126,1, Vienna. (1992).

[23] International Association for Cereal Science and Technology (I.C.C.) Method for using the Brabender Extensograph, vol 114,1, Vienna. (1992).

[24] American Association of Cereal Chemists (A.A.C.C.) Crude Protein Kjeldahl Method, Boric Acid Modification. Approved Methods of Analysis, 46 12.01, St. Paul. (2000).

[25] Halkman, K. Merck gıda mikrobiyolojisi uygulamaları. Başak Matbaacılık Ltd.Şti, 1.Baskı -Ankara, (2005) 175-179.

[26] Dursun, S., Ekmek Zenginleştirmede Protein Kaynağı Olarak Balık Etinin Kullanımı. (Doktora Tazi), Pamukkale Üniversitesi Fen Bilimleri Enstitüsü, Denizli, Turkey. (2006).

[27] Mohammed, I., Ahmed, A.R., and Senge, B. Dough Rheology and Bread Quality of Wheat-Chickpea Flour Blends, Industrial Crops and Products, 36 (2012) 196-202.

[28] Dursun, S., Yapar, A., ve Çelik, İ. Kadife Balığı (*Tinca Tinca L.,* 1758) Etiyle Zenginleştirmenin Hamurun Reolojik Özellikleri ve Ekmeğin Duyusal Özellikleri Üzerine Etkisi. Gıda Teknolojileri Elektronik Dergisi, 4-3 (2010) 44-58.

[29] Çakmak, H., Altinel, B., Kumcuoglu, S., and Tavman, S. Chicken Meat Added Bread Formulation for Protein Enrichment. Food and Feed Research 40-1 (2013) 33-41.

[30] Mohammed, I., Ahmed, A.R. and Senge, B., Dough Rheology and Bread Quality of Wheat-Chickpea Flour Blends, Industrial Crops and Products, 36 (2012) 196-202.

[31] Anonymous, Türk Gıda Kodeksi Mikrobiyolojik Kriterler Yönetmeliği, Date of Access; 24.06.2018, Avaliable Link; https://kms.kaysis.gov.tr/Home/Goster/40873

Novel Fluorene and Pyrrole Comprising Copolymers: Effect of Copolymer Feed Ratio on Electrochromic and Electrochemical Properties

Serife O. HACIOGLU [1,*] iD

[1] *Iskenderun Technical University, Department of Engineering Science, 31200, Hatay, Turkey*

Abstract. Herein, synthesis of two homopolymers namely, poly-2,2′-(9,9-dioctyl-9h-fluorene-2,7-diyl)bisthiophene (PBT), poly-pyrrole-3-carboxylic acid (PP3CA) and fluorene and pyrrole comprising five novel copolymers (CoP1, CoP2, CoP3, CoP4, CoP5) were electrochemically synthesized. Each electrolytic solution was prepared with different monomer feed ratios to investigate the effect of comonomer ratio on electrochromic and electrochemical properties. After synthesis, homopolymers and copolymers were compared in terms of their electrochemical, spectroelectrochemical and colorimetry properties. The number of studies on electrochromic characterization of pristine P3CA group was limited in literature, hence in this study P3CA was electrochemically inserted into the polymer chain via copolymerization.CoP1 with 1:1 (BT: P3CA) monomer feed ratio exhibited the lower optical band gap and red shifted neutral state absorption compared to PP3CA, additionally light yellow color of PP3CA turned out to be multichromic for CoP1with the insertion of BT unit via electrocopolymerization.

Keywords: Fluorene, pyrrole, copolymerization, electrochromism

Fluoren ve Pirol İçeren Kopolimerler: Kopolimer Besleme Oranının Elektrokimyasal ve Elektrokromik Özellikler Üzerine Etkisi

Özet. Bu çalışmada, poli-2,2′-(9,9-dioktil-9h-fluoren-2,7-diyl)bistiyofen (PBT) ve poli-pirol-3-karboksilik asit (PP3CA) olarak adlandırılan iki polimerin ve ayrıca fluoren ve pirol gruplarını içeren 5 tane yeni kopolimerin (CoP1, CoP2, CoP3, CoP4, CoP5) sentezi elektrokimyasal yöntemlerle gerçekleştirilmiştir. Kopolimer çözeltileri BT ve P3CA monomerlerinin farklı besleme oranlarında karışımı ile hazırlanarak, monomer besleme oranının kopolimerin elektrokimyasal ve elektrokromik özellikleri üzerine etkisi incelenmiştir. Elektrokimyasal polimer sentezlerinin ardından tüm homopolimer ve kopolimerlerin elektrokimyasal, elektrokromik ve kolorimetrik çalışmaları yapılmıştır. Literatürde P3CA monomerinin elektrokromik çalışmalarının az olması nedeniyle, bu yapı BT monomeri ile beraber kopolimer zincirine katılmıştır. Kopolimerler içinde, 1:1 (BT: P3CA) monomer besleme oranı ile hazırlanan CoP1 kopolimeri, PP3CA homopolimeri ile kıyaslandığında daha düşük bant aralığı ve multikromik özellikler göstermiştir.

Anahtar Kelimeler: Fluoren, pirol, kopolimerizasyon, elektrokromizm

1. INTRODUCTION

Electrochromic polymers are types of organic materials which can change their colors with applied potential have gained a great attention in recent years especially for many display and optoelectronic applications. In addition, electrochromism could be achieved with very low potential difference which strongly depends on the structure of the polymers. Although many inorganic molecules and organic compounds were widely used as electrochromic materials, organic conducting polymers (CPs) have drawn great interest due to their superior properties, such as relatively low cost, easy structural modification via chemical synthesis, color tunability, fast switching

time and high coloration efficiency [1-5]. As a result of these attractive properties, CPs have been used not only for electrochromic applications but also in wide range of technological areas such as organic photovoltaics (OPVs), organic light emitting diodes (OLEDs), field effect transistors (FETs), sensors and super capacitors (SCs) over the last two decades [6-10]. In order to use the CPs for the abovementioned applications, the value of the band gap and corresponding HOMO-LUMO energy levels are crucial factors. In recent years, the synthesis of multipurpose smart polymers with enhanced electronic and optical properties are the main purpose of the researchers in this field and this purpose can be achieved with controlling the structural alterations [11].

In literature, bond length alternation, planarity, interchain alternation, resonance effect, diverse pendant groups and donor-acceptor theory were well known strategies for controlling electronic and optoelectronic features of CPs, however donor-acceptor approach is considered as the most proper one to design CPs with unique and enhanced physicochemical properties. [12-14] Combination of different donor and acceptor units in the polymer backbone yields multipurpose copolymers with enhanced electrochemical and optical properties such as switching time, neutral and oxidized state colors and coloration efficiency. Another popular strategy for structural modification is copolymerization of different monomers. Via copolymerization, physicochemical behaviors could be altered easily and the units which can not be polymerized could be inserted into the polymer backbone [15,16]. Copolymerizationcan be performed via chemically or electrochemically in the presence of at least two comonomers with different monomer feed ratios. When compared to chemical copolymerization, electrochemical one has some certain advantages such as simplicity, easy and fast polymer synthesis and synthesis of well adhered copolymer film on an electrode surface. Additionally, after electrocopolymerization the electro-optical behaviors of the resulting copolymer films could be investigated with the same electrode easily [17].

In literature, different type of units such as; benzothiadiazole (BTd), quinoxaline (Qx), benzotriazole (BTz), carbazole (Cz), bithiophene, propylenedioxythiophene (ProDOT), fluorene and 3,4 ethylene dioxythiophene (EDOT) were widely used for electrochemical copolymerization and electrochromic applications. [18-20] Among a

great deal of electroactive polymers, polyfluorenes aroused interest as a blue light emitter with their high thermal and chemical stability and photostability both in solution and solid state. [21] However, some crucial drawbacks such as; poor solubility, aggregation in the solid state and high energy barrier for hole injection limited the possible application fields of PF. Copolymerization of fluorene with different comonomers resulted multipurpose functional copolymers with enlarged application fields [22,23]. Another interesting and popular comonomer unit is pyrrole (Py) due to some certain structural advantages such as; high electrical conductivity, easy preparation, chemical stability, structural versatility and biocompatibility. These unique properties increased the applicability of Py comprising polymers in different fields especially electrochemical and biological applications [24-26].

In the light of these, the main purpose of this study is to combine the promising properties of fluorene and Py monomers via electrochemical copolymerization technique. Herein, syntheses of two homopolymers (PBT and PP3CA) and design of five novel copolymers (CoP1, CoP2, CoP3, CoP4, CoP5) of BT and P3CA in different monomer feed ratios were performed. The electrochomical, spectroelectrochemical and colorimetric properties of resulting homopolymers and copolymers were explored and reported. Finally, the effect of copolymer feed ratio on electrochromic and electrochemical properties were also discussed.

2. EXPERIMENTAL

2.1. Materials and Equipments

2,2′-(9,9-Dioctyl-9h-Fluorene-2,7-Diyl)bisthio phene (BT), pyrrole-3-carboxylic (P3CA) (Fig. 1) are commercially available monomers and purchased from Sigma- Aldrich Chemical Co. Ltd. and used without any further purification. GAMRY 600 potentiostat/galvanostat was used for cyclic voltammetry studies and UV-Vis spectra characterizations were monitored at ambient temperature and conditions via Varian Carry 5000 UV-Vis spectrophotometer.
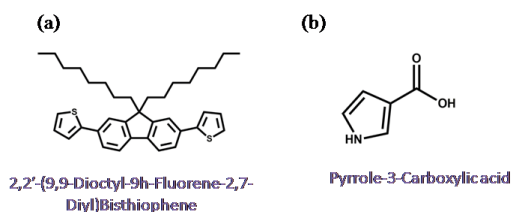
Figure 1. Molecular structures of 2,2′-(9,9-Dioctyl-9h-fluorene-2,7-diyl)bisthiophene (BT), pyrrole-3-carboxylic acid (P3CA).
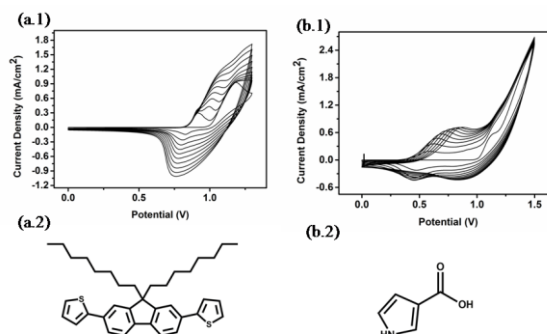

Figure 2. Cyclic voltammograms of BT and P3CA in 0.1 M LiClO$_4$- NaClO$_4$ /ACN solution at a scan rate of 100 mV.s^{-1} with corresponding monomer structures.

3. RESULTS AND DISCUSSIONS

3.1. Electrochemical copolymerization and characterizations

Cyclic Voltammetry (CV) is a very useful and widely used technique to determine the electroactivity of the compounds and also for quantitative analysis such as; HOMO-LUMO energy levels and oxidation/reduction potentials. Besides, electrochemical polymerization could be performed via CV with simple chemicals.

In this study electrochemical polymerizations for both homopolymers PBT (0.01 M) and PP3CA (0.01 M) and copolymers CoP1, CoP2, CoP3, CoP4, CoP5 (with a monomer feed ratio (PBT: P3CA) 1:1, 1:3, 1:5, 3:1 and 5:1) were performed via CV in 0.1 M LiClO$_4$ - NaClO$_4$ /ACN electrolyte/solvent couple. Both electropolymerizations were performed in a three electrode system comprising ITO coated glass slide (the working electrode), platinum wires (the counter electrode) and Ag wire (the pseudo reference electrode).The monomer structures and CVs for electrochemical polymerization of BT and P3CA are depicted in Figure 2. For electrochemical copolymerization, the compatibility of the oxidation potentials for two different monomers are vital for efficient copolymer film synthesis. As seen, in the first cycle of the CV, an irreversible monomer oxidation peaks were recorded at 1.18 V and 1.13 V, respectively. These similar oxidation potentials make BT and P3CA good candidates for copolymerization studies. During the CV, the increase in the current response indicates the successful electrochemical polymerization as the cycle number increased.

After electrochemical polymerization, single scan CVs were recorded in a monomer free medium for both homopolymers and corresponding oxidation peaks were obtained at 1.00 V and 0.75 V with 0.79 V and 0.44 V onset potentials, respectively (Figure 5). The HOMO-LUMO energy levels of the electroactive polymers were very crucial to test their applicability in different fields, for this reason HOMO energy levels of each homopolymers were calculated from the onsets of the corresponding oxidation potentials as -5.54 eV for PBT and -5.19 eV for PP3CA. Eqn 1 was used for HOMO energy level calculations and the results were summarized in Table 1.

$$HOMO= -(4.75\ eV + E_{onset}^{ox}) \qquad\qquad Eqn.1$$

In literature, P3CA derivatives were widely used for biological applications [27-28]. Herein, copolymerization technique was used to enhance the electrochemical behaviors of P3CA comprising electroactive polymers. As mentioned before, the compatibility of the oxidation potentials for monomers are very important for efficient copolymerization, in this study PBT monomer was used as a second monomer and five different copolymers (CoP1, CoP2, CoP3, CoP4, CoP5) with 1:1, 1:3, 1:5, 3:1 and 5:1 (PBT: P3CA) monomer feed ratios were synthesized electrochemically. Comonomer feed ratios of PBT: PP3CA were decided in order to investigate the effect of P3CA and BT units on electrochromic behaviors in detail. For that purpose initially CoP1 with 1:1 comonomer feed ratio was synthesized, then the effect of increasing P3CA and BT units on electrochromic characters were investigated stepwise. 1:5 and 5:1 comonomer feed ratios were chosen as the limit since after this ratio the copolymers exhibited PPBT and PP3CA like characters. Similar to the preparation of homopolymers, 0.1 M LiClO$_4$- NaClO$_4$ /ACN

electrolyte/solvent system was used for electrochemical copolymerization. As seen in Figure 3 and Figure 4, an increase in anodic and cathodic current densities were observed for all copolymers which prove the continuous copolymerization and the deposition of copolymer films on ITO coated glass slides. Then single scan CVs were recorded for all copolymers in a monomer free medium. From single scan CVs, oxidation potentials were calculated as 0.79/1.05V (CoP1), 0.53/0.98 V (CoP2), 0.83 V (CoP3), 0.76/1.05 V (CoP4) and 0.80/1.10 V (CoP5). Besides, corresponding HOMO energy levels were calculated from Eqn 1 and reported in Table 1 as -5.31eV(CoP1), -5.04 eV(CoP2), -5.29 eV(CoP3), -5.60 eV(CoP4) and -5.61eV(CoP5), respectively. As seen, two oxidation potentials at around 0.75 V and 1.00 V were observed for CoP1, CoP2, CoP4 and CoP5 which prove the successful insertion of comonomer units (BT and P3CA) into the copolymer chains. CVs of all copolymers (CoP1, CoP2, CoP3, CoP4 and CoP5) for both electrochemical copolymerizations and single scans recorded in a monomer free medium were reported in Figure 3 and Figure 4.
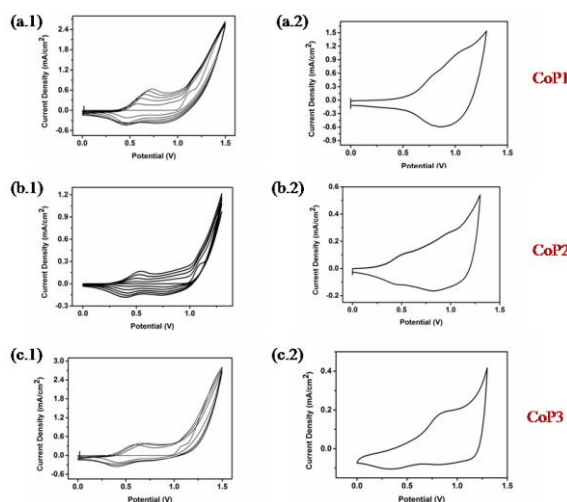
Figure 3. Cyclic voltammograms of (a.1) CoP1 (b.1) CoP2 (c.1) CoP3 during the electropolymerization on ITO- coated glass electrode and (a.2, b.2, c.2) single scan cyclic voltammograms of the resulting copolymers.

Cyclic voltammograms of CoP1, CoP2 and CoP3 during the electropolymerization and single scan CVs of the resulting copolymers were depicted in Figure 3. As seen, CoP1 with 1:1 (BT:P3CA) comonomer feed ratio exhibited two oxidation peaks at 0.79 V and 1.05 V with higher current density compared to those of CoP2 and CoP3. When P3CA ratio was increased into the copolymer chain, electroactivity of CVs depleted with lower current density as seen in single scan

CVs which can be dedicated to the poor electroactive character of P3CA.
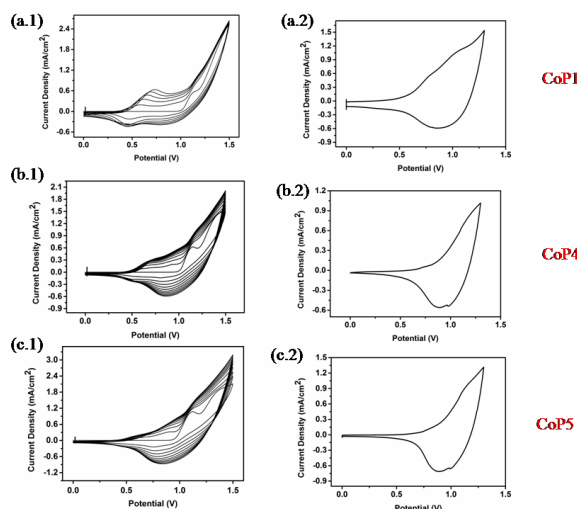
Figure 4. Cyclic voltammograms of (a.1) CoP1 (b.1) CoP4 (c.1) CoP5 during the electropolymerization and (a.2, b.2, c.2) single scan cyclic voltammograms of the resulting copolymers.

Cyclic voltammograms of CoP1, CoP4 and CoP5 during the electropolymerization and single scan cyclic voltammograms of the resulting copolymers were illustrated in Figure 4. As seen, the increasing amount of BT unit into copolymer chain affected electrochemical behaviors positively with increasing current density and electroactivity. Besides, as mentioned before copolymers exhibited two oxidation potentials at around 0.75 V and 1.00 V arising from P3CA and BT comonomers, respectively. As BT comonomer feed ratio was increased from CoP1 to CoP5, the intensity of the latter one increased significantly which proves the increasing number of BT unit into the copolymer chain. (Figure 4)
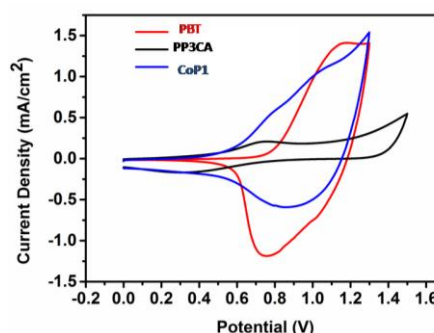

Figure 5. Single scan cyclic voltammograms for PBT, PP3CA and CoP1.

In order to investigate the effect of different comonomer units (P3CA and BT) on electrochemical behaviors, single scan CVs for PBT, PP3CA and CoP1 were recorded and reported in Figure 5. As mentioned before, BT unit was

inserted into the copolymer structure in order to improve the electrochemical behaviors and as seen in Figure 5, CoP1 exhibited higher current density and higher electroactivity compared to those of PP3CA which enlarge the application fields of P3CA comprising copolymers

Table 1. Summary of electrochemical and spectroelectrochemical properties of PBT, PP3CA and corresponding copolymers

	Monomer feed ratio (BT: P3CA)	E^{mon}_{ox} (V)	$E_{p\text{-}doping}$ (V)	E^{ox}onset (V)	HOMO (eV)	λ_{max} (nm)	λ_{max}^{onset} (nm)	E_g^{op} (eV)
PBT	1:0	1.18	1.00	0.79	-5.54	430	540	2.29
PP3CA	0:1	1.13	0.75	0.44	-5.19	397	600	2.07
CoP1	1:1	-	0.79/1.05	0.56	-5.31	412	650	1.91
CoP2	1:3	-	0.53/0.98	0.29	-5.04	420	560	2.21
CoP3	1:5	-	0.83	0.54	-5.29	400	611	2.03
CoP4	3:1	-	0.76/1.05	0.85	-5.60	419	584	2.12
CoP5	5:1	-	0.80/1.10	0.86	-5.61	424	628	1.98

3.2. Spectroscopic Characterization

After electrochemical copolymerization and characterizations, the spectral behaviors were recorded with UV-VIS spectrophotometer in order to investigate the electronic transitions and changes in optical properties upon applied potential. The effect of the changing monomer feed ratio on the optoelectronic properties of the fluorene and pyrrole comprising electroactive copolymers were examined by spectroelectrochemical studies. In addition, from these studies some crucial parameters such as; maximum absorption wavelengths (λ_{max}), optical band gap and polaron/bipolaron bands were determined.

Before stepwise oxidation, electrochemically synthesized copolymer films were reduced to neutral states by applying a constant potential to remove any trapped charge and dopant ions. Then, the neutral films were oxidized stepwise and electronic absorption spectra were recorded in a monomer free 0.1 M LiClO$_4$-NaClO$_4$ /ACN solution.

As seen in Figure 6 and Figure 7, the maximum absorption wavelengths (λ_{max}) for homopolymers and copolymers were centered at 430 nm (PBT), 397 nm (PP3CA), 412 nm (CoP1), 420 nm (CoP2), 400 nm (CoP3), 419 nm(CoP4) , 424 nm (CoP5). As mentioned before the P3CA homopolymer exhibited poor electrochemical behaviors, in addition the neutral state absorption of P3CA was centered in the UV region which limit the

application fields. In this study, insertion of fluorene derivatives into the copolymer structure with different monomer feed ratios enhanced the electrochromic and spectroelectrochemical behaviors. As seen in Figure 6, while P3CA homopolymer showed light yellow color both in the neutral and oxidized states, CoP1 with 1:1 (BT: P3CA) monomer feed ratio exhibited multichromic behavior. While homopolymers showed λ_{max} values centered at 430 nm (PBT) and 397 nm (PP3CA), all copolymers exhibited λ_{max} values between those values, additionally as the P3CA feed ratio was increased in the copolymer structure an obvious red shift was observed.

During spectroelectrochemical measurements, new absorption bands were observed at around 700 nm for both homopolymers and copolymers due to the formation of charge carriers named as polarons (radical cations) on the polymer backbone. During stepwise oxidation, the intensity of the polarons increased significantly, meanwhile the intensity of the neutral state absorptions gradually diminished.

Another important parameter of electroactive polymers for variety of applications is the optical band gap value which can be calculated from neutral state absorption. Herein, optical band gaps of both homopolymers and copolymers were determined from the onset of their lowest energy π-π* transitions as 2.29 eV (PBT), 2.07 eV (PP3CA), 1.91 eV (CoP1), 2.21 eV (CoP1), 2.03 eV (CoP1), 2.12 eV (CoP1), 1.98 eV (CoP1) , respectively. When homopolymers and copolymers were compared in terms of optical characters, while PBT

exhibited the highest optical band gap due to its UV-region covered absorption, CoP1 with 1:1 (BT: P3CA) monomer feed ratio showed the lowest optical band gap due to its red shifted absorption.
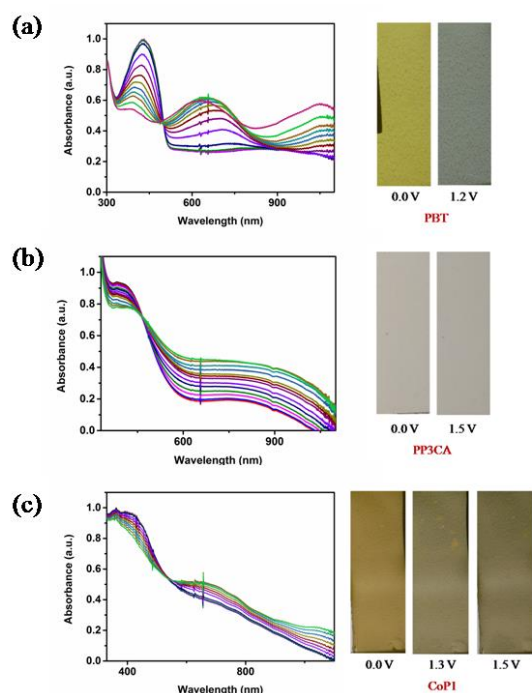

Figure 6. UV-Vis spectra of (a) PBT (b) PP3CA and (c) CoP1 during a slow oxidation process in a 0.1 M LiClO4-NaClO4 /ACN monomer-free solution with corresponding colors in the neutral and oxidized states.
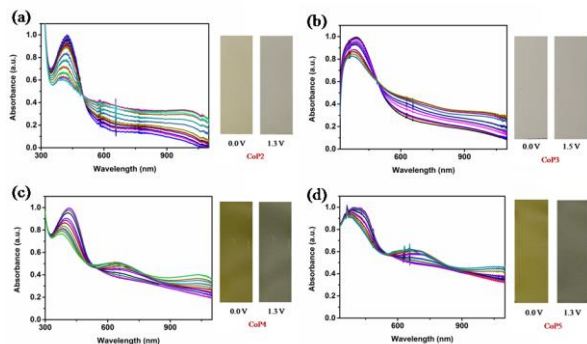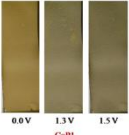

Figure 7. UV-Vis spectra of (a) CoP2 (b) CoP3 (c) CoP4 and (d) CoP5 during stepwise oxidation in a 0.1 M LiClO4-NaClO4 /ACN monomer-free solution with corresponding colors in the neutral and oxidized states.

Finally, colorimetric studies were performed in order to report the colors of all copolymers both in the neutral and oxidized states. For colorimetric studies photographs of the polymers films were recorded and reported in Table 2 with the corresponding L, a, b values according to CIE (Commission Internationale de l'Eclairage) coordinates. CIE coordinates were widely used to report the colors of materials in a more scientific way. While 'L' represents the brightness of the color, 'a' represents the color between red/magenta

and green and 'b' represents the color between yellow and blue in the colorimetric measurements, The corresponding L, a, b results for both homopolymers and copolymers were reported in Table 2. As mentioned before, the light yellow color of P3CA homopolymer observed both in the neutral and oxidized states were changed to multichromic behavior via insertion of BT unit into the copolymer chain with 1:1 (BT: P3CA) monomer feed ratio. Additionally, lower optical band gap and red shifted neutral state absorption were investigated for CoP1. In this study P3CA group was electrochemically inserted into the copolymer chain with copolymerization technique, and as a separate study the P3CA comprising copolymers will be used for biosensor applications in our research group.

Table 2. Colorimetric measurements of the homopolymers and copolymers.

Polymer	Applied potential	L	a	b	
PBT	0.0 V	66	-8	48	
	1.2 V	55	-5	7	
PP3CA	0.0 V	71	1	6	
	1.5 V	69	0	6	
CoP1	0.0 V	52	4	39	
	1.3 V	41	-1	23	
	1.5 V	49	1	21	
CoP2	0.0 V	72	-2	16	
	1.3 V	68	-1	8	
CoP3	0.0 V	72	2	6	
	1.5 V	69	0	5	
CoP4	0.0 V	42	-4	38	
	1.3 V	44	-3	15	
CoP5	0.0 V	54	-3	39	
	1.3 V	47	-2	13	

4. CONCLUSION

Fluorene and pyrrole bearing electrochromic homopolymers (PBT and PP3CA) and novel copolymers (CoP1, CoP2, CoP3, CoP4, CoP5) with different monomer feed ratios were synthesized via electrochemical technique. After successive electropolymerization, the electrochemical, spectroelectrochemical and colorimetric properties were investigated for all polymers. All copolymers exhibited different electrochemical and optical properties when compared to their homopolymers. While homopolymers PBT and PP3CA exhibited λ_{max} values centered at 430 nm and 397 nm, all copolymers exhibited λ_{max} values between those values. In addition, in terms of optical behaviors as

the P3CA feed ratio was increased in the copolymer structure the obvious red shift was observed on spectroelectrochemical characterizations. While PBT showed yellow and green colors in the neutral and oxidized states, the light yellow color was observed for P3CA in both states. However multichromic behavior was explored for CoP1 via insertion of BT unit into the copolymer chain with 1:1 (BT: P3CA) monomer feed ratio. Additionally, lower optical band gap and red shifted neutral state absorption were investigated for CoP1 compared with pristine PP3CA. Finally, in this study P3CA group was electrochemically inserted into the copolymer chain successfully and electrochromic characters were investigated in detail, in future the P3CA bearing copolymers will be used for biosensor applications in our research group.

ACKNOWLEDGMENTS

REFERENCES

[1] Sonmez G., Shen C.K.F., Rubin Y. and Wudl F., A red, green, and blue (RGB) polymeric electrochromic device (PECD): the dawning of the PECD era, Angew. Chem. Int. Ed., 43 (2004) 1498-502.

[2] Xu G., Zhao J., Liu J., Cui C., Hou Y. and Kong Y., Electrochemical synthesis and characterization of imidazole-containing polymers, and their electrochromic devices application organic and bioelectrochemistry, J. Electrochem Soc, 160(11), (2013) G149-G155.

[3] Kumar A., Welsh D.M., Morvant M.C., Piroux F., Abboud K.A. and Reynolds J.R., Conducting poly(3,4-alkylenedioxythiophene) derivatives as fast electrochromics with high-contrast ratios, Chem. Mater. 10 (1998) 896–902.

[4] Balan A., Gunbas G., Durmus A. and Toppare L., Donor−acceptor polymer with benzotriazole moiety: enhancing the electrochromic properties of the "donor unit", Chem. Mater. 20 (2008) 7510– 7513.

[5] Krebs E.F.C., Electrochromic displays: The new black, Nat. Mater. 7 (2008) 766–767.

[6] Yang C., Kim J. Y., Cho S., Lee J. K., Heeger A. J. and Wudl F., Functionalized methanofullerenes used as n-type materials in bulk-heterojunction polymer solar cells and in field-effect transistors, J. Am. Chem. Soc., 130 (2008) 6444−6450.

[7] Ma C., Toya M. and Xu C., Flexible electrochromic device based on poly (3,4-(2,2-dimethylpropylenedioxy)thiophene), Electrochim. Acta 54 (2008) 598-605.

[8] Soylemez S., Hacioglu S.O., Kesik M., Unay H., Cirpan A. and Toppare L., A novel and effective surface design: conducting polymer/β-cyclodextrin host–guest system for cholesterol biosensor, ACS Appl. Mater. Interfaces, 6 (2014) 18290−18300.

[9] Xu Z.,Yu D. and Yu M.,The synthesis and photoluminescence characteristics of novel 4-aryl substituted thiophene derivatives with bis-diarylacrylonitrile unit, Dyes and Pigments, 95 (2012) 358-364.

[10] Ermiş E., Yigit D. and Güllü M., Synthesis of poly(N-alkyl-3,4-dihydrothieno[3,4-b][1,4]oxazine) derivatives and investigation of their supercapacitive performances for charge storage applications, Electrochim. Acta, 90 (2013) 623-633.

[11] Mullekom H. A. M., Vekemans J. A. J. M., Havinga E. E. and Meijer E. W., Developments in the chemistry and band gap engineering of donor- acceptor substituted conjugated polymers, Mater. Sci. Eng., R32 (2001) 1–40.

[12] Zhang C., Hua C., Wang G., Ouyang M. and Ma C., A novel multichromic copolymer of 1,4-bis(3-hexylthiophen-2-yl)benzene and 3,4-ethylenedioxythiophene prepared via electrocopolymerization, J. Electroanal. Chem., 645 (2010) 50-57.

[13] Roncali J., Molecular Engineering of the Band Gap of π-Conjugated Systems: Facing Technological Applications, Macromol. Rapid Commun., 28 (2007) 1761–1775.

[14] Gunbas G. and Toppare L., Green as it Gets; Donor-Acceptor type Polymers as the Key to Realization of RGB Based Polymer Display Devices, Macromol. Symp., 297 (2010) 79-86.

[15] Nie, G., Qu, L., Xu J. and Zhang S., Electrosyntheses and characterizations of a new soluble conducting copolymer of 5-cyanoindole and 3,4-ethylenedioxythiophene, Electrochim. Acta, 53 (2008) 8351−8358.

[16] Soylemez S., Hacioglu S. O., Uzun S. D. and Toppare L., A low band gap benzimidazole derivative and its copolymer with 3,4-ethylenedioxythiophene for electrochemical studies. J. Electrochem. Soc., 162 (1) (2015) H6-H14.

[17] Aydın A. and Kaya I., Syntheses of novel copolymers containing carbazole and their electrochromic properties, J. Electroanal. Chem., 691 (2013) 1−12.

[18] Kuo C.-W., Wu T.-L., Lin Y.-C., Chang J.-K., Chen H.-R. and Wu T.-Y., Copolymers based on 1,3-bis(carbazol-9-yl)benzene and three 3,4-ethylenedioxythiophene derivatives as potential anodically coloring copolymers in high-contrast electrochromic devices, Polymers, 8 (2016) 368-383.

[19] Carbas B. B., Novel electrochromic copolymers based on 3-3′-dibromo-2-2′-bithiophene and 3,4 ethylene dioxythiophene, Polymer, 113 (2017) 180-186.

[20] Ergun E. G. C., Covering the more visible region by electrochemical copolymerization of carbazole and benzothiadiazole based donor-acceptor type monomers, Chinese J. Polym. Sci., 37 (2019) 28–35.

[21] Wu F. I., Shih P. I., Shu C. F., Tung Y. L. and Chi Y., Highly efficient light-emitting diodes based on fluorene copolymer consisting of triarylamine units in the main chain and oxadiazole pendent groups, Macromolecules, 38 (2005) 9028-9036.

[22] Lee J. H., Cho H. J., Cho N. S., Hwang D. H., Kang J. M., Lim E. H., Lee I. J. and Shim H. K., Enhanced efficiency of polyfluorene derivatives: Organic–inorganic hybrid polymer light-emitting diodes, J. Polym. Sci. A: Polym. Chem., 44 (2006) 2943-2954.

[23] Carbas B. B. ¸ Kivrak A. and Önal A. M., A new processable electrochromic polymer based on an electron deficient fluorene derivative with a high coloration efficiency, Electrochim. Acta, 58 (2011) 223– 230.

[24] Toshima N. and Ihata O., Catalytic synthesis of conductive polypyrrole using iron (III) catalyst and molecular oxygen, Synth. Met., 79 (1996) 165-172.

[25] Lee S., Cho M. S. and Nam J. D., New strategy and easy fabrication of solid-state supercapacitor based on polypyrrole and nitrile rubber, J. Nanosci. Nanotechnol., 8 (2008) 4722-4725.

[26] Vaitkuviene A., Kaseta V., Voronovic J., Ramanauskaite G., Biziuleviciene G., Ramanaviciene A. and Ramanavicius A., Evaluation of cytotoxicity of polypyrrole nanoparticles synthesized by oxidative polymerization, J. Hazard Mater., 250 (2013) 167-174.

[27] M.-B. Edyta, Siekiera I., Krolikowska A., Donten M. and Nowicka A. M., Combination of copolymer film (PPy-PPyCOOH) and magnetic nanoparticles as an electroactive and biocompatible platform for electrochemical purposes, Electrochim. Acta, 263 (2018) 454-464.

[28] Özcan A. and Ilkbas S., Poly(pyrrole-3-carboxylic acid)-modified pencil graphite electrode for the determination of serotonin in biological samples by adsorptive stripping voltammetry, Sens. Actuators B, 215 (2015) 518–524.

The Effect of Semi-Circular Protrusions on Cylinder to Flow Structure

Ferhat KOCA [1] iD *, Adnan ÖZTÜRK* [2*] iD

[1] *Sivas Cumhuriyet University Faculty of Technology, Department of Automotive Engineering*

58140 Campus, Sivas

2 *Sivas Cumhuriyet University Faculty of Engineering, Department of Mechanical Engineering*

58140 Campus, Sivas

Abstract. In this study; two dimensional, viscous, incompressible, fully developed and turbulent flows on the surface of the cylinder placed in a channel were analyzed using numerical methods. Momentum and continuity equations were solved numerically by ANSYS FLUENT program using finite volume method. The effect of the half cylinder (d = 4.4 mm) placed on the cylinder diameter (D) 44 mm in different positions (0°, 45°, 90°, 135° and 180°) on the flow structure was examined. Streamlines and the turbulence kinetic energy contours were drawn for the Reynolds number 10^4 value depending on cylinder diameter. As a result, downstream flow characteristics of cylinders having semi-circular protrusions placed in different positions were examined and drag force coefficients (C_D) were obtained. It was concluded that the protrusion on the cylinder placed at different angles changed the flow structure and controlled the separation.

Keywords: Cylinder, CFD analysis, Drag force coefficient, Flow control

Silindir Üzerindeki Yarı-Yuvarlak Çıkıntıların Akış Yapısı Üzerine Etkisi

Özet. Bu çalışmada, bir kanala yerleştirilen silindir yüzeyi üzerinde iki boyutlu, viskoz, sıkıştırılamaz, gelişmiş ve türbülanslı akış, sayısal yöntemler kullanılarak analiz edilmiştir. Momentum ve süreklilik denklemleri ANSYS FLUENT programı ile sonlu hacimler yöntemi kullanılarak sayısal olarak çözülmüştür. Farklı konumlarda (0°, 45°, 90°, 135° ve 180°) 44 mm çapında (D) bir silindir üzerine yerleştirilmiş yarım silindirin (d = 4.4 mm) akış yapısına etkisi incelenmiştir. Akım çizgileri ve türbülans kinetik enerji konturları, silindir çapına bağlı olarak Reynolds sayısı 104 değeri için çizilmiştir. Sonuç olarak, farklı konumlara yerleştirilmiş yarı dairesel çıkıntılara sahip olan silindirlerin akım yönünde akış özellikleri incelenmiş, sürtünme direnç katsayıları (CD) elde edilmiştir. Farklı açılarda yerleştirilen silindir üzerindeki çıkıntının akış yapısını değiştirdiği ve ayrımı kontrol ettiği sonucuna varılmıştır.

Anahtar Kelimeler: Silindir, HAD analizi, Direnç katsayısı, Akış kontrolü

1. INTRODUCTION

The flows on the circular cylinder have attracted intensive interest from the past to the present for both experimental and numerical studies. These types of flow structures are encountered in many engineering applications such as wind-affected buildings, cooling towers and chimneys in thermal power plants, large silos, refineries, electronic circuits. Knowing of the flow structure and physics on the bodies, determining of the fluid forces acting on the bodies, the separation zones arising from the flow interaction between the body and its surroundings have great importance in the determination of the multi-vortex systems interacting with the body [1]. In addition, active and passive methods are developed in order to eliminate

the effects of these vortices or to reduce them to a minimum level. Some of these methods are moving the surface through which the fluid flows, adding or drawing various gases at specific speeds, using other surfaces to prevent air flowing from the boundary surface, and cooling the surface through which the fluid flows. Active methods are used to control the energy level of the flow and the applications of these methods are expensive. In passive methods the flow structure is not directly changed, the desired form of the flow structure is obtained by changing the structural form of the body.

In the study of Canpolat and Sahin, a groove is cut into the surface of a circular cylinder and the effect of this groove on the flow structure is examined by particle imaging [2]. The groove, which was designed in a square shape, was patterned longitudinally on the surface of the cylinder with a diameter of 50 mm, and in different positions (between 0° and 150° degrees) starting from the stagnation point. They observed that the critical position angle of the grooved structure is 80° degrees, and stated the flow is controllable for positions less than 80° degrees. In the study of Gundemir and Tastan, the effects of the longitudinal-groove roughness, which is placed on the outer surface of the pipe, on the drag force acting on the pipe were experimentally studied and compared with uniform sand roughness [3].

Oguz et al. studied the effect of braid wires having different thickness and permeability ratio wound around a circular cylinder with a diameter of 50 mm when the Reynolds number (Re_D) is 5000 [4]. They determined four different permeability rates ranging between 0.5 and 0.8 with an increment of 0.1, and thickness of the wires wrapped on the cylinder to be 1 mm, 2 mm, 3 mm and 4 mm in this study. Thus, the flow structure behind the cylinder was tried to be controlled by braid wires wound around the cylinder. Using the particle imaging technique, they observed that the turbulence kinetic energy (TKE) contours and Reynolds shear stress values for the cylinder with wires having thicknesses of 1 mm and 2 mm increased, but for the cylinder with wires having thicknesses of 3 mm and 4 mm decreased compared to the values of the plain cylinder. For the permeability ratio of 0.6 mm and the wire thickness of 4 mm, TKE and Reynolds shear stress values are shown that the braid wires control the flow behind the cylinder. Considering the result of the frequency values, they stated that optimal control of the flow is provided when the permeability ratio is 0.6 mm and wire thickness is 4 mm.

In the study of Akar and Kucuk, it is aimed to control flow structure downstream of the inner cylinder with different diameters by a surrounding outer cylinder that has 0.5 porosity [5]. The diameter of outer cylinder was chosen as D_o=100mm. The perforation hole diameters of the cylinder were d=10mm. The depth-averaged free stream velocity was U=100m/s which corresponded to Re_D=10000 based on outer cylinder diameter. Flow characteristics downstream of the cylinder were investigated by using particle image velocimetry (PIV) technique. PIV experiments were performed at the mid-section of water 200mm. It has been observed that the perforated outer cylinder decreased vortex shedding downstream of the inner cylinder with different diameters. For high diameter ratios, $D_i/D_o \geq 0.7$ perforated outer cylinder lost its effect on the flow control.

Ranjith et al. studied the flow analysis on a circular cylinder having helical coatings using the HAD method [6]. They examined the effectiveness of helical coatings that suppress the vortex-induced vibration (VIV) of the helical cylinder at two different Reynolds numbers (100 and 28000) by providing three initial helical coatings around the circular cylinder. Static pressure, velocity magnitude, vorticity contours, drag C_D coefficient and lift C_L coefficient were obtained. They reported that the helical-coated cylinder has a higher coefficient of friction than the plain cylinder and the helical coatings can reduce VIV by about 99%.

Yeo and Jones studied the behavior of the flow around the surface using numerical methods in order to understand the interaction on the helical coated circular cylinder surfaces and the Karman vortex-induced vibrations [7]. They examined the flow around the yawed cylinder with various spiral patterns using three-dimensional discrete vortex simulation (DES) at number of $Re_D = 1.4 \times 10^5$ depending on the free flow rate and the cylinder diameter, D. As a result, they presented that the helical models strongly influence the flow structures around the cylinder and the development of the associated forces on the cylinder. They stated that suitable cylinder surfaces can reduce large-amplitude and low-frequency vibrations induced by the flow.

Lam et al. performed the Large Eddy Simulation (LES) to examine the three-dimensional properties of turbulent flow past cylinders having yaw angles from 0° to 60° at a Reynolds number of 3900 [8]. They examined the force coefficients and the relationship between the vortex frequency and the yaw angles for both wavy cylinders and circular cylinders. Differences in the vortex structure between the wavy cylinder and the circular cylinder were found to be significant when yaw angles are small. It is emphasized that the differences are insignificant at large angles and the critical angle value is stated to be 45°.

In this study, the effect of a single cemi-circular protrusion placed on a cylinder with a diameter of 44 mm in different positions on the flow structure has been examined for the $Re_D = 10^4$. To the best of our knowledge, the effect of the channels placed along the length of the cylinder in the studies related to this subject was examined, but the effect of the small diameter half cylinder placed in different positions on the flow structure was firstly investigated in the present study.

2. MATERIAL AND METHOD

The cylinders to be analyzed were formed by adding semi-circular protrusions in different positions as seen in Figure 1. In the study, five different designs were formed using the 45° increase between 0° and 180° in the counterclockwise direction and semi-circular protrusions placed on the horizontal axis. The schematic of the flow field is presented in Figure 2.
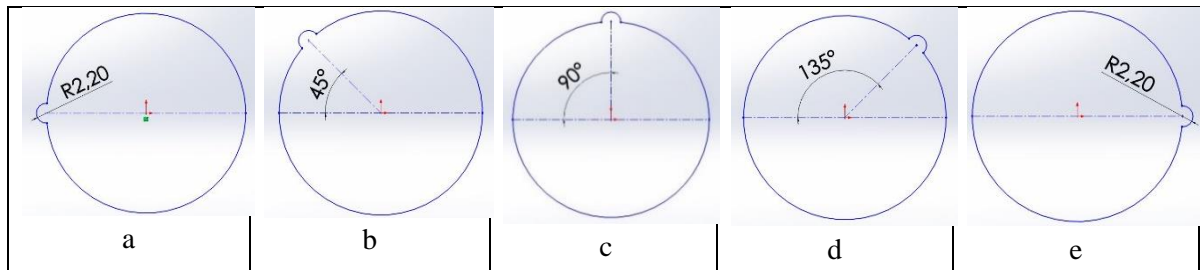

Figure 1. Positions of protrusions on the cylinder for a) 0°, b) 45°, c) 90°, d) 135°, e) 180°
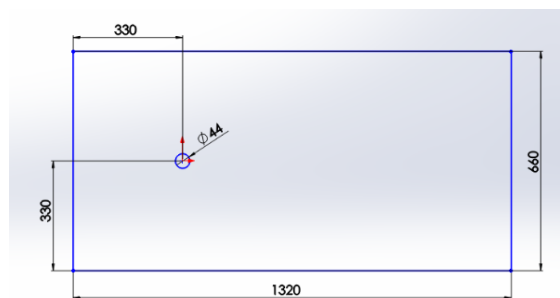

Figure 2. The schematic of the flow field (mm)

The mesh structure of the flow field and mesh independence graph are presented in Figure 3. The edge sizing method was used to refine the mesh around the hole to obtain acceptable results. Accordingly, the circumference of the hole was divided into 100 equal elements, and the triangular mesh was used. The mesh consisting of 17415 mesh elements and 8999 nodes was produced and analyzed.
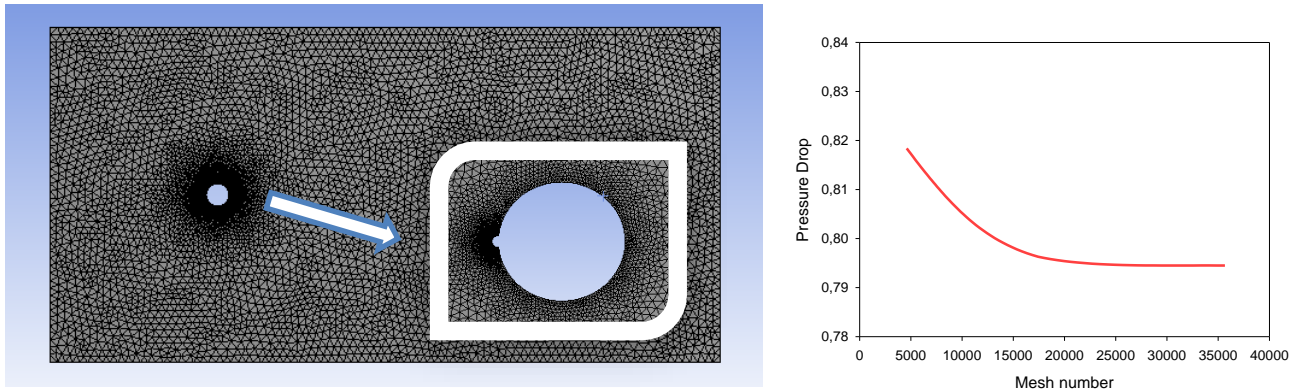

Figure 3. Mesh structure and independence

Figure 4 shows the boundary conditions of the flow fields. The velocity inlet and pressure outlet boundary conditions were used at the inlet and outlet of the flow channel. The side surfaces of the channel were defined as a wall where there is no fluid inlet and outlet with no-slip boundary condition. Also, in order to obtain forces acting on the surface of the cylinder, the surface of the cylinder was defined as a wall.
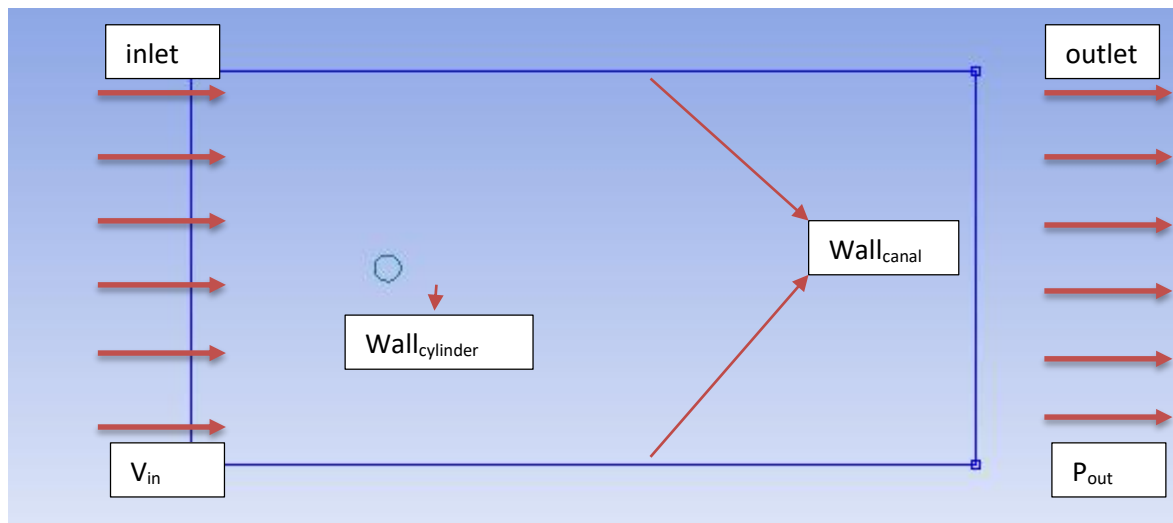

Figure 4. The boundary conditions of the flow fields

For 2D cartesian coordinate system, continuity, momentum, and energy equations were solved by using the Boussinesq approach and the conservation equations were defined as follows.

Continuity Equation:

$$\frac{\partial u}{\partial x} + \frac{\partial v}{\partial y} + \frac{\partial w}{\partial z} = 0 \qquad (1)$$

Momentum Equation:

$$u\frac{\partial u}{\partial x} + v\frac{\partial v}{\partial y} + w\frac{\partial w}{\partial z} = -\frac{1}{\rho}\frac{\partial P}{\partial x} + v\left(\frac{\partial^2 u}{\partial x^2} + \frac{\partial^2 v}{\partial y^2} + \frac{\partial^2 w}{\partial y^2}\right) \qquad (2)$$

Energy Equation:

$$u\frac{\partial T}{\partial x} + v\frac{\partial T}{\partial y} + w\frac{\partial T}{\partial z} = \alpha\left(\frac{\partial^2 T}{\partial x^2} + \frac{\partial^2 T}{\partial y^2} + \frac{\partial^2 T}{\partial z^2}\right) \qquad (3)$$

The Eqs. (1-3) are arranged according to the following boundary conditions:
All the walls and the cylinder were modeled to be monolithic and adiabatic.
In the free current zone, $u = 0.228\ m/s$ ($Re_D = 10^4$ depending on the cylinder diameter)
$\partial T/\partial x = 0$, on the side walls: $v = 0$, upper and lower walls: $w = 0$,

The dimensionless parameters used in this study as follows;

$$Re_D = \frac{\rho\ u\ D}{\mu} \qquad (4)$$

where ρ is fluid density, u is free stream velocity, and μ is fluid viscosity.

Drag coefficient;

$$C_D = \frac{F_D}{\frac{1}{2}\rho\ A\ u^2} \qquad (5)$$

where F_D is the drag force on the cylinder created by the fluid, A is the area of the cylinder perpendicular to the flow direction.

Strouhal (St) Number:

$$St = \frac{f_s\ D}{u} \qquad (6)$$

here f_s is the vortex frequency value.

This study was made under the following assumptions:

- Flow is 2D, time-independent and turbulent,
- The fluid used is incompressible (ρ=998 kg/m^3)
- Aluminum is used as the boundary of the cylinder and the channel material,
- There is no heat transfer between layers.
- The fluid flows into the channel at a certain speed in the X-direction,
- The thermal properties of the fluid are constant,
- There is no heat generation in the fluid and at the boundaries.

3. RESULTS AND DISCUSSIONS

The properties to be obtained such as the distances (a, b, c, d) from the center of the cylinder and the locations (F_1, F_2) of the vortices to be compared in the results of analysis, the location of the streamlines in which the flow separation occurs (A), and the junction location (S) of the streamlines formed behind the cylinder are shown in Figure 5. The distances of the vortex centers to the center of the cylinder are shown in (a) and (b) on the horizontal axis, and in (c) and (d) on the vertical axis. It is investigated how the position of the vortices formed in the downstream region changes relative to the semi-circular protrusions placed on the cylinder. The F_1 and F_2 value shows the center position of the upper and lower vortex, respectively. These vortices are caused by the effect of the circular cylinder placed upstream. The saddle point (S) indicates the location of the endpoint of the vortex's circulation zone. The distances between all these points as well as their position relative to the cylinder center are extremely important in order to change the vortex control mechanism to the desired form. The vortices must be kept under control to eliminate or minimize the negative effects caused by the resistance and oscillation movements on the cylinder.
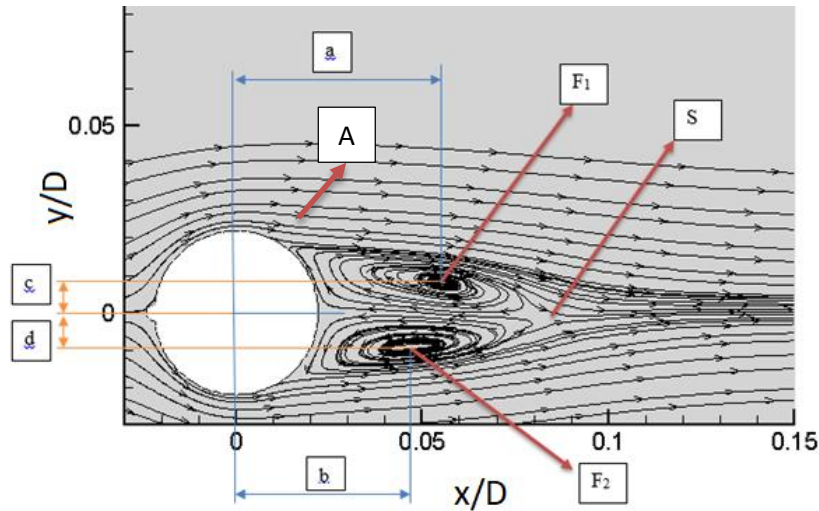
Figure 5. View of received result values

Figure 6 shows the streamlines and TKE contours according to the positions of semi-circular cylinders placed on the cylinder with different position angles. When the figures are examined, it is seen that F_1 and F_2 vortex centers vary for different models. The vortex centres and the separation point positions are given in Table 1. The X-values in F_1 and F_2 correspond to the values of (a) and (b) and the Y-values correspond to the values of (c) and (d), respectively.

While the vortex points approach the X-axis for the models with 135° and 180°, these points become distanced from the X-axis for the models with 45° and 90° and so the wake area gets larger. When the vortex positions according to the Y axis were examined, it was observed that models with 0° and 135° degrees were the closest models to the axis, and vortex centers farther from the axis occurred at the position of 45°, 90° and 180° degrees. This leads to streamline for the models with 0° and 135° degrees.

When the locations of the saddle points, S are examined in Table 1, it is confirmed that the 0° and 135° semi-circular protrusion position models are similar and have narrow downstream field than the other models. While this S-point is very close to the X-axis at all angle values, this point is at the most distant point in the Y-axis at 90°. At the same time, the greatest TKE values are seen at 90° in Fig. 6 because of the maximum values of the vortex forms for the 90° position model. The growth of the downstream area and the high TKE value cause to increase the vortex movements and thus the frequency values change.

Table 1. The vortex centers and the separation point positions

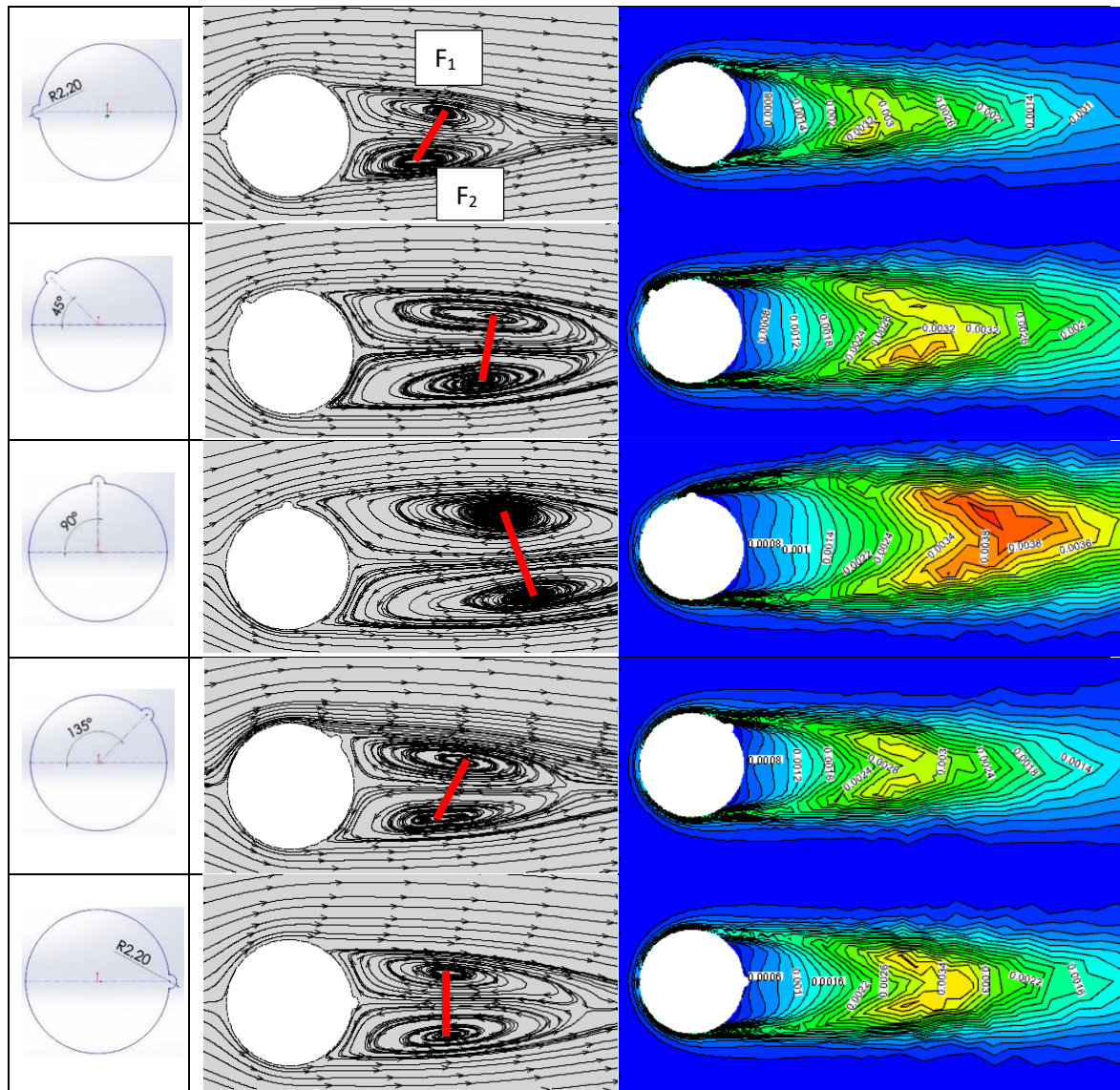|		F_1	F_2	S	Separation Point	Separation Angle (º)
0°	x/D	0.054	0.045	0.082	0.0106	118,78
	y/D	0.008	-0.008	-0.0009	0.0193	
45°	x/D	0.075	0.085	0.141	0.0067	107,62
	y/D	0.022	-0.009	0.007	0.0211	
90°	x/D	0.075	0.086	0.134	0.0013	93,07
	y/D	0.020	-0.009	0.008	0.0242	
135°	x/D	0.0603	0.051	0.096	0.0114	121,10
	y/D	0.0089	-0.011	-0.0003	0.0189	
180°	x/D	0.0545	0.0534	0.1032	0.0071	108,60
	y/D	0.0110	-0.0105	-0.0016	0.0211	

Figure 6. Streamlines and TKE contours of the models

The separation point and angle values are given in Table 1, and also these separation points are shown angularly in Fig. 7. The earliest separation point has occurred at 93,07° in the model where the protrusion has at 90° position, while the latest separation point is seen at 121,1° in the model at 135° protrusion position. When the separation point angles are examined, the flow separations are close to each other for the models in the 0° and 135°, and 45° and 180° positions, while the model with 90° position is different from other models and it has an early separation.

108,6"
121,1"
93,07"
107,62"
118,78"

180° 135° 90° 45° 0°
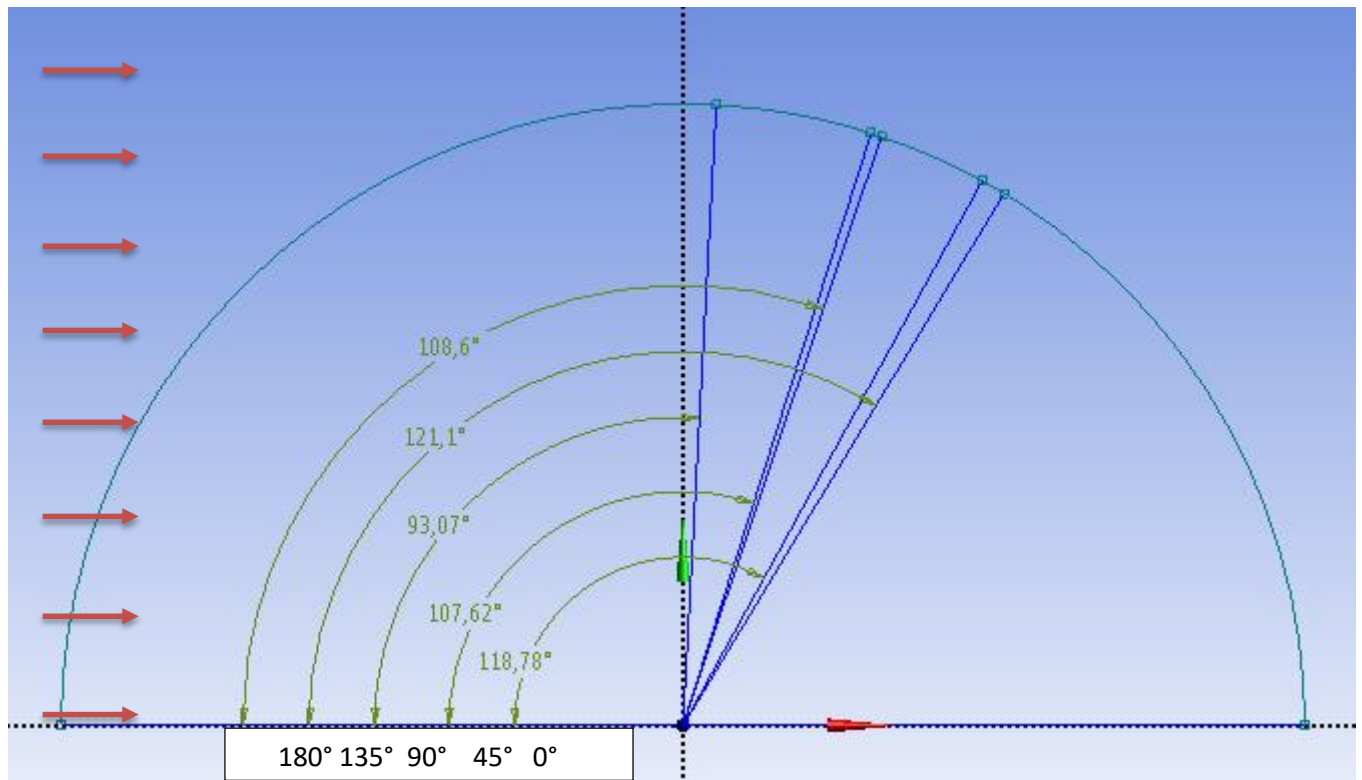
Figure 7. The angular position of separation points

The drag coefficient, C_D and pressure drop as a function of the semi-circular protrusion position on the cylinder is given in Fig. 8. The pressure drop and drag coefficient curve are obtained in parallel and in relation to each other. For the 0° position model, which divides the free flow region symmetrically into two parts, the lowest C_D value is obtained due to the lowest pressure drop. These pressure drop and drag coefficient values obtained at the 135° and 180° position models are very close to the 0° position, and highest at 90° models.
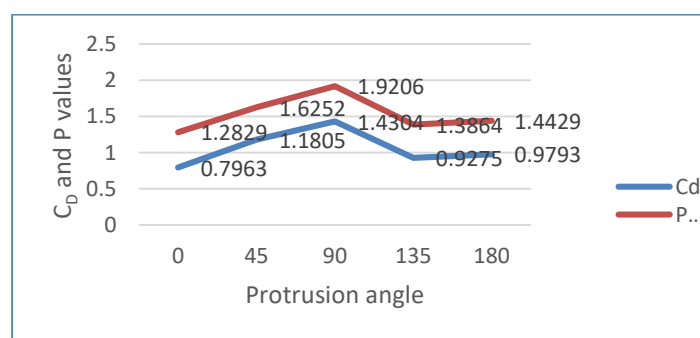

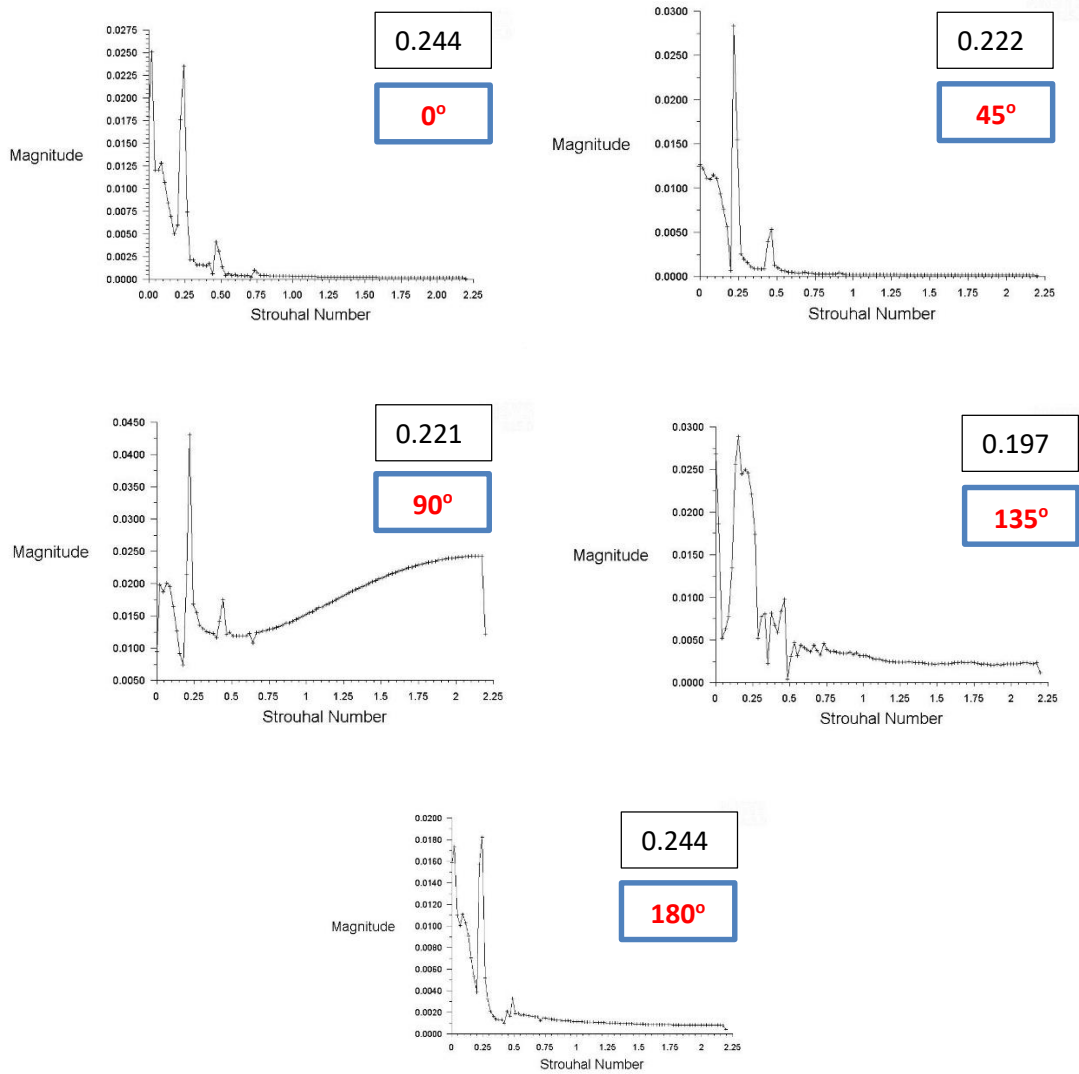**Figure 8.** C_D drag coefficient and P values versus semi-circular protrusions angles

Figure 9. Magnitude versus Strouhal (St) number in different positions

Strouhal number, St formed by the oscillation movements created by the flow is one of the dimensionless numbers depending on the frequency, cylinder diameter, and flow rate. Figure 9 shows the amplitude values connected to the St numbers at the specific point selected (x/D = 1, y/D=0.5) by using time-dependent CFD analysis. Accordingly, the lowest St number is seen in the 135° model. St numbers were obtained to be the same for models with 0° and 180° and to be close to 45° and 90° models. Minimum vortex frequency, f_s was occurred for 135° model, (1,02 Hz) calcuated with the Equation 6.

4. CONCLUSION

In this study, the effect of the half cylinder with a diameter of d = 4.4 mm (d / D = 0.1) on the cylinder (D = 44 mm) in the channel at different positions (0°, 45°, 90°, 135° and 180°) on the flow structure was investigated in 2D. The downstream flow characteristics have been investigated for $Re_D = 10^4$ based on free flow rate and the cylinder öiameter in the 15D x 30D channel, and then the streamlines and TKE contours are given. The effect of protrusion was investigated by finding vortex centers and C_D drag

coefficient. The amplitude of the vortices as depending on St numbers, and the location of the flow separation points from streamline graphics were obtained. According to the obtained value;

The downstream flow structure is influenced by all models, the vortex centers and the streamline points are changed.

- Models with 0° and 135° were found to be the closest flow structure.
- For all models, flow separation was shown clockwise at different angles on the X-axis. The early and latest flow separation points were seen in the model with 90° and 135° protrusion position, respectively.
- Drag coefficient and the pressure drop were found to be minimum at the models with 0° and 135° degrees and to be maximum at the models with 90°.
- The lowest value of the Strouhal number, which is an indicator of the downstream oscillation movement, was obtained to be 0,197 at the model with 135°.
- It was seen that the protrusion on the cylinder placed at different angles changes flow structure and controls the separation.
- In later studies, the different states of the flow control structures can be examined by changing both the size and the shape geometry of the roughness.

ACKNOWLEDGE

REFERENCES

[1] Celik S., Karakus C., Akilli H., Sahin B., Investigation of flow structure on finite-cylinder by particle imaging measurement technique (PIV), Installation Engineering, Issue 125 (2011) 33-51

[2] Canpolat C., Sahin B., Influence of single rectangular groove on the flow past a circular cylinder, International Journal of Heat and Fluid Flow 64 (2017) 79-88

[3] Gundemir O., Tastan K., Effects of longitudinal groove-roughness elements on the drag force exerted by the flow on a pipe, J. Fac. Eng. Arch. Gazi Univ. 23 (3) (2008) 637-644

[4] Oguz B., Akar M. A., Pınar E., Akilli H., Sahin B., Control of flow structure in the wake region of circular cylinder with meshy wire in deep water, Pamukkale University Journal of Engineering Sciences, 22(4) (2016) 280-284

[5] Akar M. A., Kucuk M., Control of the unsteady flow structure behind the cylinder with passive control method, Pamukkale University Journal of Engineering Sciences 20 (4) (2014) 123-128

[6] Ranjith E. R., Sunil A. S., Lippin P., Analysis of flow over a circular cylinder fitted with helical strakes, Procedia Technology 24 (2016) 452-460

[7] Yeo D. H., Jones N. P., Computational study on aerodynamic mitigation of wind-induced, large-amplitude vibrations of stay cables with strakes, Journal of Wind Engineering and Industrial Aerodynamics 99 (2011) 389-399

[8] Lam K., Lin Y. F., Zou L., Liu Y., Investigation of turbulent flow past a yawed wavy cylinder, Journal of Fluids and Structures 26 (2010) 1078-1097

Investigation of The Gamma Ray Shielding Behaviour of (90-x)TeO2—xMoO3—10ZnO Glass System Using Geant4 Simulation Code and WinXCOM Database

Ali AŞKIN[1]* iD, Murat DAL[2] iD

[1]*Munzur University, Faculty of Engineering, Mechatronic Engineering Department, Tunceli, TURKEY*

[2]*Munzur University, Faculty of Engineering, Civil Engineering Department, Tunceli, TURKEY*

Abstract. In this study, mass attenuation coefficients (μm), transmission fractions (T), mean free path (MFP) and half value layer (HVL) of the (90-x)TeO2—xMoO3—10ZnO glass system (x=10, 20 and 30 mol%) were calculated at the gamma ray photon energies of 356 keV, 662 keV, 1173 keV and 1330 keV. Shielding parameters of the glass system were calculated from the Monte Carlo simulations carried out with the Geant4 model of a high purity germanium (HPGe) detector and from the WinXCOM database software. The used Geant4 model was validated by comparing the experimentally determined mass attenuation values of the PbO—BaO—B2O3 glass system to the values calculated with Geant4. The findings of the present study reveals that the glass system containing 10% mol MoO3 exhibits better photon shielding performance compared to the glass with 30% mol of MoO3 due to the higher amount of TeO2 existed in its chemical formula.

*Keywords***:** Geant4, Sımulation, Glass, Photon attenuation.

(90-x)TeO2—xMoO3—10ZnO Cam Sisteminin Gama Işını Zırhlama Özelliklerinin Geant4 Simulasyon Kodu ve WinXCOM Veri Tabanı Kullanılarak Araştırılması

Özet. Bu çalışmada 90-x)TeO2—xMoO3—10ZnO cam sisteminin (x=10, 20 and 30 %mol) kütle zayıflatma katsayıları (μm), geçirgenlik oranları (T), ortalama serbest yol (MFP) ve yarı değer (HVL) parametreleri 356 keV, 662 keV, 1173 keV and 1330 keV gama foton enerjilerinde hesaplanmıştır. Zırhlama parametrelerini yüksek saflıkta germanium (HPGe) dedektörünün Geant4 modeli ile gerçekleştirilen Monte Carlo simulasyonları ve WinXCOM veri tabanı kullanılarak hesaplanmıştır. Geant4 modelinin geçerliliği PbO—BaO—B2O3 cam sistemi için deneysel olarak bulunan kütle zayıflatma katsayayıları Geant4 ile elde edilen sonuçlarla karşılaştırılarak sağlanmıştır. Bu çalışmanın sonuçları kimyasal formülünde yüksek oranda TeO2 bulunmasından dolayı %10 mol MoO3 içeren cam sisteminin radyayon zırhlama özelliklerinin %30 mol MoO3 cama göre daha iyi olduğunu göstermiştir.

*Anahtar Kelimeler***:** Geant4, Simülasyon, Cam, Foton zayıflatma..

1. INTRODUCTION

Investigation of the radiation shielding properties of materials is an increasing interest for researchers due to the wide use of radioactive isotopes in diverse fields, such as nuclear power plants, radiology and radiotherapy departments of hospitals, nuclear research and accelerator centers, agriculture, oil plants and archeology. Therefore, determination and knowledge of the radiation shielding properties of the materials used in these

---

* Corresponding author. *Email address:* *aliaskin@munzur.edu.tr*

kind of places are of crucial importance to protect humans against the hazardous effects of the ionizing radiation. Gamma rays are one of the more penetrating radiation type and materials with high density and high atomic number are needed for their effective shielding. Lead is known as the best gamma ray attenuating material. Whereas, weight, price and toxicity of lead make it unpractical and uneconomical for the shielding of large areas. Recently, radiation shielding properties of different natural or synthetically produced materials, such as concrete, sand, cement, bricks, tiles, glasses, clay materials, polymers and alloys has been studied by different researchers [1,8].

Having the advantages of optical transparency and easy preparation and production make the glasses attractive for the researchers to investigate and explore their shielding properties. Numerous studies reported that glasses are promising materials when used as gamma attenuator [9,11]. Because of this, synthesis of new glass systems have been made by several groups in order to improve their shielding potential. The gamma ray attenuation characteristics of the newly synthesized glasses have been determined either by using the experimental techniques or by using the Monte Carlo simulation codes.

Six glass pieces with composition of PbO-Li2O-B2O3 were prepared by using the melt quenching technique and the shielding properties of the samples were experimentally determined at four different gamma ray energies. The results of the study showed that the increase of PbO content increases the shielding efficiency [12]. The effect of La2O3 on the radiation attenuation characteristics of the lanthanum calcium silicoborate glasses is experimentally measured at eight different photon energies between 224 keV and 662 keV. It was reported that the increase of the La2O3 concentration results in an increase the shielding ability of the lanthanum calcium silicoborate glasses [13]. Five different samples of Bi2O3-BaO-B2O3-Na2O quaternary glass system were produced and their structural and gamma ray shielding features were investigated experimentally by Dogra et al. [14]. It was reported that the samples have higher mass attenuation and lower half value layer compared to barite concrete at 662 keV. In addition to the experimental techniques, Monte Carlo simulations can be employed to study the radiation interaction parameters of the materials especially in the absence of the expensive experimental equipments or in the absence of the fabricated samples. Modelling of an experimental set-up consisting of a detector, a gamma ray source and an attenuator and performing the measurements in the computer environment provide an ease of use and save time. Shielding properties of 80TeO2—5TiO2—(15-x)WO3—xAnOm glasses were investigated by using MCNP5 code and WinXCOM. The results of this study revealed that using of 5Er2O3 in the places of xAnOm significantly increases gamma ray and neutron shielding behavior [15]. Gamma and neutron shielding capabilities of 20BaO/SrO—(x)Bi2O3—(80-x)B2O3, where x value was changed between 10 and 60 mol, glasses has been investigated computationally by using the MCNP5 code and WinXCOM. It was published that the addition of Bi2O3 increases the shielding effectiveness of the glass system [16].

In this study, the complete geometry of a high purity germanium (HPGe) spectrometer produced by Canberra semiconductors was coded into Geant4 in order to determine the mass attenuation coefficients (μm), transmission fractions (T), half value layer (HVL) and mean free path (MFP) of the (90-x)TeO2—xMoO3—10ZnO glass system from the Monte Carlo simulations. In addition to the Monte Carlo simulations, μm values of the selected glass system have been also determined using the WinXCOM database and compared to the results from Geant4.

2. MATERIALS AND METHODS

2.1. Theoretical Background

Mass attenuation coefficient is a substantial parameter defining the penetration and diffusion of gamma ray photons within the material. Beer-Lambert's law as given by equation (1) was used to calculate the mass attenuation coefficients of the selected glass system.

$$I = I_0 \cdot e^{-\mu \cdot x} \tag{1}$$

Where I and I_0 are the transmitted and incident photon intensities respectively, x (cm) is the thickness of the material and μ (cm^{-1}) is the linear attenuation coefficient of the sample. In order to measure the incident photon intesity, Monte Carlo simulations were performed at each selected energy without the sample placed between the source and the detector. Simulations were then repeated with the sample placed between the source and the detector to obtain the attenuated photon intensities. The logarithm of transmission [ln(I/I$_0$)] is plotted versus sample thickness and the slope of linear fit to these data points results in linear attenuation coefficient. The mass attenuation coefficient (μm) is widely used for the calculation of photon transmission and energy deposition within a material. μm of any material is then calculated by dividing the linear attenuation coefficient with the density of sample:

$$\mu_m = \mu/\rho \tag{2}$$

The transmission fraction, T, is the fraction of the transmitted photon intensity (I) to the incident photon intensity (I$_0$). Plotting of T versus x can be used to estimate the decrease in the photon intensity with respect to the material thickness. This parameter is calculated as:

$$T = I/I_0 \tag{3}$$

The half-value layer (HVL) is the thickness of a material needed to reduce the intensity of the incident radiation by one-half. Its dependence to the linear attenuation coefficient, μ, is defined by the Eq. (4)

$$HVL = \ln(2)/\mu \tag{4}$$

The mean free path (MFP) defined as the average distance travelled by a photon between two successive interactions is equal to the reciprocal of the linear attenuation coefficient as given in next equation:

$$MFP = 1/\mu \tag{5}$$

2.2. Geant4 Model of HPGe Detector

Geant4 is a Monte Carlo simulation toolkit is based on the object oriented C++ programming and used for the modeling of the detectors for the high energy, nuclear, accelerator, medical and low

energy physics applications. The Geant4 kernel manages runs, events and tracking of passage of particle through matter. It allows users to simulate all aspects of an experimental set up such as geometry of detector, primary particle generation of events, types of particles and physics processes such as electromagnetic, hadronic and decay physics that manages particle interactions [17].

In this work, the simulated detector geometry is based on the HPGe detector produced by the Canberra semiconductors. The core of the detector consists of a 2.2 kg HPGe crystal installed as an ionization detector. The crystal is 82 mm in diameter and 81.5 mm in height. The core cavity of crystal is 10.5 mm in diameter and 62.5 mm in height. The detector has a 1 mm thick copper endcap window placed 6.3 mm from the top of germanium crystal. The thickness of the crystal dead layer is 0.8 mm. Fig. 1 shows the Geant4 model of the HPGe detector geometry.

As shown in Fig. 2, the detector and the gamma ray source were surrounded with lead shields. A cavity with 3 mm in diameter and 50 mm in height is defined at the center of the both shields to create a narrow beam in order both to ensure that the Beer-Lambert's law is valid and to minimize the variance and systematic errors. The chemical composition in mol% and weight fractions of elemental composition along with the densities of $(90-x)TeO_2—xMoO_3—10ZnO$ (shortly referred as TMZ) glass system has been coded into Geant4 according to the values as given in Table 1 [18]. During the simulations, the thickness of the glass sample was varied from 1 cm up to 5 cm with 1 cm increment and simulations were repeated for the new thickness. The glass sample was placed between the source and the detector as an attenuator and the mass attenuation values of the TMZ glass systems have been reported at the gamma ray energies of 356 keV ([133]Ba), 662 keV (^{137}Cs), 1173 keV (^{60}Co) and 1330 keV (^{60}Co).
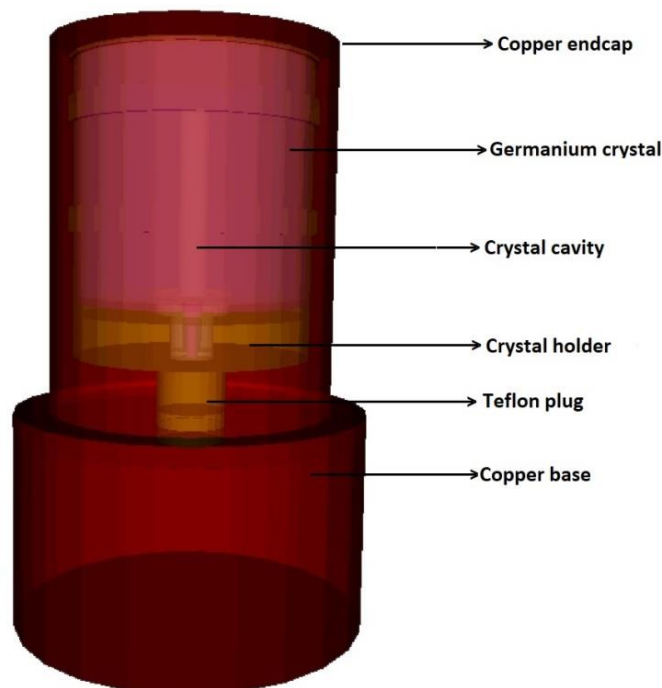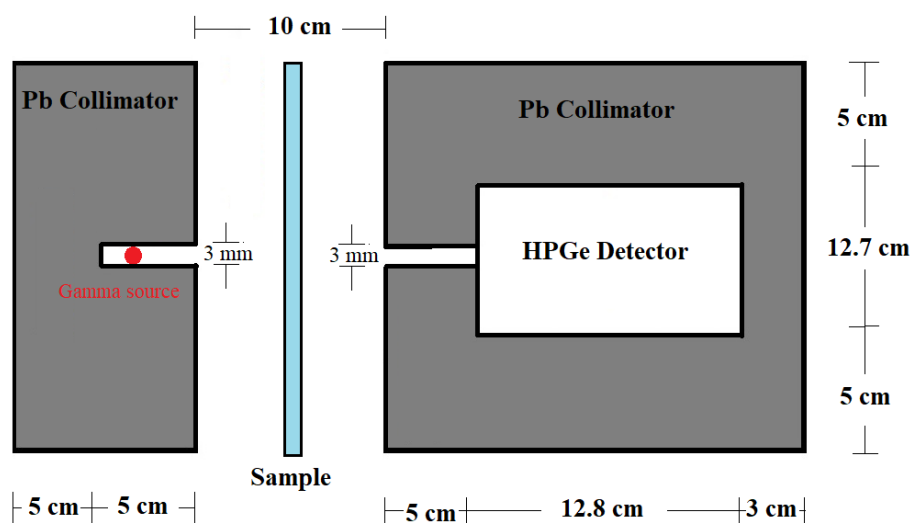

Figure 1. Geant4 model of the HPGe detector.

Figure 2. Schematic of the Geant4 set-up used to perform Monte Carlo simulations

Table 1. The chemical composition and density of $(90-x)TeO_2$—$xMoO_3$—$10ZnO$ glass system

Code	Glass sample in mol (%)	Mass fraction (%)				Density (gr/cm^3)
		Te	O	Mo	Zn	
TMZ**10**	$80TeO_2$—$10MoO_3$—$10ZnO$	67.9	21.3	6.45	4.35	5.103
TMZ**20**	$70TeO_2$—$20MoO_3$—$10ZnO$	60.0	22.6	13.0	4.4	5.066
TMZ**30**	$60TeO_2$—$30MoO_3$—$10ZnO$	52.0	24.0	19.56	4.44	4.976

2.3. WinXCOM Database Software

WinXCOM database can also be used to calculate μ_m values of any material and this software does not require any experimental setup [19]. Calculation of the μ_m values is based on the mixture rule given by the following equation.

$$(\mu_m)_{glass} = \sum_i^n w_i(\mu_m)_i \qquad (6)$$

Where w_i and $(\mu_m)_i$ are the weight fraction and mass attenuation coefficient of the ith element respectively.

3. RESULTS AND DISCUSSION

3.1. Validation of the Geant4 model

Prior starting the Monte Carlo simulations for the $(90-x)TeO_2$—$xMoO_3$—$10ZnO$ glass system, the validty of the Geant4 model of was proven by comparing the experimentally obtained mass attenuation values of $20MoO_3$-xBi_2O_3-$(80-x)B_2O_3$ glasses (x = 10, 20, 30, 40 mol%) [20] to the Geant4 based simulation results. The findings from the both studies are shown in Table 2. The relative difference of the experimental and Geant4 results vary between 0.7% - 12.4%. From the validation of the Geant4 model, we are confident about the reliability of the values determined as the shielding parameters of $(90-x)TeO_2$—$xMoO_3$—$10ZnO$ glasses and any other glass system which has not been investigated previously.

Table 2. Mass attenuation coefficients of MoO_3-Bi_2O_3-B_2O_3 (MoBiB) glasses calculated with Geant4 and comparison to experimental data [20] for the validation of the Geant4 model.

Glass sample	356 keV		662 keV		1173 keV		1330 keV	
	Geant4	**Exp.**	**Geant4**	**Exp.**	**Geant4**	**Exp.**	**Geant4**	**Exp.**
MoBiB10	0.2402 ± 0.0092	0.2136 ± 0.0128	0.1029 ± 0.0052	0.0977 ± 0.0048	0.0657 ± 0.0033	0.0594 ± 0.0071	0.0512 ± 0.0053	0.0549 ± 0.0028
MoBiB20	0.2269 ± 0.0098	0.2201 ± 0.00134	0.1055 ± 0.0046	0.0986 ± 0.0059	0.0607 ± 0.0050	0.0603 ± 0.0029	0.0518 ± 0.0050	0.0554 ± 0.0029
MoBiB30	0.2354 ± 0.012	0.2234 ± 0.0136	0.1078 ± 0.0050	0.0996 ± 0.050	0.0599 ± 0.0046	0.0605 ± 0.0029	0.0581 ± 0.0044	0.0555 ± 0.0029
MoBiB40	0.2434 ± 0.0080	0.2302 ± 0.0138	0.0973 ± 0.0046	0.1011 ± 0.051	0.0579 ± 0.0039	0.0610 ± 0.0030	0.0513 ± 0.0042	0.0556 ± 0.0029

3.2. Photon Shielding Behavior of TeO_2—MoO_3—ZnO Glass System

The Geant4 and WinXCOM results of μ_m values for the $(90-x)TeO_2$—$xMoO_3$—10ZnO glass ternary (x = 10, 20, 30 mol%) are given in Table 3. The relative differences (RD%) between the results from the both toolkits were calculated by using the following formula;

$$RD\,(\%) = \frac{R_G - R_W}{R_W} \times 100 \tag{7}$$

where R_G and R_W is the results from Geant4 and WinXCOM respectively.

As can be seen from the results presented in Table 3, the relative difference (RD) varies between 0.8% and 4.1% and the results from Geant4 and WinXCOM are in agreement. Furthermore, it is observed that μ_m decreases with the increasing photon energy. This trend in μ_m is expected since the high energy photons have more penetration and diffusion ability within materials. Furthermore, in order to estimate the mass attenuation values at the photon energies which were not simulated, a four parameter (p0, p1, p2, p3) exponential fit in the form of $\mu_m = p0 + p1 \cdot \exp(p2 + p3 \cdot E)$ has been applied to the mass attenuation data calculated for all TMZ glass samples to obtain an equation to reproduce the mass attenuation coefficients at any desired energy within the range between 356 and 1330 keV. As shown in Table 4, the mass attenuation values calculated from the best fitted equations at the photon energies of 427.9 keV ([125]Sb), ([134]Cs), 834,8 keV ([54]Mn), 1274.6 keV ([22]Na) are in agreement with the results calculated using Geant4. It can therefore be concluded that these equations are reliable to calculate the mass attenuation of TMZ glass samples at any desired energy between 356 and 1330 keV.

Table 3: Comparison of mass attenuation coefficients (cm^2/g) of the TeO_2—MoO_3—ZnO (TMZ) glass ternary obtained using Geant4 simulations and WinXCOM

Glass Sample	356 keV		RD	662 keV		RD	1173 keV		RD	1330 keV		RD
	Geant4	**XCOM**	**%**	**Geant4**	**XCOM**	**%**	**Geant4**	**XCOM**	**%**	**Geant4**	**XCOM**	**%**
TMZ10	0.120 ± 0.003	0.123	2.4	0.0763 ± 0.006	0.0750	1.7	0.0520 ± 0.005	0.0533	2.4	0.0487 ± 0.004	0.0497	2.0
TMZ20	0.123 ± 0.004	0.122	0.8	0.0744 ± 0.004	0.0750	0.8	0.0524 ± 0.006	0.0535	2.0	0.0491 ± 0.005	0.0500	1.8
TMZ30	0.125 ± 0.003	0.120	4.1	0.0740 ± 0.004	0.0749	1.2	0.0527 ± 0.005	0.0537	1.8	0.0497 ± 0.005	0.0502	1.0

Table 4. Best fitted equations for estimation of mass attenuation and comparison to Geant4 results.

Glass Sample	Best Fitted Equation	Energy (keV)	Mass Attenuation Coefficient (cm²/g)		Percentage Difference
			Fitted Equation	Geant4	
TMZ10	$\mu_m = 0.0437 + 0.0939 \cdot \exp(0.777 - 0.00276 \cdot E)$	427.9 (^{125}SB)	0.106	0.110	3.6
TMZ20	$\mu_m = 0.0460 + 0.214 \cdot \exp(0.125 - 0.00324 \cdot E)$	834.8 (^{54}Mn)	0.0622	0.0628	0.9
TMZ30	$\mu_m = 0.0475 + 0.235 \cdot \exp(0.144 - 0.00353 \cdot E)$	1274.6 (^{22}Na)	0.0505	0.0499	1.2

Fig. 3 shows the plot of the transmission values of TMZ glasses with respect to the glass thickness at the photon energies of 356 keV, 662 keV, 1173 keV and 1330 keV. Again, due to the penetration abilities of the high energy photons, a big difference is observed between 356 keV and 1330 keV. Transmission increases with the increase of photon energy. At the photon energies of 356 and 1330 keV the transmission values of 5 cm thick TMZ10 glass are 0.0433 and 0.281 respectively. Fig. 3 also shows that, among the simulated glasses, the lowest transmissions for all photon energies occur for the TMZ10 sample and highest transmissions occur for the TMZ30 sample. This behaviour is due to the higher fraction of TeO2 existed in TMZ10 glass and the atomic number of Te (Z = 52) is higher than the atomic number of Mo (Z = 42). Since the decrease in the Te content in TMZ30 is compensated by the increase in Mo atoms, the transmission values for all glasses are close to each other at the selected energies. Furthermore, for the photon energies starting from 1100 keV, pair production is the dominating photon interaction mechanism and above this energy interaction mechanism becomes almost independent of chemical structure.
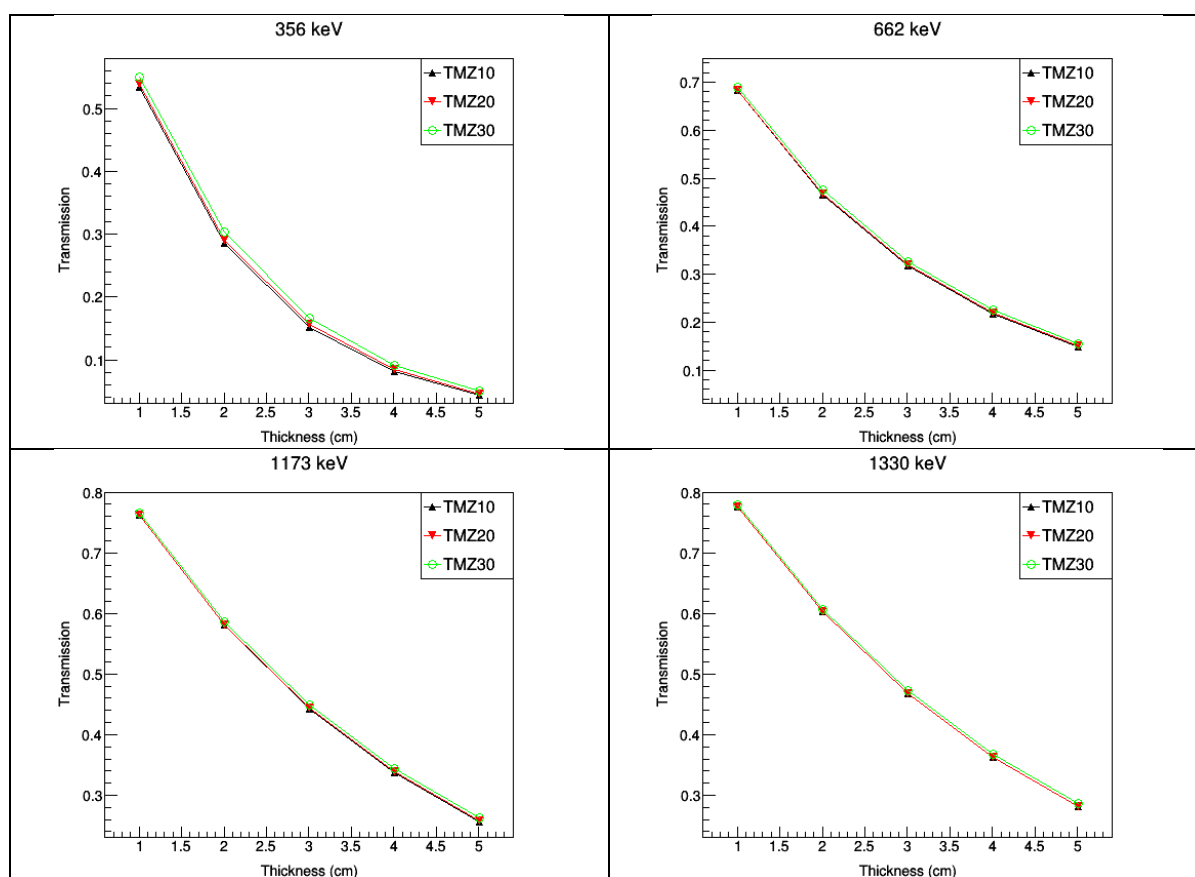
Figure 3. Transmission factor versus the thickness of TeO₂—MoO₃—ZnO (TMZ) glass system at 356, 662, 1173 and 1330 keV photon energies.

The two important parameters characterizing the shielding ability of the TMZ glass system are the mean free path (MFP) and the half value layer (HVL) of the glass system. It is important to mention here that the lesser the value of MFP and HVL of given material, the better the shielding properties it would possess and thanks to the lower value of MFP and HVL, better shielding performance can be obtained by using a thinner layer of the selected material. Fig. 5 and Fig. 6 show the plot of MFP and HVL values of the TeO_2—MoO_3—ZnO glass system versus the photon energies. As can be seen from these two plots, TMZ10 has the lowest and TMZ30 has the highest values of MFP and HVL at the given photon energies. Depending on the close atomic numbers of Te and Mo elements, the observed differences for the MFP and HVL values are around 5.3% at 356 keV and 1.6% at 1330 keV for the 10% and 30% MoO_3 concentrations respectively.
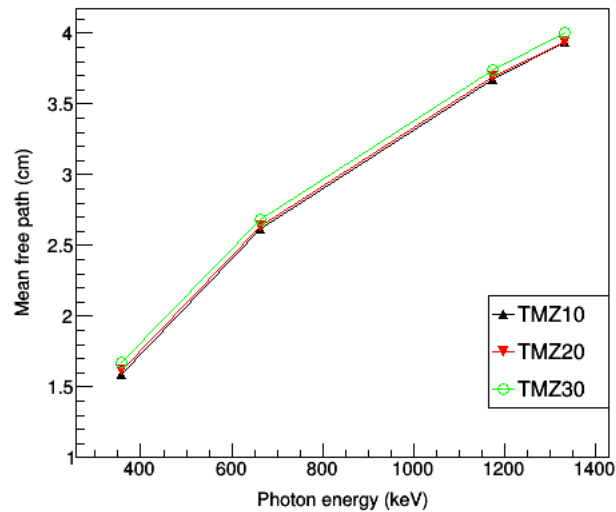

Figure 4. Mean free path of the TeO_2—MoO_3—ZnO glass system as a function of photon energy.

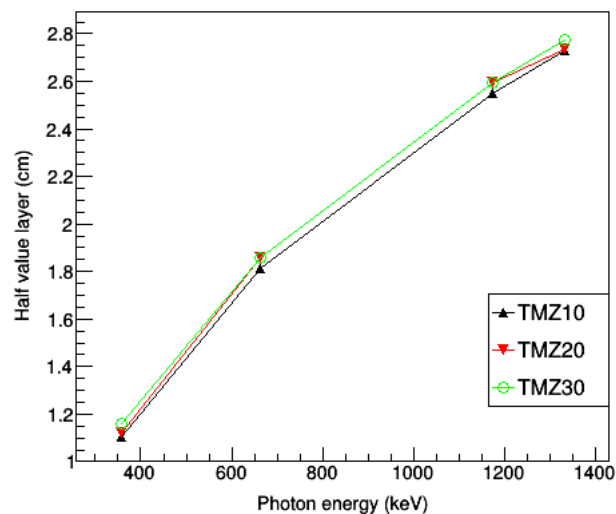**Figure 5.** Half value layer of the TeO_2—MoO_3—ZnO glass system as a function of photon energy.

In order to see the dependence of the mass attenuation coefficient and half value layer on the fraction of MoO_3 existed in the selected glasses, these parameters were plotted versus the 10%, 20% and 30% mol of MoO_3 and the dependencies were shown in Fig. 6 and Fig. 7 respectively. For 10% and 30% mol of MoO_3, the mass attenuation values change from 0.120 to 0.125 at 356 keV and from 0.0487 to 0.0497 at 1330 keV respectively. In the same way, the half value layers change from 1.104 to 1.162 at 356 keV and from 2.732 to 2.775 at 1330 keV. These findings also support that the decrease occurred for Te atoms are partially compensated by the increase in the Mo atoms in the glass structure. Therefore, mass attenuation values for the minimum and maximum MoO_3 concentrations do not show a significant change.
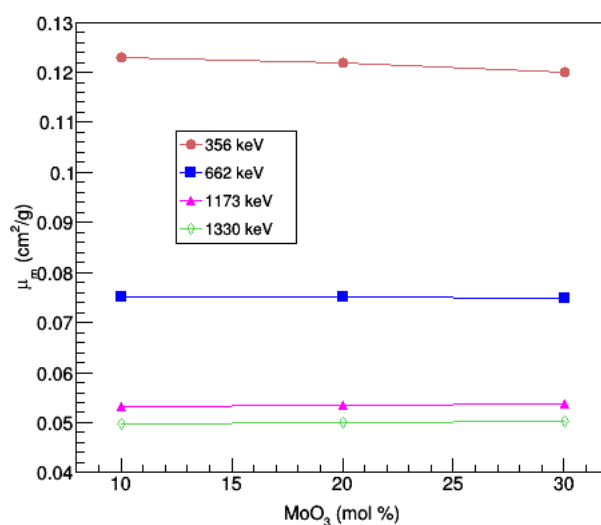

Figure 6. Dependence of mass attenuation values on the MoO_3 amount in the glasses
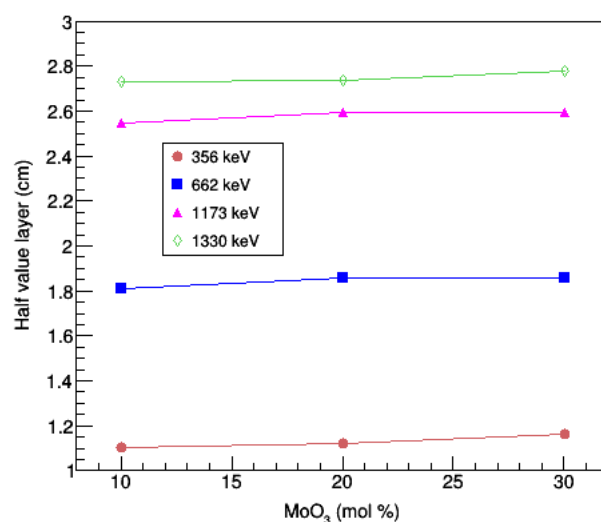

Figure 7. Dependence of half value layer on the MoO_3 amount in the glasses

4. CONCLUSION

In this study the photon shielding parameters of $(90-x)TeO_2$—$xMoO_3$—$10ZnO$ glass ternary (x = 10, 20, 30 mol%) was investigated computationally using Geant4 and WinXCOM database software to exploit the shielding potential of the selected glass system. Monte Carlo outputs of the Geant4 have been analyzed and the following conclusions were arrived;

- Geant4 model of HPGe detector can be a reliable alternative to the experimental techniques especially in the absence of equipments or material samples to determine the shielding capability of any other materials.
- Mass attenuation coefficients determined using Geant4 and WinXCOM agrees well. Mass attenuation values are high at lower energy region and they decrease as the photon energy increases and stay almost unchanged at the energy region above 1100 keV. This trend observed in mass attenuation coefficients can be explained by the photon interaction mechanisms at low, medium and high energy regions in terms of photoelectric effect, Compton scattering or pair production respectively.
- Thanks to the function obtained from the best fit applied to the simulated data, mass attenuation values at any desired energy can be calculated.
- Increase of the MoO_3 fraction from 10% to 30% in the glass structure causes an increase in the transmission fraction, half value layer and mean free path of the selected glass system and therefore weakens the shielding ability.

REFERENCES

[1] Gokce H.S., Ozturk B.C., Cam N.F., Cakir O.A., Gamma-ray attenuation coefficients and transmission thickness of high consistency heavyweight concrete containing mineral admixture, Cem & Concr. Comp. 92 (2018) 56-69.

[2] Akkas A., Tugrul A.B., Addemir A.O., Marsoglu M., Radiation shielding effect of boron carbide aluminum metal matrix composite, Acta Physica Polonica A. 127 (2015) 947-949.

[3] Kurudirek M., Heavy metal borate glasses: potential use for radiation shielding, J. Alloy. Compd. 727 (2017) 1227–1236.

[4] Sharaf J.M., Hamideen M.S., Photon attenuation coefficients and shielding effects of jordanian building materials, Ann. Nucl. Energy. 62 (2013) 50-56.

[5] Olukotun S.F., Gbenu S.T., Ibitye F.I., Oladejo O.F., Shittu H.O., Fasasi M.K., Balogun F.A., Investigation of gamma radiation shielding capability of two clay materials. Nucl. Eng. Technol. 50 (2018) 957-962.

[6] Singh V.P., Shirmardi S.P., Medhat M.E., Badiger N.M., Determination of mass attenuation coefficient for some polymers using monte carlo simulation, Vacuum. 119 (2015) 284-288.

[7] Singh V.P., Medhat M.E., Shirmardi S.P., Comparative studies on shielding properties of some steel alloys using geant4, mcnp, WinXCOM and experimental results, Rad. Phys. Chem. 106 (2015) 255-260.

[8] J. Singh, H. Singh, J. Sharma, T. Singh, P.S. Singh, Fusible alloys: a potential candidate for gamma rays shield design, Prog. Nucl. Energy. 106 (2018) 387-395.

[9] Kumar, A., Kaur, R., Sayyed, M.I., Rashad, M., Singh, M., Ali, A.M., 2019. Physical, structural, optical and gamma ray shielding behavior of $(20+x)PbO-10BaO-10-Na_2O-10MgO-(50-x)B_2O_3$ glasses, Physica B Condens. Matter. 552 (2019) 110-118.

[10] Bagheria R., Moghaddam A.K., Shirmardi B. Azadbakht S.P., Saleh M., Determination of gamma-ray shielding properties for silicate glasses containing Bi_2O_3, PbO, and BaO, J. Non-Cryst. Solids. 479 (2018) 62-71.

[11] Tijani S.A., Kamal S.M., Al-Hadeethi Y., Arib M., Hussein M.A., Wageh S., Dim L.A., Radiation shielding properties of transparent erbium zinc tellurite glass system determined

at medical diagnostic energies, J. Alloy. Compd. 741 (2018) 293-299.

[12] Kumar A., Gamma ray shielding properties of PbO-Li$_2$O-B$_2$O$_3$ glasses, Radiat. Phys. Chem. 136 (2107) 50-53.

[13] Kaewjaeng S., Kothan S., Chanthima N., Kim H., Kaewkhao J., Gamma radiation shielding materials of lanthanum calcium silicoborate glasses, Materials Today: Proceedings. 5 (2018) 14901-14906.

[14] Dogra M., Sinh K.J., Kaur K., Anand V., Kaur P., Singh P., Bajwa B.S., Investigation of gamma ray shielding, structural and dissolution rate properties of Bi2O3-BaO-B2O3-Na2O glass system, Radiat. Phys. Chem. 144 (2018) 171-179.

[15] Dong M.G., El-Mallawany R., Sayyed M.I., Tekin H.O., Shielding properties of 80TeO2-5TiO2-(15-x)WO3-xAnOm glasses using WinXCOM and mcnp5 code. Radiat. Phys. Chem. 141 (2017) 172-178.

[16] Sayyed M.I., Lakshminarayana G., Dong M.G., Ersundu M.C., Ersundu A.E., I.V. Kityk, Investigation on gamma and neutron radiation shielding parameters for Bao/Sro-Bi2O3-B2O3 glasses. Radiat. Phys. Chem. 145 (2018) 26-33.

[17] Agostinelli S., Allison J., Amako K., Apostolakis J., Araujo H., et al., 2003. Geant4-a simulation toolkit, Nucl. Instr. Meth. Phys. A 506 (2003) 250-303.

[18] Liu J.L., Wang W.C., Xiao Y.B., Huang S.J., Mao L.Y., Zhang Q.Y., Nd^{3+}-doped TeO$_2$–MoO$_3$–ZnO tellurite glass for a diode-pump 1.06 μm laser, J. Non-Cryst. Solids. 506 (2019) 32-38.

[19] Gerward L., Guilbert N., Jensen K.B., Lerying H., WinXCom - A program for calculating X-ray attenuation coefficients, Radiat. Phys. Chem. 71 (2004) 653-654.

[20] Sayyed M. I., Kaky K. M., Gaikwad D. K., Agar O., Gawai U. P., Baki S. O., Physical, structural, optical and gamma radiation shielding properties of borate glasses containing heavy metals (Bi2O3/MoO3), J. Non-Crystalline Solids, 507, 30-37 (2019)

Local Spin Induced Magnetism In The Monolayer Nanographene

Yasin Göktürk YILDIZ [iD]

Department of Electronics and Automation, Kırıkkale University, 71100, Kırıkkale, Turkey.

Abstract. In this paper, we investigated local spin orientation (up or down) effects on magnetizations of the monolayer nanographene by using effective field theory developed by Kaneyoshi. It is found that the monolayer nanographene and its components have very small magnetization ($mC_1 \approx mC_2 \approx mC_3 \approx mMLNG \approx 2.31 \times 10^{-18} \approx 0$) at $T \approx 0.00$ for the $Jd_1 < 0$ (C_1-spin up, C_2-spin down and C_3-spin up). On the other hand, for $Jd_2 < 0$, $Jd_3 < 0$, $Jd_4 < 0$, and $Jd_5 < 0$, the monolayer nanographene and its components (C_1, C_2 and C_3 atoms) have very large local spin induced magnetization ($mC_1 \approx mC_2 \approx mC_3 \approx mMLNG \approx 1; 1 >> 2.31 \times 10^{-18}$) than those of the $Jd_1 < 0$. These results clearly indicate that the local spin orientation in the monolayer nanographene has very strong effect on its magnetism.

***Keywords*:** Nanographene, Monolayer nanographene, Spin, Spin orientation, Magnetism, Effective field theory.

Tek Tabakalı Nanografende Lokal Spin Etkili Manyetizma

Özet. Bu çalışmada, Kaneyoshi tarafından geliştirilen etkin alan teorisi kullanılarak, tek tabakalı nanografenin mıknatıslanmalarına lokal spin yönelimlerinin (yukarı ya da aşağı) etkileri incelendi. Tek tabakalı nanografenin ve bileşenlerinin $Jd_1 < 0$ (C_1-spin yukarı, C_2-spin aşağı ve C_3-spin yukarı) için $T \approx 0.00$'da çok küçük mıknatıslanmaya ($mC_1 \approx mC_2 \approx mC_3 \approx mMLNG \approx 2.31 \times 10^{-18} \approx 0$) sahip olduğu bulundu. Diğer taraftan, $Jd_2 < 0$, $Jd_3 < 0$, $Jd_4 < 0$ ve $Jd_5 < 0$ için, tek tabakalı nanografen ve bileşenleri (C_1, C_2 ve C_3 atomları), $Jd_1 < 0$'dakinden çok büyük lokal spin etkili mıknatıslanmaya ($mC_1 \approx mC_2 \approx mC_3 \approx mMLNG \approx 1; 1 >> 2.31 \times 10^{-18}$) sahiptirler. Bu sonuçlar açıkça, lokal spin yönelimlerinin, tek tabakalı nanografenin manyetizması üzerinde çok güçlü bir etkiye sahip olduğunu göstermektedir.

***Anahtar Kelimeler*:** Nanografen, Tek tabakalınanografen, Spin, Spin yönelimi, Manyetizma, Etkinalanteorisi.

1. INTRODUCTION

Monolayer graphene discovered in 2004 by Novoselov et al.[1]. It is a new material that consists of Carbon atoms with honeycomb (hexagonal) lattice in one atom thickness. Because of its unique properties such as it consists of one layer, being strongest than steel, having high thermal and electrical conductivity, it is a promising material that can be used in areas such as; transistors, battery charges, energy storing devices, magnetic drug delivery systems, artificial magnetic systems, flat screens, coating material in automobiles and planes. Therefore, mono, two and multilayer graphene systems had come in to center of

interest. Although it has a short history as 15 years, many works have been done on graphene and graphene based systems by using different experimental [2-22] and theoretical methods [23-29].

On the other hand, effective field theory developed by Kaneyoshi, which successfully identifies many magnetic nanosystems such as nanoparticles, thin films, nanowires and nanotubs [30-47] and enables the magnetic properties of these nanosystems to be successfully obtained, modeling nanosystems, it has emerged as a successful theoretical method which is used for defining and examining magnetic systems and applied continuously to different nanosystems. For example, using the effective field theory, the magnetic properties of the cubic nanowire [48], the hexagonal Ising nanowire [49], the mixed Ising nanoparticles [50], the spin-1 Ising nanotube [51], cylindrical transverse spin-1 Ising nanowire [52], cubic nanowire [53], a kinetic cylindrical Ising nanotube [54], honeycomb thin film [55], diluted transverse Ising nanowire [56], core/shell nanowire system [57], a mixed core/shell nanotube [58], core/shell spin-1 Ising nanowire [59] and cylindrical Ising nanowires [60-63] were investigated in detailed in literature.

Although the magnetic properties of many nanosystems were investigated using effective field theory, a small number of studies were reported on the magnetic properties of nanographene systems were investigated by using effective field theory in the literature [64-71]. However, local spin orientation effects on the magnetizations of the monolayer nanographene (MLNG) have not been studied yet for $\Theta CTA=1300$. Therefore, in this paper, we investigate the local spin orientation (up or down) effects on magnetizations of the MLNG by using effective field theory developed by Kaneyoshi in detailed.

This paper is organized as follows. Section 2 describes the theoretical methods. Section 3 introduces the theoretical results and discussion. Section 4 is reserved for the conclusions.

2. THEORETICAL METHOD

The aim of this paper to investigate the local spin orientation (up or down) effects on magnetizations of the monolayer nanographene (MLNG) by using effective field theory developed by Kaneyoshi [72]. To obtain the the local spin orientation (LSO), we the exchange interactions between C1, C2 and C3 atoms of the MLNG. Namely, when $J_{d1}<0$, the spin direction of the C1 and C2, C2 and C3 is opposite, when $J_{d2}<0$ and $J_{d3}<0$, the spin direction of the C1 and C3 is opposite, when $J_{d4}<0$, the spin direction of the C1 and C2 is opposite, and when $J_{d5}<0$, the spin direction of the C2 and C2 is opposite. However, when all J>0 [73], all of the the spin of the MLNG are up (see Fig.2(f)).
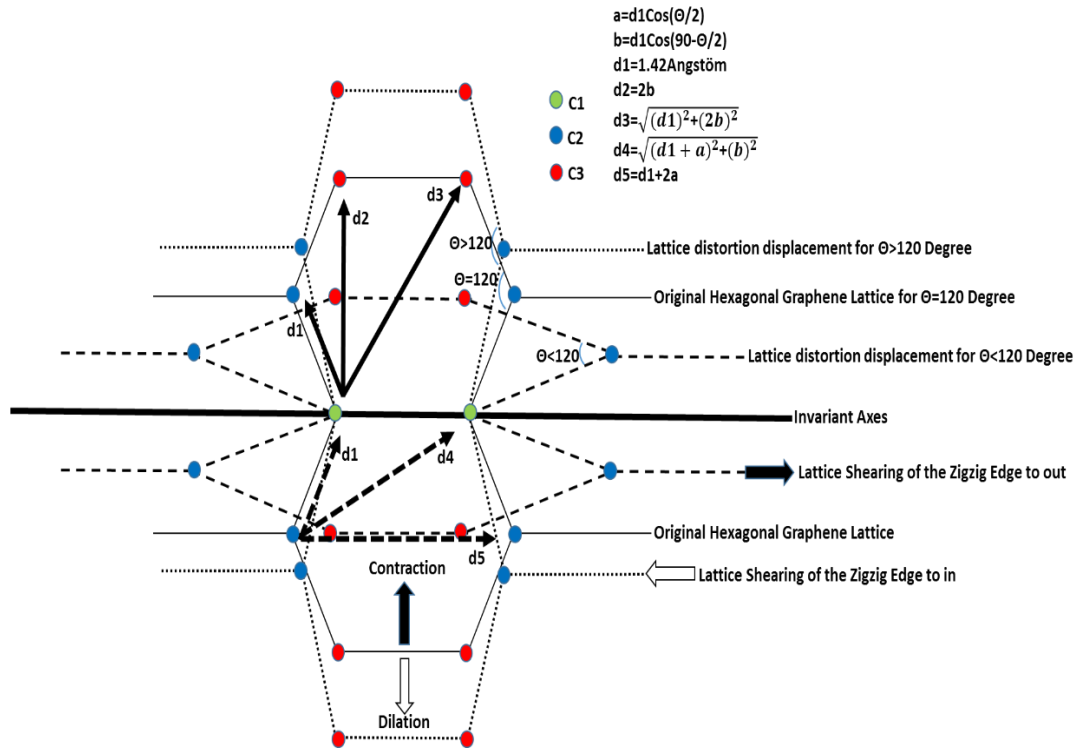
Figure 1. (Color online) Schematic representation the MLNG [73].

In our previous work [73], we investigated the effects of the twinning angle on the magnetizations of the MLNG. Since the MLNG system is same, we shall follow the same model and the same equations of the effective field theory of the MLNG given in our previous work [73] in detailed. Therefore, the Hamiltonian and the magnetizations of the MLNG and its components C1, C2 and C3 are given by [73],

Hamiltonian;

$$H = -J_{d1}\sum_{\langle C1,C1\rangle} S_{C1}^z S_{C1}^z - J_{d1}\sum_{\langle C1,C2\rangle} S_{C1}^z S_{C2}^z - J_{d1}\sum_{\langle C2,C3\rangle} S_{C2}^z S_{C3}^z - J_{d1}\sum_{\langle C3,C3\rangle} S_{C3}^z S_{C3}^z$$
$$-J_{d2}\sum_{\langle C1,C3\rangle} S_{C1}^z S_{C3}^z - J_{d2}\sum_{\langle C2,C2\rangle} S_{C2}^z S_{C2}^z - J_{d3}\sum_{\langle C1,C3\rangle} S_{C1}^z S_{C3}^z - J_{d4}\sum_{\langle C1,C2\rangle} S_{C1}^z S_{C2}^z$$
$$-J_{d5}\sum_{\langle C2,C2\rangle} S_{C2}^z S_{C2}^z - h(\sum_{C1} S_{C1}^z + \sum_{C2} S_{C2}^z + \sum_{C3} S_{C3}^z) \tag{1}$$

Magnetizations;

$$m_{C1} = [\cosh(J_{d1}\nabla)+m_{C1}\sinh(J_{d1}\nabla)]^1[\cosh(J_{d1}\nabla)+m_{C2}\sinh(J_{d1}\nabla)]^2[\cosh(J_{d4}\nabla)+m_{C2}\sinh(J_{d4}\nabla)]^2$$
$$[\cosh(J_{d2}\nabla)+m_{C3}\sinh(J_{d2}\nabla)]^2[\cosh(J_{d3}\nabla)+m_{C3}\sinh(J_{d3}\nabla)]^2 F_{s-1/2}(x)\big|_{x=0},$$

$$m_{C2} = [\cosh(J_{d1}\nabla)+m_{C1}\sinh(J_{d1}\nabla)]^1[\cosh(J_{d4}\nabla)+m_{C1}\sinh(J_{d4}\nabla)]^1[\cosh(J_{d2}\nabla)+m_{C2}\sinh(J_{d2}\nabla)]^1$$
$$[\cosh(J_{d5}\nabla)+m_{C2}\sinh(J_{d5}\nabla)]^1[\cosh(J_{d1}\nabla)+m_{C3}\sinh(J_{d1}\nabla)]^1$$
$$[\cosh(J_{d4}\nabla)+m_{C3}\sinh(J_{d4}\nabla)]^1 F_{s-1/2}(x)\big|_{x=0},$$

$$m_{C3} = [\cosh(J_{d2}\nabla)+m_{C1}\sinh(J_{d2}\nabla)]^1[\cosh(J_{d3}\nabla)+m_{C1}\sinh(J_{d3}\nabla)]^1[\cosh(J_{d1}\nabla)+m_{C2}\sinh(J_{d1}\nabla)]^1$$
$$[\cosh(J_{d4}\nabla)+m_{C2}\sinh(J_{d4}\nabla)]^1[\cosh(J_{d1}\nabla)+m_{C3}\sinh(J_{d1}\nabla)]^1 F_{s-1/2}(x)\big|_{x=0}, \tag{2}$$

In the Hamiltonian, J_i (i = d1, d2, d3, d4 and d5) is the exchange interaction between two nearest and next neighbor Carbon atoms. The values of the J_i are obtained by using the relationship $J_i = k_i/nd_i$; where, k_i (i = 1, 2, 3, 4 and 5) is a constant that defines the type of magnetization and nd_i (i = 1, 2, 3, 4 and 5) is the normalized lattice distance such as, $nd_1 = d_1/1Å = 1.42Å/1Å = 1.42$. $S^z = \pm 1$ is the Pauli spin operator. h is the external magnetic field. In the magnetizations, $\nabla = \partial/\partial x$ is the differential operator and the function of $F_{S-1/2}(x)$ is defined by as follows for the spin-1/2 Ising particles [73].

$$F_{s-1/2}(x) = \tanh[\beta(x+H)] \tag{3}$$

where $\beta = 1/k_B T_A$, k_B is the Boltzmann's constant, T_A is the absolute temperature. We used the reduced temperature, $T = k_B T_A/J$, and the reduced applied field, i.e. $H = h/J$ in all calculations. The total magnetization of the MLNG is given by [73],

$$MT_{MLNG} = \frac{1}{10}[2\ m_{C1} + 4\ m_{C2} + 4\ m_{C3}]. \tag{4}$$

3. THEORETICAL RESULTS

We obtained the temperature and local spin orientation dependence of the magnetization of the monolayer nanographene (MLNG) for the critical twinning angle ($\Theta_{CTA}=130^0$) of zigzag edge in Figs.2(a)-(f). In Fig.2(a), magnetizations of the MLNG (MTMLNG) and its component (mC1, mC2 and mC3) are obtained for Jd1<0 (in other word, C1-spin up, C2-spin down and C3-spin up). As we clearly see that antiferromagnetic orientations of the spin of the nearest neighbor atoms (Jd1<0) cause almostly zero magnetization (mC1≈mC2≈mC3≈mMLNG≈2.31×10^{-18}≈0) at T≈0.00 (this means that TC≈0.00). On the other hand, antiferromagnetic orientations of the spin of the next-nearest (Jd2<0 and Jd4<0) and third-nearest (Jd3<0 and Jd5<0) neighbor atoms cause a very highest magnetization behaviors than those of the nearest neighbor atoms (Jd1<0) (mC1≈mC2≈mC3≈mMLNG≈1>>mC1≈mC2≈mC3≈mMLNG≈2.31×10^{-18}≈0) at T≈0.00 in Figs.2(b), (c), (d), (e) and for all J>0 in Fig.2(f) for which the local spin induced Curie temperature are obtained as TC=1.57, 2.15, 1.04, 2.47 and 2.738 (after Ref. [73]), respectively. By using these results, we suggest that it is possible to obtain magnetism with the changing of the local spin direction of the MLNG and other magnetic systems. We call such magnetism as local spin induced magnetism (LSIM) and local spin induced Curie temperature (LSIT$_C$).
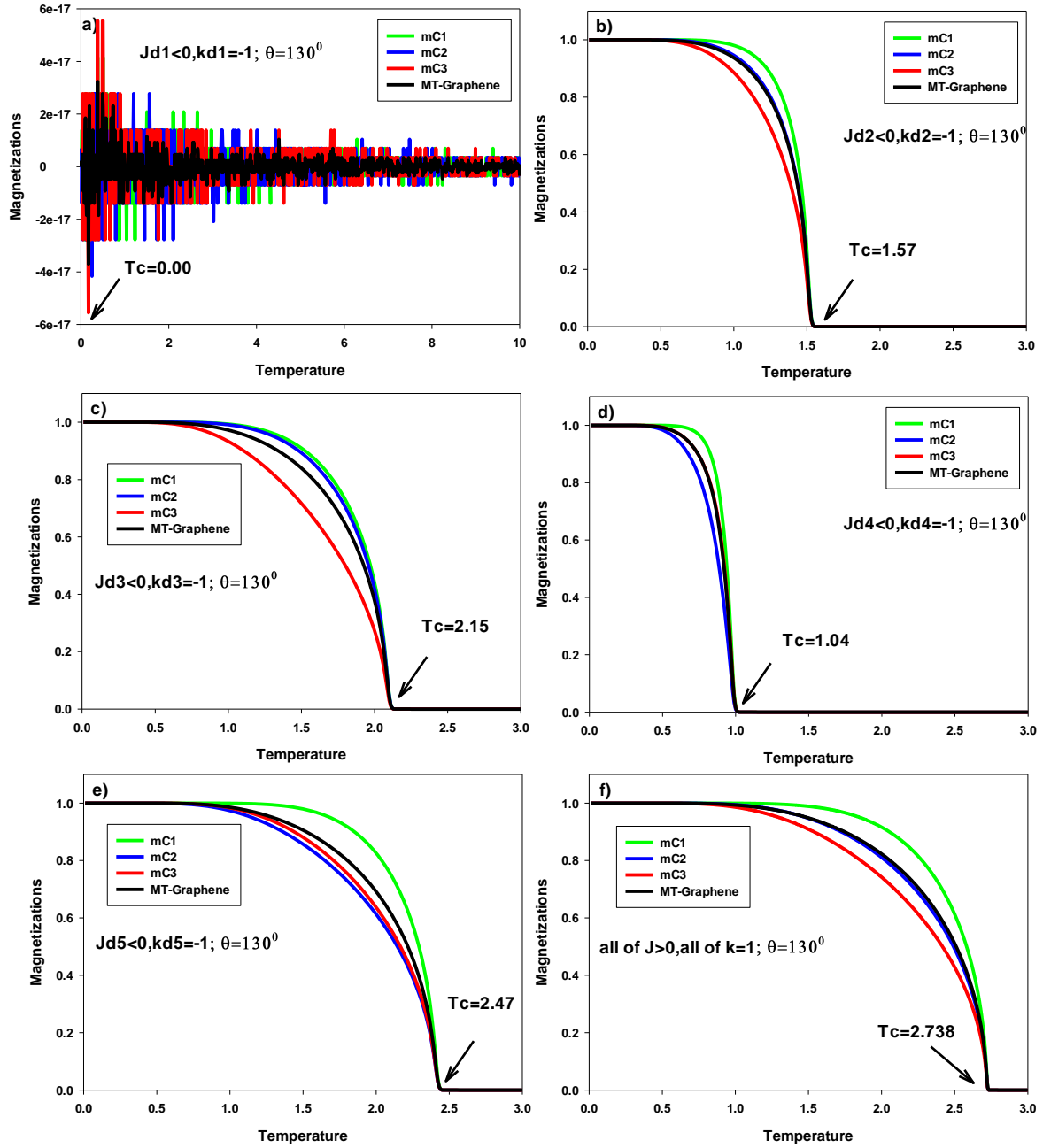
Figure 2. (Color online) Local spin induced magnetism (LSIM) and local spin induced Curie temperature (LSIT$_C$) in the MLNG.

4. CONCLUSIONS

Local spin orientation (up or down) effects on magnetizations of the monolayer nanographene (MLNG) by using effective field theory developed by Kaneyoshi. It is found that;

1. MLNG and its components have a very small magnetism $m_{C1} \approx m_{C2} \approx m_{C3} \approx m_{MLNG} \approx 2.31 \times 10^{-18} \approx 0$ at $T \approx 0.00$ for Jd1<0.

2. MLNG and its components have very large magnetism $m_{C1} \approx m_{C2} \approx m_{C3} \approx m_{MLNG} \approx 1$ at $T \approx 0.00$ for $J_{d2} < 0$, $J_{d3} < 0$, $J_{d4} < 0$, $J_{d5} < 0$ and all J>0.

3. Curie temperature of the MLNG and its components is differ for each $J_{d1}<0$, $J_{d2}<0$, $J_{d3}<0$, $J_{d4}<0$, $J_{d5}<0$ and all $J>0$.

4. We call such magnetism as local spin induced magnetism (LSIM) and local spin induced Curie temperature ($LSIT_C$)

5. We hope that our results open a door to understanding of the magnetism in MLNG and other magnetic systems.

Acknowledgments

REFERENCES

[1] Novoselov K. S., Geim A. K., Morozov S. V., Jiang D., Zhang Y., Dubonos S. V., Grigorieva I. V., Firsov A. A., Electric Field Effect in Atomically Thin Carbon Films, Science, 306 (2004) 666-669.

[2] Wallace P. R., The Band Theory of Graphite, Phys. Rev., 71 (1947) 622-634.

[3] Geim A. and Novoselov K., The rise of graphene, Nature Mater., 6 (2007) 183-191.

[4] Kedzierski J., Hsu P. L., Healey P., Wyatt P. W., Keast C. L., Sprinkle M., Berger C., de Heer W. A., Epitaxial Graphene Transistors on SiC Substrates. Electron Devices, IEEE Trans., 55 (2008) 2078-2085.

[5] Wu Y. Q., Ye P. D., Capano M. A., Xuan Y., Sui Y., Qi M., Cooper J. A., Shen T., Pandey D., Prakash G., Reifenberger R., Top-gated graphene field-effect-transistors formed by decomposition of SiC, Appl. Phys. Lett., 92 (2008) 092102.

[6] Lin Y. M., Garcia A. V., Han S. J., Farmer D. B., Meric I., Sun Y., Wu Y., Dimitrakopoulos C., Grill A., Avouris P., Jenkins K. A., Wafer-Scale Graphene Integrated Circuit, Science, 332 (2011) 1294-1297.

[7] Guo Z., Dong R., Chakraborty P. S., Lourenco N., Palmer J., Hu Y., Ruan M., Hankinson J., Kunc J., Cressler J. D., Berger C., de Heer W.A., Record Maximum Oscillation Frequency in C-Face Epitaxial Graphene Transistors, Nano Lett., 13 (2013) 942-947.

[8] Fiori G. and Iannaccone G., Multiscale Modeling for Graphene-Based Nanoscale Transistors, Proceedings of the IEEE, 101 (2013) 1653-1669.

[9] Schwierz F., Graphene transistors, Nature Nano., 5 (2010) 487-496.

[10] Novoselov K. S., Geim A. K., Morozov S. V., Jiang D., Katsnelson M. I., Grigorieva I. V., Dubonos S. V., Firsov A. A., Two-dimensional gas of massless LXXXIII Dirac fermions in graphene, Nature, 438 (2005) 197-200.

[11] Zhang Y., Jiang Z., Small J. P., Purewal M. S., Tan Y. W., Fazlollahi M., Chudow J. D., Jaszczak J. A., Stormer H. L., Kim P., Landau-Level Splitting in Graphene in High Magnetic Fields, Phys. Rev. Lett., 96 (2006) 136806.

[12] Katsnelson M. I., Novoselov K. S., Geim A. K., Chiral tunnelling and the Klein paradox in graphene, Nature Phys., 2 (2006) 620-625.

[13] Castro Neto A. H., Guinea F., Peres N. M. R., Novoselov K. S., Geim A. K., The electronic properties of graphene, Rev. Modern Phys., 81 (2009) 109-162.

[14] Nair R. R., Sepioni M., Tsai I-Ling, Lehtinen O., Keinonen J., Krasheninnikov A. V., Thomson T., Geim A. K., Grigorieva I. V., Spin-half paramagnetism in graphene induced by point defects, Nature Phys., 8 (2012) 199-202.

Yıldız / Cumhuriyet Sci. J., Vol.40-3 (2019) 753-761

[15] Liu Y., Tang N., Wan X., Feng Q., Li M., Xu Q., Liu F., Du Y., Realization of ferromagnetic graphene oxide with high magnetization by doping graphene oxide with nitrogen, Scientific Reports, 3 (2013) 02566.

[16] Giesbers A. J. M., Uhlirova K., Konecny M., Peters E. C., Burghard M., Aarts J., Flipse C. F. J., Inter-induced room-temperature ferromagnetism in hydrogenated epitaxial graphene, Phys. Rev. Lett., 111 (2013) 166101.

[17] Qin S., Guo X., Cao Y., Ni Z., Xu Q., Strong ferromagnetism of reduced graphene oxide, Carbon, 78 (2014) 559-565.

[18] Sarkar S. K., Raul K. K., Pradhan S. S., Basu S., Nayak A., Magnetic properties of graphite oxide and reduced graphene oxide, Phys. E, 64 (2014) 78-82.

[19] Ning G., Xu C., Hao L., Kazakova O., Fan Z., Wang H., Wang K., Gao J., Qian W., Wei F., Ferromagnetism in nanomesh graphene, Carbon, 51 (2013) 390-396.

[20] Raj K. G., Joy P. A., Ferromagnetism at room temperature in activated graphene oxide, Chem. Phys. Lett., 605 (2014) 89-92.

[21] Ramakrishna Matte H. S. S., Subrahmanyam K. S., Rao C.N.R., Novel magnetic properties of graphene: presence of both ferromagnetic and antiferromagnetic features and other aspects, J. Phys. Chem. C. 113 (2009) 9982–9985.

[22] Ray S. C., Soin N., Makgato T., Chuang C. H., Pong W. F., Roy S. S., Ghosh S. K., Strydom A. M., McLaughlin J. A., Graphene supported graphone/graphane bilayer nanostructure material for spintronics, Scientific Reports, 4 (2014) 03862.

[23] Jansen H. J. F., Freeman A. J., Structural and electronic properties of graphite via an all-electron total-energy local-density approach, Phys. Rev. B, 35 (1987) 8207-8214.

[24] Johansson L., Owman F., Mårtensson P., Persson C., Lindefelt U., Electronic structure of 6H-SiC (0001), Phys. Rev. B, 53 (1996) 13803-13807.

[25] Mounet N., Marzari N., First-principles determination of the structural, vibrational and thermodynamic properties of diamond, graphite, and derivatives, Phys. Rev. B, 71 (2005) 205214.

[26] Olse T., Thygesen K. S., Random phase approximation applied to solids, molecules, and graphene-metal interfaces: From van der Waals to covalent bonding, Phys. Rev. B, 87 (2013) 075111.

[27] Ohta T., Bostwick A., Seyller T., Horn K., Rotenberg E., Controlling the electronic structure of bilayer graphene, Science, 313 (2006) 951-954.

[28] Masrour R., Bahmad L., Benyoussef A., Size effect on magnetic properties of a nano-graphene bilayer structure: A Monte Carlo study, J. Mag. Mag. Mater., 324 (2012) 3991-3996.

[29] Orlof A., Ruseckas J., Zozoulenko I. V., Effect of zigzag and armchair edges on the electronic transport in single-layer and bilayer graphene nanoribbons with defects, Phys. Rev. B, 88 (2013) 125409.

[30] Kaneyoshi T., Magnetizations of a nanoparticle described by the transverse Ising model, J. Mag. Mag. Mater., 321 (2009) 3430-3435.

[31] Kaneyoshi T., Ferrimagnetic magnetizations of transverse Ising thin films with diluted surfaces, J. Mag. Mag. Mater., 321 (2009) 3630-3636.

[32] Kaneyoshi T., Magnetizations of a transverse Ising nanowire, J. Mag. Mag. Mater., 322 (2010) 3410-3415.

[33] Kaneyoshi T., Phase diagrams of a transverse Ising nanowire, J. Mag. Mag. Mater., 322 (2010) 3014-3018.

[34] Kaneyoshi T., Clear distinctions between ferromagnetic and ferrimagnetic behaviors in a cylindrical Ising nanowire (or nanotube), J. Mag. Mag. Mater., 323 (2011) 2483-2486.

[35] Kaneyoshi T., Some characteristic properties of initial susceptibility in a Ising nanotube, J. Mag. Mag. Mater., 323 (2011) 1145-1151.

[36] Kaneyoshi T., Ferrimagnetism in a ultra-thin decorated Ising film, J. Mag. Mag. Mater., 336 (2013) 8-13.

[37] Kaneyoshi T., Reentrant phenomena in a transverse Ising nanowire (or nanotube) with a diluted surface: Effects of interlayer coupling at the surface, J. Mag. Mag. Mater., 339 (2013) 151-156.

[38] Kaneyoshi T., Ferrimagnetic magnetizations in a thin film described by the transverse Ising model, Phys. Stat. Sol. (B), 246 (2009) 2359-2365.

[39] Kaneyoshi T., Magnetic properties of a cylindrical Ising nanowire (or nanotube), Phys. Stat. Sol. (B), 248 (2011) 250-258.

[40] Kaneyoshi T., Phase diagrams of a cylindrical transverse Ising ferrimagnetic nanotube, effects of surface dilution, Sol. Stat. Comm., 151 (2011) 1528-1532.

[41] Kaneyoshi T., The possibility of a compensation point induced by a transverse field in transverse Ising nanoparticles with a negative core–shell coupling, Sol. Stat. Comm., 152 (2012) 883-886.

[42] Kaneyoshi T., Ferrimagnetism in a decorated Ising nanowire, Phys. Lett. A, 376 (2012) 2352-2356.

[43] Kaneyoshi T., The effects of surface dilution on magnetic properties in a transverse Ising nanowire, Phys. A, 391 (2012) 3616-3628.

[44] Kaneyoshi T., Phase diagrams in an Ising nanotube (or nanowire) with a diluted surface; Effects of interlayer coupling at the surface, Phys. A, 392 (2013) 2406-2414.

[45] Kaneyoshi T., Characteristic phenomena in nanoscaled transverse Ising thin films with diluted surfaces, Phys. B, 407 (2012) 4358-4364.

[46] Kaneyoshi T., Phase diagrams in a ultra-thin transverse Ising film with bond or site dilution at surfaces, Phys. B, 414 (2013) 72-77.

[47] Kaneyoshi T., Characteristic behaviors in an ultrathin Ising film with site- (or bond-) dilution at the surfaces, Phys. B, 436 (2014) 208-214.

[48] Jiang W., Li X. X., Liu L. M., Chen J. N., Zhang F., Hysteresis loop of a cubic nanowire in the presence of the crystal field and the transverse field, J. Mag. Mag. Mater., 353 (2014) 90-98.

[49] Ertaş M., Kocakaplan Y., Dynamic behaviors of the hexagonal Ising nanowire, Phys. Lett. A, 378 (2014) 845-850.

[50] Kantar E., Keskin M., Thermal and magnetic properties of ternary mixed Ising nanoparticles with core-shell structure: effective-field theory approach, J. Mag. Mag. Mater., 349 (2014) 165-172.

[51] Magoussi H., Zaim A., Kerouad M., Effects of the trimodal random field on the magnetic properties of a spin-1 Ising nanotube, Chin. Phys. B, 22 (2013) 116401.

[52] Kocakaplan Y., Kantar E., Keskin M., Hysteresis loops and compensation behavior of cylindrical transverse spin-1 Ising nanowire with the crystal field within effective-field theory based on a probability distribution technique, Eur. Phys. J. B, 86 (2013) 40659.

[53] Jiang W., Li X. X., Liu L. M., Surface effects on a multilayer and multisublattice cubic nanowire with core/shell. Phys. E, 53 (2013) 29-35.

[54] Deviren B., Şener Y., Keskin M., Dynamic magnetic properties of the kinetic cylindrical Ising nanotube, Phys. A, 392 (2013) 3969-3983.

[55] Wang C. D. and Ma R. G., Force induced phase transition of honeycomb-structured ferroelectric thin film, Phys. A, 392 (2013) 3570-3577.

[56] Bouhou S., Essaoudi I., Ainane A., Saber M., Ahuja R., Dujardin F., Phase diagrams of diluted transverse Ising nanowire, J. Mag. Mag. Mater., 336 (2013) 75-82.

[57] Zaim A., Kerouad M., Boughrara M., Effects of the random field on the magnetic behavior of nanowires with core/shell morphology, J. Mag. Mag. Mater., 331 (2013) 37-44.

[58] Şarlı N., Band structure of the susceptibility, internal energy and specific heat in a mixed core/shell Ising nanotube, Phys. B, 411 (2013) 12-25.

[59] Şarlı N., Keskin M., Two distinct magnetic susceptibility peaks and magnetic reversal events in a cylindrical core/shell spin-1 Ising nanowire, Sol. Stat. Comm., 152 (2012) 354-359.

[60] Keskin M., Şarlı N., Deviren B., Hysteresis behaviors in a cylindrical Ising nanowire, Sol. Stat. Comm., 151 (2011) 1025-1030.

[61] Yüksel Y., Akıncı Ü., Polat H., Investigation of bond dilution effects on the magnetic properties of a cylindrical Ising nanowire, Phys. Stat. Sol. (B), 250 (2013) 196-206.

[62] Akıncı Ü., Effects of the randomly distributed magnetic field on the phase diagrams of the Ising Nanowire II: continuous distributions, J. Mag. Mag. Mater., 324 (2012) 4237-4244.

[63] Akıncı Ü., Effects of the randomly distributed magnetic field on the phase diagrams of Ising nanowire I: discrete distributions, J. Mag. Mag. Mater., 324 (2012) 3951-3960.

[64] Şarlı N., Akbudak S., Polat Y., Ellialtıoğlu M. R., Effective distance of a ferromagnetic trilayer Ising nanostructure with an ABA stacking sequence, Phys. A, 434 (2015) 194-200.

[65] Şarlı N., Akbudak S., Ellialtıoğlu M. R., The peak effect (PE) region of the antiferromagnetic two layer Ising nanographene, Phys. B, 452 (2014) 18-22.

[66] Lu Z. M., Si N., Wang Y. N., Zhang F., Meng J., Miao H. L., Jiang W., Unique magnetism in different sizes of center decorated tetragonal nanoparticles with the anisotropy, Phys. A, 523 (2019) 438-456.

[67] Wu C., Shi K. L., Zhang Y., W. Jiang, Magneticproperties of iron nanowire encapsulated in carbon nanotubes doped with copper, J. Magn. Magn. Mater. 465 (2018) 114-121.

[68] Zou C. L., Guo D. Q., Zhang F., Meng J., Miao H. L., Jiang W., Phys. E, 104 (2018) 138-145.

[69] Wang K., Yin P., Zhang Y., Jiang W., Phase diagram and magnetization of a graphene nanoisland structure, Phys. A, 505 (2018) 268-279.

[70] Wang J. M., Jiang W., Zhou C. L., Shi Z., Wu C., Magnetic properties of a nanoribbon: An effective-field theory, Superlattices and Microstructures, 102 (2017) 359-372.

[71] Jiang W., Wang Y. N., Guo A. B., Yang Y. Y., Shi K. L., Magnetization plateaus and the susceptibilities of a nano-graphenes and wich-like structure, Carbon, 110 (2016) 41-47.

[72] Kaneyoshi T., Differential Operator Technique In The Ising Spin Systems, Acta. Phys. Pol. A 83 (1993) 703-737.

[73] Yıldız Y. G., Origin of the hardness in the monolayer nanographene. Phys. Lett. A, 383 (2019) 2333-2338.

Comparison of Data Transfer Performance of BitTorrent Transmission Protocols

Halil ARSLAN [1,*] iD *, Özkan CANAY* [2] iD

[1] *Cumhuriyet University, Engineering Faculty, Dept. of Computer Engineering, Sivas, TURKEY*
[2] *Sakarya University, Adapazarı Vocational School, Dept. of Computer Technologies, Sakarya, TURKEY*

Abstract. BitTorrent, one of the distributed file sharing protocols, is regarded as one of the first examples of decentralized Internet philosophy and is among the important research areas in this context. TCP was initially used as the transport layer protocol in BitTorrent, and the transition to the uTP protocol was made because of the problems of latency and excessive bandwidth consumption. Later, with WebTorrent, which is a BitTorrent protocol adapted to the web, WebRTC was proposed as a transport layer protocol. Thus, BitTorrent protocol is enabled to work directly through Internet browsers without using any plugin. In this study, the data exchange sizes in the torrent shares of these three transmission protocols have been compared and the advantages and disadvantages of these protocols were demonstrated in this context.

*Keywords***:** BitTorrent, WebTorrent, TCP, uTP, WebRTC.

BitTorrent İletim Protokollerinin Veri Aktarım Başarımlarının Karşılaştırılması

Özet. Dağıtık dosya paylaşım protokollerinden BitTorrent, merkezi olmayan internet felsefesinin ilk örneklerinden olarak kabul edilmekte ve bu bağlamda önemli araştırma alanları arasında yer almaktadır. BitTorrent'te iletim katmanı protokolü olarak başlangıçta TCP kullanılmış, gecikme ve bant genişliğinin aşırı tüketilmesi problemlerinden dolayı uTP protokolüne geçiş yapılmıştır. Daha sonra BitTorrent protokolünün Web'e uyarlanmış hali olan WebTorrent ile iletim katmanı protokolü olarak WebRTC önerilmiştir. Bu sayede herhangi bir eklenti kullanmadan doğrudan internet tarayıcıları üzerinden BitTorrent protokolünün çalışması sağlanmıştır. Yapılan çalışmada, bu üç iletim protokolünün torrent paylaşımlarındaki veri alışveriş boyutları karşılaştırılmış ve bu bağlamda avantaj ve dezavantajları ortaya konulmuştur.

*Anahtar Kelimeler***:** BitTorent, WebTorrent, TCP, uTP, WebRTC.

1. INTRODUCTION

The BitTorrent protocol supports file sharing over peer-to-peer networks (P2P) using the TCP [1] and uTP [2] protocols. On the web side, the same function is performed with WebRTC via WebTorrent [3]. When the TCP protocol is used as the transmission protocol, BitTorrent protocol clogs the bandwidth in DSL and cable modems, and causing delays on interactive communications

[4]. For these reasons, the problem of consuming the full bandwidth is solved by using uTP as the transmission protocol [4]. In the following years Aboukhadijeh [5] suggested WebTorrent by making some protocol changes to run the BitTorrent protocol over WebRTC. WebTorrent is a simple JavaScript API that runs in the browser without the need for an extra plugin [6].

WebTorrent uses RTCDataChannel of WebRTC for P2P communication of BitTorrent protocol. Thus, WebRTC has been used as a data transmission layer for the BitTorrent protocol and the WebTorrent protocol has emerged [3]. In this way, man in the middle attacks are prevented [7] [8] and completely browser based torrent clients have emerged. This study examines the transport layer protocols recommended for the BitTorrent protocol, and compares the packet numbers and bandwidth usage that affect network performance.

2. DATA TRANSMISSION ON BITTORRENT

2.1. TCP

BitTorrent was designed by Bram Cohen in 2001 to seamlessly integrate with the web by defining the content URL for file sharing. When TCP (Transmission Control Protocol) is used as the transmission layer in the BitTorrent protocol, multiple TCP connections are opened and shared [9]. The most important advantage over HTTP is that it supports a large number of downloads from different sources with a slight increase in the file resource load. This causes delays in the Internet connection due to the filling of the sender buffer in DSL and cable modems [10].

Although this problem is solved by constantly limiting BitTorrent bandwidth, it is necessary for users to rearrange the restriction when they pass to different bandwidth networks [1]. At the same time, when bandwidth utilization increases, fixed limitations cause repeat latency and interruption. If the bandwidth utilization drops, the unused bandwidth will not be evaluated. Due to these problems, uTP protocol has been developed to dynamically adjust the bandwidth usage [11].

2.2. uTP

TCP protocol includes Additive Increase/ Multiplicative Decrease (AIMD) [12] to use equal bandwidth between TCP connections. However, BitTorrent uses a lot more bandwidth than applications that use a single TCP connection because it builds multiple TCP connections to peer nodes with the P2P architecture. Basically, to solve this problem BitTorrent has developed a UDP-based micro transport protocol (uTP) [13] based on new congestion control (Low Extra Delay Background Transport-LEDBAT) [14].

The uTP protocol dynamically runs on the unused portion of the bandwidth. The protocol controls the connection flows with the sliding window algorithm and preserves the data integrity with consecutive sequence numbers [15]. uTP basically uses a one-way delay measurement as the congestion control gain. The sender places a 32-bit time stamp in the data packet defining the sending time. The receiver calculates the one-way delay measurement and stores it as a delay vector. If the smallest value in the stored delay vectors is less than 100, the window size is increased. If it is higher than 100, it is decreased. This congestion control approach does not fill the send buffer and does not cause interruptions and delays in the user's Internet connection [11].

2.3. WebRTC

WebRTC (Web Real-Time Communications) is a JavaScript-based, open source free project that provides real-time communication without the need for additional extensions on browsers [16]. It is supported by browsers such as WebRTC, Firefox, Opera and Chrome, and platforms like Android and IOS, which are rapidly spreading at the point of browser support with HTML5 [17]. WebRTC provides a set of features for peer-to-peer communication and video conferencing in HTML, for instance connecting to remote peers using NAT traversal technologies such as ICE, STUN, and TURN, and sending data directly to remote users or receiving fragments from remote peers [18].

The main purpose of WebRTC is to access peripherals such as cameras and microphones in a secure way through the web application and to provide real-time data flow between peers. WebTorrent, which uses WebRTC as the transmission protocol, is a browser-based special torrent client that uses WebRTC data channels to connect to the BitTorrent network and does not need any additional downloads. In this sense, WebTorrent can offer direct torrent downloads

from browser to browser using WebRTC peer connections and WebSocket-based tracker protocol with partial changes to the BitTorrent protocol. However, WebRTC based WebTorrent and TCP / UDP based BitTorrent clients cannot communicate directly with each other. Transmission applications called hybrid clients are needed for this [19].

3.   METHODOLOGY AND MODEL
In order to compare the packet numbers and sizes that WebRTC, uTP and TCP protocols used during the transfer in BitTorrent usage, an appropriate model has been prepared to the network topology shown in Figure 1.
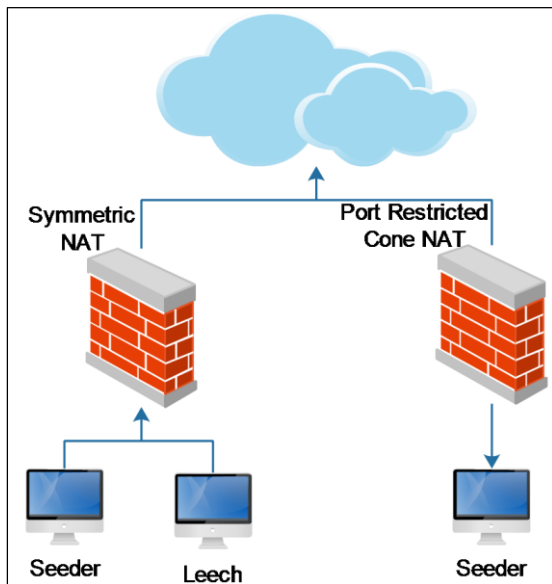

Figure 1. Application model

BitTorrent version 7.9.9 was used as the official processor of the BitTorrent protocol for TCP communication. For uTP communication, BitTorrent client is configured and transfer is made via uTP. The JavaScript-based WebTorrent client for WebRTC has been used over Google Chrome version 55.0.2883.87. For TCP and uTP transmissions with the BitTorrent client, all incoming and outgoing TCP and UDP connections have been allowed on the firewall of client's operating system. No settings have been made in the browser or operating system for WebRTC transmission.

The BitTorrent client has been used with default settings for uTP forwarding; by default, the

security settings will support unencrypted connections on outbound connections, and encrypted and unencrypted connections on incoming connections. In order for BitTorrent client to be able to transmit TCP, the default transmission method uTP protocol is set to passive and the TCP protocol is activated. By default, security settings are configured to allow unencrypted connections for outgoing connections and to support encrypted and unencrypted connections for incoming connections. End-to-end security on the WebRTC is not optional, as it is standard, no extra security settings have been set.

The first sharer is located under the Port Restricted Cone NAT, and the internet connection is realized on this way. The second sharer and client are located under Symmetrical NAT. Two sharers and one client are used for each transmission protocol. Two files of 100KB and 1MB in size, have been uploaded to both sharers and downloaded by the client respectively. Two files were requested separately for TCP, uTP and WebRTC protocols and network data were monitored. Six downloads were made in total. Packets transferred from starting client side communication until completion of downloading are captured, packet numbers and packet sizes are calculated and compared for each protocol separately.

4.   RESULTS AND DISCUSSION
In this study, the use of WebRTC, TCP and uTP as the transmission layer in the BitTorrent protocol is discussed. This transport layer protocol has been examined through the methodology and model presented in Chapter 3. The first sharer made a 100KB file share with BitTorrent uTP, and the second sharer shared this downloaded torrent via itself. After this process, two shareholders of the torrent with the same content were created. The client started downloading torrent content using uTP. The client receives part of the file from the shareholder on its own network and the other part from the shareholder behind a different NAT. Communication between the nodes behind Symmetric NAT and Port Restricted Cone NAT has been successfully

established. Subsequently, 1 MB file sharing was performed over the same model and the same transmission protocol.

The BitTorrent client for TCP transmission is configured to transmit TCP only, 100Kb and 1Mb files are downloaded separately from the two sharers. NAT transitions have been successful. As a result of this communication, the bandwidth and number of packets used by the client are shown in Table 1.

Table 1. Bandwidth and number of packets on BitTorrent TCP connection

File	Bandwidth	Num. of Packets
100KB	112,482 byte	150
1MB	1,119,539 byte	1,140

BitTorrent client for uTP transmission is configured, 100KB and 1MB files are downloaded separately from two sharers. Bandwidth and number of packets used by the client as a result of this communication are shown in Table 2.

Table 2. Bandwidth and number of packets on Bittorrent uTP connection

File	Bandwidth	Num. of Packets
100KB	119,772 byte	197
1MB	1,120,156 byte	1,010

For WebRTC transmission, a browser-based application that transmits WebTorrent via WebRTC runs on two shareholders; 100KB and 1MB torrents were uploaded to the first sharer. The second sharer has downloaded the torrent with the created torrent link via WebRTC and started sharing. As a result of the process, two shareholders of the file were created. Some parts of the file are downloaded from the sharer on the same network and the other parts are downloaded from the sharer behind the different NAT. The NAT transition was successful.

Since the client network is Symmetrical NAT, and the other sharing network is Port Restricted Cone NAT, it has been observed that the TURN server has been activated and data is relayed via this server. For this reason, it has been observed that STUN and TURN processes have been successfully performed in accordance with the ICE framework. The bandwidth and number of packets used by the client as a result of the transmission through WebRTC via WebTorrent are shown in Table 3.

Table 3. Bandwidth and number of packets on WebRTC Transmission

File	Bandwidth	Num. of Packets
100KB	136,246 byte	345
1MB	1,680,905 byte	5,467

After the completion of the transfer within using all the protocols, bandwidth and number of packets used for the 100KB file are shown in Figure 2 and Figure 3, respectively.
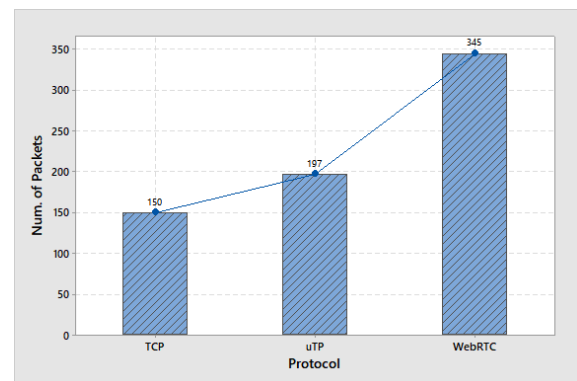

Figure 2. Total number of packets for 100KB file transfer

In the 100KB file transfer, TCP has completed the transfer with 150 package, uTP used 197 packet, and WebRTC used 345 packets for this communication.
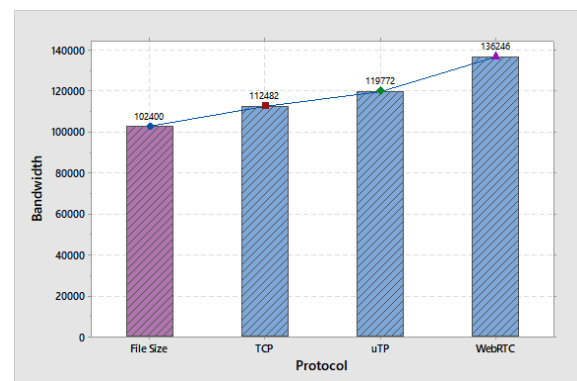

Figure 3. Bandwidth utilization for 100KB file transfer

In this sharing process, the total size of data sent outside the file size (overhead) was approximately 10KB (10,082 byte) in the TCP protocol, 17KB (17,372 byte) in the uTP protocol, and 33KB (33,846 byte) in the WebRTC protocol.

After all the transfers are complete with all protocols, bandwidth utilization and number of packets for the 1MB file are presented comparatively in Figure 4 and Figure 5.

uTP protocol works on UDP basis and it is observed that the added control packets and the congestion control algorithm increase the communication size because the transferred data should be sent lossless to the other side and thus use more packets and bandwidth than the TCP protocol. The WebRTC protocol seems to use quite a lot of packets and bandwidth compared to uTP and TCP. It can be said that the main factor that increases the number of packets is the signaling packets and the data fragments sent with low payload caused by the activation of the TURN Server.
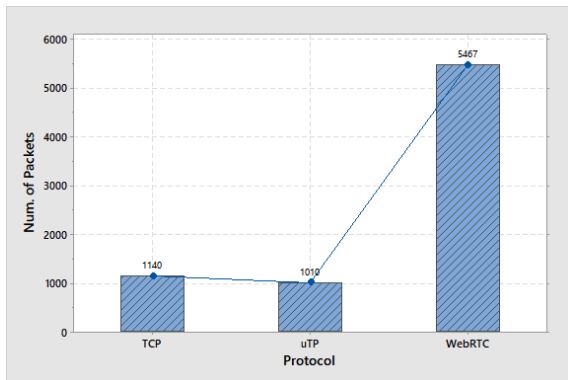

Figure 4. Total number of packets for 1MB file transfer

It is considered that the reason for the excessive use of bandwidth in WebRTC is the dTLSv1.2 protocol used for end-to-end security after signaling and the overhead caused by the TURN server.
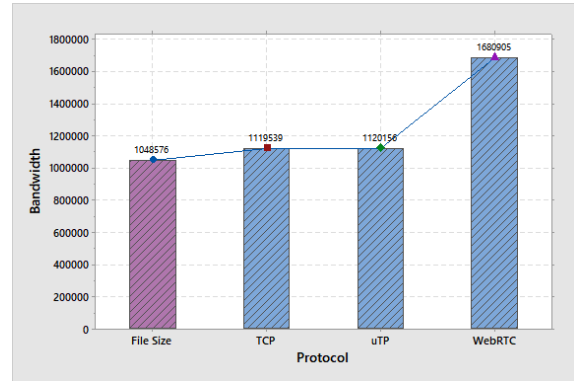

Figure 5. Bandwidth utilization for 1MB file transfer

5. CONCLUSION

Although it is observed that WebRTC is the protocol that has the most packet traffic and bandwidth usage in file transfers made with BitTorrent protocols the use of this protocol seems to be advantageous compared to the uTP and TCP protocols in the use of BitTorrent because it provides significant convenience at the end-user point, such as platform, installation and configuration requirements. Over time, it is expected that WebRTC's connection efficiency will be improved. Also, it's observed that on the BitTorrent Protocol running on TCP and uTP, encrypted connection for connection security is optional and can be running by giving special permissions to the operating system firewall.

BitTorrent (WebTorrent) protocol running on WebRTC brings significant advantages such as working on web browsers, no need for additional software installation, no need for specific firewall permission, providing dTLSv1.2 protocol as standard for connection security, user security, and end-to-end confidentiality. In future studies, the security parameters of BitTorrent transmission protocols can be examined and their advantages and disadvantages can be demonstrated.

REFERENCES

[1] Gong, Y., Rossi, D., Testa, C., Valenti, S., & Täht, M. D. Fighting the bufferbloat: on the coexistence of AQM and low priority congestion control. Computer Networks, 65 (2014) 255-267.

[2] Adamsky, F., Khayam, S. A., Jäger, R., & Rajarajan, M. Stealing bandwidth from BitTorrent seeders. Computers & Security, 46 (2014) 126-140.

[3] Aboukhadijeh, Feross. Streaming torrent client for the web. https://github.com/feross/webtorrent. Retrieved February 1, 2017.

[4] Norberg, A. uTorrent transport protocol. http://www.bittorrent.org/beps/bep_0029.html. Retrieved January 30, 2017.

[5] Aboukhadijeh, F. WebTorrent: Using WebRTC and Mad Science to Bring BitTorrent to the Web. Software Delivery Craftsmanship Matters (2014)

[6] Burgstaller, F., Derler, A., Kern, S., Schanner, G., & Reiter, A. Anonymous communication in the browser via onion-routing. IEEE 10th International Conference on P2P, Parallel, Grid, Cloud and Internet Computing (3PGCIC) (2015) 260-267.

[7] A Study of WebRTC Security. NTT Communications project. http://webrtc-security.github.io/. Retrieved January 29, 2017.

[8] Feher, B., Sidi, L., Shabtai, A., & Puzis, R. The Security of WebRTC. arXiv preprint: 1601.00184. (2016) 1-10.

[9] Cohen, B. Incentives build robustness in BitTorrent. Workshop on Economics of Peer-to-Peer systems, 6 (2003) 68-72.

[10] Testa, C., & Rossi, D. Delay-based congestion control: Flow vs. BitTorrent swarm perspectives. Computer Networks, 60 (2014) 115-128.

[11] Adamsky, F. Analysis of bandwidth attacks in a bittorrent swarm (Doctoral dissertation). University of London. (2016)

[12] Chiu, D. M., & Jain, R. Analysis of the increase and decrease algorithms for congestion avoidance in computer networks. Computer Networks and ISDN systems, 17(1) (1989) 1-14.

[13] Rossi, D., Testa, C., Valenti, S., & Muscariello, L. LEDBAT: the new BitTorrent congestion control protocol. Proceedings of IEEE 19th International Conference on Computer Communications and Networks (2010) 1-6

[14] Testa, C., & Rossi, D. On the impact of uTP on BitTorrent completion time. IEEE International Conference on Peer-to-Peer Computing (2011) 314-317.

[15] Adamsky, F., Khayam, S. A., Jäger, R., & Rajarajan, M. P2P file-sharing in hell: exploiting BitTorrent vulnerabilities to launch distributed reflective DoS attacks. 9th USENIX Workshop on Offensive Technologies (2015)

[16] Arslan, H., Tuncel, S., & Yuksek, A. G. Comparison of the Web based multimedia protocols for NAT traversal performance. IEEE 23nd Signal Processing and Communications Applications Conference (SIU) (2015) 915-918.

[17] WebRTC - Real Time Communications in the browser. http://www.webrtc.org. Retrieved February 1, 2017.

[18] Hickson, I. WebRTC 1.0: Real-time Communication Between Browsers. http://www.w3.org/TR/webrtc/. Retrieved February 1, 2017.

[19] Aboukhadijeh, F. WebTorrent. JSConf Asia. https://2014.jsconf.asia/. Retrieved February 1, 2017.

Effects of Calcined Phosphogypsum on the Geotechnical Parameters of Fine-Grained Soils

Ahmet ŞENOL [1,*] iD

[1] *Cumhuriyet University, Faculty of Engineering Department Civil Engineering, 58140 Sivas*

Abstract. In this article, the using of waste materials has been studied such as phosphogypsum in the alteration of fine-grained soils in order to upgrade the geotechnical properties as a construction material. Standard Proctor test, unconfined compressive strength tests and California bearing ratio were carried out on Calcined Phosphogypsum (CPG) stabilized soil samples. It was determined that the phosphogypsum with additives calcined at the low temperature 150 ºC. Treatment with CPG generally reduces the maximum dry density but CPG increase the optimum moisture content. Compressive strength, California bearing ratio were performed to investigate effects of additive mixtures of stabilized and natural soil specimen. The empirical results show that stabilized samples with CPG additive mixtures have high durability as compared to unstabilized samples. These contribution blends have also improved the dynamic behaviors of the soil samples. As a result, we conclude that CPG additive mixtures can be completely used as an additive material to strength of granular soils in highway constructions and embankment applications. The experiment results understood that the stabilized fine-grained soil specimens containing CPG show high resistance to the CBR and unconfined compressive strengths as compared to natural fine-grained soil samples.

Keywords: Soil stabilization, waste materials, phosphogypsum, fine-grained soils.

İnce Taneli Zeminlerin Geoteknik Özelliklerinde Kalsine Edilmiş Fosfojips'in Etkisi

Özet. Bu çalışma, bir yapı malzemesi olarak ince taneli zeminlerin geoteknik özelliklerini yükseltmek için fosfojips gibi atık maddelerin kullanımını değerlendirmektedir. Kalsine Fosfojips (CPG) ile stabilize edilen zemin numuneleri üzerinde, standart proctor deneyi, Kaliforniya taşıma gücü ve serbest basınç ve optmum su muhevası deneyleri yapılmıştır. Gübre fabrikası atığı olan fosfojips 150 ºC gibi düşük sıcaklıkta kalsine edilmiştir. Kalsine edilmiş fosfojips (CPG) katılan ince taneli zeminlerin maksimum kuru yoğunluğu azalmıştır, ancak optimum su muhtevası değerleri artmıştır. Serbest basınç mukavemetinin, California taşıma gücü oranının, doğal ve stabilize zemin örnekleri üzerindeki etkileri araştırılmıştır. Deney sonuçları, stabilize edilmemiş numunelere kıyasla CPG katkılı karışımların daha yüksek dayanıklılığa sahip olduğunu göstermektedir. Sonuç olarak, CPG katkılı karışımların, yol inşaatları ve hafriyat dolgu uygulamaları için ince taneli zeminlerin dış etkilere karşı mukavemetinde başarılı bir şekilde kullanılabileceği sonucuna varılmıştır. Test sonuçları, CPG içeren stabilize ince taneli zemin numunelerinin, doğal ince taneli zemin numunelerine kıyasla daha yüksek CBR direnci ve serbest basınç mukavemeti sergilediğini göstermektedir.

Anahtar Kelimeler: Zemin stabilizasyonu, atık malzemeler, fosfojips, ince taneli zeminler.

---

1. INTRODUCTION

Chemical improvement is the variety of the properties of a locally existing soil to improve its mechanical capacity. The lime stabilization and cement stabilization are two most frequently used chemical improvement methods [1]. To further improve the properties of stabilized soil, phosphogypsum can be added to the soil as an additive. In this study, phosphogypsum, an industrial waste, has been used as a chemical stabilization ingredient to improve the mechanical properties of chosen soils. Phosphogypsum (PG) is industrial waste of products in phosphoric fertilizer factories. Roundly 3500 tons per day of PG are produced every year in Bandırma-BAGFAŞ plant of Turkey; these wastes are tried to be made harmless by various ways in landfills, rivers and waste ponds.

Phosphogypsum consists of some impurities such as P_2O_5, F^-, essentially of calcium sulfate and organic substances. The use of phosphosypsum as construction material is restricted. The reason for this is the presence of purity in it. The gypsum and cement industries currently use only a small proportion of this by-product as a retarder for cement and for the construction of bricks and gypsum plaster [1–8]. Phosphogypses were reused with some achievement in the road substructures and cylinder compressed concrete [9-10]. Phosphogypsum can be improved by fly ash with thermal power plant waste that other industrial waste and Portland cement for possible use in soil improvement. Phosphophosum mixed with cement has long been studied for about ten years [11,12]. Phosphogypsum is not enough for road infrastructure or embankment construction lonely. Blends prepared with fly ash, phosphogypsum, and Portland cement provide slightly higher geotechnical values maximum dry unit weight and OMC values for improved phosphogypsum mixtures, in comparison with unimproved phosphogypsum mixtures. Most of these studies suggested that cement with C_3A content less than 7% can be used with phosphogypsum [13]. The planned properties of soil-cement mixture and soil type describes cement content requirements. The amount of clay in the soil is decisive for stabilization in generally. Some studies suggest that the amount of cement content can be chosen between 5 %-15% by clay. [14,15]. Researchers are also advised to prepare almost too close to the optimum water content and maximum dry unit weight values when preparing mixtures containing phosphogypsum (PG). [16,17].

Many methods to change the geotechnical properties of fine-grained soils have been proposed to date. These methods can be expressed as stabilization by chemical ejection, wetting, other soil displacement, compression control, moisture control, additional load loading and thermal methods [18-20]. In particular, new studies are carried out to reduce swelling behavior and permeability. These studies ultimately increase the Strength properties. [21-23]. Many researches have studied natural materials and fabricated products such as geofiber to change the fine-grained soils.

The main purpose of this study is to investigate the suitability of phosphogypsum calcined at the low temperature 150 ºC to increase on the geotechnical properties of fine-grained soils as a stabilization material. Stabilized and natural fine-grained soil samples were tested in laboratory conditions to obtain better results.

2. MATERIALS AND METHODS
2.1. Fine-Grained Soil

The fine-grained soil has been supplied from the basalt quarry crusher plant deposits of Mesudiye-Çatalkaya, Ordu, Northeast of Turkey (Fig.1). The material used in experimental studies remain within the boundaries of the base material granulometry determined by the General Directorate of Highways of Turkey. X-ray diffraction (XRD) pattern of the fine-grained soil and the grain-size distribution are given in Figs. 2 and 3. Meanwhile, its engineering and index properties are summarized in Table 1.

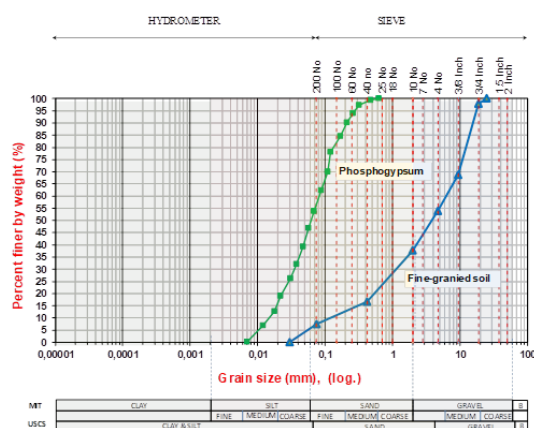**Fig. 1.** Location map of the fine-grained soils used.

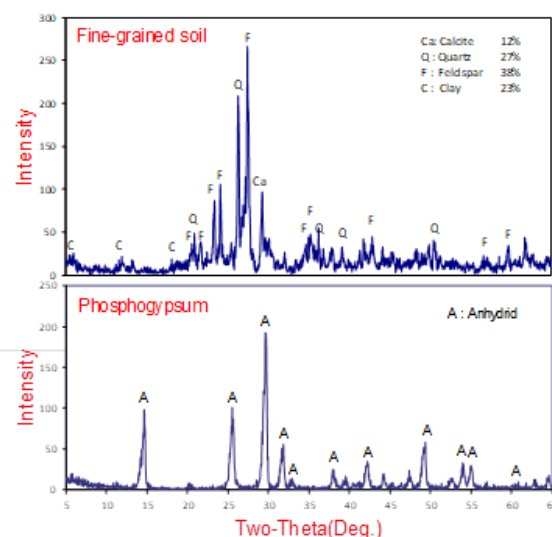**Fig. 2.** The grain-size distributions of fine-grained soil and phosphogypsum.

Fig. 3 X-ray diffraction (XRD) pattern of the fine-grained soil and the phosphogypsum

Table 1 Engineering properties of Phosphogypsum and fine-grained soil.

Property	Fine-grained soil	Phosphogypsum
Density		
Density, (Mg/m3)	2.649	2.39
Grain-size		
Gravel (> 2000 μm), %	60	--
Sand (2000–75 μm), %	35	55
Silt (2–75 μm), %	5	45
Clay (< 2 μm), %	--	--

2.2. Phosphogypsum

Bandırma-Turkey Fertilizer Plant which PG used in the research was brought here, obtains PG as a by-product in the process of producing phosphoric acid production by phosphate rock. The chemical compositions of waste phosphogypsum is seen in Table 2. Important component of PG is calcium sulfate and, consequently, PG (pH less than 3) exhibits acidic properties. The relative density of PG is 2.87, the optimum water content is 12-13 % and the maximum dry density is 14.53 kN/m^3, according to the standard Proctor test. The grain size distribution range is 0.5–1.0 mm. PG can be classified as a silty soil also seen from the Fig 1., a ML (USCS) or A-4 (AASHTO) soil, with almost no plasticity. PG determined by The Nuclear Research and Training Center in Çekmece/Turkey, known as ÇNAEM are ^{226}Ra: 22 Bq kg^{-1}, ^{238}U: 9.0 Bq kg^{-1}, ^{232}Th: 1.0 Bq kg^{-1} and ^{40}K:11 Bq kg^{-1}. As a result of the measures taken by Bagfas fertilizer plants, phosphogypsum

has been classified as a weak radioactive substance [24].

The PG was stored outdoors fields, and the convenient amount of PG was air-dried and calcined at low temperature. The required amount of calcined phosphogypsum (CPG) measured depending on weight of waterless soil and incorporated to the soil. The ingredients (soil +

CPG) were first added and mixed in dry condition for 3 min, and then to a certain extent water was added and the mixer was stirred for 2 minutes. The mixture was put into the mold and compressed. The amount of water added to the mixture is determined as the optimum water content.

Table 2 The chemical compositions of waste phosphogypsum

Chemical parameters	SiO_2	Al_2O_3	Fe_2O_3	CaO	SO_3	Na_2O	P_2O_5	F	CaO_{free}	Loss on ignition
PG	3.44	0.88	0.32	32.04	44.67	0.13	0.50	0.79	0.81	21.06

2.3. Experimental Study

Soil sample can be classified as an A-1,A-3 soil according to the the AASHTO soil classification system and according to the Unified Soil Classification System SP-SM type.

The mixtures were composed of different percentage of calcined phosphogypsum by holding the optimum water content. The mixture proportions of the bonding agents are given in Table 3. Phosphogypsum was used as unworked and calcined materials for making the adhesive agent. A appropriate amount of phosphogypsum was air dried and sieved through a 4.75 mm sieve before using. To create calcined gypsum, phosphogypsum was heated in an electric oven at 150 °C for 6 hours. The calcined material was desiccated in a closed container to room temperature to avoid any contamination.

Maximum dry density and OMC of all mixtures were obtained by SPT with respect to AASHTO T - 99 and ASTM. When the compression process was in progress, the soil determined by the amount of water was placed in a mold of standard sizes in five layers, and compacted by 56 blows of rammer dropped from a distance of 457 mm at each layer, subjecting the soil to total compactive effort.

The unconfined compression (UC) tests were implemented according to ASTM 266 and unconfined compression strength values (qu) were determined. Samples with a 30 cm length and 15 cm diameter were prepared. The samples were placed in a great desiccator (humidification

vessel) to prevent from drying while waiting a turn at the compression machine. Six samples were prepared for each ratio and tested at a deformation rate 0.5 mm / min.

The homogeneous soil blend was created by adding the required amount of stabilizer. The required water determined is poured into soil mixtures. The species were molded at maximum unit weight and OMC in accordance with ASTM D1557. Geotechnical tests as SPT and unconfined compressive strength (qu) tests were applied on soil samples prepared with stabilizer addition at variable percentages in order to examine their influence. Tables 3. Presents Compaction features and the definition of soil mixtures. Each soil samples used in the unconfined compressive strength test was statically compacted in the cylindrical mold (15cm in diameter and 30cm high) at the optimum water content and maximum dry density. For curing, the samples were closely covered and placed in any box. Ambient temperature fixed to 21 °C. The species cured for 7 days and after curing unconfined compressive strength test was conducted.

2.4. California bearing ratio tests

CBR method is the most common method for evaluating the comparative resistance of soils in road construction. California bearing ratio (CBR) tests were performed using a cylindrical test mould kit on samples compacted in three layers at maximum dry unit weight and the OMC determined by conducting standard Proctor tests.

The tests were performed following AASHTO T193. According to AASHTO T193-63 and ASTM D1883-73, the soaking period for CBR samples for normal soil is 96 h or 4 days.

The CBR specimens prepared with different proportions of CPG to soil at its optimum water content were compacted and then soaked in water. The results of CBR tests obtained are tabulated in Table 3. For evaluating of efficiency of CPG improvement on CBR's results and also swelling potential of soil the soaked and unsoaked CBR tests are conducted on natural soil samples at first and the amount of swelling is obtained about 1 percent. Then specimens are prepared with different mixtures of CPG. These samples are exposed to a temperature of 23 degrees Celsius for 28 days while maintaining the same humidity. After that unsoaked CBR results of samples were calculated. After that, the prepared samples were immersed in water for 96 hours and reading of swelling is controlled. Then saturated CBR tests results were calculated. The results are showed in Table 3and Fig 6. It appears that the addition of 20% CPG gives the maximum percentage increase in CBR value (ratio of obtained CBR value/highest CBR value) after curing for 96 hours; see Fig. 5 (a). The CBR amounts of prepared specimens with different CPG percentage (5, 10, 15 and 20 percent) show that improving soil with CPG is most suitable.

Table 3. Detail of Soil-CPG Mixtures for Tests Conducted

Combination		MDUW (kg/m³)	OWC (%)	CBR$_{average}$	CBR$_{rate}$ of increase	Percent swell CBR (%)	Max. stress (kPa)	Axial strain (%)
SOIL	SOIL	2225	4.3	184.53	1,0	3.05	637.43	13.800
SOPG5	SOIL+ PHOSPHOGYPSUM 5 %	2220	5.3	209.04	1,1	2.67	906.13	12.933
SOPG10	SOIL+ PHOSPHOGYPSUM 10 %	2151	5.5	218.86	1,2	2.56	1061.08	10.467
SOPG15	SOIL+ PHOSPHOGYPSUM 15 %	2140	7.0	229.58	1,2	2.43	1211.12	9.733
SOPG20	SOIL+ PHOSPHOGYPSUM 20 %	2059	7.64	239.41	1,3	2.35	1379.80	8.600

3. RESULT AND DISCUSSION

3.1. Analysis of compaction parameters in mixtures

Figs. 4. shows the effects of bonding agent mixtures on the OMC and the maximum dry densities. The results presents that the supplement of bonding agent mixtures revealed an increase in OMC and a reduction in maximum dry density. The high dry unit weights and the low OMC occur in unimproved samples, while the low dry unit weights and the high OMC occur in improved samples with 20% CPG bonding agent mixtures. The reason why increased in OMC is an increase in the total particle surface area of the improved samples due to the addition of finer materials. That's why, the OMC increased in the improved samples. Depending upon an increase in OMC, the maximum dry unit weights decreased in the improved specimens gradually. It was found that the OMC ranged from 4 to 8% for fine grained soil and the maximum dry densities ranged from 2.2 to 2.05 in Mg/m³ for fine grained Soil.
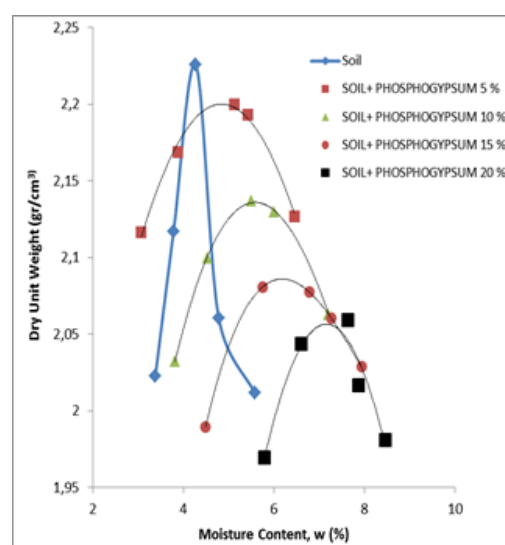

Fig. 4. Effects of CPG on the dry unit weight and moisture content.

3.2. Analysis of compressive strength in mixtures

Fig. 5 presents the effects of bonding agent mixtures on the compressive strength. It is observed that the compressive strength results increase by the addition of bonding agent mixtures in the improved samples. The CPG particles stabilize the soil matrix at the interfaces with the soil textures, resulting in a denser improved soil sample. Unconfined compressive strengths of unimproved soils were in all situations lower than improved soils. There is significant benefit strength with addition of CPG. The benefit in unconfined compressive strength is dependent on the CPG content. A high increase in unconfined compressive strength take placed with 20% of CPG content for soil.

3.3. Analysis of CBR in additive mixtures

The CBR test was performed to investigate the behavior of samples stabilized with additives. These tests were carried out in the Modified Proctor mold by adding the additive and adding the additive. These tests were repeated on day 28. The effects of additive mixtures on CBR are given in Figure 6. With increasing amounts of CPG additive, it has been shown that CBR values are increased and this is achieved in all mixtures. Depending on the amount of additive, the compressive strength and CBR were found to be increased. It is seen from the results of natural

samples and stabilized samples that there is a linear relationship between the compressive strength and CBR values.
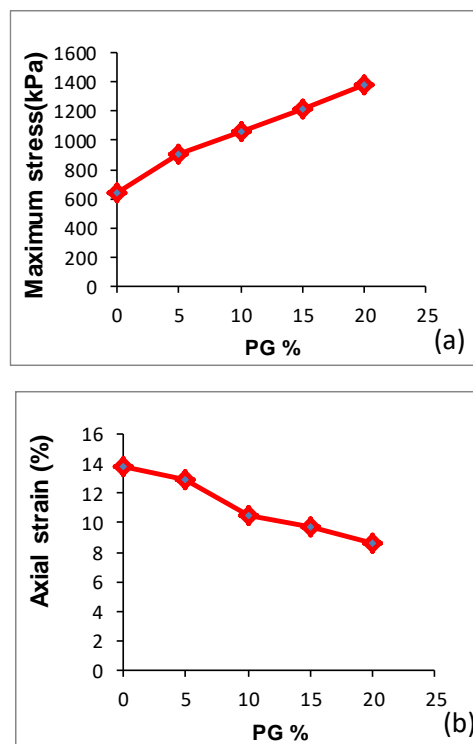

Fig. 5. Unconfined compressive strength (a) and strain (b) of soil stabilized with addition of CPG.
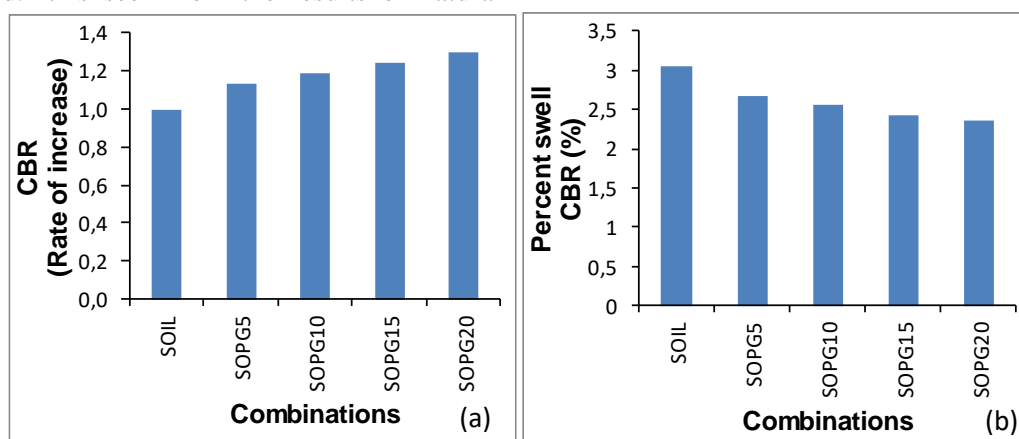

Fig. 6. The effects of different CPG content increase in (a) CBR values, (b) percent swell CBR

4. CONCLUSION

In this study, the geotechnical effects of phosphosypsum additive blended granular soils

are investigated and the following results are obtained:

• Experimental results showed that, with the addition of phosphosypsum additive, the maximum dry density of the mixtures decreased and the optimum moisture content increased.

• Additive mixtures increased compressive strength. It has played an important role in the development of CBRs of granular soils. Generally, in all mixtures, the compression strength and CBR values are increased by the addition of CPG additive. Maximum compressive strength and CBR values are obtained by adding 20% of additive mixtures.

In addition, waste materials, such as phosphosypsum, can potentially reduce the costs of balancing by using waste in a cost-effective manner. In addition, the use of various industrial wastes such as phosphosypsum not only solve the environmental problems but also provides a new source for the construction industry.

REFERENCES

[1] Degirmenci N., Okucu A. and Turabi Ayse., Application of phosphogypsum in soil stabilization, Building and Environment, 42 (2007) 3393–3398.

[2] Singh M., Influence of blended gypsum on the properties of Portland cement and Portland slag cement, Cement and Concrete Research, 30 (2000) 1185–8.

[3] Altun IA. and Sert Y., Utilization of weathered phosphogypsum as set retarder in Portland cement, Cement and Concrete Research, 34 (2004) 677–80.

[4] Singh M., Treating waste phosphogypsum for cement and plaster manufacture, Cement and Concrete Research, 32 (2002) 1033–8.

[5] Kumar S., A perspective study on the fly ash-lime-gypsum bricks and hollow blocks for cost housing development, Construction and Building Materials, 16 (2002) 519–25.

[6] Kumar S., Fly ash–lime–phosphogypsum hollow blocks for walls and partitions, Building and Environment, 38 (2003) 291–5.

[7] Singh M. and Garg M., Cementitious binder from fly ash and other industrial wastes. Cement and Concrete Research, 29 (1999) 309–14.

[8] Verbeek CJR. and du Plessis BJGW., Density and flexural strength of phosphogypsum-polymer composites, Construction and Building Materials, 19 (2005) 265–74.

[9] Gregory CA., Saylak D. and Ledbetter WB., The use by-product of phosphogypsum for road bases and subbases, Transportation Research Board, Washington, DC, (1984) 998.

[10] Chang WF., A demonstration project: roller compacted concrete utilizing phosphogypsum, Florida Institute for Phosphate Research Bartow, FL., 01 (1988) 068-072

[11] Kolias S., Kasselouri-Rigopoulou V. and Kaarhalios., A., Stabilization of clayey soils with high calcium fly ash and cement, Cement and Concrete Composites, 27 (2005) 301–13.

[12] Roy A., Kalvakoalve R. and Seals RK., Microstructure and phase characteristics of phosphogypsum cement mixtures, Journal of Materials in Civil Engineering, 8 (1998), 11-18.

[13] ASTM C 150., Standard specification for Portland cement, Annual book of ASTM, Philadelphia, USA: The American Society for Testing and Materials, 04.01-04.02 (2002) 01-02

[14] Rahman AMD., Lateric soil in construction, Building and Environment, 21 (1986) 57–61.

[15] Pericleous MI. and Metcalf JB., Resilient modulus of cement-stabilized phosphogypsum, The Journal of Materials of Civil Engineering, 8 (1996) 7-10.

[16] Federal Highway Administration., User guidelines for waste and byproduct materials, FHWA-RD-97-148, Washington DC. (1997).

[17] Chen, F.H., Foundations on Expansive Soils. Elsevier, (1988).

[18] Steinberg, M., Geomembranes and the Control of Expansive Soils in Construction. McGray-Hill, New York, (1998)

[19] Nelson, J.D., Miller, D.J., Expansive Soils: Problems and Practice in Foundation and Pavement Engineering. John Wiley and Sons, Inc., New York, (1992).

[20] Yong, R.N., Ouhadi, V.R., Experimental study on instability of bases on natural and lime/cement-stabilized clayey soils, Applied Clay Science,35 (2007) 238–249.

[21] Puppala, A.J. and Musenda, C., Effects of fiber

reinforcement on strength and volüme change in expansive soils, Transportation Research Record,00-716 (2002) 134–140

[22] Akbulut, S., Arasan, S. and Kalkan, E., Modification of clayey soils using scrap tire rubber and synthetic fibers, Applied Clay Science, 38 (2007) 23–32.

[23] Moavenian, M.H. and Yasrobi, S.S., Volume change behavior of compacted clay due to organic liquids as permeant, Applied Clay Science, 39 (2008) 60–71.

[24] Degirmenci, N., The using of waste phosphogypsum and natural gypsum in adobe stabilization, Constr. Build. Mater., 22 (2008) 1220-1224.

Cumhuriyet Science Journal

CSJ

Assesment of outdoor radioactivity and health risk in Adıyaman Province of Turkey

Muhammet KARATAŞLI iD

Beykent University, Faculty of Engineering and Architecture, Department of Electronics and Communication

Engineering, İstanbul, TURKEY

Abstract. This study was conducted to determine the outdoor absorbed gamma dose levels in and around Adiyaman province in the southeast of Turkey. Measurements were performed using a portable plastic scintillator at 94 different points (Eberline Smart Portable (ESP-2) model). Three readings were made for each measurement and the mean of these three values were determined and the gamma dose values were determined for each measurement region. External gamma irradiation velocities were measured between 63.5 (nGy/h) and 380.2 (nGy/h) levels in Adıyaman and surrounding areas and the mean value was calculated as 144.3 (nGy/h). This value corresponds to the average effective dose equivalent of 177 μSv per year. The lifetime averages of cancer risk values for ICRP 103, BEIR VII and ICRP 60 were found to be 0.071, 0.079 and 0.089, respectively. The results obtained with the results of similar studies in other provinces in Turkey and compared with the world average

Keywords: Cancer risk, gamma dose, annual effective dose, Adıyaman Province.

Adıyaman İlinde Dış Mekan Radyoaktivitesi ve Sağlık Risklerinin Değerlendirilmesi

Özet. Bu çalışma Türkiye'nin güneydoğusunda bulunan Adıyaman ili ve çevresinde açık havada soğurulan gama radyasyon doz seviyesini belirlemek için yapılmıştır. Ölçümler önceden belirlenmiş 94 farklı noktada (Eberline Smart Portable (ESP-2) model) portatif bir plastik sintilatör kullanılarak yapıldı. Her ölçüm için üçer okuma yapılmış ve bu üç değerin ortalaması alınarak her bir ölçüm bölgesi için gama doz değerleri belirlendi. Adıyaman ve çevresinde dış gama dozu kullanılarak, dış gama ışınlanma hızları 63.5 (nGy/h) ile 380.2 (nGy/h) değerleri arasında ölçüldü ve ortalama değer 144.3 (nGy/h) olarak hesaplandı. Bu değer yıllık etkin doz eşdeğeri 177 μSv değerinde etkin doz ortalamasına karşılık gelmektedir. Adıyaman ve çevresinde yaşam boyu kanser risk değerleri ICRP 103, BEIR VII ve ICRP 60 için yüzdelik ortalamaları sırasıyla sırasıyla 0,071, 0,079 ve 0,089 olarak bulundu. Elde edilen sonuçlarla Türkiye'de diğer illerde yapılan benzer çalışmaların sonuçları ve dünya ortalamaları ile karşılaştırılmıştır.

AnahtarKelimeler: Kanser riski, gama doz., yıllık etkin doz, Adıyaman.

1. INTRODUCTION

Although most people think that radiation is released only from man-made devices and structures (medicine, industry, research, nuclear power plants, agriculture and animal husbandry), they emit radiation to the environment in which we live in very long-lived radioactive elements that have taken place in nature since the formation of the

universe. Natural radiation is the main source of radiation that people are exposed to in their environment. While living things are under the influence of a dose of 85% from natural radiation sources, they are under 15% of artificial radiation sources [1,2].

The major contribution to natural radiation is the naturally occurring U-238, Th-232 and their degradation products, Ra-226, Rn-222 and U-235, which are derived from radioactive elements such as K-40 [3]. The mass activity concentration is the radiation intensity corresponding to the absorbed dose in the air at a height of 1 m. Therefore, the radiation dose measured in the air is closely related to the radio-core concentrations in the soil [4,5].

The contribution of cosmic temperatures to natural radiation varies with height and is taken as constant at certain latitude values as they rise up from sea level [6,7].

Nuclear weapons experiments conducted on the earth from 1945 to the present day and the Chernobyl nuclear accident that occurred in 1986 caused the spread of radioactive elements to the environment. However, these radiations can also be called ground level radiation, and the geological and geographic, geographic and geographic region, so the soil and rocks with the geographic height, the level of the level of the level of radiation affect [9,10].

In order to determine whether the area inhabited in terms of natural radiation is healthy or not, it is necessary to determine the concentrations of radio-nuclei that constitute natural sources of radiation and the effect of radiation on human beings and to determine the effect of radiation on biological systems. Therefore, studies have been conducted to evaluate the doses and types of radiation caused by environmental factors, as well as the risks it may pose to human health [2].

In this study, determination of the dose level of gamma radiation absorbed in the outdoor in and around Adıyaman province is important in terms of determining the rate of exposure of the natural radiation to the radiation caused by various nuclear applications. The results presented in this study were compared with the results of Turkey's and the world average of similar studies conducted in different regions. The results of the study may serve as a reference for future assessments.

2. MATERIALS AND METHODS

2.1. Geology of the survey area

Adiyaman, which has a surface area of 7614 km², is located between the northern latitudes of the 37° 25'-38° 10' and the eastern longitudes of the 37° 27' – 39° 15'. The land structure of the province has a rugged view that descends from north to south. Adıyaman and its surroundings are shown in Figure 1.

On the lands of Adıyaman, one of the oldest settlements in the world, findings about all phases of human history have been obtained. Adıyaman, the 8th wonder of the world known as the Nemrut Mountain works, the ruins of the Commagene civilization, the 4th largest dam in the world, the Atatürk Dam, the Çamgazi dam, the winter camp organization, the world championship is a city with the world's first [11].

Figure 1. Map of the study area; Adıyaman province, Turkey [12].

The north of Adiyaman is mountainous and the south is ovalık. The plain runs from the south to the banks of the EuphratesRiver and the Atatürk Dam. A few kilometers north of the province and the central district, the mountainous areas begin to rise northward. These mountains, which are part of the southeastern Taurus, extend in the east-west direction. In the mountainous areas to the north, which make up more than one third of the face, the highland climate prevails [13].

There are several units of magmatic, metamorphic and sedimentary rocks formed in the geological time period from Mesozoic to the present day. Mesozoic units are the oldest of these geological units. Eocene limestones anticline structures are exposed in the eroded or faulted areas of Plio-Quaternary deposits. Apart from this, the base area consists entirely of Plio-Quaternary fillings. The youngest formations are the Quaternary alluviums in the valley floor and slab systems [14].

The number of stations with the altitude and catchment area of each district were given in Table 1. The geographic coordinates of the stations were determined by using GPS devices.

2.2. Gamma Scintillation Detector

In this study, a device with Eberline Smart Portable (ESP-2) model, portable microcomputer and SPA-6 model plastic scintillation detector connected to the end was used for determination of gamma radiation levels. The Eberline Smart Portable (ESP-2) is a portable radiation inspection instrument that can be mounted with radiation detectors, a microcomputer-based and data-recording instrument. This instrument is designed for use in routine radiation examinations and allows multiple readings and can be subsequently connected to a computer and printer. ESP -2 is designed as an interface for the user, it has seven multi-function on / off buttons and a liquid crystal display (LCD). The data is given either as scientific or moving point recording and in selectable units of measurement. In addition, the instrument consists of an external headset and speaker system for use in high radiation areas [15,16].

Table 1. Distribution of stations in the research region of Adıyaman

District	Latitude (N)	Longitude (E)	Altitude (m)	Catchment area (km^2)	Population (2017)	Number of Stations
AdıyamanCenter	37.759722	38.259722	669	1702	301589	33
Gölbaşı	37.7768518	37.6374277	867	784	49059	8
Kahta	37.7750854	38.6139386	750	1490	120859	14
Besni	37.6890364	37.8545142	930	1330	75499	13
Samsat	37.5762285	38.4677502	610	338	7530	6
Tut	37.7886992	37.9097588	1050	350	9936	6
Çelikhan	38.0255984	38.2366530	1388	584	15326	4
Gerger	38.0280715	39.0341811	750	702	18244	6
Sincik	38.0364507	38.6125706	1325	364	17034	4

3. RESULTS AND DISCUSSION

In order to determine the dose level of gamma radiation absorbed outdoors in 94 different regions in and around Adıyaman, the height of gonad (reproductive organs) in humans is approximately 1m above the ground. Measurements were taken with Eberline portable detector. Three different readings were made at a radius of 5 meters while the measurements were taken in each region and the mean of these three values were determined and gamma dose values were determined for each measurement region.

The results of the measurements of the external gamma dose obtained in the open air at a height of 1 meter from the ground in the 94 different regions of Adıyaman and around it are given in Table 2. During the determination of the gamma dose values, three readings were made at each measurement site. Gamma dose values were determined for each measurement point by taking the average of the three values. The results include both cosmic and terrestrial radionuclides.

While the contribution of terrestrial gamma radiation in the air is very large, space-based cosmic rays also contribute to the ratio. Measurements carried out at a height of 1 m from the ground are important in terms of measurement in the outdoors, in the level of reproductive organs in humans.The results of gamma irradiation rates were obtained in μR/h in the measurements performed for one minute in the open air. As can be seen in Table 2, the results obtained in the measurements were converted to nGy/h elde, which was the absorbed dose rate using a conversion factor (8.7 nGy / μR) from the definition of Rontgen [17].

Table 2. Gama exposure dose rate and absorbed dose rate for each districts of the Adıyaman

District	GEDR (Gamma Exposure Dose Rate) (μR/h)			ADRA (Absorbed Dose Rate in Air) (nGy/h)		
	Minimum	Maximum	Mean	Minimum	Maximum	Mean
AdıyamanCenter	10.8	40.3	15.5	94	350.6	134.4
Gölbaşı	7.3	43.7	19.7	63.5	380.2	171
Kahta	9.2	19.6	13.7	80	170	118.8
Besni	13.1	34.3	18.7	114	298.4	163
Samsat	13.2	22.3	16.4	114.8	194	143
Tut	11.4	24.5	19.3	99.2	213.2	167.9
Çelikhan	21.2	29.5	24.7	184.4	256.7	214.7
Gerger	7.8	17.6	13.5	67.9	153.1	117.2
Sincik	12.3	18.2	15.9	107	158.3	138.1
Region	7.3	43.7	16.6	63.5	380.2	144.3

By using a dose ratio of the gamma radiation absorbed in the air, the annual effective dose equivalent (AEDE) may be the amount of exposure to which the human is exposed to radiation for one year. Using the equation below, the annual effective dose equivalent is calculated [18,19].

$$AEDE=ADRA*DCF*OF*T \tag{1}$$

Here, the annual effective dose equivalent of AEDE, ADRA is the ratio of gamma radiation dose absorbed in the air; The environmental gamma dose conversion factor was determined to be 0.7 Sv/Gy to convert the absorbed dose ratio to the annual effective dose equivalent. In addition, when a person spent 20% of the time he was exposed to rays during a year (8760 h / y) he spent outside the home in open spaces, a coefficient of 0.2 was used as out-of-home occupation factor. In addition, lifetime risk of cancer ELCR Denk. (2)[20,22].

$$ELCR=AEDE*DL*RF \tag{2}$$

Here, the AEDE is the annual effective dose equivalent, the average life expectancy of DL (average 70 years), and the risk factor for RF, and for stochastic effects, ICRP risk factors for lethal cancer in the whole population, respectively (1/Sv), RF ICRP 103, BEIR VII [23] (NRC, 2006) and for ICRP 60, 0.057, 0.064 and 0.072 are used [24].

Table 3 shows the AEDE and the ELCR values of people who have been exposed for one year in Adıyaman and its surroundings, calculated by Equation1 and Equation2, and environmental gamma radiation for one year.

Table3. The average annual effective dose values and lifetime cancer risk

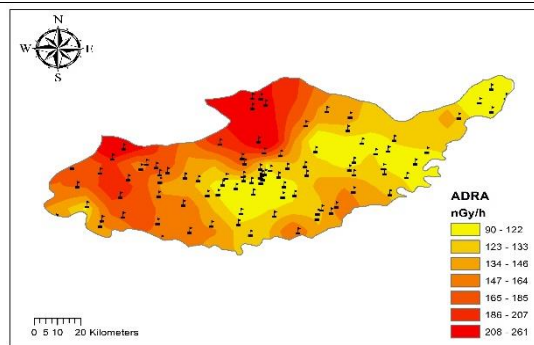| District	AEDE (µSv/y	Lifetime cancer risk %		
		ICRP 103	BEIR VII	ICRP 60
AdıyamanCenter	164.8	0.066	0.074	0.083
Gölbaşı	209.7	0.084	0.094	0.106
Kahta	145.7	0.058	0.065	0.073
Besni	199.9	0.080	0.090	0.101
Samsat	175.4	0.070	0.079	0.088
Tut	205.9	0.082	0.092	0.104
Çelikhan	263.3	0.105	0.118	0.133
Gerger	143.7	0.057	0.064	0.072
Sincik	169.4	0.068	0.076	0.085
Region	177.0	0.071	0.079	0.089

Figure 2ADRA in Adıyaman

In addition, the absorbed gamma dose map obtained from the measurements for Adıyaman and its surroundings was drawn. Figure 2 shows the general distribution of the absorbed gamma dose rate across the province in the form of an isodose map. The dark regions represent areas with high abundance of absorbed gamma dose in Adıyaman and its vicinity.The arithmetic mean of the gamma dose measurements performed in 94 different regions in and around Adıyaman province was calculated as 144.3 nGy/s. The mean value of the annual effective dose equivalent calculated using the external gamma dose was found to be 177 µSv/y. This value is greater than the value of 73.6 µSv/y [25], which is determined as the world average of the annual effective dose equivalent, as shown in Table 4. Also it found was greater than the average annual effective dose equivalent in other provinces outside the studies

5

carried out in the province of Adıyaman in the study average annual effective dose equivalent Balikesir province in Turkey.

Table 4. Absorbed dose rate in air (94 readings) and the corresponding annual effective doses for the districts of Adıyaman and comparison with literature

	ADRA (Absorbed Dose Rate) (nGy/h)	AEDE (Annual effective dose) (µSv/y)
Hatay [2].	61.9	75.9
Çankırı [26].	69.6	87.7
Trabzon [27].	59	72.4
Tekirdağ [28].	43.85	53.77
Çanakkale [29].	66.4	81.4
Şanlıurfa[10].	60.9	74.7
Kastamonu [30].	54.81	67.21
İstanbul [31].	65	79.7
Balıkesir [32].	127	155.8
Yalova [33].	84	103
Kırklareli [22].	118	144.7
Kahramanmaraş [15].	64.8	79.5
Worldwide [25].	60	70

4.CONCLUSİON

The arithmetic average of gamma dose measurements in Adıyaman and its vicinity is less than 1 mSv/y, as determined by the ICRP as the limit value of the annual effective dose equivalent of 144.3 nGy/h [34]. The lifetime averages of cancer risk values for ICRP 103, BEIR VII and ICRP 60 in Adıyaman and its vicinity were found to be 0.071, 0.079 and 0.089, respectively.

The issue of radiation has become one of the most controversial phenomena in the world after the unfortunate nuclear reactor accidents, and people's sensitivities to this issue are increasing day by day. In parallel with this awareness, people's demand for information on radiation is increasing. Therefore, it is extremely important for people to be informed about the natural radiation that they will be exposed to stay in according to their geographic and geological characteristics. Therefore, this study, environmental gamma dose measurements in Adıyaman and its districts can be used as baseline data for future studies and a reference for future evaluations

can be made. It will also be very useful in terms of radiation monitoring in the event of any nuclear accident in the future and in the evaluation of radiological risks to human health.

REFERENCES

[1] UNSCEAR, 2008. United Nations Scientific Committee on the Effects of Atomic Radiation, United Nations Publication, New York, USA.

[2] Karataşlı, M. 2018. Hatay İli ve çevresinde gama radyasyon ölçümü, Afyon Kocatepe Üniversitesi Fen ve Mühendislik Bilimleri Dergisi, 18, 3,780-785.

[3] Smith, J. and Beresford, N.A. 2005. Chernobyl, Catastrophe and Consequences. Springer, 310, New York.

[4] Beck, H.L, 1982. The Natural Radiation Environment II. USERDA Conf.-720805-P2, The Physics of Environmental Gamma Radiation Fields, 101-104.

[5] NCRP, Report No. 50, 1977. National Council on Radiation Protection and Measurements, (1977), Environmental Radiation Measurement, ISBN. 0- 913392-32-4.

[6] Eisenbud, M. 1987. Environmental Radioactivity, Third Edition, ISBN. 0-12-235153, Academic Pres, Inc., London.

[7] Karataşlı, M., and Özer, T. 2017. Investigation of Radiation Activity Growing Peanuts in Osmaniye, *Süleyman Demirel University Journal of Natural and Applied Sciences*, 21, 3, 1017-1023.

[8] Karataşlı, M. 2018. Dozimeters in business safety, *İstanbul Aydın Üniversitesi Dergisi,10* (1), 15-31.

[9] Karataşlı, M. 2018. Radionuclide and heavy metal content in the table olive (Olea europaea l.)from the Mediterranean region of Turkey, *Nuclear Technology & Radiation Protection*, 33,4, 1-7.

[10] Bozkurt, A., Yorulmaz, N., Kam, E., Karahan, G. and Osmanlıoğlu, A. E. 2007. Assessment of environmental radioactivity for Şanlıurfa region of Southeastern Turkey. *Radiation Measurements*, 42, 8, 1387-1391.

[11] http://www.cografya.gen.tr/tr/adiyaman/ (24.01.2019).

[12] Aykut, M., and Taşar, G.E. 2018. Contributions To The Knowledge Of Adephagan Fauna In Adiyaman Province, Turkey (Coleoptera: Dytiscidae, Gyrinidae, Haliplidae And Noteridae),*Munis Entomology & Zoology*, 13, 1, 249-255.

[13] http://www.adiyamankulturturizm.gov.tr/TR-61334/genel-bilgiler.html (23.01.2019).

[14] Karadoğan, S., and Tonbul, S. 2013. Geomorphological properties of Adıyaman Basin, *The Journal of Academic Social Science,* 1,1, 182-217.

[15] KARATAŞLI, M. 2019. Determination of outdoor absorbed gamma dose rates of Kahramanmaraş Provınce, Turkey, Cumhuriyet University, Cumhuriyet Science Journal. 40 (1), 102-107.

[16] Değerlier, M. 2007. Determination ofEnviromental Natural Radioactivity of Adana and The Annual Effective Dose Equivalent Due to Natural Radiation, Ph.D. Thesis, Department Of Physics Institute Of Natural And Applied Sciences University of Çukurova, Adana

[17] Baykara, O. 2005. The determinations of natural radioactivity in the intersect zone of the North Anatolian Fault and East Anatolian Fault. PhD thesis, Firat University Graduate School of Natural and Applied Science, Physics Department, Elazig, Turkey (in Turkish).

[18] UNSCEAR, 2000. Report of the United Nations Scientific Committee on the Effects of Atomic Radiation, Sources, Effects, and Risks of Ionizing Radiation. United Nations sales publication, New York. United Nations.

[19] Karataşlı, M., Turhan, Ş., Varinlioğlu, A., and Yeğingil, Z. 2016. Natural and fallout radioactivity levels and radiation hazard evaluation in soil samples. *Environmental Earth Science*, 75, 424, 1-9.

[20] UNSCEAR 2008. Report of the United Nations Scientific Committee on the Effects of Atomic Radiation, Sources, Effects, and Risks of Ionizing Radiation. United Nations sales publication, New York. United Nations.

[21] Ramasamy V., Sundarrajan M., Paramasivam K., Meenakshisundaram V., and Suresh G., 2013. Assessment of spatial distribution and radiological hazardous nature of radionuclides in high background radiation area, Kerala, India. *Applied Radiation Isotopes*, 73:21-31.

[22] Taskin, H., Karavus, M., Ay, P., Topuzoglu, A., Hidiroglu, S., and Karahan, G. 2009. Radionuclide concentrations in soil and lifetime cancer risk due to gamma radioactivity in Kirklareli, Turkey. *Journal of Environmental Radioactivity*, 100,1, 49–53.

[23] NRC,2006. National Academy of Sciences. National Research Council Committee to Assess Health Risks from Exposure to Low Levels of Ionizing Radiation. Report of VII

[24] ICRP, 2007. International Commission on Radiological Protection. Recommendations of the ICRP. ICRP Publication 103. Ann. ICRP 37 (2–4).

[25] UNSCEAR, 2000. United Nations Scientific Committee on the Effect of Atomic Radiation to the General Assembly, Sources, Effects and Risk of Ionizing Radiation, United Nations, New York, USA.

[26] Kapdan, E., Taşkın, H., Kam, E., Osmanlıoğlu, A.E., Karahan, G., and Bozkurt A. 2011. A study of environmental radioactivity measurements for Cankiri. Turkey. *Radiation Protection Dosimetry*, 150, 3, 398–404.

[27] Kurnaz, A., Kucukomeroglu, B., Damla, N., and Cevik, U. 2011. Radiological maps for Trabzon, Turkey. *Journal of Environmental Radioactivity*, 102, 4, 393–399.

[28] Kam, E., Yarar, Y., and Bozkurt, A. 2010. A study of background radioactivity level for Tekirdag. *Turk Radiat Prot Dosimetry,*138, 40–44.

[29] Kam, E., Bozkurt, A., and Ilgar, R. 2010. A study of background radioactivity level for Canakkale. Turkey. *Environmantal Monitoring and Assessment,* 168, (1-4), 685– 690.

[30] Kam, E., and Bozkurt, A. 2007. Environmental radioactivity measurements in Kastamonu region of northern Turkey. *Applied Radiation and Isotopes,* 65, 440–444.

[31] Karahan, G. and Bayulken, A. 2000. Assesment of Gamma Dose Rates Around Istanbul. *Journal of Envrionmental Radioactivity*, 47, 2, 213-221.

[32] Kapdan, E., Varinlioglu, A., and Karahan, G. 2012. Outdoor radioactivity and health risks in Balikesir, Northwestern Turkey, *Radiation Protection Dosimetry*, 148, 3, 301–309.

[33] Kapdan, E., Varinlioglu, A. and Karahan, G. 2011. Radioactivity Levels and Health Risks due to Radionuclides in the Soil of Yalova, Northwestern Turkey. *International Journal of Environmental Research*, 5(4), 837-846.

[34] ICRP, 1990. The International Commission on Radiological Protection, ICRP Publication 60. Recommendations of the International Commission on the Radiological Protection, Pergamon Press Inc., ICRP, USA.

AUTHOR GUIDELINES

Thank you for choosing to submit your paper to Cumhuriyet Science Journal. The following instructions will ensure we have everything required so your paper can move through pre-evaluating, peer review, production and publication smoothly. Please take the time to read and follow them as closely as possible, as doing so will ensure your paper matches the journal's requirements.

Submission

Cumhuriyet Science Journal is an international, peer-reviewed, free of charge journal covering the full scope of both natural and engineering sciences. Manuscripts should be submitted by one of the authors of the manuscript as online submission after registration to the Cumhuriyet Sciences Journal. Microsoft Word (.doc, .docx, .rtf), files can be submitted. There is no page limit. If there is a problem while uploading the files of manuscript, please try to reduce their file size, especially manuscripts including embedded figures. Submissions by anyone other than one of the authors will not be accepted. The submitting author takes responsibility for the paper during submission and peer review. If for some technical reason submission through the online submission systme is not possible, the author can contact csj@cumhuriyet.edu.tr for support.

Submission or processing charges

Cumhuriyet Science Journal does not charge any article submission, processing charges, and printing charge from the authors.

Terms of Submission

Papers must be submitted on the understanding that they have not been published elsewhere (except in the form of an abstract or as part of a published lecture, review, or thesis) and are not currently under consideration by another journal. The submitting author is responsible for ensuring that the article's publication has been approved by all the other coauthors. It is also the authors' responsibility to ensure that the articles emanating from a particular institution are submitted with the approval of the necessary institution. Only an acknowledgment from the editorial office officially establishes the date of receipt. Further correspondence and proofs will be sent to the author(s) before publication unless otherwise indicated. It is a condition of submission of a paper that the corresponding author permit editing of the paper for readability. All enquiries concerning the publication of accepted papers should be addressed to csj@cumhuriyet.edu.tr. Please note that Cumhuriyet Science Journal uses iThenticate software to screen papers for unoriginal material. By submitting your paper to Cumhuriyet Science Journal are agreeing to any necessary originality checks your paper may have to undergo during the peer review and production processes. Upon receiving a new manuscript, the Editorial office conducts initial pre-refereeing checks to ensure the article is legible, complete, correctly formatted, original, within the scope of the journal in question, in the style of a scientific article and written in clear English. Any article that has problems with any of the journal criteria may be rejected at this stage.

Peer Review

This journal operates a single blind review process. All contributions will be initially assessed by the editor for suitability for the journal. Papers deemed suitable are then typically sent to a minimum of two independent expert reviewer to assess the scientific quality of the paper. The author is required to upload the revised article to the system within 15 days by making the corrections suggested by the referee. The article will be rejected if there are no fixes in it. The Editor is responsible for the final decision regarding acceptance or rejection of articles. The Editor's decision is final

Title and Authorship Information

The following information should be included

Paper title

Full author names

Full institutional mailing addresses

Corresponding address

Email address

Abstract

The manuscript should contain an abstract. The researchers who are native speakers of Turkish have to add Turkish title and abstract as well. The abstract should be self-contained and citation-free and should be 250-300 words.

Keywords

Keywords of the scientific articles should be selected from the web address of www.bilimadresleri.com

Introduction

This section should be succinct, with no subheadings.

Materials and Methods

This part should contain sufficient detail so that all procedures can be repeated. It can be divided into subsections if required.

Conflicts of interest

Sample sentence if there is no conflict of interest: The authors stated that did not have conflict of interests.

Acknowledgements

Sample sentences for acknowledgements: The work was supported by grants from CUBAP (T-11111). We would like to acknowledge Prof. Mehmet Sözer, MD, for his precious technical and editorial assistance. We would like to thank

References

References to cited literature should be identified by number in the text in square brackets and grouped at the end of the paper in numerical order of appearance. Each reference must be cited in the text. Always give inclusive page numbers for references to journal articles and a page range or chapter number for books. References should be styled and punctuated according to the following examples

[1] Keskin B. and Ozkan A.S., Inverse Spectral Problems for Dirac Operator with Eigenvalue Dependent Boundary and Jump Conditions, Acta Math. Hungar., 130-4 (2011) 309– 320.

[2] National Cancer Institute, Surveillance Epidemiology and End Results. Cancer of the Corpus and Uterus, NOS. Available at: http://seer.cancer.gov/statfacts/html/corp.html?statfacts_page=corp. Retrieved March 2, 2008. (Sample reference of website)

[3] Isaacson K.B., Endometrial ablation. In: UpToDate, Basow, DS (Ed), UpToDate, Waltham, M.A., 2008. (Sample reference of Uptodate topics)

[4] Speroff L., Fritz M.A., Anovulation and The Polycystic Ovary. In. Speroff L., Fritz M.A., (Eds). Clinical Gynecologic Endocrinology and Infertility. 7th ed. Philadelphia, Pa: Lippincott Williams and Wilkins; 2005: chap 12. (Sample reference of online book chapters found in websites).

[5] Mazur M.T., Kurman R.J., Dysfunctional Uterine Bleeding. In: Mazur M.T., Kurman R.J., (Eds). Diagnosis of endometrial biopsies and curettings. A practical approach. 2nd ed. Berlin: Springer, 2005; pp 100-120. (Sample reference of printed book chapters)

Preparation of Figures

Each figure can be integrated in the paper body or separately uploaded and should be cited in a consecutive order. Figure widths can be 4-6 inch as 300 dpi. The labels of the figures should be clear and informative. The name and the subtitles of the figures must be 9-point font.

Preparation of Tables

Tables should be cited consecutively in the text. Every table must have a descriptive title and if numerical measurements are given, the units should be included in the column heading. Tables should be simple with simple borders and text written as left text. The name and the subtitle of the tables must be 9-point font

Proofs

Corrected proofs must be returned to the publisher within 2 weeks of receipt. The publisher will do everything possible to ensure prompt publication. It will therefore be appreciated if the manuscripts and figures conform from the outset to the style of the journal.

Copyright

Ethical Guidelines

New methods and ethically relevant aspects must be described in detail, bearing in mind the following:

Human Experiments. All work must be conducted in accordance with the Declaration of Helsinki (1964). Papers describing experimental work on human subjects who carry a risk of harm must include:

A statement that the experiment was conducted with the understanding and the consent of the human subject.

A statement that the responsible Ethical Committee has approved the experiments.

Animal Experiments. Papers describing experiments on living animals should provide:

A full description of any anaesthetic and surgical procedure used.

Evidence that all possible steps were taken to avoid animal suffering at each stage of the experiment. Papers describing experiments on isolated tissues must indicate precisely how the donor tissues were obtained.

Submission Preparation Checklist

As part of the submission process, authors are required to check off their submission's compliance with all of the following items, and submissions may be rejected that do not adhere to these guidelines.

The submission has not been previously published, nor is it before another journal for consideration (or an explanation has been provided in Comments to the Editor).

The submission file is in Microsoft Word document file (Times New Roman) format.

Where available, URLs for the references have been provided.

The text is single-spaced; uses a 11-point font; employs italics, rather than underlining (except with URL addresses); and all illustrations, figures, and tables are placed within the text at the appropriate points, rather than at the end.

The text adheres to the stylistic and bibliographic requirements outlined in the Author Guidelines, which is found in About the Journal.

If submitting to a peer-reviewed section of the journal, the instructions in Ensuring a Double-Blind Review have been followed.